CORA Cork Open Research Archive
Cartlann Taighde Oscailte Chorcaí

Title	Macroporous metal oxide battery electrode performance analysis and operando spectroscopy
Authors	Grant, Alex
Publication date	2023
Original Citation	Grant, A. 2023. Macroporous metal oxide battery electrode performance analysis and operando spectroscopy. PhD Thesis, University College Cork.
Type of publication	Doctoral thesis
Rights	© 2023, Alex Grant. - https://creativecommons.org/licenses/by-nc/4.0/
Download date	2026-11-16 10:06:53
Item downloaded from	https://hdl.handle.net/10468/15972



UCC
University College Cork, Ireland
Coláiste na hOllscoile Corcaigh

Macroporous Metal Oxide Battery Electrode Performance Analysis and Operando Spectroscopy



ucc

Coláiste na hOllscoile Corcaigh, Éire
University College Cork, Ireland

Thesis Presented by:

Alex Grant, B.Sc. (Hons)

School of Chemistry

University College Cork, Ireland

For the degree of Doctor of Philosophy to the National University of Ireland, Cork

Supervisor: Prof. Colm O' Dwyer

October 2023

Declaration

This statement is to certify that the work presented in this thesis is my own research and that no part of this thesis has been submitted previously for consideration for another degree at University College Cork or any other research institute. All research was performed under the direction of Prof. Colm O' Dwyer and references are made to the contributions of other authors. I have read and understood the terms and conditions regarding plagiarism prior to submission, as outlined by University College Cork

Signed

_____

Alex Grant

Dedicated to

Mam and Dad

Acknowledgements

At the time of writing, I am 25 years old, and have spent 8 years in UCC, which I would never have foreseen when I moved to Cork here first. The first two years of this PhD were particularly unexpected, with the madness of Covid-19, numerous lockdowns with the lab shutdown, what seemed like an endless 4 year deadline and found myself constantly wondering what possessed me to go down this route. With the pandemic in the rear-view mirror, the last 2 years of the PhD have been much different. The combination of being able to work consistently, and the ability to see the people that make it all easier changed everything. The main takeaway from all of this is that I've had nothing but the best of support along all the ups and downs, meaning that there is a lot of thanks in order.

Professor Colm O' Dwyer, you gave me the opportunity to work in this area in the first place. In terms of research, you were always ready with ideas on how to progress, where I was going wrong and what to do next. Given the doubts and indecision of the first two years, your patience was endless, and you accommodated me no matter what. I can't thank you enough as you saw me through the process.

On a daily basis, it's the people I worked and had lunch with every day that made the PhD enjoyable. Regardless of whether the research was going well or poorly, getting a chat with any of the lads at lunchtime solved all my problems and let me reset. From lab 343, Umair, Yan, Alex, and Matthew were all a massive help. Sitting next to Aoife every day in the office, the lab along with all our trips to Atlanta, Belfast, Strasbourg, and Galway meant you had to

put up with the brunt of my moods, but you were usually able to to pull me out of them. Outside the group, there's too many to name, but I'll give a special mention to Niall, Rachel, Eadaoin, Will and Paddy here. As for Ash, we only had the chance to meet at the end, but you helped me see things through with your relentless positivity.

All my family helped me along the way, particularly my sister Ciara, aunt Roberta and my grandmother Nuala. Mick, Kay, and Noel have always been kept in mind as well. Saving the best for last, I must thank Mam and Dad. While everyone mentioned so far helped me along the way, it cannot be understated how important your help was for me. This thesis is dedicated to both of you as it would not have been written without you, and I don't know where I'd be without you either.

Publications

1) **Grant, A.**; Carroll, A.; Zhang, Y.; Gulzar, U.; Ahad, S. A.; Geaney, H.; O'Dwyer, C. Comparing Cycling and Rate Response of SnO2 Macroporous Anodes in Li-Ion and Na-Ion Batteries. Journal of The Electrochemical Society 2023, 170 (12), 120505. DOI: 10.1149/1945-7111/ad0ff5.

2) **Grant, A**.; Lonergan, A.; O'Dwyer, C. Thickness control of dispersion in opal photonic crystals. Optical Materials 2023, 142, 114053. DOI: 10.1016/j.optmat.2023.114053.

3) **Grant, A.**; O'Dwyer, C. Real-time non-destructive methods for examining battery electrode materials. Applied Physics Reviews 2023, 10 (1). DOI: 10.1063/5.0107386

4) **Grant, A.**; O'Dwyer, C. Asymmetrical optical response of opal photonic crystals with graded thickness. ECS Advances 2023, 2 (4), 043501. DOI: 10.1149/2754-2734/ad0cd4.

5) Carroll, A.; **Grant, A.**; Zhang, Y.; Gulzar, U.; Douglas-Henry, D.; Nicolosi, V.; O'Dwyer, C. The effect of TiO2 and GeO2 composite mixing on the behaviour of macroporous Li-Ion battery anode materials. Journal of The Electrochemical Society 2023, 170 (12), 120521. DOI: 10.1149/1945-7111/ad1371.

6) Zhang, Y.; **Grant, A.**; Carroll, A.; Gulzar, U.; Ferguson, M.; Roy, A.; Nicolosi, V.; O'Dwyer, C. Water-soluble binders that improve electrochemical Na-ion storage properties in a NaTi2(PO4)3 Anode. Journal of The Electrochemical Society 2023, 170 (5), 050529. DOI: 10.1149/1945-7111/acd3b8.

7) Gulzar, U.; Lonergan, A.; Egorov, V.; Zhang, Y.; **Grant, A.**; Carroll, A.; O'Dwyer, C. Methods—Ampero-Coulometry: A new technique for understanding Li-sulfur electrochemistry. Journal of The Electrochemical Society 2023, 170 (3), 030503. DOI: 10.1149/1945-7111/acbca0.

Poster Presentations

- Operando Raman Spectroscopy Revealing Li Consumption Source and Phase Changes at the Electrode/Electrolyte Interface in Li-Ion Battery Systems, *E-MRS 2023 Spring Meeting, May 29 – June 2, 2023, Strasboug, France.*

Oral Presentations

- Thickness-Based Dispersion in Opal PhCs**,** *242nd ECS Meeting, October 9-13, 2022, Atlanta, GA, USA.*
- Operando Raman Spectroscopy of Phase Changes in Nanocrystalline Metal Oxide Li-Ion Battery Electrodes, *242nd ECS Meeting, October 9-13, 2022, Atlanta, GA, USA.*
- Operando Raman Spectroscopy of Phase Changes in Nanocrystalline Li-ion Battery Electrodes**,** *Early Career Researcher Regional Symposium on Electrochemistry, November 4, 2022, Queen's University Belfast, Ireland.*
- High-Capacity Inverse Opal Tin Oxide Electrodes for Li-Ion and Na-Ion Energy Storage, *E-MRS 2023 Spring Meeting, May 29 – June 2, 2023, Strasbourg, France.*
- Inverse Opal Electrodes for Sustainable Battery Technology, *74th Irish Universities Chemistry Research Colloquium, June 14-15, University of Galway, Ireland.*

Thesis Abstract

Vast consumption of fossil fuels has catapulted greenhouse gas emissions which have contributed to increasing the global average temperature at a frightening rate. Thankfully, sun, wind and tides have massive potential to provide energy in an environmentally friendly way. However, maintaining these energy sources at the global scale required to realise the transition from fossil fuels to renewable energy is difficult, given that their supply is often location and weather dependent. Fortunately, there is a solution, and energy storage is the key to a green energy future. Currently, battery systems are the most suitable option. These systems can be implemented in large-scale grid storage facilities, electric vehicles (EVs), portable electronics like laptops and mobile phones, right down to fingernail-sized microbatteries for medical devices and hearing aids. Despite decades of research, the demand for increased functionality has grown at such a rate that the development of appropriate technology has proven difficult. Additionally, the materials typically used in production of commercial batteries such as cobalt, graphite and Li are coupled with concerns related to ethics, CO_2 emissions, and availability.

This thesis delves into three realms, all related to the development and optimisation of battery electrode materials, and efficient approaches to monitor their deterioration. The first realm is optical analysis of opal photonic crystals (PhCs) which are used as templates for battery electrodes. PhCs are a particular type of nanostructure which demonstrate iridescent colours when exposed to light. The observed colours originate from a phenomenon known as the photonic band gap (PBG), the band of frequencies which are reflected

from the crystal. The PBG is dependent on the structure and refractive index contrast of the material. Consequently, the PBG can be controlled by changing the structural parameters of the crystal. Opals are a type of PhC which are used as templates for inverse opals (IOs), which have shown promise as battery electrodes due to their high surface area to volume ratio, thin pore walls and interconnectivity, which removes the need for conductive additives and binders. The most fascinating aspect of their potential is the correlation between their structural properties and their optical response since the primary route of battery performance deterioration is through the structural degradation of the battery electrode materials. Opals of different thicknesses can be constructed while the reflected colours remain unchanged once the periodicity of the crystal is maintained. However, the intensities of the reflected frequencies are thickness dependent. The optical response of these materials can therefore be used to determine crystal thickness, and vice versa. Optimising the electrochemical performance of IO (IO) battery electrodes requires formation of an excellent opal template which can be directed and evaluated by this non-destructive optical spectroscopy approach.

With a method established for perfecting opal quality established, the second realm explores the electrochemical performance of sustainable battery systems, in the form of SnO_2-based electrode materials in lithium-ion (Li-ion) and sodium-ion (Na-ion) chemistries. Li-ion is the most widely used commercial battery chemistry. As Li reserves are depleted, alternatives must be considered. Na stands as a practically infinite resource, extracted easily from sea salt. Na-ion batteries operate under similar principles to Li-ion, but

optimisation of appropriate electrode materials has proved challenging. Graphite stands as the gold standard anode material for Li-ion, but its capacity is dramatically reduced in Na-ion systems. Furthermore, the carbon emissions from the processing of natural graphite and production of synthetic graphite are worrying. SnO_2 is one of the thirty most abundant elements on earth and stands as a promising replacement for graphite in Na-ion batteries. However, massive volume expansion prevents its widespread adoption. Routes to overcome this volume expansion involve the design of state-of-the-art nanostructures, the route taken in this thesis using the IO architecture. While this electrochemical exploration provides an explanation of the underlying chemistry governing the rate behaviour and stability of the IO electrodes, the structural changes which arise in the electrode during cycling prompt deeper investigations. Furthermore, the rapid nature of the associated electrochemical processes prompt real-time measurements, which are addressed next in the thesis in the form of operando Raman spectroscopy.

The third realm is the application of operando methods to battery performance analysis, an approach which litters the literature in recent years. Traditionally, analysis of battery electrodes and the electrolyte were performed ex-situ. The battery was disassembled, the materials were removed and analysed. Ex-situ analysis is useful prior to cycling and for postmortem analysis. A more effective analytical approach is the use of in-situ techniques. These involve stopping the battery at a certain voltage, disassembly, and analysing the electrodes and electrolyte in that state. This approach is useful for determining what changes occur to the battery at different states of charge.

However, these materials are often sensitive to the environment, and the in-situ results are not representative of the state of the material prior to disassembly. Furthermore, electrochemical reactions can occur over nanoseconds or even less, while the structural changes can be short-lived. As a result, in-situ analysis can fail to capture many of the changes which occur during cycling. Operando techniques involve analysis of battery components during electrochemical cycling. Disassembly is not required, and structural changes can be tracked continuously, capturing any metastable and ultrashort phases. Operando Raman spectroscopy can be used to monitor structural changes to the electrode at the atomic scale, along with evolution of the electrolyte non-destructively.

This thesis has been written to showcase the benefits of combining optical, structural, and electrochemical analysis, moving from ex-situ to operando techniques, and optimising performance of sustainable battery technologies with a view to transitioning from Li-ion to Na-ion chemistry with environmentally friendly electrode materials to develop the first PhC, lab-based operando battery diagnostics system.

Table of Contents

Chapter 1 Thesis Overview.....1

Chapter 2 Literature Review: Real-Time Non-Destructive Methods for Examining Battery Electrode Materials 5

2.1. Introduction.....7

2.2. High Energy Operando X-Ray Methods for Battery Electrode Materials Analysis 13

2.2.1. Synchrotron X-Ray Diffraction (XRD) 13

2.2.2. X-Ray Computed Tomography (X-Ray CT).....19

2.3. Operando Transmission Electron Microscopy (TEM)).....28

2.3.1. Cryo-TEM: Importance of Sample Preparation and Stability 30

2.4. Atom Probe Tomography – Compositional Profiling of Electrode Materials Atom by Atom.....34

2.5. Operando Optical Spectroscopic Methods 45

2.5.1. In-Situ Raman Scattering of Phase Changes in Battery Electrodes.....46

2.5.2. In-Situ ATR-FTIR for Probing Electrolyte Decomposition at the Electrode/Electrolyte Interface 53

2.5.3. Tracking the Optical Signature of PhC Electrodes in Real Time.....58

2.6. Internal Sensing of Battery Response – Fiber Bragg Grating Sensors and Probes 67

2.7. Nuclear Magnetic Resonance Analyses of Mass Shifting in Battery Systems.....77

2.8. Electrochemical-Acoustics – Listening to a Battery's Health.....88

2.9. Battery Operation in a Dynamic Service Environment – Building a Sensor Network.....97

2.10. Conclusions and Outlook.....100

2.11. References 103

Chapter 3 Experimental 115

3.1. Introduction.....116

3.2. Sample Preparation.....116

3.2.1. Substrate Preparation.....116

3.2.2. Evaporation-Induced Self-Assembly of Opals 117

3.2.3. IO Formation by Template Infiltration 119

3.2.4. Electrode Washing....121
3.2.5. Sputter Coating....121
3.3. Cell Preparation....122
3.3.1. Electrolyte Preparation....122
3.3.2. Electrode Preparation....123
3.3.3. Cell Assembly....123
3.3.4. Operando Cell Assembly....124
3.4. Structural Characterisation Methods....128
3.4.1. Scanning Electron Microscopy....128
3.4.2. Transmission Electron Microscopy....130
3.4.3. Electron Diffraction Spectroscopy....131
3.4.4. Optical Transmission Spectroscopy....132
3.4.5. Raman Spectroscopy....133
3.4.6. X-Ray Photoelectron Spectroscopy....136
3.4.7. X-Ray Diffraction....137
3.5. Electrochemical Characterisation Methods....139
3.5.1. Cyclic Voltammetry....139
3.4.2. Galvanostatic Cycling....142
3.4.3. Differential Capacity Analysis....145
3.6. References....148

Chapter 4 Thickness Control of Dispersion in Opal PhCs....150
4.1. Introduction....152
4.2. Experimental....156
4.2.1. Materials and Substrate Preparation....156
4.2.2. Evaporation-Induced Self-Assembly....157
4.2.3. Microscopy and Spectroscopy....157
4.3. Results and Discussion....158
4.3.1. Volume Fraction-Thickness Relationship....158
4.3.2. Opal Thickness Control....166
4.3.3. Accuracy of Bragg-Snell Model Under Investigated Conditions....169
4.4. Conclusions....176
4.5. Appendix: Supplementary Material....178
4.6. References....188

Chapter 5 Asymmetric Optical Response from Graded Opal PhCs....191
5.1. Introduction....193

5.2. Experimental 195
5.2.1. Materials and Substrate Preparation 195
5.2.2. Evaporation-Induced Self-Assembly.....195
5.2.3. Microscopy and Spectroscopy.....196
5.3. Results and Discussion 197
5.4. Conclusions.....209
5.5. References 211

Chapter 6 Comparing Cycling and Rate Response of SnO_2 Macroporous Anodes in Li-ion and Na-ion Batteries.....213
6.1. Introduction.....215
6.2. Experimental 220
6.2.1. Preparation of SnO_2 IOs 220
6.2.2. Materials Analysis.....221
6.2.3. Cell Assembly 222
6.2.4. Electrochemical Characterisation 222
6.3. Results and Discussion 223
6.3.1. Structure of Macroporous SnO_2 Electrode Material.....223
6.3.2. Voltammetric Comparison in Li-ion and Na-ion Cells 229
6.3.3. Galvanostatic Cycling Comparison in Li and Na Half Cells 236
6.3.4. Comparing Rate Capability in Li- and Na-ion Cells 240
6.3.5. Reversibility of Conversion between SnO_2 and Metallic Sn 244
6.4. Conclusions.....255
6.5. Appendix: Supplementary Material 258
6.6. References 263

Chapter 7 Operando Raman Spectroscopy of Metal Oxide Electrodes in Li-ion and Na-ion Batteries 269
7.1. Introduction.....271
7.2. Materials and Methods 277
7.2.1. Electrodes 277
7.2.2. Electrolytes 279
7.2.3. Operando Cell Assembly 279
7.2.4. Electrochemical Characterisation 282
7.2.5. Operando Raman Spectroscopy 282
7.3. Results and Discussion: Operando Spectroscopy of Li-ion Batteries using Sapphire Window as Proxy.....284
7.3.1. IO TiO_2 Anode – 'Ring system' Electrode Stack.....284
7.3.2. NMC Cathode – 'Ring system' Electrode Stack 288

7.3.3. TiO_2 Slurry – Mesh Electrode Stack 294
7.4. Results and Discussion: Operando Raman Spectroscopy of TiO_2 Anode in Na-ion Battery – Coated Separator Electrode Stack 297
7.5. Conclusions 303
7.6. Appendix: Supplementary Material 305
7.7. References 310

Chapter 8 Conclusions and Future Perspectives 315
8.1. Conclusions 316
8.2. Future Perspectives 321

Chapter 1

Thesis Overview

Chapter 2 provides a comprehensive literature review of operando methods for modern battery systems which can be performed non-destructively. These methods cover the electromagnetic spectrum, from high energy X-ray analysis performed in synchrotron facilities to low energy benchtop systems which take advantage of radio wave energy. Design of an appropriate operando cell is the main difficulty encountered in the literature, and there is a substantial focus on the operando methodology required in each case. State-of-the-art systems are reviewed across a range of battery chemistries and an array of electrode materials to communicate the importance of correlating the electrochemical processes which occur during cycling to structural changes to the electrode which can often only be captured in real-time.

Chapter 3 catalogs experimental techniques used throughout the work included in this thesis and is divided into four subsections. Sample preparation, cell assembly, structural and electrochemical characterisation methods. The intention of the former two sections is to ensure that the reader can prepare the electrode materials and assemble each cell design so that the experiments can be repeated exactly as they were performed here. For the latter two sections, a brief summary of the concept behind each analytical technique is included, referencing artefacts specific to the application of each of the techniques to the type of analysis performed in this thesis, followed by the specific parameters used in each chapter.

Chapter 4 examines the optical response of opal PhCs, which are used as templates for battery electrode materials known as inverse opals (IOs). Opals are grown by evaporation-induced self-assembly (EISA) and the

relationship between sphere solution volume fraction and crystal thickness is established. The effects of crystal thickness on the associated optical response are then explored for a range of five volume fractions for opals grown at three different temperatures. Structural and optical analysis are used in tandem to discover the conditions under which there is a breakdown in the characteristic periodicity which defines these opals using Bragg-Snell theory.

Chapter 5 investigates the asymmetric optical response of opals due to an observed thickness gradient which occurs as a result of the EISA growth process. Unique optical fingerprints for opals grown under a range of conditions are demonstrated via 3D angle-resolved transmission spectra, highlighting the effect of the thickness gradient in each case.

Chapter 6 focuses on battery performance. The rate response of SnO_2 IO anodes in both Li-ion and Na-ion batteries. SnO_2 anodes offer high capacities in both systems but suffer from significant volume expansion. The IO morphology is used here to combat volume expansion and improve rate performance. Galvanostatic cycling shows impressive capacity retention and rate performance in the Na-ion system. Cyclic voltammetry (CV) analysis uncovers an interesting difference in the reversibility of the oxidation reaction from metallic Sn to SnO_2 in Na-ion batteries compared to Li-ion batteries.

Chapter 7 presents the results obtained from operando Raman spectroscopy experiments on Li-ion and Na-ion batteries. Three methodologies are detailed based on the electrode stack configuration using the same spectroelectrochemical cell. Changes at the electrode/electrolyte interface are examined for three electrode materials in the same electrolyte.

Changes to the electrolyte occur at the points of oxidation of both TiO_2 and Li nickel manganese cobalt oxide (NMC), even though these redox reactions occur in two different voltage windows for each material. The benefits of each electrode configuration are discussed and an outlook on future improvements to the methodology and analysis are presented. Operando Raman spectroscopy of a TiO_2 electrode in a Na-ion battery successfully detects phase changes to the electrode from anatase TiO_2 to amorphous Na titanate using a less fluorescent electrolyte.

Chapter 2

Literature Review: Real-Time Non-Destructive Methods for Examining Battery Electrode Materials

Adapted from: Grant, A.; O'Dwyer, C. Real-time nondestructive methods for examining battery electrode materials. Applied Physics Reviews 2023, 10 (1). DOI: 10.1063/5.0107386

Abstract

With the importance of Li-ion and emerging alternative batteries to our electric future, predicting new sustainable materials, electrolytes and complete cells that safely provide high performance, long life, energy dense capability is critically important. Understanding interface, microstructure of materials, the nature of electrolytes and factors that affect or limit long term performance are key to new battery chemistries, cell form factors and alternative materials. The electrochemical processes which cause these changes are also difficult to probe because of their metastability and lifetimes, which can be of nanosecond to sub nanosecond time domains. Consequently, developing and adapting high-resolution, non-destructive methods to capture these processes proves challenging, requiring state-of-the-art techniques. Recent progress is very promising, where optical spectroscopies, synchrotron radiation techniques, and energy-specific atom probe tomography and microscopy methods are just some of the approaches that are unravelling the true internal behaviour of battery cells in real-time. In this review, we overview many of the most promising non-destructive methods developed in recent years to assess battery material properties, interfaces, processes, and reactions under operando conditions in electrodes and full cells.

2.1. Introduction

Substantial progress in battery technology is essential if we are to succeed in an energy transition towards a more carbon-neutral, fossil-fuel-free society. Moving towards more sustainable energy harvesting and storage technologies that become part of a circular economy is essential. Materials sustainability will become an overriding factor in the years to come, conjointly with consumer demands that are ever-increasing. Under such a scenario, the production of Li-ion batteries is expanding considerably across the globe reviving the issue of finite Li(1) reserves, and the volume of critical raw materials such as cobalt and nickel, as pertinent examples. This concern has driven researchers to explore new, potentially more sustainable chemistries, including Na-ion,(2, 3) metal–air chemistries Li(Na)–O_2,(4, 5) Li–S,(6, 7) and multivalent (Mg, Ca)(8) redox flow batteries (RFBs) and aqueous-based technologies.(9) Electrode degradation represents one important challenge to the development of rechargeable batteries. While the existence of this challenge is well known and widely researched, the electrochemical processes responsible are continually being examined and assessed.(10-14) Unsurprisingly, attempts to understand these processes have involved analysis of the composite materials. Data of this nature has vastly improved the performance of batteries and the understanding of degradation processes. However, such research has been limited mainly to the study of electrode materials in isolation, i.e., before or after cycling, failing to capture short-lived or metastable processes. There is no surprise that a further understanding of battery materials requires their analysis during operation. These requirements call for state-of-the-art methodologies. Since 2008,(15) many studies have adopted such an

approach with great success. However, as it becomes a necessity for batteries to be charged every day, the need for more power has grown at a rate far greater than the improvements made in battery capacity.(16) Development and implementation of real-time, operando battery diagnostics may alleviate these shortcomings.

New analytical methods and lab-scale capabilities for existing large-infrastructure techniques are needed to probe specific battery chemistries and speed up analysis, screening and prediction of behaviour, performance, and safety for future electrification, so that new technologies can be brought to the market more rapidly to meet societal demands. Advances could include the development of remote, non-invasive and passive *operando* techniques(17) to complement present battery management systems(18) – but a real impact would come from powerful methods that are accessible outside synchrotron facilities, and operable in any lab. Right now, the consensus for small and EV-level batteries is that failures modes need to be tracked in real-time, and as such many battery companies are investing in accessories for advanced operando methods for their new battery chemistries. A recent commentary in Ref.(19) deals with exactly this need, highlighting the requirement for an interdisciplinary approach to advance imaging, modelling and testing technologies. Improved links between industry and academia are vital, links which would reduce costs solve technical issues and vastly accelerate commercialisation of the right technologies.

Rather than just probing a single material, operando techniques have provided an understanding of how the various materials function

cooperatively, particularly within the working battery. This has been particularly important for the understanding of the electrode/electrolyte interface. Operando imaging and spectroscopic techniques such as NMR(20), MRI(21) and electron paramagnetic resonance (EPR)(22) have recently enabled the visualisation and quantification of Li (and Na) microstructures. While these measurements do not simultaneously address phase, structural changes, and material arrangement during charge-discharge, they nevertheless offer powerful insight into side reactions and surface chemistries of battery materials. Recently, Co addressed the efficiency in charge passed in Sn and other electrode materials to address the issue of side reactions using operando NMR and neutron depth profiling to quantify the amount of alloyed or intercalated Li as a function of charge(23-25), directly imaging the coulombic efficiency of the overall convoluted processes in the anode material. Methods for imaging the movement of reaction fronts and reaction kinetics are becoming increasingly powerful. In-situ high-resolution TEM(26, 27) has been at the forefront of these advances, providing in-depth insights into interfacial processes and Li-driven local structural changes (for example in SnO_2 and Si) with a much higher resolution than MRI methods. Significant advances in synchrotron methodologies have allowed spectroscopic, two-dimensional transmission X-ray microscopy, full three-dimensional tomographic reconstructions and diffraction-based methods to be performed (such as Bragg coherent diffraction imaging), often in parallel; these have been used, for example, to track particle expansion with lithiation(28), and the evolution of strains and movement of dislocations within particles(29). If materials exhibit magnetic character, it is also feasible to monitor lithiation-induced changes to

magnetic properties as a sensitive probe of charge-discharge dynamics in a few materials, and supercapacitive behaviour in hybrid materials with ferromagnetic character.(30, 31) Optical methods that probe index changes in materials that undergo intercalation/alloying vs pseudocapacitive charge storage and compensation mechanisms are also feasible in principle.

Revolutionary insights into the phenomena that underlie the operation of energy storage devices has the potential to uncover not only the basis for material selection, but how material at electrode level, and arrangement, affect performance. It may generally provide a way of analysing open questions and performance limitations including degradation mechanisms in a whole range of technologies including electrochromics, supercapacitors, solar cells, photoelectrochemical systems or water splitting where light-matter interactions are essential. One important consideration in all analytical techniques, some of which are addressed in this review, is the importance of expertise in operation, processing, and interpretation of the data. A recent report on atom-probe tomographic analysis for Li-ion battery materials(32) is a recommended read, where it becomes clear how many parameters that are technique-specific need to be considered for any meaningful analysis of battery materials by such advanced, deeply-probing and high resolution methods. Artefacts abound, and expertise in instrumentation, acquisition, processing, and interpretation is critically important.

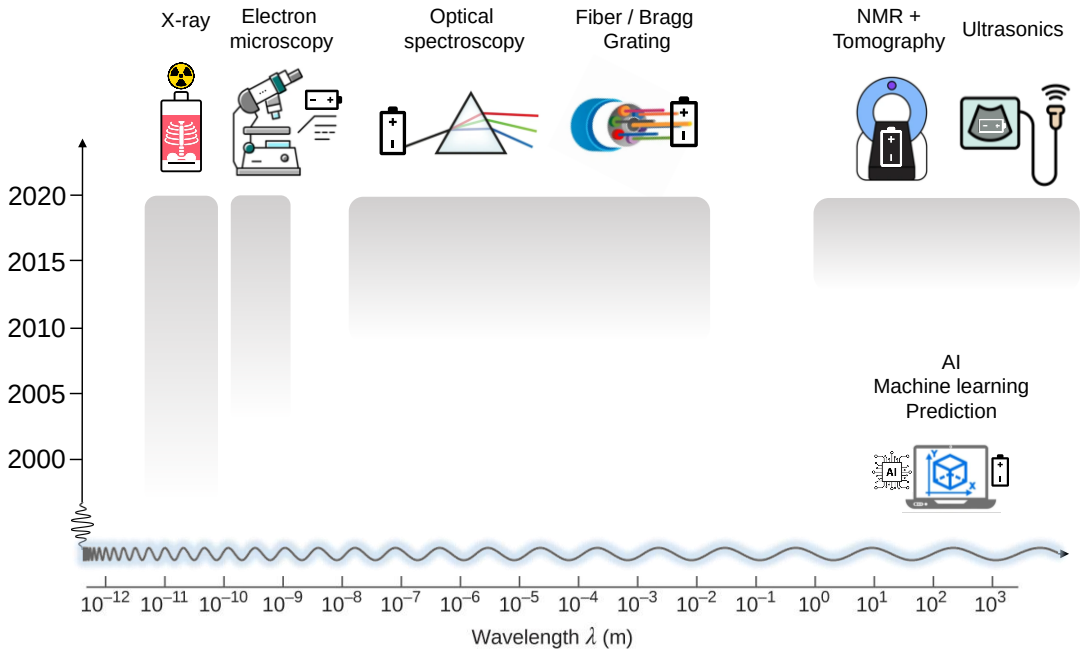


Figure 2.1. Advancement of operando non-destructive method for examining batteries and battery materials in the last two decades. Specific references for many of these methods can be found throughout this review. Notably, methods span the breadth of the electromagnetic spectrum and since 2020, many of these techniques can be done in synchrotron facilities and in laboratory settings with benchtop-sized infrastructure. AI, machine learning and computational prediction underpins many modern advancements to speed up discovery and troubleshoot potential issues prior to large scale financial and time-investment.

Figure 2.1 depicts some of the operando methods that have recently been developed over the last two decades and the methods span the energy spectrum from X-rays through to very low frequency radio waves. Many new methods are being developed specifically for batteries, but the need to analyse important materials, interfaces and electrochemical reactions seeded the research that led to new operando cells, synchrotron techniques and analytical methods assisted by powerful computational approaches, to smaller benchtop/laboratory systems that are also very powerful in their capability. The terms ex-situ, in-situ and operando are used throughout this work to describe measurements of battery materials. Ex-situ measurements involve cycling a

cell, stopping the process at a specific state of charge (SOC), and extracting the electrode before measurement. For in-situ measurements, data collection occurs without extracting the electrode. For operando measurements, data collection is performed during electrochemical cycling. Operando techniques can be considered a special case of in-situ, with the two terms often being used interchangeably throughout the literature. In this review, the distinct differences between the two modalities are distinguished with detail on the usefulness of operando techniques.(15, 33)

The objective of this work is first to provide an overview of some of the most powerful non-destructive methods used to examine battery electrode materials in real-time to date. Secondly, we will summarise some of the most promising initiatives being developed to accurately measure materials, cells, performance, and diagnostic analyses related to battery performance and health assessment in real-time. Techniques are grouped according to the region of the energy spectrum which is utilised. Key case studies are summarised for each group of techniques across a range of materials and battery chemistries. The central issues which arise in the application of each technique are addressed, outlining cell assembly considerations, benefits and limitations, materials preparation, resolution/accuracy, and extracted information. The result is a work which serves as a manual which, upon reading, informs the reader on the required methodology of the desired technique, what results can be expected, and the common pitfalls to avoid. For each non-destructive method described here, the progression towards useful operando measurement and understanding, and its combination with complementary analytical techniques to monitor the electrochemical

processes occurring in electrochemical cells, is of vital importance to the development of the next generation of batteries.

2.2. High Energy Operando X-Ray Methods for Battery Electrode Materials Analysis

2.2.1. Synchrotron X-Ray Diffraction (XRD)

X-ray diffraction (XRD) is an analytical technique often used to obtain detailed information about the structure of crystalline materials, and the chemical and physical properties they possess. Battery electrode materials are very often crystalline, with highly ordered architectures that allow control of ion and electron transport throughout. As a result, XRD is a powerful technique for characterizing these materials when conducted and analysed with due care and rigour for measurement and interpretation.

Traditional lab based XRD methods are useful for determining the phases of crystalline electrode materials. The quality of generated results can be evaluated by two primary variables. Firstly, the signal to noise ratio (SNR). SNR is affected by several properties but is primarily dependent on the intensity of the X-ray beam. The second is peak width, usually quantified using the full width half maximum (FWHM), which is a function of the beam diameter. Smaller beam diameters result in the reduction of the FWHM and sharper peaks. Synchrotron XRD proves a superior approach in its characterisation capabilities, with the obvious drawback of requiring the use of expensive large-scale facilities. Its superiority can be summarised by the 4 main advantages over the traditional lab-based approach: (1) Greater beam intensity creating more intense peaks with an improved signal to noise ratio (SNR). (2) Higher

collimation that reduces angular beam divergence and increases the monochromatic character of the beamline. (3) The degree to which the beam is parallel is improved which removes the need for focusing geometry that can be inaccurate at low angles. (4) Improved peak: background ratio for samples which produce background fluorescence, unlike the pre-sample monochromators often used in traditional setups. For operando battery measurements, where the target samples may be difficult to access due to cell components which may attenuate the X-ray beam, the enhanced accuracy and response provided through the synchrotron approach is useful.

A variety of approaches can be taken in the application of XRD to battery systems in operando to examine electrode materials. The basic concept is to evaluate the change in diffraction pattern over time during electrochemical cycling. Such work has been performed for anode and cathode materials in Li-ion systems(34) along with a range of potentially more sustainable battery chemistries such as (Na-ion),(35, 36) potassium-ion (K-ion),(37) and Li-sulfur (Li-S).(38, 39) In Kirshenbaum et al.,(40, 41) the approach is taken a step further. Energy-dispersive X-ray diffraction (EDXRD) is used to gain insight into the composition of a Li/$Ag_2VP_2O_8$ cell. EDXRD is suitable for in-situ analysis of materials due to its rapid data collection rate and fixed scattering angle, the latter allows for high-accuracy measurement of lattice parameters that are present in the material. In the study, in-situ EDXRD is performed at two discharge rates and the non-discharged cell is combined with ex-situ X-ray absorption spectroscopy (XAS) measurements to determine the optimal conditions for a conductive network to be formed which results in

spatial resolution of the electrochemical reduction process within the electrode inside an intact electrochemical cell.

The presence of heterogeneities in electrode materials is common, especially when mass loading is enhanced through incorporating structures with increased thickness. EDXRD is performed here through the cross-section of the cell perpendicular to the surface of the face-to-face electrode configuration from the Li metal counter electrode through the electrolyte to the cathode. Given that a gradient in current density and Li-ion flux is unavoidable, and that the phases of both electrode and electrolyte species are determined by the electrochemical reactions that often depend on the degree of Li uptake, heterogeneity in the crystalline phases detected across the cell are expected. To further solidify findings, the measurements are performed at multiple locations across the width of the cell to identify any asymmetries which may be present. Consequently, short-lived, metastable phases are monitored which were not previously accessible. One of the most important aspects of the data here is the ability to track structure formation within the cell materials. The EDXRD data provides insight into the locations at which different phases occur, with a tomographic-like profile of the cell shown in Figure 2.2.

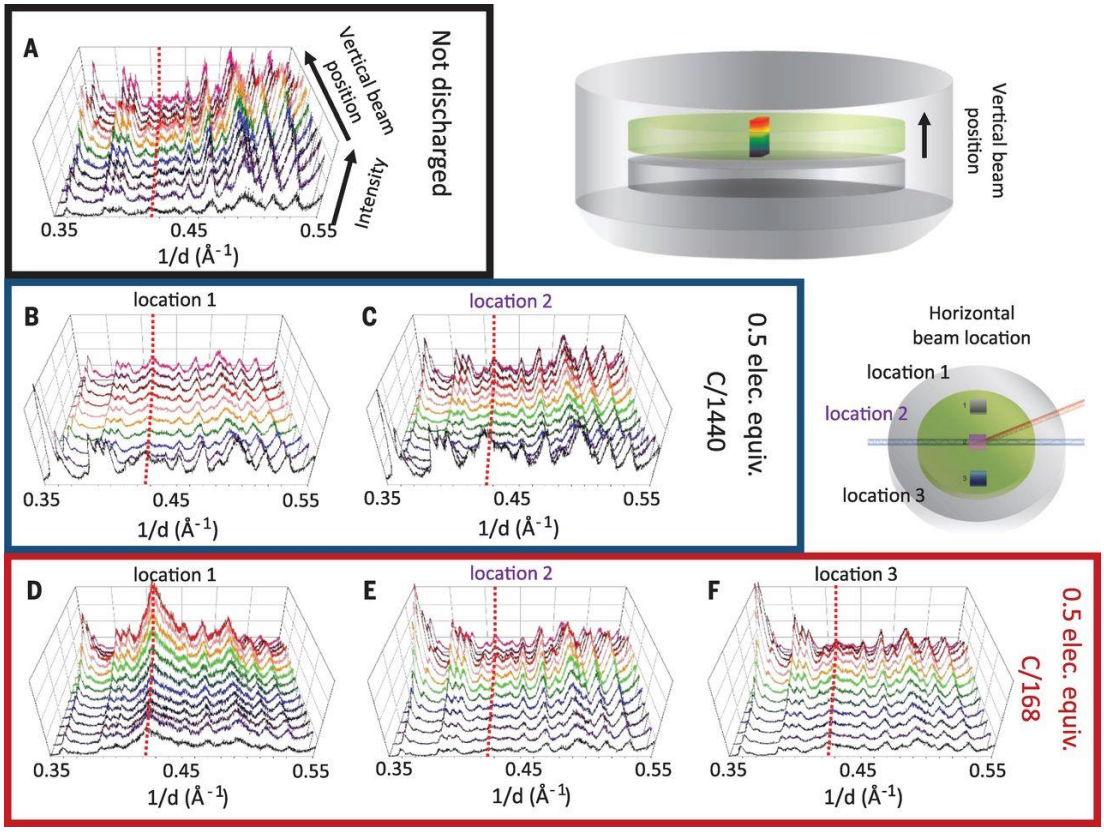


Figure 2.2. Spectra resulting from spatially resolved in-situ EDXRD measurements within three coin cells: (A) A non-discharged cell, (B and C) two different locations within a cell discharged to 0.5 elec. equiv. at a rate of C/1440, and (D to F) three different locations within a cell discharged to 0.5 elec. equiv. at a rate of C/168. Spectra were obtained every 20 mm through the cathode; for clarity, only half of the scans are presented in the figure. Spectra toward the top of the figure (red hues) were obtained within the side of the cathode closer to the stainless-steel coil cell top, and spectra toward the bottom of the figure (black hues) were obtained closer to the Li anode. Adapted from ref. (42). Copyright AAAS 2015.

Using this data combined with impedance measurements, changes in battery resistance can be analysed. Study of both the structural changes and impedance in the cell (electrochemical impedance spectroscopy (EIS)) simultaneously during cycling enables rationalisation of the changes in battery resistance, which determines the nature of the discharge mechanism. Compilation of these results provides an overview of the conductive pathways formed from reduction products and the impact on the discharge mechanism.

The two techniques prove complementary and the relationships between cathode reduction, electrochemical cell discharge and impedance are established.(43) Insights into the electrochemical and structural processes which can occur are gained with the determination of the conditions required for an optimal conductive network in the cathode and the elucidation of a rate-dependent discharge mechanism. The advantages of combining the data obtained from ex-situ and in-situ techniques are evident from the results.

As discussed by Kirshenbaum et al. above, in-situ XRD provides the ability to detect certain phases which occur at different SOCs of a battery including material phases that are difficult or often impossible to be reliably detected ex-situ in a post-mortem analysis from cell-disassembly. However, the lifetimes of certain processes are shorter than the time taken to disassemble the cell and perform the required measurements and others are extremely sensitive to changes in their local environment, which can include access to changes in electrolyte, salt concentration (even when carefully contained in battery-grade storage environments) and especially to water and ambient air for more typical post-mortem analyses. Therefore, operando techniques must be used to capture this information.

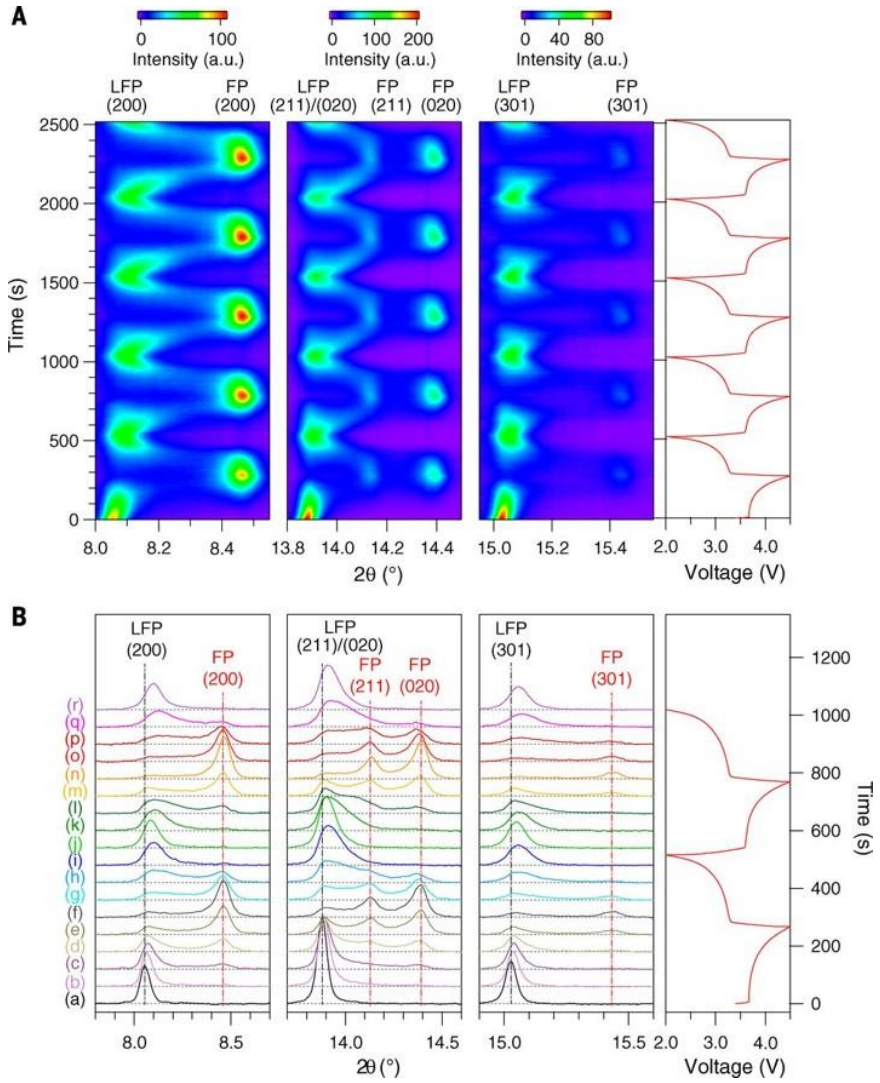


Figure 2.3. In-situ XRD patterns during galvanostatic charge and discharge at a rate of 10 C. (A) Diffraction patterns for (200), (211), (020), and (301) reflections during the first five charge-discharge cycles. The horizontal axis represents the selected 2θ regions, and time is on the vertical axis. Diffraction intensity is colour coded with the scale bar shown on top. The corresponding voltage curve is plotted to the right. LFP, $LiFePO_4$; FP, $FePO_4$. (B) Selected individual diffraction patterns during the first two cycles and voltage profile. The baseline is represented by horizontal dashed grey lines. Black vertical lines mark the positions of $LiFePO_4$ peaks at the start of reaction; red vertical lines mark the position of $FePO_4$ peaks formed during the first cycle. Adapted from ref. (44). Copyright AAAS 2014.

In Liu et al.,(45) operando XRD with high temporal resolution was used to analyse metastable structures formed during the high-rate cycling of $LiFePO_4$ electrodes and determine the effects of strain vs compositional

variation. These results are compared to simulated XRD patterns of some of the structures predicted to form during cycling. Disagreement between data indicates the formation of metastable structures not detected ex-situ, i.e., particles with lattice parameters that vary from the predicted composition. The results are also used to quantify the compositional variation during cycling. The operando XRD patterns (Figure 2.3) show the absence of any particle interface (disappearance of Bragg reflections corresponding to second particle), indicating that strain effects did not occur. Based on work prior to this study, reactions in the electrode material were predicted to proceed via a process which would cause, using conventional wisdom, poor battery performance, while these measurements indicate the contrary. The utilisation of operando XRD here provides the ability to explain this disagreement, by capturing processes which could not be detected previously using ex-situ or even in-situ methods.

2.2.2. X-Ray Computed Tomography (X-Ray CT)

The operando synchrotron XRD discussed thus far here provides a host of useful information on battery electrode materials including the degree of crystallinity and lattice parameters of the species present with their evolution over time. Such information can be used to enhance understanding of how electrochemical cycling affects the constituent materials. However, the benefits of the application of X-ray microscopy to battery systems has provided the community with high resolution models that stand as a clear visual representation of the constituent materials. These models are provided in the form of tomographic profiling of the electrochemical cell. A huge advantage of

the microscopy approach is that it does not have to be performed in synchrotron facilities but can be incorporated into a lab setting.

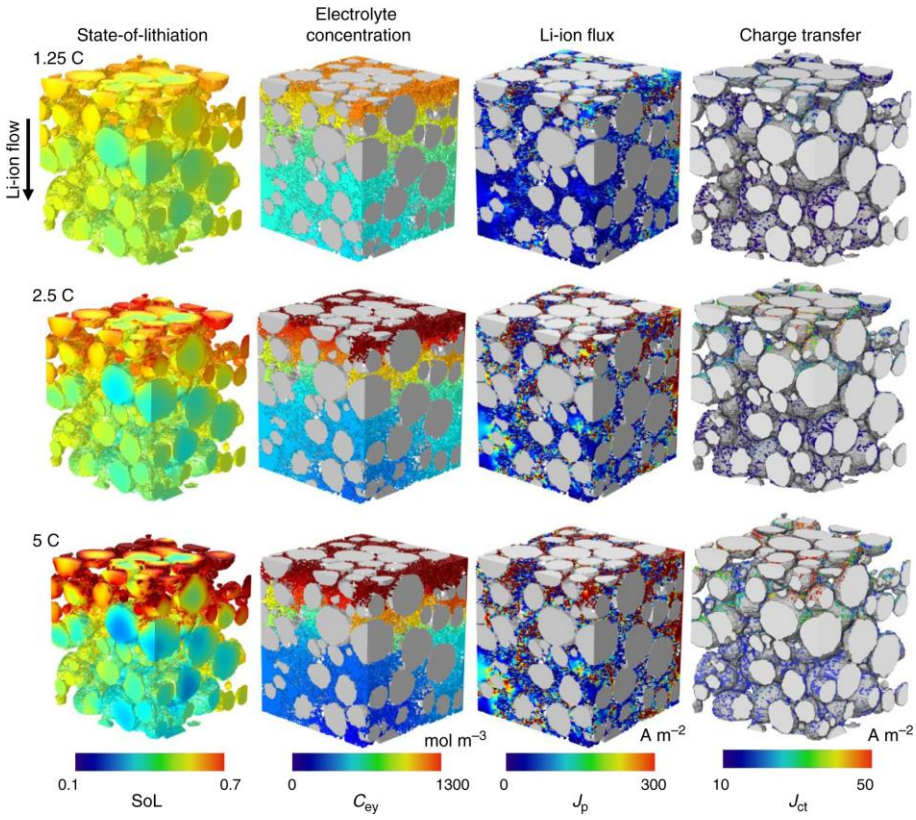


Figure 2.4. Simulated discharge of the reconstructed cathode and an ideal Li anode (half-cell) at 1.25, 2.5 and 5 C. The ionic current flows from the top (separator side) to the bottom (current collector side). Field variables at 50% depth-of-discharge (DoD) are shown here. Reproduced from ref. (46). Copyright Nature Publishing Group 2020.

In Lu et al., a novel X-ray nano-computed tomography (CT) dual-scan superimposition (DSS) technique is used to probe some of the key parameters of electrode materials which affect battery performance.(46) A 3D volume of a Li-ion half-cell is reconstructed with an NMC111 cathode vs a Li metal anode, and achieved at the nanoscale for the first time. The study investigates how the structural characteristics of the cathode such as porosity, tortuosity and thickness affect electrochemical processes within the cell such as state of lithiation (SoL), electrolyte salt concentration (C_{EY}), Li-ion flux and charge

transfer at different rates. Adaptations to the initial microstructure are also made to probe the evolution of the same electrochemical processes in novel microstructure designs.

Figure 2.4 shows the computed evolution of the half-cell during discharge at three different rates of 1.25C, 2.5C and 5C, from the top row to the bottom row. Each individual schematic depicts the half cell with current flow in the through-thickness direction. The top corresponds to the region of the cathode closest to the separator. The bottom represents the region closest to the current collector. Each column represents one of the key electrochemical parameters of the cell. In the first two columns of Figure 2.4, SoL, and electrolyte salt concentration of the cell at 50 % depth of discharge (DoD) is shown. At the lowest rate, there is a uniform distribution observed in each case. As the rate is increased, a severe gradient develops due to the competition between mass transport dynamics and reaction kinetics. Lithiation occurs only where the active material, NMC particles in this case, are exposed to the Li ions flowing through the electrolyte in the form of Li salts. As the cell is discharged at low rates, the Li ions flow along the electrode slowly, maximising the amount of active material they access. As the rate is increased, Li ions bombard the active material closest to the separator, maximising charge transfer in this region. Consequently, mass transport is slow, meaning that the ions are unable to supply reactant into deeper regions of the electrode at a sufficient rate. NMC close to the current collector are therefore not utilised, resulting in severe capacity loss in the cell.

The third column shows the distribution of Li^+ ion flux J_P. At low C-rates (1.25 C), the flux is evenly distributed. At higher C-rates (above 2.5 C),

heterogeneity is evident due to the non-uniformity of the pore microstructures, with much higher flux in narrow pores. High flux causes local Ohmic heating, which can lead to electrolyte decomposition and thermal runaway. The fourth column shows the charge transfer J_{CT} which represents reactivity. The reactivity distribution is shown on a particle-by-particle basis, with reactivity more homogeneous at low C-rates. J_{CT} is much higher close to the separator than near the current collector, due to the mass transport limitation already mentioned.

The simulations based on the reconstructed cathode microstructure show that the inhomogeneous lithiation that occurs during cycling occurs primarily due to the broad distribution of particle size. As a result, changes in both the level of porosity and pore size in the direction of lithiation leads to a variation in Li-ion diffusion path lengths. The imbalanced utilisation of NMC lowers the energy density of the cell, which inhibits the long-term structural integrity of the electrode. Subsequent simulations were performed to investigate the use of next generation electrode designs, exploring the effects from the manipulation of particle size, pore size distribution, and electrode compression, to probe the effects of specific structural alterations to the performance of the cell.

A full interrogation of the causes of inhomogeneous lithiation based on the microstructural size distributions of the electrode and how this leads to poor battery performance is provided. The gradients of the electrolyte concentration and SoL increase with C-rate and depth of discharge, highlighting the issues that occur in battery performance at higher rates. It is particularly evident that particle size, pore size and the level of porosity are the

main factors which determine the distribution and direction of flow of Li ions during discharge. Uneven intercalation between particles occurs as a result, leading to the underutilisation of capacity and reduced power density. The study also describes the effects of calendaring on the microstructural evolution of the electrodes, a further look at the process can be found elsewhere.(47) Overall, the dual-scan superimposition (DSS) computational technique and modelling used here represents a truly non-destructive method for investigating electrode degradation mechanisms based on the distribution of electrode particles within the cell.

Given that X-ray computed tomography has moved to the lab, analysis of battery materials' absorption coefficients is possible with voxel sizes down to ~50 nm. The most recent approaches combine artificial intelligence and analysis techniques including machine learning, with nano-CT on the lab scale. The motivation has been to develop powerful and accurate predictive models of the electrochemical response of battery materials and electrodes, from variations to microstructure and composition variations that can be visualised in 3D with postmortem analysis and predictive models for new materials or existing materials under various operando conditions. X-ray CT has superior resolution compared to nano-CT imaging, but developments in high-resolution nano-CT systems are underway. The technique is a non-destructive tool and provides opportunities for operando investigations in battery materials and solid-state battery interfaces and solid electrolytes, to name a few. Combing nano-CT imaging data and computational modelling, reconstructed volumes, and parameters such as pore tortuosity, particle size etc. can be extracted and incorporated into the models to simulate

electrochemical response. Machine learning and related approaches are necessary to obtain an accurate and representative volume of the material under examination in CT images. Some recent reviews have outlined the details and opportunities of X-ray CT(48, 49) and also computationally-supported nano CT imaging(48) for battery research. The importance of data quality, interpretation and curation is a consistent in the application of CT imaging for battery materials analysis and extracting meaningful data requires careful workflow and data processing. Opportunities exist not only for 3D visualisation but for obtaining digital twins of battery electrodes to watch their behaviour in real-time and translate this knowledge to prediction of similar materials under different conditions, or for screening new materials of battery chemistries with particle size and interface-level resolution in real time in 3D.

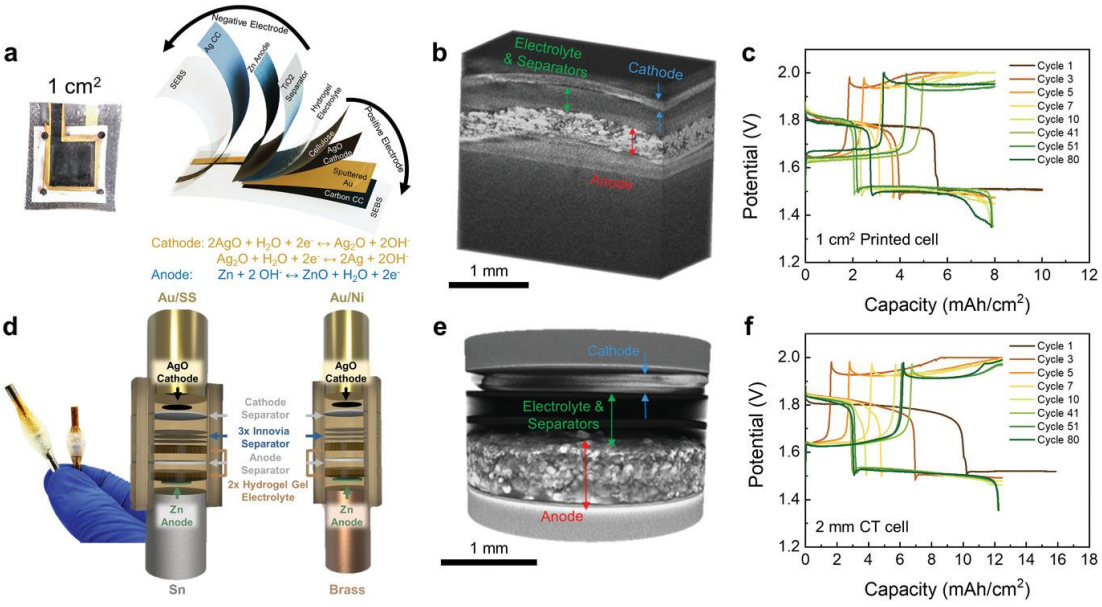


Figure 2.5. Cell design and performance of a Zn-AgO printed cell (a) and in-situ CT cell (d). 3D X-ray CT tomographic reconstructions (b, e), and electrochemical performance (c, f) for Zn-AgO printed cell (top row) and in-situ CT cell (bottom row). Adapted from Ref. (49). Copyright Wiley VCH 2017.

As a representative example, Scharf et al.(49), showed how in-situ X-ray micro-CT in combination with electrochemical battery cell characterisation could be used to interrogate how gassing at the current collector influence the performances of Zn-AgO batteries. Their results and process, representatively overviewed in Figure 2.5, revealed that OER and HER gas evolution depended on the choice of current collector material. While the likelihood of gas evolution processes could in principle be extracted from basic electrochemical knowledge of this metal in such an electrolyte, the micro-CT provided useful additional quantification on z-axis volumetric expansion within the electrode. Simply changing the current collector made an obvious improvement in performance giving a high cycling capacity of 12.5 mAh cm^{-2} for more than 325 cycles in a 4 cm^2 form factor, corresponding to volumetric energy density of 100.6 Wh L^{-1}. The development here of the in-situ cells is also important for future application of micro-CT and related methods, as the cell construction is a necessity to allow accurate probing by CT instrumentation and they showed how the approach could provide meaningful examination of cell degradation over long term cycling.

In-situ and operando X-ray techniques represent a powerful array of tools which can be used to investigate the electrochemical behaviour of battery electrode materials at different states of charge or discharge/during cycling with high energetic and spatial resolution. As most battery materials are crystalline, their examination using X-ray methods provides information on changes to their structure which can be correlated to electrochemical processes and overall battery performance. The major disadvantage of this family of tools is their inability to detect amorphous phases, such as electrolyte

species and the secondary electrolyte interface (SEI) layer. Involved computational methods are required to enable digital twins with accurate processing of the material volumes being imaged so that examination of representative cells can provide predictive capabilities for new materials and batteries. For battery researchers keen to take advantage of the power of operando X-ray methods, awareness, and attention to some of the common themes in the literature can improve and even fast track results. Table 2.1 stands as a summary of these key aspects. Establishment of the correct operando cell design is of paramount importance to maximise the observed response and minimise some of the artifacts which can occur. Depending on the approach used, the correct design can provide spatial resolution of the entire cell. Considerations of some of the potential pitfalls can prove extremely useful, and simple tweaks to the methodology can prevent these entirely. Considerations such as an aversion to constant data acquisition for setups where high power X-ray beams may cause sample damage. In depth ex-situ analysis to provide an understanding of the system under consideration is always recommended as a prerequisite to operando measurements.

Technique	Operando Cell Setup	Capabilities	Limitations	Local Resolution
Synchrotron X-ray Diffraction (XRD)	AMPIX cell(44, 50) Tubular RATIX cell(51) Windowed coin cell(52, 53) Li-O_2 capillary cell(54) Custom Li-S pouch cell(55)	Average structural information Crystallinity Phase purity Atomic position Lattice parameter	High Cost Requires standard reference data Limited information extracted for amorphous materials	0.01 °
Synchrotron Energy Dispersive XRD (EDXRD)	Standard coin cell(41, 56)	Tomographic Profiling with Depth of Discharge Spatial Resolution of species evolving during cycling Rapid data collection	Beam profile attenuated by coin cell steel casing Beam damage in constant data acquisition mode	< 20 µm*
X-ray Computed Tomography (X-ray CT)	Computed reconstructions of target cell components(46, 48, 49)	Spatial resolution of: i. Porosity ii. Surface Area iii. Tortuosity iv. Particle Distribution v. Charge Transfer Gradient vi. State of Lithiation	Curation of “clean” data and precise interpretation necessary Detailed algorithms and various software packages required (e.g., COMSOL)	~ 10 nm

* Spatial resolution – Sensitivity to which X-ray diffraction signals could be correlated to location within the electrode.

Table 2.1. Overview of state-of-the-art in-situ and operando X-ray techniques applied to battery systems, referencing the cell design and some of the key characteristics related to each technique.

2.3. Operando Transmission Electron Microscopy (TEM)

Operando methods for studying materials and processes in Li-ion batteries in a transmission electron microscope (TEM) have existed since ca. 2012(57, 58). The initial open-cell holders allowed in-situ measurements, and some operando investigations under vacuum. Some of the cell types were limited, requiring solid state electrolytes, or suffered from electron beam polymerisation or damage, and others demonstrated the concept using materials that were somewhat atypical for Li-ion batteries (at least commercial or near-commercial chemistries). However, the technique proved to be useful in interrogating nanoscale and (in some cases) atomic-scale resolution of real-time changes to materials during discharging and charging, and readers are referred to some original papers and reviews(59). A notable disadvantage of the open-cell method was the localised contact to the electrode, which limited the active mass involved in the electrochemical process. It did show new possibilities for investigating the interface in high resolution and spawned the development of closed cell operando TEM.

Closed-cell versions of cell holder for operando TEM were iteratively developed, with continuous improvement in capabilities to allow measurements with more common liquid electrolytes and electrode materials, while improving the sensitivity and contrast that was limited in earlier designed due to more severe electron scattering from metallic materials(60). Liquid electrolytes in the TEM were developed by Muller et al. to have a flow electrolyte configuration(61) with a glassy carbon electrode, following from the silicon nitride membrane container approach for single Si NW measurements in the Si-Li metal cell demonstrated by Wang et al.(62) There were several

other variations on the sealed liquid cell design for battery measurements (see Figure 2.6) in the TEM, some including graphene instead of SiN_x to reduce scattering and improve contrast in the materials under analysis, particularly when thick liquid electrolytes were used to generate a more realistic comparison to the type of battery cell under consideration.(63, 64)

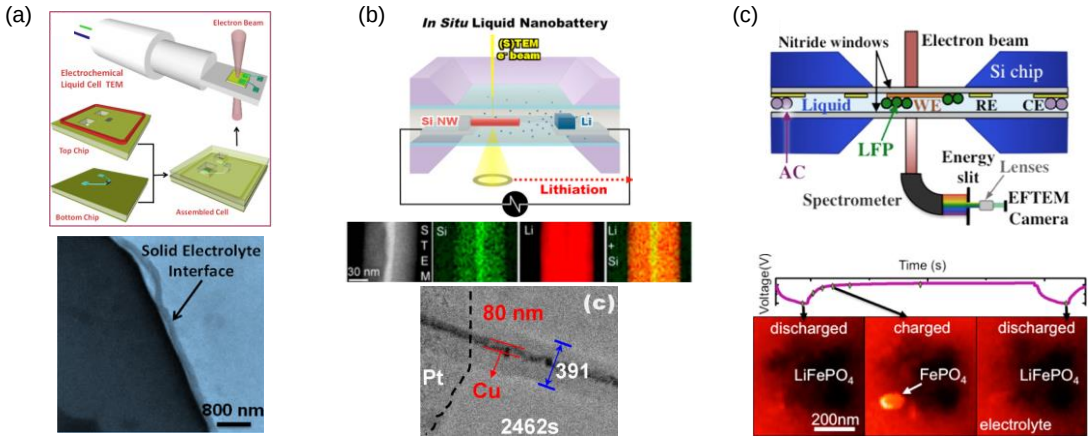


Figure 2.6. (a) Setup for in-situ liquid electrochemical cell to examine electrode-electrolyte interfaces. Adapted with permission from Nano Lett. 14, 1745 (2014). Copyright 2014 American Chemical Society. (b) A liquid electrochemical operando cell (Si NW electrode) using SiN_x membranes of ~50 nm in thickness to seal the liquid, while still allowing transmission of the high energy electrons for imaging. This liquid cell allowed elemental analysis and imaging of Li_xSi around a Si NW electrode. Adapted with permission from Nano Lett. 13, 6106 (2013). Copyright 2013 American Chemical Society. (c) SiN_x membraned liquid cell holder to allow operando EFTEM of $LiFePO_4$ cathodes. Adapted with permission from Nano Lett. 14, 1453 (2014). Copyright 2014 American Chemical Society.

These closed cell variations for operando TEM revealed some useful new insights into battery material behaviour and high resolution data on the nature of some important interfaces with the electrolyte. Real-time lithiation was observed using the important $LiFePO_4$ cathode material while dendrite growth, and Li stripping and thinning mechanisms were observable using

electron microscopy under charging and discharging conditions. Since then, many other findings have reported the detail of observations that readers can refer to for specifics(64).

2.3.1. Cryo-TEM: Importance of sample preparation and stability

Cryogenic electron microscopy, pioneered by Taylor and Glaeser(65) was originally developed to solve the challenge of beam and vacuum-sensitive biological cells and macromolecules. Dehydration and structure collapse are caused in vacuum, while certain features of biological and also sensitive battery materials required approaches to limit exposure to the electron beam. Before looking at some of the advances the cryo-TEM has offered, the beam-sensitivity issue had to be solved. Reducing beam power or electron density was key to preventing additional chemical processes on materials, at interfaces and within certain electrolytes. Obtaining a high SNR is also important and to do this the field adapted methods used in other fields to acquire movies containing thousands of short frame exposures at lower beam current. Often used in astronomical imaging for deep sky objects and for planetary imaging, the method known as ‘lucky imaging’ involves the acquisition of thousands of short exposures as movies with additive stacking algorithms used to integrate the final exposure to improve the SNR and mitigate beam damage or beam-induced modification to the materials-under-test. Wang et al. outlined an approach that details the steps from sample preparation (in this case electrodeposited Li metal) to loading into the TEM, with caveats for the surface polishing of the active material deposited on grids for examination.

One pertinent example from Wang et al., where cryo-EM was used to analyse the nature of Li metal anodes and SEI formation, in addition to cathode electrolyte interface (CEI) formation on $LiMn_{1.5}Ni_{0.5}O_4$ cathode materials(66). The technique avoided the problem of Li reactivity under an electron beam(67). This report showed an example of SEI on electrodeposited Li and tracked the morphology of the deposited Li and the crystalline Li fluoride, oxide and carbonates components of the SEI. Li et al. in 2017 showed a detailed study of SEI formation and the nature of the dendrite structure using cryo-TEM(68) using a specially designed method to freeze the sample (Figure 2.7(a,b)), and it was one of several papers analyzing the SEI this way that shed light on the link between the composition, crystallinity and morphology of this complex but critically important interfacial overlayer in Li-ion batteries. They directly observed the interactions of Li with the interphase and the growth of the dendrites that are very problematic in cells, due to short circuiting issues. Dendritic Li ribbons exhibited a crystalline structure (Figure 2.7 (c,d)), often with various termination crystallographic facets and formed kink defects during their growth. The morphology was dependent on the type of electrolyte additive used, and in the case of fluoroethylene carbonate (FEC) a more-ordered SEI nanostructure was formed, with a multilayered structure (Figure 2.7(e))(69). By comparison to directly imaged SEI at the Li interface in standard electrolyte, they postulated that the stability often seen with FEC with some anodes is due to this mechanically more robust layered SEI structure, visible for the first time using cryo-EM. LiF, known to improve cyclability is difficult to detect in electron microscopy, and efforts to directly image

compounds containing lighter, lowly scattered elements such as F, C, S, and O will help considerably in operando electron microscopy-based techniques.

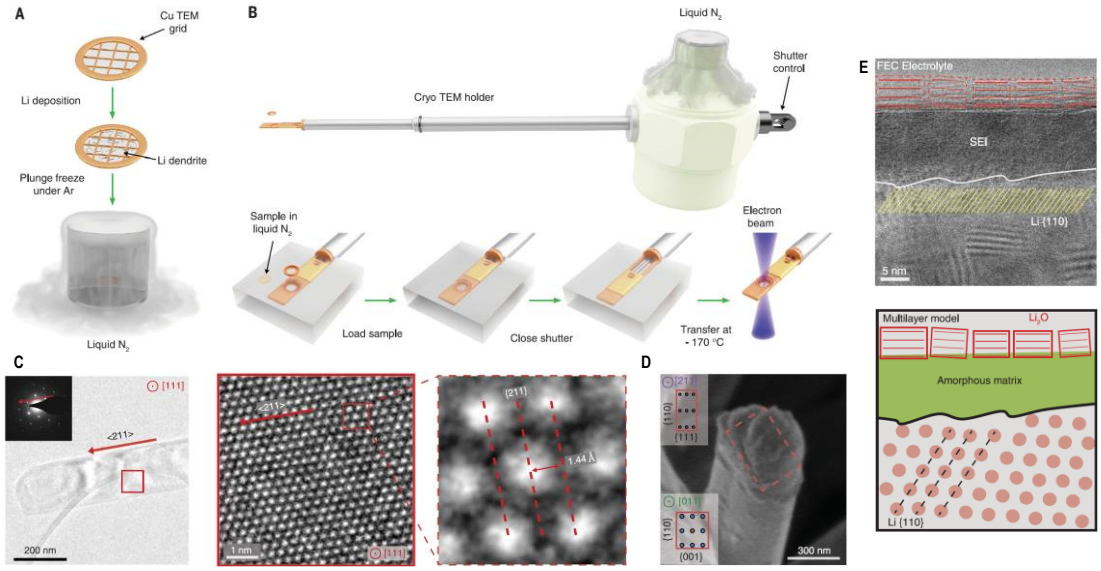


Figure 2.7. (a) Setup where Li metal dendrites are electrochemically deposited directly onto a Cu TEM grid and then plunged into liquid nitrogen after battery disassembly. (b) The specimen is then placed onto the cryo-TEM holder in liquid nitrogen, kept isolated at –170°C. (c) TEM of Li metal dendrites growing along the <211> directions with corresponding SAED pattern (electron dose rate <1 e $Å^{-2}$ s^{-1} for ~30 s). (e) Atomic-resolution image and schematic of the multilayered SEI structure on Li dendrites in FEC-containing electrolyte. Electron dose rate ~1000 e $Å^{-2}$ s^{-1} for ~30 s. Adapted with permission from Science 358, 506 (2017). Copyright 2017 American Association for the Advancement of Science.

Corroborating measurements at cryogenic temperatures for reactive and sensitive materials are still important to ensure that the vitrified and frozen material represents that of its room temperature counterpart and that no phase changes or other changes occur during cooling, and that operando measurements track processes that do occur in a cell. Cryo-TEM, cryo-focused ion beam (FIB) and cryo-scanning transmission electron microscopy (STEM) have unveiled some important findings on Li metal anodes, sulfide cathodes and SEI composition and from the data so far, sets clear

requirements and sanity checks for electron microscopy/spectroscopy operando measurement in reactive settings such as battery cells. While electron-based operando methods may help identify various (and often elusive) Li (super)oxide and polysulfide mechanisms in electrolytes and the changes in chemical speciation from electrolyte to surfaces using spectroscopic methods. Some of these requirements are consistent with other operando techniques and correlation and consistency between reports will require fully detailed measurements parameters.

TEM methods for operando investigations will likely take on correlative approaches involving complimentary techniques such as tomography, holography, 4D TEM(70), and others to probe not only the structure and compositions at various SOD or DOD, but to potentially watch, identify and quantify fast (electro)chemical processes at the atomic scale. These developments will take time and likely be limited to certain material-electrolyte combinations. Very complex operando techniques that are developed with new modalities and tackle some of the limitations of earlier methods may prove to be warranted as new battery chemistries are proposed where a much shorter discovery-to-deployment timeframe is needed compared to Li-ion technology.

2.4. Atom Probe Tomography – Compositional Profiling of Electrode Materials Atom by Atom

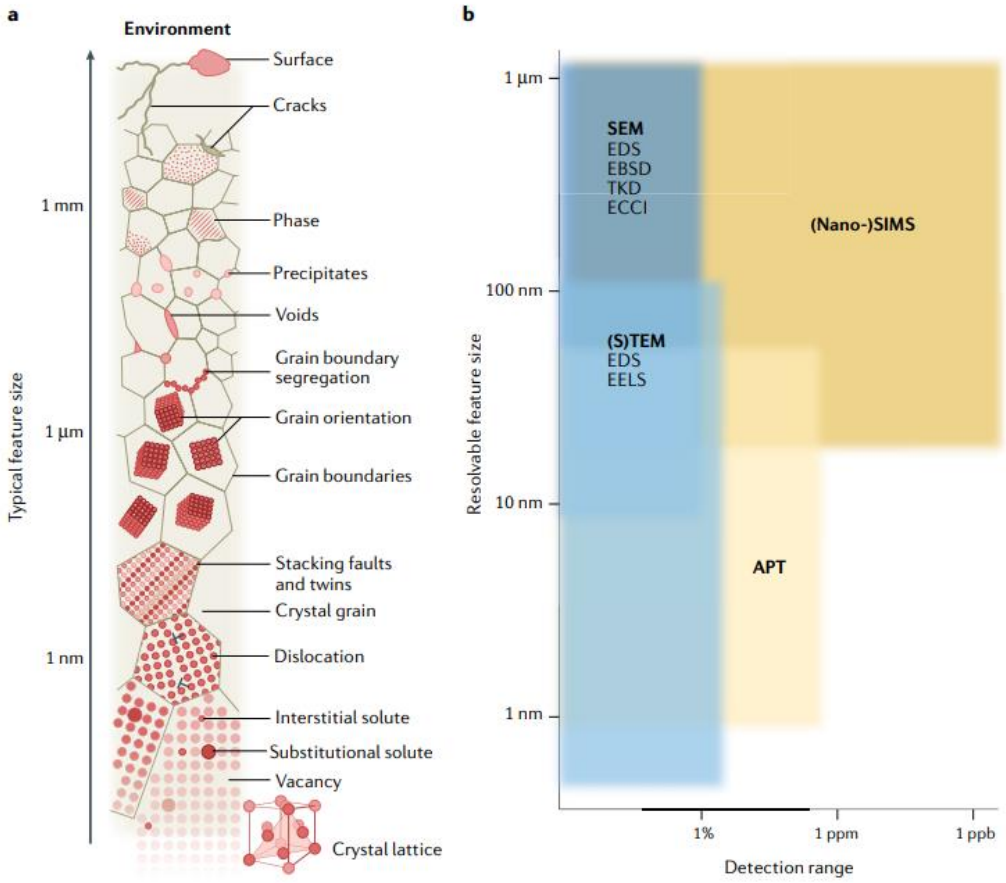


Figure 2.8. Features of microstructured materials with their relative sizes and some analytical techniques used to resolve them. (a) A range of common structural features of interest, from the atomic arrangement of a crystal lattice, through a range of crystalline defects, phases, and grains, to imperfections at the surface. (b) Sensitivity and analysable feature size for some structural analysis techniques. Atom probe tomography (APT); Electron backscattered diffraction (EBSD); Electron-channelling contrast imaging (ECCI); Energy-dispersive X-ray spectroscopy (EDS); Electron energy loss spectroscopy (EELS); Scanning electron microscopy (SEM); Secondary ion mass spectrometry (SIMS); (Scanning) transmission electron microscopy ((S)TEM); Transmission Kikuchi diffraction (TKD). Adapted with permission from ref. (71). Copyright Springer Nature Limited 2021.

The techniques discussed thus far utilise X-ray and electron beam radiation, which can often result in instability in sensitive battery electrode materials due to beam damage. Atom probe tomography (APT) can be used for

compositional mapping of materials in three dimensions with sub nanometre resolution using an electric field. A combination of field ion microscopy (FIM) and time-of-flight mass spectrometry (TOFMS) permits single particle detection capabilities. Unlike traditional microscopic methods where magnification is provided via the control of radiation paths, APT utilises an electric field with a high curvature and is performed using either a straight flight-path instrument(72) or reflectron-fitted instrument.(73) Taking advantage of both microscopy and spectrometry, complementary information concerning both the atomic structure and atomic species of the specimen is provided.

APT is partially destructive in nature as the imaging and identification of the corresponding ion involves their removal from the surface of the specimen. However, given that APT can be applied atom by atom, surface destruction can be minimised, providing an accurate profile of the composition of the material under optimal conditions. The removal of atoms from the material is also beneficial, providing access of the atom probe to layers beneath the surface. APT is therefore not only a surface technique but can provide three-dimensional compositional profiling to volumes of $10^3 – 10^6$ nm^3, corresponding to billions of atoms.(74)

Battery electrode materials tend to be a form of Li-based metal oxide and are often semiconductors. Field evaporation process models were developed mainly for metals, but in the application of APT to less conductive materials the difference in regime must be accounted for. An in-depth overview of the concept and inception of APT, along with the challenges and limitations associated with its analysis of metals compared to less conductive materials is provided elsewhere.(71) When the required electric field is applied in the

atom probe, the reaction of the specimen is to shift its positive and negative charges to form an equal and opposite electric field, a process known as screening. For metals, the screening depth is typically less than 0.1 nm. As a result, only atoms at the actual surface experience the maximum electric field strength. For semiconductors, the screening depth is much greater, found to be ~2 nm for silicon.(75) The change in depth is due to the lower number density of electrons, which is reduced by a factor of 10^7 that weakens the screening effect. The greater field penetration causes bending of the electron band structure (band bending). These effects become more pronounced for more electronically insulating materials. Given that the screening effect in semiconductors reduces their response to the high voltage pulsing of the electric field used to induce field ionisation for APT, alterations are made.

Laser pulsing is incorporated to the setup when APT is applied to non-metals. Given that the electronic response is not sufficient, the incident laser thermally activates the ionisation process.(76) The temperature change induced by the laser pulse causes tunnelling of electrons into the specimen surface while the corresponding positive ions are accelerated along the field lines to the detector. Unsurprisingly, laser pulsing has associated difficulties. A host of additional processes must then be considered, such as interactions between the laser beam and electric field, including absorption, carrier diffusion and recombination,(77) and thermal diffusion.(78) The increased field penetration depth for semiconducting metal oxides mean that sub-surface atoms are field evaporated, rather than just those at the actual surface which lowers the spatial resolution of the technique. The molecular structure of semiconducting materials also affects the resolution of APT.

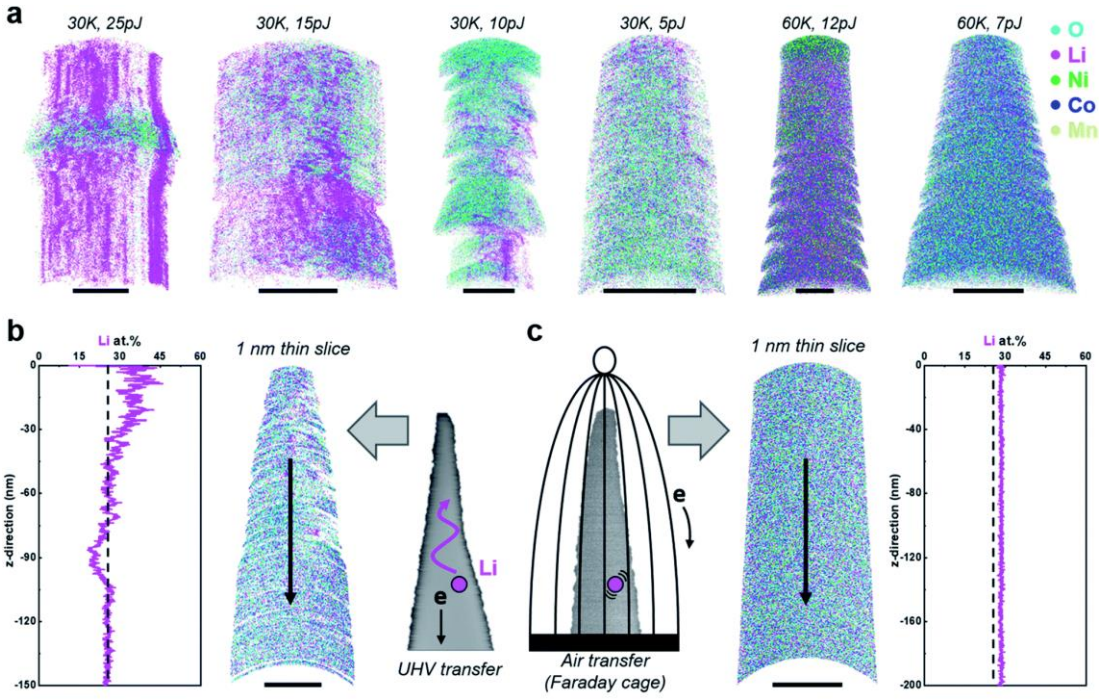


Figure 2.9. (a) 3D atom maps of NMC811 samples obtained under a range of pulse energies and cryogenic specimen temperatures after UHV transferring. Scale bars are all 10 nm. APT results from (b) UHV and (c) air transferred samples. The nominal Li composition of NMC811 in each of the 1D composition profiles are indicated by the black dashed lines. Both APT measurements were performed at a base temperature of 60 K and a pulsed laser energy of 5 pJ. Scale bars in the atom maps are (b) 20 and (c) 50 nm. Reproduced with permission from ref. (32). Copyright RSC 2022.

Field evaporation of molecular ions and cluster ions occurs, particularly problematic for compound semiconductors such as oxides but can also occur in the monoatomic case such as Ge, Si, Sn. These clusters result in a high proportion of multiple events rather than the single event detection desired.(79) Field evaporation of molecular ions also causes their dissociation in the presence of the electric field. This results in neutral molecules which go undetected by the atom probe, further affecting resolution.

The predominant issue in the application of APT to battery electrode materials is process-driven in-situ delithiation, caused by the governance of

the technique by an intense electric field. Most battery electrode materials are reactive metal oxides, so careful handling and transfer is required. Operando implementation of APT to battery systems has yet to be achieved, given the myriad of difficulties associated with the application of the technique to materials in general. Amongst these difficulties are the effects of the processes used in preparation of the specimens for analysis, along with the environment to which they are exposed during transport. Sample preparation is highly specific, usually performed using electropolishing or focused-ion beam methods. The specimen must be needle-shaped due to the curvature of the electric field.

A recent work used APT to probe pristine Li-containing anode and cathode materials and addressed the efficacy of two of the conventions that are typically followed in its practise,(32) namely cryogenic specimen preparation and the use of ultra-high vacuum (UHV) during transport. These conventions are followed due to the belief that they mitigate some of the associated difficulties, primarily, unwanted in-situ delithiation. Preparation methods and transport are performed with and without these difficulty-mitigating steps for several widely used electrode materials to assess their importance. The highly involved specimen preparation and experimental setup is detailed, specific to each material. APT is then performed under a range of experimental conditions for each of the materials. Figure 2.9 (a) shows the 3D atomic composition profiles under a range of pulse energies and two different cryogenic temperatures. Significantly different composition profiles are generated in each case, indicating the importance of choosing the optimal preparation conditions. Figure 2.9 (b) and (c) compare the effects of transport

under UHV and in ambient air. Specimen transport in air resulted in Li composition close to its nominal value, consistent along the full probe length of the specimen while those specimens transported under UHV resulted in a non-uniform composition profile which fluctuated much further from the nominal value. The results prove that previously established transport conventions are not completely reliable. UHV transport is typically used to prevent the adsorption of atmospheric species onto the surface of the specimen which can occur very quickly. For example, a single layer of O_2 can adsorb onto the surface of reactive metals in less than 0.3 s while adsorption can take up to 70 days under UHV conditions. However, the efficacy of the UHV can be questioned here due to evidence in results from this investigation which show that both naturally occurring intrinsic shielding and intentional extrinsic shielding can enhance protection from the electric field. The adsorbed species under ambient conditions may act as a shield from the electrostatic field of the probe and prevent field penetration. The aforementioned Li migration is the primary challenge inherent to the analysis of alkalis by APT. The purpose of the electric field is to trigger the field evaporation of surface atoms, making the prevention of unwanted atomic migration difficult.

Cryogenic specimen preparation (sharpening) is performed (1) as it has been shown to reduce damage to beam-sensitive materials and prevent contamination of unwanted species and (2) increases resolution of produced images. Vibration of atoms about their rest position can cause aberrations to their trajectories that appear as artefacts in the form of blurred images. Cryogenic cooling also combats some of the previously mentioned issues typical of semiconducting metal oxide battery materials, such as thermal

diffusion and band bending.(80) Temperatures are usually in the range of 20 K – 80 K. The key outcome as evident in Figure 2 (a)-(c) is that cryogenic specimen temperatures are important to enhance the quality of the compositional profiles. However, a material-specific optimal temperature must be found, approximated in the case of NMC811 at 60 K.

Maximising knowledge of behaviour at the nanoscale is achieved by performing APT with complementary microscopy and spectroscopy techniques. In 2015, APT under UV laser pulsing of LMO_2-based (M= Mn, Ni, Co) cathode nanoparticles was performed alongside STEM, scanning X-ray transmission microscopy (STXM) and near edge X-ray absorption fine structure (NEXAFS). APT reconstruction revealed the distribution of Li, Mn, and O at the nanoscale. (81) STEM imaging revealed the atomic scale structure, and STXM imaging combined with NEXAFS spectroscopy provided insight into the chemical state of the elements. Integration of this powerful host of techniques can thereby result in a comprehensive understanding of composition, structure and chemical state at the nanoscale. However, access to such a wide range of instrumentation is often unavailable to the typical battery researcher. In 2021, application of STEM and APT to commercially used NCM cathode material demonstrated that the combination of these two advanced microscopy techniques provides sufficient information to directly correlate atomic-scale structural changes to electrochemical performance.(82) The primary outcome was that irreversible structural modifications occur once Li leaves the cathode during charging. Intercalation of Li back into the cathode during subsequent discharges is inhibited. These structural obstructions could partially explain the infamous decrease in capacity after the first cycle in Li-ion

battery systems, and analogies can be drawn to other battery chemistries such as Na-ion and K-ion.

One important aspect of the APT process in keeping with the theme of this review is in the selection of laser parameters used for experiments. Laser wavelengths used in the literature are typically near-UV to UV and the choice has major implications on the species-specific information provided. An investigation into the effects of laser pulse energy and wavelength on APT of LFP cathode material demonstrated the difference in results between the use of 355 nm (UV) and 532 nm (green) lasers at an energy of 50 pJ per pulse.(83) The green laser resulted in the selective loss of Li corresponding to a ~33 % deficiency with a minor oxygen deficiency. The authors suggest that the loss of Li was likely a result of the selective direct current evaporation of Li between or after pulses. For the UV laser, results were much more favourable, with Li, Fe and P present in close to nominal ratios. Meanwhile, oxygen loss was greater at up to 10 % at. Laser pulse energy was then lowered from 50pJ to 1 pJ, which increased oxygen concentration to nearer its stoichiometry.(84) The results indicate that for those interested in the application of APT to Li-based battery electrode materials, a UV laser source is most suitable to minimise in-situ delithiation from the atom probe. However, it must be reiterated that experimental conditions for APT are typically material dependent. Green laser energy is absorbed less efficiently than UV for many Li-based materials due to their inherent optical absorption properties with a bandgap at 196 nm (6.34 eV),(85) while alternative wavelengths may be more suited to Li-free materials such as TiO_2, given that its electronic bandgap lies at ~374 nm (3.2 eV).(86)

For the battery researcher, APT is a powerful addition to the arsenal of techniques used to characterise electrode materials. Given that modern electrode materials are typically nanoparticulate or nanostructured, the sub nanometre resolution of structural features enabled by APT is highly applicable. Complex specimen preparation and process-driven artefacts in produced images limit its performance. However, the ability to provide insight into the changes that occur between individual ions is invaluable to understanding battery systems which operate based on their movement. Operando APT of battery electrode materials during electrochemical cycling is yet to be achieved, to our knowledge.

Technique	Electrode Material	Capabilities	Limitations	Local Resolution
Electron Microscopy	Silicon(68) $LiFePO_4$(61) $LiNi_xMn_yO_z$(66) Germanium(87) $LiMn_2O_4$(88) $LiCoO_2$(89)	Atomic resolution imaging Energy filtered spectroscopy Imaging of interfaces Crystal structure changes Composition mapping	Beam damage Complex sample holders for liquid electrolytes Limited electrode interfacial area under test Contrast and SNR limitation from material thickness/ Z number Limited active material manipulation Secondary electron surface reactions/radical formation Need for cryo-operation	< 1 nm
Atom Probe Tomography	LTO anode(32) NMC cathode(82) L(N)MO cathode(81, 90)	3D nanoscale compositional profiling Atomic species detection and quantification Evaluation of surface and bulk properties at the nanoscale Grain boundary evaluation	Highly involved specimen-specific sample preparation involving FIB lift out and cryogenic cooling under vacuum Process-driven in-situ delithiation Complexities in semiconducting materials:	< 1 nm

		Stacking fault detection Single ionic event detection Segregation of impurities Multi-scale defect detection	-Increased screening depth -Interactions between laser pulse and electric field -Lower surface electron density	

Table 2.2. Summary of a select few examples of materials investigated using operando EM and APT measurements.

2.5. Operando Optical Spectroscopic Methods

Moving from the higher energy end of the spectrum to optical wavelengths provides access to a host of phenomena which occur in battery materials and removes the need for expensive equipment and the use of large-scale facilities. While X-ray methods and APT provide information at an atomic level, optical spectroscopic or “spectroelectrochemical” techniques provide the ability to probe surface characteristics at both the nanoscale and macroscopic level using electromagnetic radiation in the ultraviolet (UV) to infrared (IR) range in a non-destructive fashion.

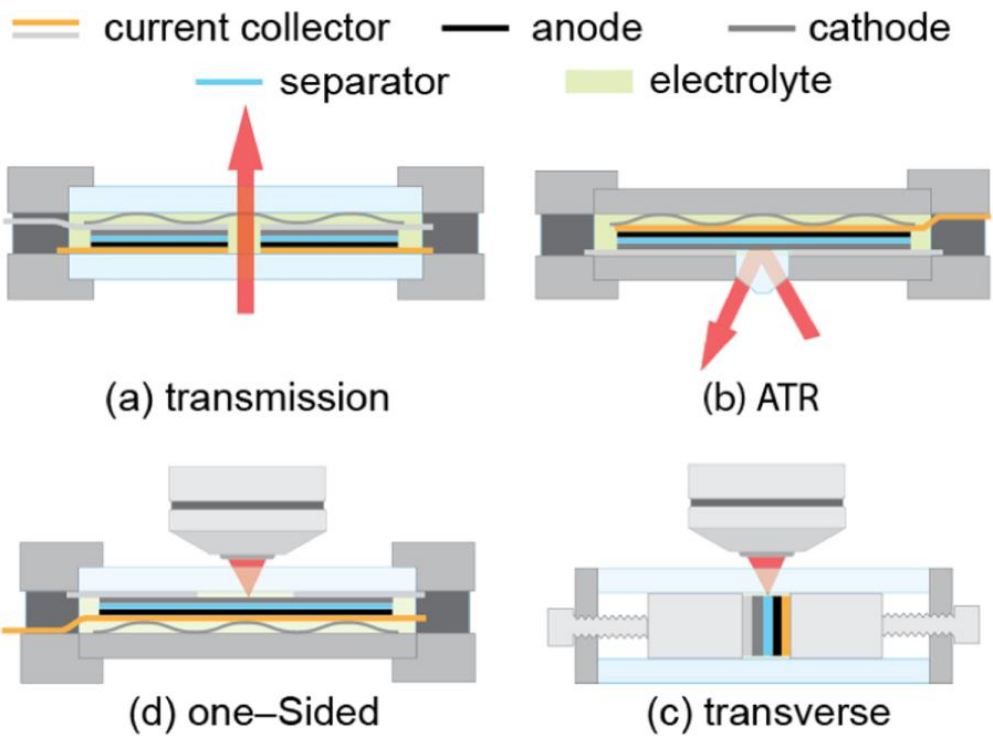


Figure 2.10. Operando spectrochemical cell designs for optical spectroscopic methods grouped into the 4 primary configurations which appear in the literature. Reprinted from ref. (91). Copyright 2022 IOP Publishing.

For applications to battery systems, the most common of these techniques are Raman spectroscopy followed by IR spectroscopy. More

recently, the potential of direct UV-Visible spectroscopy to decipher macroscopic changes in electrode materials has also been realised. A prerequisite for all operando optical techniques is a novel cell design to provide access to the incident beam. In a recent review of operando optical spectroscopic studies of batteries, a distribution of literature available concerning individual focus areas is provided, the focus areas in order of decreasing occurrence are Li intercalation, polysulfide formation/shuttling, non-Li-ion electrode reactions, SEI formation/degradation, electrode structure, electrolyte reactions/decomposition. Our review of operando techniques is focused on their application to battery electrode materials. Consequently, particular variations of the three aforementioned optical techniques of Raman, IR and UV-Vis and their application to electrode materials are addressed. In most cases, designs involve the target anode or cathode material, a thin separator and small electrolyte volumes. For probing electrode materials, electrolyte volumes must be chosen such that the spectroscopic response of electrolyte species are minimised to prevent significant attenuation of signals originating from electrode species. While specific cell designs vary between groups and approaches, they can be grouped into 4 primary configurations: transmission, ATR, one-sided, and transverse as depicted in Figure 2.10.(91)

2.5.1. In-Situ Raman Scattering of Phase Changes in Battery Electrodes

Raman spectroscopy is commonly used to determine the composition of both crystalline and amorphous materials. The technique is based on the energy exchange and direction change associated with light incident on a molecule. The molecule gains energy and the energy of the photons scattered from the

molecule can be measured to determine the composition of the molecule. These energies are observed as peaks on a Raman scattering spectrum, each peak corresponding to a specific molecular bond vibration or optical phonon for Raman-active molecules. For a molecule to be Raman-active, there must be a net change in its polarizability upon excitation. The technique is particularly useful for multi-layered materials such as the porous metal oxides often used in battery electrodes.(92) Information can be revealed on crystal structure, electronic structure, lattice vibrations and flake thickness of layered materials, and can be used to probe the strain, stability, charge transfer, stoichiometry, and stacking order.(93) The correlation between the capacity of intercalation in an electrode to the degree of disorder in the material can also be determined.(41) Such characteristics can be analysed during cycling once an appropriate operando cell design is incorporated.(94) Window materials used include sapphire, KBr, diamond and fluorite glass CaF_2.(95) The cells are referred to as spectroelectrochemical cells, providing the ability to perform electrochemical and optical measurements simultaneously.(96) The most common Raman laser frequencies are 532 nm, 638 nm, and 785 nm, with 1064 nm used in certain cases. Sapphire or quartz are typically the window materials chosen, both with adequate transparency in this range. In choosing beam frequency, the two priorities are (1) to maximise Raman intensity leading to maximal SNR and (2) to minimise fluorescence such that masking of Raman signals produced by the electrode/electrolyte material is prevented. Lower energy lasers often require high power and longer exposure times to enhance SNR, which may lead to beam associated sample damage. The target sample and its associated properties must also be considered prior to beam choice as

each material can produce certain artifacts in the Raman spectra obtained. For example, nanoparticle size has a significant effect on the associated Raman signal. Most industrial cathode materials consist of nanoparticulate powders. Small nanoparticles tend to fluoresce, meaning lower energy lasers (such as 785 nm) are a more appropriate choice due to their greater fluorescence suppression. For more sensitive electrode materials such as silicon wafers, higher energy lasers (such as 532 nm) require lower laser power and shorter accumulation times compared to a near-IR beam.

In terms of the interpretation of operando Raman spectra, there are 4 primary spectral evolutions which can be used to elucidate structural changes within an electrochemical cell.(97) (1) Appearance of a new band which indicates the presence of a new Raman mode or transformation of a previous phase to a new one. (2) Shift of vibrational mode which indicates changes in particle size and corresponding interlayer spacing. Red shifts to lower wavenumbers indicate an expansion or lengthening of the constituent bonds of the corresponding phase, while blue shifts to higher wavenumbers indicate a contraction or shortening of the constituent bonds. (3) Change in band profile, change in bandwidth is indicative or the degree of order in the probe area. Increasing bandwidth during operando measurements represent a shift towards disorder in the system. (4) Change in band intensities. Origin of band intensity fluctuations are more difficult to track and can be a result of an array of changes. Common causes include a change to the concentration of the corresponding phase or blocking of the original signal due to interference from other species. For example, blocking of characteristic electrode Raman modes by electrolyte species.

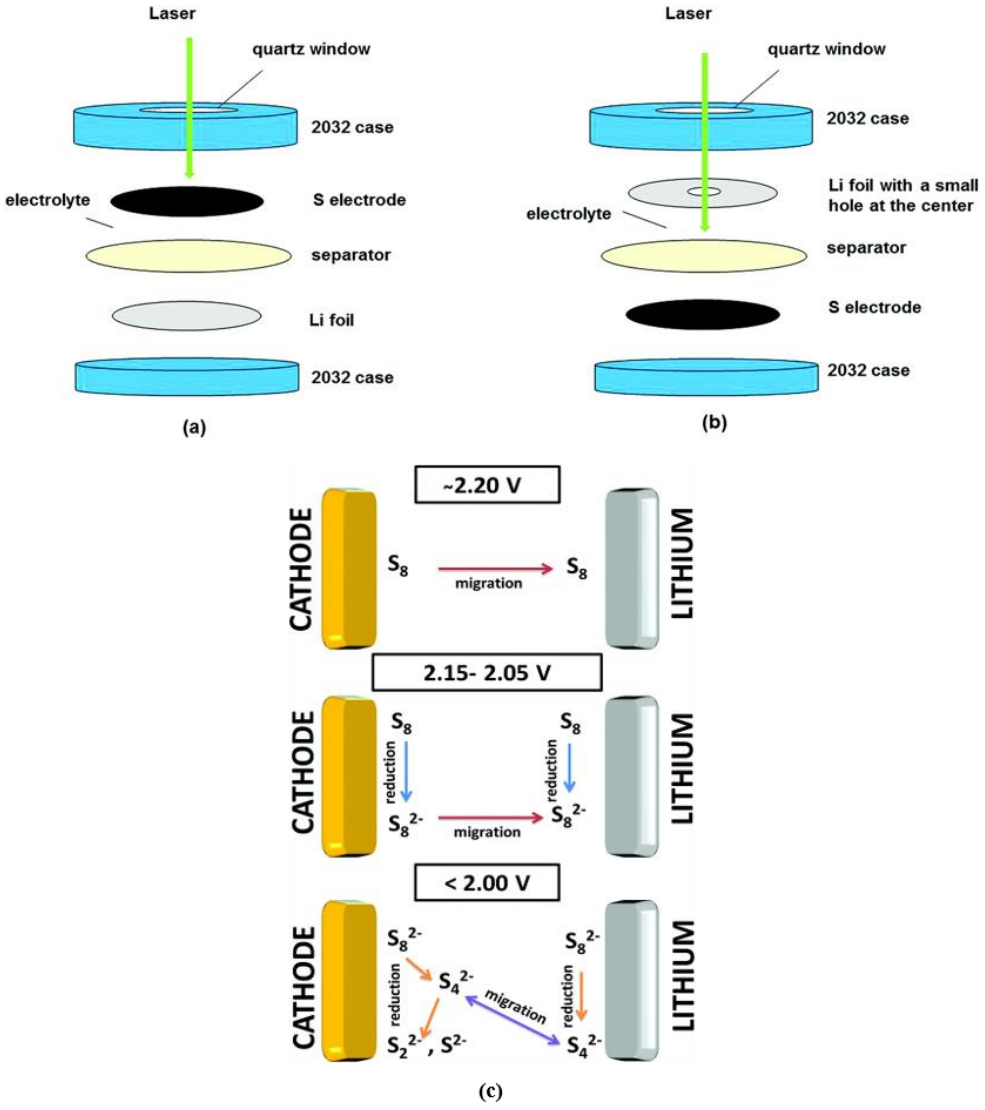


Figure 2.11. In-situ Raman cell designs for monitoring changes in (a) the cathode and (b) electrolyte near Li metal. (c) Schematic of the reduction process from in-situ Raman measurements at both the cathode and Li metal sides depicting the evolution of polysulfide species in a Li-S battery. Adapted with permission from ref. (98). Copyright RSC 2017.

In Nakagawa et al., (99) the changes in the surface crystallinity of edge plane HOPG (graphite) anodes are probed using in-situ Raman spectroscopy. The corresponding spectra show that surface crystallinity is significantly lowered within only a single charge/discharge cycle. The combination of these results with considerations of the intercalation mechanism of Li^+ provides

information on the structural degradation of the graphite surface. Conventional Raman spectroscopy is limited to near-surface regions predominantly, depending on the optical characteristics (scattering, absorption, etc.) at the incident probe wavelength. More intricate adjustments are required to permit deeper penetration. Like the techniques mentioned previously, in-situ Raman measurements require a more complex electrochemical cell. Here, a three-electrode cell was equipped with an optically flat window made of Pyrex glass to permit light transmission.(41)

In Zhu et al.,(98) in-situ Raman and in-situ XRD are used to probe electrode degradation mechanisms in a Li-S battery. Li-S batteries have a very high theoretical capacity of 1675 mAh g^{-1}, but there are significant issues with the associated discharge mechanism. Here, analysis of the mechanism based on the influence of the electrolyte on the dissolution of sulfur and polysulfides is presented. The short lifetimes of the polysulfide species mean there is a clear motivation for the introduction of in operando measurements. While the same species are detected in each case, the rates of polysulfide formation and diffusion to the anode depend on the electrolyte and the associated ionic mobilities of the various species in the electrolyte. In-situ Raman scattering measurements of the Li-S battery in an ionic liquid electrolyte (LiTFSI–PY13–FSI) and ether-based electrolyte (LiTFSI–DOL–DME) are shown in Figure 2.11 (c) and provide a summary of the evolution of the polysulfide species occurring at both cathode and anode.

The in-situ Raman spectroscopy performed here provides a clear picture of the discharge mechanism of a Li-S battery, the effects of the chosen electrolyte and compares the phase changes of ionic species in the electrolyte

in the vicinity of both the sulfur cathode and Li metal anode. The cell designs used allow measurements to be performed non-destructively in real-time, capturing the true behaviour of the system during discharge. Application to more traditional battery systems containing common electrolytes is straightforward. The Li-ion transport dynamics at particle level are revealed via in-situ Raman spectroscopy in Wei et al.*(100)* for a battery containing a $LiFePO_4$ cathode and electrolyte composed of $LiPF_6$ in ethylene carbonate (EC) and dimethyl carbonate (DMC) through the examination of Raman peaks originating from the C-O stretching vibration in EC. The Li-ion concentration at the cathode surface was found to fluctuate based on the redistribution of Li^+ within the pore space of the electrode.

All-solid-state Li-ion batteries (ASSBs) have also attracted attention due to increasingly widespread belief in their safety, relative to Li-ion batteries containing organic liquid electrolytes.(101-103) However, the major concern with these systems is the instability of the interface between the sulfide solid electrolytes and the electrodes. Once again, the electrochemical processes which govern the evolution of the interfacial layers require in-situ measurements. Ex-situ and in-situ Raman spectroscopy is used in Zhou et al. to probe degradation mechanisms at the electrode/SEI in real-time.(104) In-situ and ex-situ Raman spectroscopy are applied in tandem to probe the evolution of sulfide species during discharge once again. With a one-sided cell design, it is shown here that in-situ Raman measurements can be used to access the Li/SEI, and the solid/solid interfaces within the layers of the composite positive electrodes. Clever adaptations are made to the cell design that expand the range of electrode-related phenomena which occur during

cycling. Metallic coatings are applied to the borosilicate window, which then act as current collector between electrode and solid electrolyte. A 50 nm copper (Cu) coating is applied to investigate the extent of Li plating which occurs at the electrode/SEI. The Cu coating effectively acts as a substrate for Li plating while simultaneously maximising access of the Raman beam to the plating process. A 50 nm gold (Au) coating with transparent area at the center is then applied to examine the stability of $LiCoO_2$ also. The study stands as a demonstration of the versatility of some operando cell designs and shows the value of in-situ Raman spectroscopy to understand the effects of cycling on the interfaces within ASSBs and the consequential routes to electrode degradation. Given that in-situ Raman can be used at a microscale level with the appropriate beam width, application to thin film ASSBs can thus clarify local structural changes at multiple locations within the cell. An example of such is demonstrated in Matsuda et al., (105) where micro Raman spectroscopy is used to interrogate the local material structure at either side of the $LiCoO_2$ cathode by acquiring measurements at the front and back of the cell.

The implementation of operando Raman spectroscopy to investigate battery electrode degradation can shed light on the structural changes of the materials because of the electrochemical processes which occur during charge and discharge of a battery. Most success is found when ex-situ Raman measurements are used to streamline the in-situ or operando experiments. Its use in tandem with other complementary techniques can provide a detailed characterisation of structural-electrochemical relations at an atomic level. Given the correct cell design, application to a wide range of state-of-the-art

battery designs including Li-S batteries, ASSBs, and thin film batteries is possible in a small-scale lab setting.

2.5.2. In-situ ATR-FTIR for Probing Electrolyte Decomposition at the Electrode/Electrolyte Interface

Fourier transform infrared spectroscopy (FTIR) is based on the absorption of infrared light over the wide spectral range of 14,300 – 20 cm^{-1}. In most battery systems, the solvents used as electrolytes are dominated by chemical bonds with energies in the IR regime. Light absorbance as a function of wavelength is calculated to produce a series of absorption peaks. The peaks are caused by excitations of molecular vibration, rotation/vibration, lattice vibration modes, or a combination of each. Each corresponding frequency can be correlated to specific functional groups, while infrared peak intensity can be linearly correlated to the amount of species in the sample.(106)

One of the key issues which arises in battery performance assessment is the monitoring of organic species, particularly at the SEI layer. Widely used techniques such as X-ray photoelectron spectroscopy (XPS) provides little to no information on organic SEI species and electrolyte solvents. NMR provides more information on organic solvents but cannot be incorporated to probe the solvents at the surface of the electrode and monitor the SEI layer. In-situ/operando FTIR spectroscopy can be employed at the electrode surface and proves very powerful in the analysis of organic species in real-time, identifying the composition and structure of species within the cell based on the identification of the functional groups present.

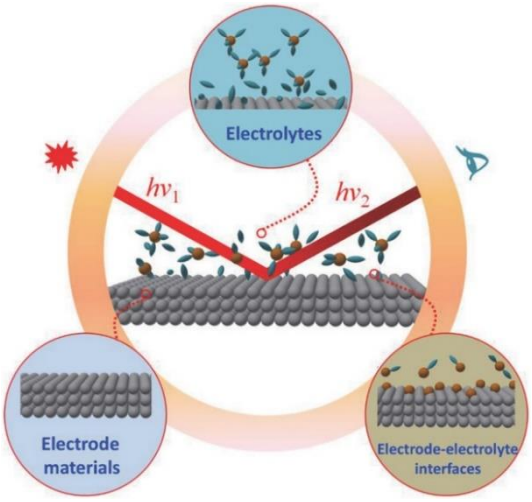


Figure 2.12. Schematic of conventional spectroscopic methods in secondary battery studies focusing on the electrode/electrolyte interface. Reproduced from ref. (107). Copyright Wiley 2018.

One of its main uses being the monitoring of electrolyte solvents, including the gaseous products formed upon oxidation and reduction of the electrolytes near the electrode interface.(108) Information can then be provided on the electrochemical changes which occur in the solvents during cycling such as solvation and desolvation. Using this information, an insight into the impact that these processes have on the electrodes and species in the vicinity of the electrodes such as the SEI layer can be obtained in real-time, some of which are schematically represented in Figure 2.12.(109, 110) Four sampling techniques are used: transmission, specular reflectance, diffuse reflectance, and attenuated total reflection (ATR).(111) While each sampling techniques has its benefits, ATR-FTIR is most often incorporated for operando measurements of battery electrode materials, where the area of interest lies at the electrode/electrolyte interface. While transmission FTIR measurements are useful for bulk properties, ATR-FTIR is essentially independent of sample

thickness, constituting an internal-reflection-based method with a typical penetration depth of 0.2-3 μm.(112) ATR-FTIR measurements are enabled by an ATR sensor of suitable optical material. The material must be optically transparent to the frequency of incident energy so that none of the useful radiation is absorbed. The material must also have an index of refraction greater than the surrounding media, so that total internal reflection occurs, with the sensor essentially acting as a waveguide. Typical sensor materials include ZnSe, diamond, Ge, Si, and thallium bromide-iodide (KRS-5). Decisions on the choice of these materials depend on the region of interest within the IR range (near-IR, mid-IR or far-IR).(113)

Like the other techniques described thus far the most challenging aspect of using in-situ FTIR to monitor cell degradation is the cell design. With the correct cell design, in-situ FTIR spectroscopy can be applied to a range of battery systems. In the analysis of battery materials, the technique serves mainly to provide insight into the Li^+ dynamics at the electrode/electrolyte interface. ATR-FTIR is extremely powerful.(114) A schematic of a representative setup is shown in Figure 2.13 (a). In contrast to traditional FTIR spectroscopy, surface sensitivity is enhanced. The precise penetration depth depends on wavelength, incident angle, and the electrode material along with any interfering electrolyte species and cell components.(115) The high surface sensitivity of the method and its dependence on multiple light reflections mean that it is extremely useful for probing composite and multi-layered materials such as those used in battery systems, remaining useful irrespective of the battery chemistry.

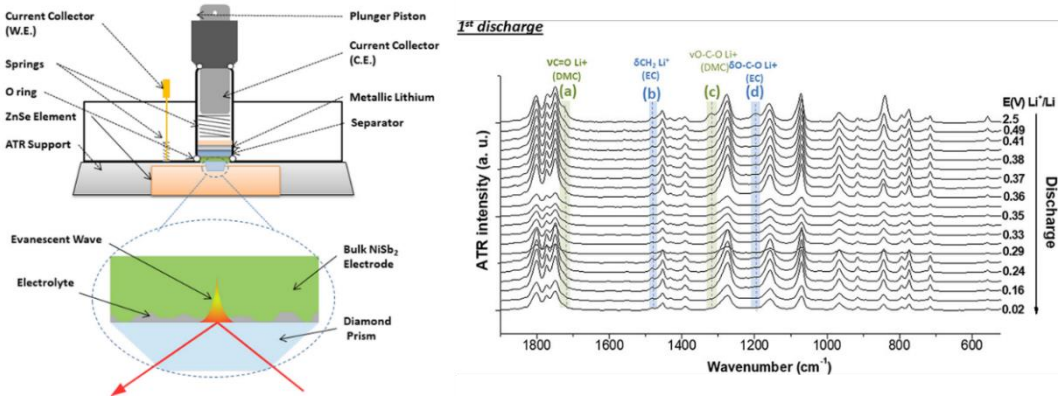


Figure 2.13. (a) Schematic of the electrochemical cell used for the operando ATR-FTIR experiment. (b) Operando IR spectra obtained during th^{e} 1st discharge of $NiSb_2$ electrode at a rate of 1 C with 1 M LiPF6 in EC: DMC (1:1) + 2 % vol VC electrolyte. Adapted from ref. (116). Copyright ACS 2017.

In Marino et al., ATR-FTIR spectroscopy is used to probe conversion-type electrode materials.(116) These materials demonstrate interesting performance in terms of capacity but are associated with poor Coulombic efficiency. Poor Coulombic efficiency is usually related to the relentless formation and desolvation of the SEI during conversion and back-conversion reactions. The setup is shown in Figure 11 (a), with a diamond prism used as a waveguide for the ATR-FTIR approach, an $NiSb_2$ electrode and $LiPF_6$ electrolyte dissolved in EC and DMC. The measurements are obtained in the vicinity of the electrode/electrolyte interface. Figure 2.13 (b) shows the corresponding IR spectra obtained at a rate of 1 C during first discharge. By examining the IR spectra and comparing to known values in the literature, the origin of each of the peaks from species present in both the electrode and the electrolyte can be determined. The shift in the peaks of the spectra during cycling means that dynamic evolution of the Li concentration in the electrolyte can be followed. Tracking of the formation and desolvation of the SEI layer is also achieved. The operando measurements confirm the phase separation of

the conversion materials during discharge, and the nanostructuring of the electrode.

Mentioned repeatedly in this review is the promising performance of silicon electrodes and their applicability to next generation battery systems. The ATR-FTIR approach is applied to thin-film amorphous silicon electrodes in operando in Corte et al.,(117) providing information into the characteristic performance issues related to the reaction of silicon to lithiation and the composition of the SEI layer formed. ATR-FTIR assesses the thickness of the SEI layer, which increases during lithiation and partially reduces during delithiation. Question marks remain over applicability of the approach to silicon-based electrodes since they are commonly in (nano)dispersed form, included in a composite with additives and binder, given thar ATR-FTIR spectroscopy is most useful with thin film materials. Nevertheless, the study improves understanding of the processes which govern silicon lithiation and can be applied to any thin film electrode material that does not demonstrate excessive IR absorption. This issue often arises in the study of pure metals. As a result, metal oxides are more suitable for IR analysis.

ATR-FTIR spectroscopy proves useful in its ability to probe causes of battery electrode degradation by analysing SEI formation on the electrode interface during cycling. While its use is demonstrated here for the analysis of silicon electrode-based systems,(114) the technique can be applied to several battery technologies even beyond Li-ion, such as Li-oxygen, Na-ion and potassium-ion.(118-120). A compendium which reviews optical spectroscopy as a tool for battery research can be found in Köhler et al., with a particular focus on UV-visible and IR spectroscopy.(121) Applications to thin film, multi-

layered battery electrode materials demonstrate the power of operando ATR-FTIR, providing detailed insight into the evolution of the SEI layer, which has a significant impact on conversion-type battery electrodes.(122, 123)

2.5.3. Tracking the Optical Signature of PhC Electrodes in Real Time

The performance and longevity of battery systems are determined primarily by the structural and electrochemical changes which occur within the component materials. In comparison to planar deposits of electroactive material, colour-coded, thin-film battery materials enable real-time diagnostics by observing their “structural” colour,(124) caused by a phenomenon known as the PBG (PBG).(125-128) When light is incident on a periodic material with a period on the order of the wavelength of incident light, photons within the PBG are reflected, producing the observed structural colour.(129, 130) The observed colouration can be correlated to a specific optical signature for each material, so optical measurements can be used to characterise their structure.(131-133) Such measurements have been widely used for battery materials in recent years(134-138) and are extremely useful for porous electrode structures such as PhCs (PhCs).(109, 139-144) Because periodically porous materials can be fashioned from self-assembly methods through to electron beam lithography and many methods in between that give exquisite control over complexity, the wider research community can grow materials with a tuneable PBG without the need for expensive equipment or complex fabrication techniques.(145) An adjustable PBG in a material gives the opportunity to monitor small changes in material properties using angle-resolved reflectance or transmission measurements(146). We see PhCs in a wide variety of disciplines, including

optical(147-149), energy storage(122, 150), biological(151-153) and medical devices(154, 155). Such structures can behave as optical waveguides(156), refractive index sensors(157, 158), biosensors(154, 159), and also provide opportunities for tuning solar absorption(160, 161). More recently, they have been assessed as binder and conductive additive-free structured electrode materials in Li-ion batteries(134-138).

The move away from the traditional and well-understood battery chemistries to more complex redox processes such as alloying and conversion, and the need to optimise more established chemistries, has motivated the development of new analytical operando techniques that allow study of the fundamental mechanisms by which these materials operate, together with the kinetics of these processes.(162-166) IO PhCs have been widely researched as anode materials for Li-ion batteries (LIBs). Composition changes, Li doping, potential-dependent electrochromism, cation insertion, rate-dependent dielectric constant modification and the photonic signatures of Li insertion into an ordered 3D structure can be achieved by making battery electrode materials in the form of IOs.(108) Some studies have analysed their optical reflectance and transmission.(16, 96, 168) As a result, there is a large body of data available when choosing potential anode or cathode materials. An extensive review of IOs and their applications to energy storage mechanisms can be found elsewhere.(169) Despite this, optical characterisation of IO battery electrodes in-situ or in operando has not been achieved.

Fundamentally, in spite of some clear parallels between materials science, electrochemistry and photonic spectroscopies, these disciplines have

not yet been combined and brought to bear on new electrode designs in emerging alternative energy storage materials neither for performance-related device improvements(170), nor fundamental assessment of new modalities, analytics or diagnostics of electrochemical materials response. The research community needs to explore interdisciplinary approaches to drive the next innovation in portable energy storage, especially when new materials and new ways of manufacturing batteries, such as 3D printing, become more advanced.(171-173)

Most transmission/reflectance studies of IO anodes have been carried out prior to cell assembly.(96) This is due mainly to the challenge presented by the closed nature of standard electrochemical cells. While the power of X-rays allows penetration of cell casings, energies in the optical range do not provide this luxury. Like Raman and FTIR spectroscopies, optical spectroscopy measurements require less intuitive cell designs which can allow light to penetrate the cell. Such adaptations have been made in Lonergan et al., where the optical transmission of IO anodes are examined when placed in a range of solvents.(174) The solvents chosen are typical of those used for electrolytes in both industry and research. The study can be considered a preliminary ex-situ experiment which provides insight into the effects of potential electrolytes on the incident beam. Just as seen for all techniques discussed thus far, this ex-situ information can be used going forward to streamline operando experiments. A transparent “flooded” cell is used in the study, a design previously used for electrochemical performance assessment of PhC anodes in excess electrolyte. The cell design allows light penetration such that measurements can be obtained non-destructively. While this

constitutes a step in the right direction by studying the materials in the assembled cell, optical measurements in real time are required to provide a better insight into battery performance.

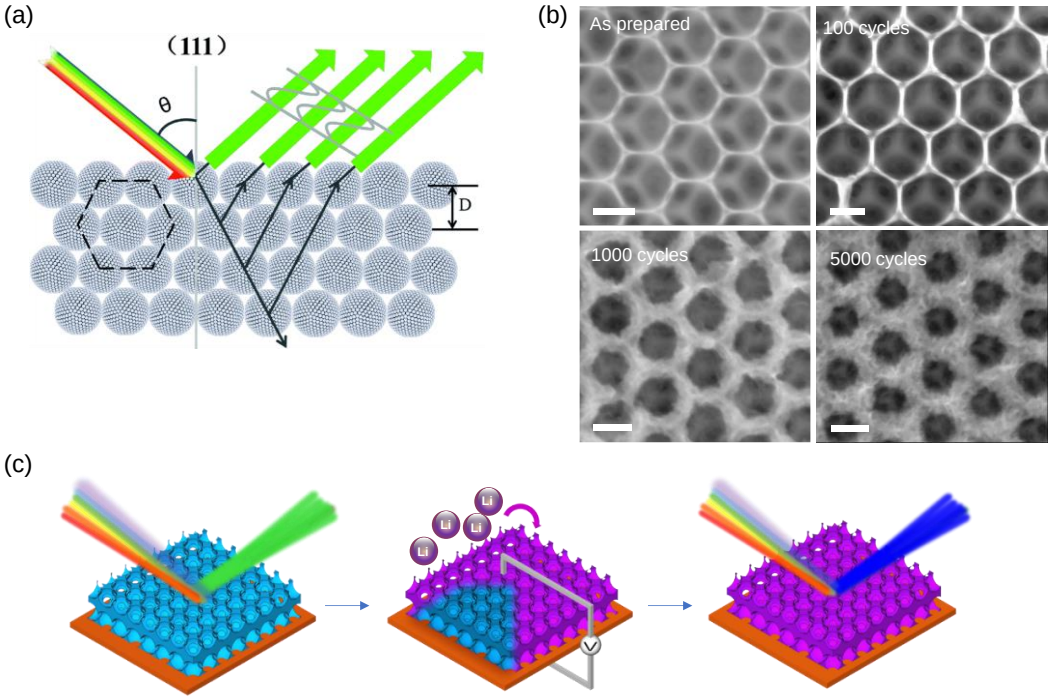


Figure 2.14. (a) Schematic of the PBG in a PhC, selectively reflecting a narrow band of photon energy. Light within the PBG is reflected from the crystal, determined by the lattice constant *D*. Reproduced from ref. (175). Copyright RSC 2019. (b) TiO_2 IO materials used as an anode in a Li-ion battery showing interconnected volumetric swelling as lithiated titanate over 100, 1000 and 5000 cycles. Scale bar = 200 nm. Adapted from Ref. (176). Copyright Wiley 2017. (c) Schematic representation of operando angle-resolved reflectance measurement of a PBG during reversible lithiation.

3D structured EES materials do not require pristine, defect-free large scale arrays(177) of electroactive deposits as would be required in photonics(178) that use semiconductive IOs for optics, telecommunications, optical interconnects, and silicon photonics, as pertinent examples. Optical techniques applied to functioning battery materials in-situ are rare and typically are used to examine the structure of electrolyte compositions of the synthetic

preparation of materials.(179-181) Only recently, PhCs have been used to enhance the photoabsorption characteristics of perovskite halide solar cells using structural colour to tune the absorption across the entire visible spectrum.(182)

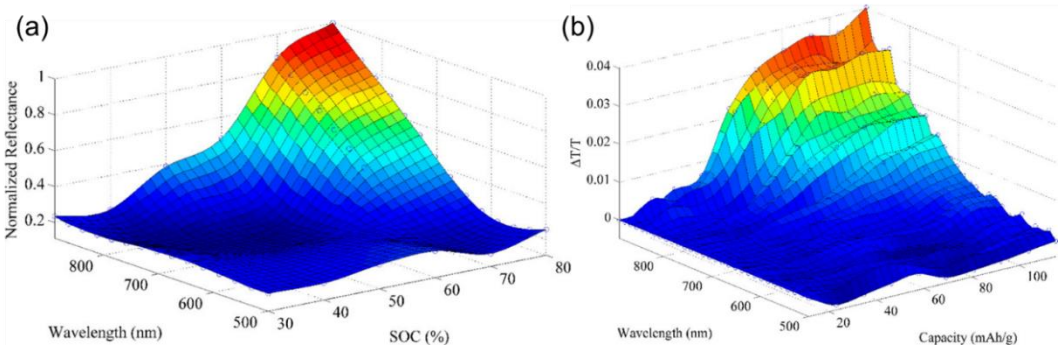


Figure 2.15. (a) In-situ optical reflectance measurements of lithiated commercial graphite electrodes at various states of charge. (b) Operando optical transmission measurements of graphite electrodes during lithiation. Adapted from ref. (168). Copyright ACS 2016.

While such measurements have not been obtained for IO anodes, operando optical analysis has been achieved for graphite anodes.(183) In 2016, Ghannoum et al. used an optical fibre sensor (OFS) to obtain information about the interaction of near infrared light with graphite during its electrochemical lithiation process in a Li-ion pouch cell. Here, the optical transmission measurements were confined to the overall intensity of the optical signal as a voltage. Further work by Ghannoum et al. in 2020 provided a more extensive optical characterisation of the system.(184) As shown in Figure 2.15, reflectance spectroscopy measurements of lithiated commercial graphite anodes at various states of charge were obtained. To obtain the measurements, the graphite anodes were extracted, and the cells

disassembled in an inert environment. Next, an OFS was embedded like the previous study, this time in a custom-designed Swagelok cell. Fiber evanescent wave spectroscopy (FEWS)(185) was used to provide in operando optical transmission measurements during lithiation of the graphite anode. Reflectance and transmission measurements both demonstrate that there is a direct correlation between the wavelengths reflected/transmitted and SoC. The results further highlight the need to monitor these changes in optical activity under operando conditions. After some adaptations, the approach used here may be the key to obtaining operando optical transmission/reflectance measurements of IO anodes.

Tracking the optical signature of PhC electrodes in operando may be an effective, low-cost route to probing their degradation mechanisms non-destructively in real-time. Progress is being made in developing the correct methodology for achieving these measurements, with particular attention to consistent cell assembly and internal pressure that does not alter the periodicity of the periodically porous material, nor inhibit volumetric or other changes that can occur during reversible ion (de)intercalation. To achieve success, factors such as cell design, light-electrolyte interaction, and electrode response to the degree of lithiation must be considered. Like the XRD and acoustic fingerprints observed for battery materials, the optical fingerprint of PhC nanostructures may prove an important asset to further understanding of the physical and chemical processes that govern battery performance. A first step in describing the optical behaviour of ordered porous battery electrodes is a model system to examine charge storage mechanisms, in-built stresses, volumetric changes and the intrinsic benefit or scaled porosity to ionic

diffusion, electrical conductivity and material interconnectedness, is accurate data in battery electrolytes. For an IO PhC of any material, such as the example shown in Figure 2.14, the following summarise the basic relationships that are useful in characterising the PBG and its dependence on the surrounding environment (air or solvent), effective refractive index and the angle of incidence for reflectance of transmission signal in a typical angle-resolved reflectance/transmission setup.

For a crystal plane (hkl) with interplanar spacing d_{hkl}, an IO material with an effective refractive index n_{eff}, some solvent of refractive index n_{sol} filling the pores, a Bragg resonance order m and some angle θ between the incident light and the normal to the crystal plane surface, the transmission minimum λ_{hkl} can be found via the Bragg-Snell model as follows: $\lambda_{\mathrm{hkl}} = \frac{2d_{\mathrm{hkl}}}{m}\sqrt{n_{\mathrm{eff}}^2 - n_{\mathrm{sol}}^2 \sin^2\theta}$, a plot of the observed minimum wavelength squared versus the sine of the angle of incidence squared should yield a linearly regressive plot with a slope $\mu_0 = -4d_{111}^2 n_{\mathrm{sol}}^2$ and an intercept $\gamma_0 = 4d_{111}^2 n_{\mathrm{eff}}^2$. From this, the interplanar spacing d_{111} and hence the centre-to-centre pore distance D can be found via the slope. The effective refractive index n_{eff} of the IO material can be estimated by dividing the intercept by the slope. Currently, there are several methods used in a wide variety of literature to approximate the effective refractive index of composite materials(186, 187).

The Drude model for IO systems can be formalised as: $n_{\mathrm{eff}} = \sqrt{n_{\mathrm{IO}}^2\,\varphi_{\mathrm{IO}} + n_{\mathrm{sol}}^2\,\varphi_{\mathrm{sol}}}$. The Parallel model for an IO system can be written as $n_{\mathrm{eff}} = n_{\mathrm{IO}}\varphi_{\mathrm{IO}} + n_{\mathrm{sol}}\varphi_{\mathrm{sol}}$. For an IO system, n_{IO} refers to the refractive index

of the crystalline IO material, n_{sol} is the refractive index of the surrounding medium, φ_{IO} constitutes the volume filling fraction of IO material in the system and φ_{sol} is the volume filling fraction of the surrounding medium. For IO PhC filled with a solvent, a Bragg-Snell relation in terms of the Drude model for n_{eff}: $\lambda_{\mathrm{min}}^2 = 4d_{111}^2(n_{\mathrm{IO}}^2\,\varphi_{\mathrm{IO}} + n_{\mathrm{sol}}^2(1 - \varphi_{\mathrm{IO}}))$. Specific details are found elsewhere(188) for a variety of solvents and substrates, but the principle allows, in general, the PBG to be a trackable parameter caused by material and effective index modification when it undergoes electrochemical modification or changes during cycling in a battery cell. Adaption to closed coin cells or similar form factors has yet to be established.

Tracking variation in PhC materials in real time spectroscopically allow, in principle, tracking of changes to effective refractive index, periodicity, and conductivity as a function of cycling parameters in voltammetric or galvanostatic conditions. Volumetric swelling and lithiation/sodiation would vary the refractive index contrast and periodicity, shifting the photonic bandgap predictably for a material that is structurally well-defined. In addition, the change or erasure of periodicity, for materials where large cyclic volumetric changes occur, would indicate whether ordered arrangement or in-situ pulverisation and relief of new surfaces is a contributory cause to coulombic efficiency, capacity loss or a limitation in charge rate behaviour for a fixed thickness. These approaches are currently being developed for relevant battery materials to tackle open questions in materials that are assembled with coating morphology and mass loadings that are more relevant to battery cells in various form factors.

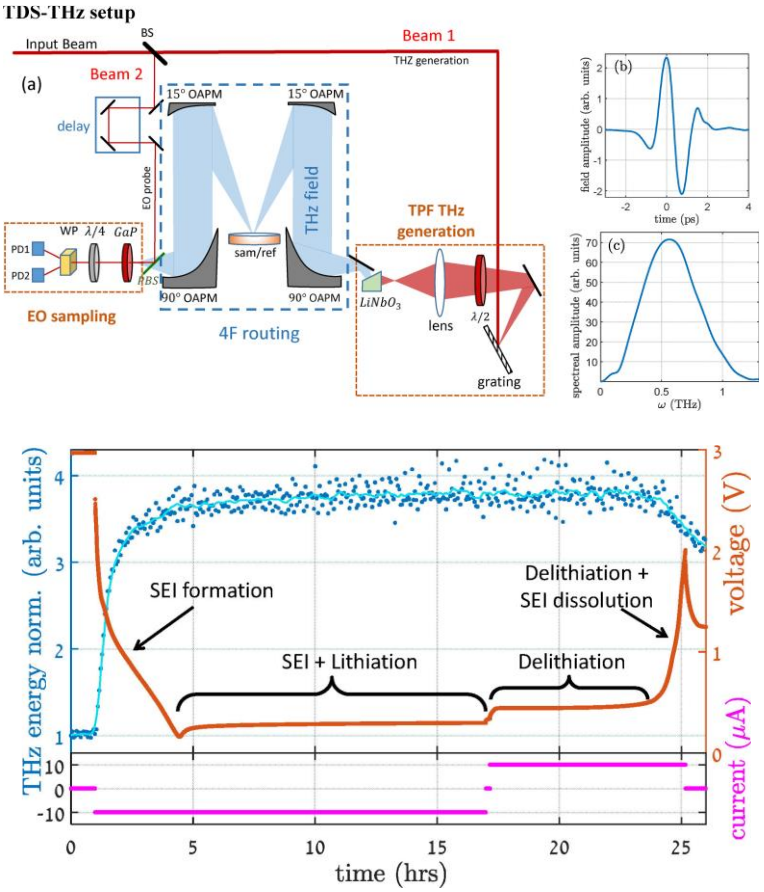


Figure 2.16. (Top) (a) Schematic of the time-domain THz spectrometer setup in reflection mode with the battery cell placed at prime focus. (b) An example of a THz signal in the time domain together with its associated amplitude spectrum. Electrooptic sampling module includes a pellicle beam splitter (PBS), a Gallium Phosphate crystal (GaP), quarter-wave plate, a Wollaston prism (WP) and two photodiodes. (Bottom) The THz signal (blue dots) in the time domain during a single full cycle. The cycle comprised the discharge (1–17 hours) followed by charging (18–26 hours). The cell voltage is shown in orange and the current in magenta. Reproduced from ref. (189). Copyright Wiley VCH 2022.

Other recent approaches have used operando terahertz time-domain reflectometry spectroscopy(189) (THz-TDS) to investigate solid electrolyte interphase evolution on silicon anodes. THz-TDS operates in the 10^{11}–10^{13} Hz frequency range(190) as a non-destructive mode. It is based on characterisation of the dielectric nature of the sample under test. For battery

materials research, THz compatible windows are readily available, and can be integrated into various form factor cells such as coin cells or larger split cells for larger window aperture. The amplitude and phase of the electric field provide the information based on attenuation of the reflected THz field following sample interactions. In this study, Krotkov et al. examined an anode comprising silicon nanoparticles, some binder, and a small addition of conductive carbon. In Figure 2.16, the basic setup for this approach is summarised along with data from an experiment that allow operando tracking of SEI formation at the surface of the silicon nanoparticles during cycling, with a pronounced dependence on the time between charge-discharge of cycles. They found that certain parts of the SEI tend to dissolve during rest periods if the film was not fully formed prior to the restart of the polarisation, particularly for elements of the SEI that are unstable at higher voltages as the charging voltage increases. The measurements show that SEI formation and reformation after dissolution is not only dependent on fresh surface formation that occurs after pulverisation or cracking from repeated volumetric changes. The signal is clear for SEI dissolution following some cracking of the underlying silicon, but that SEI stability at different voltages is not consistent and shown through changes in the effective dielectric constant of the anode during cycling.

2.6. Internal Sensing of Battery Response – Fiber Bragg Grating Sensors and Probes

Motivated by measurement systems in composite research that used Fiber Bragg grating sensors within composite matrices and laminates of materials that allow operando measurement of stress-strain and other mechanical

properties.(191) These were developed to avoid some limitation of attachment-type sensors, often based on cantilevers that give uniaxial information (depending on its orientation on the composite or device), and in many cases is limited to device-level information. Recent reports(192, 193) have begun to implement FBGs inside battery cells, to get at real-time assessment of the interplay between chemical, mechanical, thermal, and other properties and their relationship under specific battery cycling conditions. Fiber Bragg gratings used in this way are assessed by monitoring changes to reflectance or a specific splitting of reflectance peaks caused by birefringence.(194)

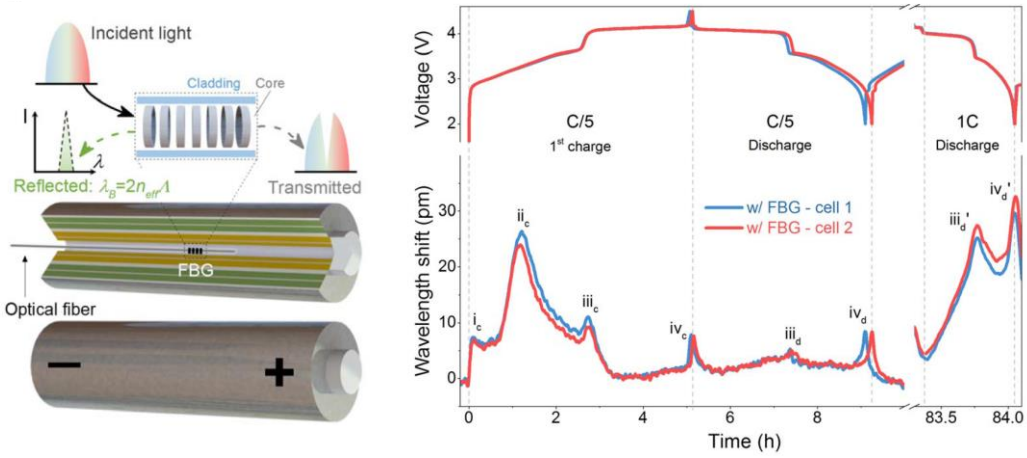


Figure 2.17. (Left) Schematic representation of the integration of optical fiber integration into a 18650 battery cell. (Right) The time-resolved voltage of the cell and spectral shift from the FBG for two separate cells over a single C/5 charge-discharge cycle and also after a discharge at 1 C. Spectral reflectance maxima 1st charge at C/5. The wavelength shift is relative to the wavelength at time = 0 h on the 1st charge at C/5. Adapted from ref. (192). Copyright Nature Publishing Group 2022.

Real-time monitoring of the dynamic chemical and thermal behaviour of a battery becomes important when safety and reliability are paramount in new cell chemistries or form factors. Blanquer et al. integrated FBG into 18650

and pouch cells to directly monitor temperature, strain and hydraulic pressure and showed they could be correlated with battery state-of-health and indeed state-of-charge. Careful adjustment of the morphology of the fibre was necessary to enable spectral changes from temperature and pressure in a manner that allowed them to be decoupled. The method summarised in Figure 2.17 was then shown to provide operando information on SEI formation and structural evolution of the electrodes. Further details on specific analyses can be found in Ref. (192) . Other work has addressed the possibility of direct SEI formation tracking under operando conditions, notably the work of Louli et al. where operando pressure measurements quantified Li inventory loss to irreversible cell volume expansion while physically detecting SEI growth during cycling.(195) The same group also adapted the approach by using multiple sensors (Figure 2.18) to measure cell-generated heat curing cycling and compared the operando measurements to those by isothermal calorimetric measurements.(193)

One major motivation from a practical standpoint is that current heat generation and dissipation measurement techniques are slow, require larger infrastructure and are limited to measurements outside the cell. The authors detail the basis of their heat mapping models, factoring a zero-dimensional model that was scalable (Figure 2.18). Three separate FBGs were used to measure ambient, internal, and surface temperatures of the cell by monitoring temperature dependent spectral shifts using a benchmark method to quantify temperature variations as a function of time following a galvanostatic pulse to the cell and extrapolation of model parameters. The approach allows the

derivation of the rate of heat generated by the cell and heat flow rates under any electrochemical conditions.

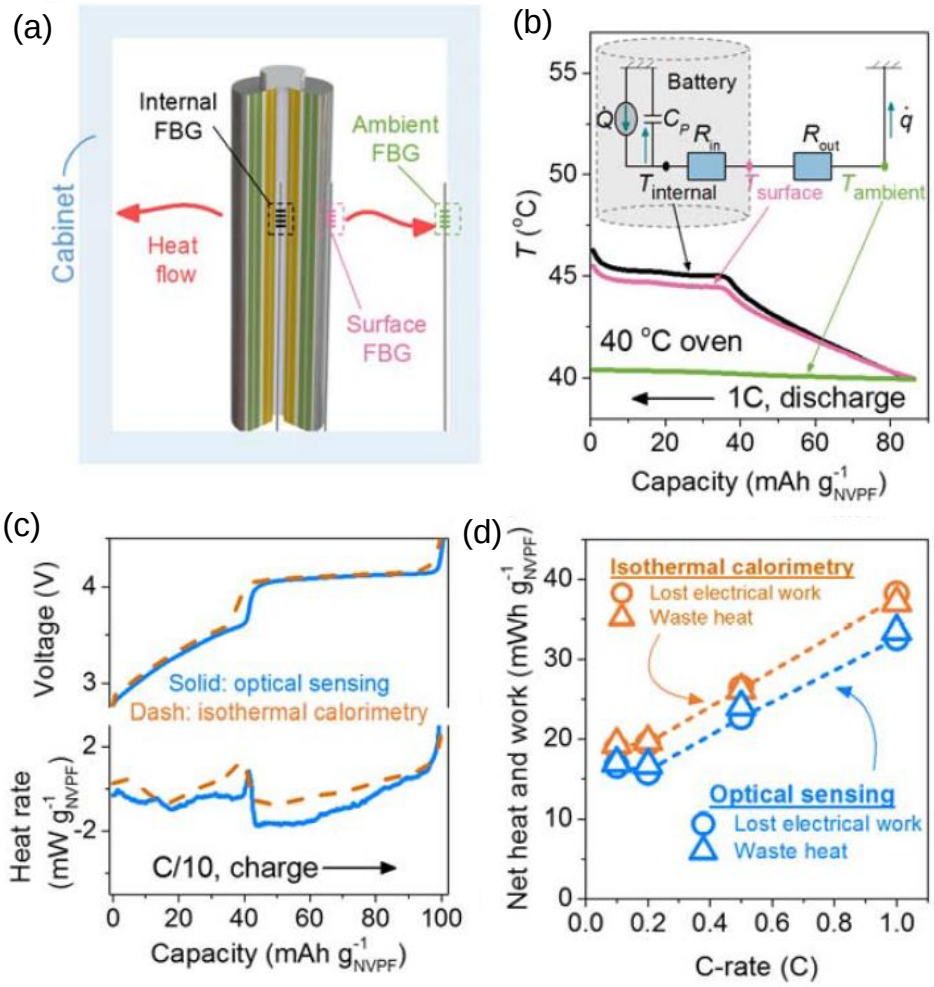


Figure 2.18. (a) Schematic of an optical sensing calorimetry experiment. (b) The thermal equivalent circuit (inset) and the measured variables including the internal ($T_{internal}$), the surface ($T_{surface}$), and the ambient ($T_{ambient}$) temperatures as a function of time at a discharge rate of 1 C. (c) The comparison of rate of heat generation from the optical fiber method (18650, blue solid lines) and the isothermal calorimetry (coin cell, orange dash lines) measured by the authors at a charge of C/10. (d) Comparison of waste heat and lost electrical work between the FBG approach (18650, blue) and the isothermal calorimetry (coin cell, orange). Adapted from Ref. (193) where more specific details on the cell chemistry and measurement conditions can be found. Copyright Nature Publishing Group, 2020.

Because of the sensitivity and relative accuracy of these approaches, it is conceivable that adaptations may allow for better thermal management systems, modification of electrolytes and other factors bespoke for new cell chemistries during direct measurement within an actual cell under cycling conditions. One very practical advantage is the ability to monitor the cell under more aggressive cycling conditions (higher charging rates for example) and to decouple heat transfer and heat accumulation in real-time within 18650 cells, and possibly other form factors too. Another important consideration in some battery materials such as alloying phases with large volume changes during reversible Li reactions, and interfaces in all solid-state batteries (ASSBs) is the measurement and quantification of stresses and their relationship to materials and their interfaces. These effects are critical for long life performance, and this is especially important for ASSBs that use solid materials and electrolytes with pristine interfaces and no porous component to buffer any changes in internal stresses. Using FBGs and moving the sensing capability inside the battery has obvious potential benefits for localised measurements compared to sensors located outside the entire cell.

In work by Blanquer et al., FBG sensors installed into Swagelok battery cells were used to directly measure internal stress evolution in liquid and solid-state electrolyte systems following Bae et al., whose approach showed operando strain measurements using an optical fiber grating in Li-ion battery electrodes.(196) Figure 2.19 summarises the overall approach using a liquid-based electrolyte in this case, where the spectral shifts were measured at specific states of charge and discharge as time-resolved data. The optical

signal was monitored during battery cycling, further translated into stress, and correlated with the voltage profile. While the details specific to the alloying compound (In, Si) can be found in Ref. (192), we summarise here for readers some of the basic parameters that allow for spectral shift, conversion to stress data and the basis for birefringence observations that underly this technique.

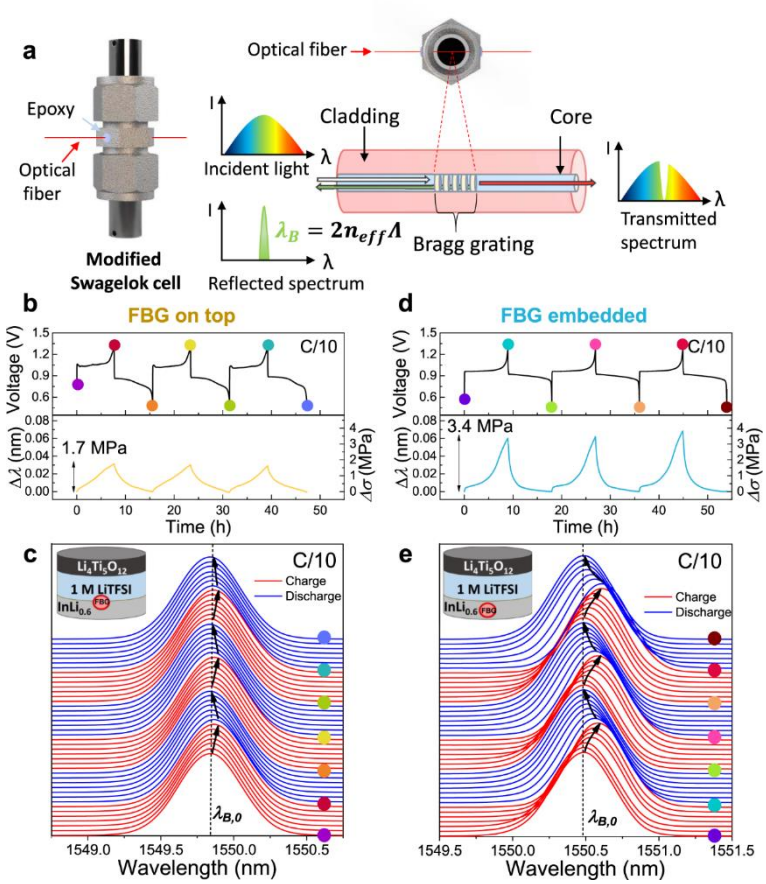


Figure 2.19. (a) Integration of an FBG into an in-house-modified Swagelok cell with a graphical summary of the working principle of an FBG optical sensor. (b) Time-resolved voltage (top) and $\Delta\lambda_B$ and $\Delta\sigma$ (bottom) evolution from the FBG sensor of an $InLi_{0.6}$ – LTO cell in a 1 M LiTFSI in DOL:DME electrolyte. The FBG was put at the anode/electrolyte interface. (c) Reflectance spectra from the FBG sensor located at the anode/electrolyte interface for the cycles shown in (b). (d, e) Analogous plots to (b, c), for a cell with the FBG sensor embedded within the $InLi_x$ electrode. Adapted from Ref. (192). Copyright Nature Publishing Group 2022.

Measurements that build on these fundamentals may be possible for certain cells where open questions remain about particular materials,

interfaces, or diagnostics. This may need new thinking for FBG placement, or indeed other techniques that allow operando tracking of optical responses unique to the materials, such as PhCs or periodically patterned electrodes. When light travels through the optical fiber, the FBG sensor acts as a reflector for a specific wavelength, namely the Bragg wavelength (λ_B) which is defined as $\lambda_B = 2n_{eff}\Lambda$, where n_{eff} is the effective refractive index of the FBG in its immediate environment and Λ is the Bragg grating period. Any temperature (T), hydraulic pressure (P), or strain (ε) change detected by the FBG sensor changes the value of n_{eff}, Λ or both which causes a shift of the reflection maxima. Then, under a condition when the FBG is strained one can describe the shift of $\Delta\lambda_B$ (197-199) as

$$\Delta\lambda_B = \left(1 - \frac{n_{eff}^2[p_{12} - \nu(p_{11} + p_{12})]}{2}\right)\varepsilon$$

where $\Delta\lambda_B$is the spectra shift compared to the initial measurement, p_{11} and p_{12} are the strain-optical coefficients of the fiber being used together with the Poisson ratio, ν. As such, the longitudinal strain measured spectrally can be converted simply to stress using Hooke's law according to $\sigma = \varepsilon E$, using E which is the Young's modulus of the fiber. In some cases, cycling a battery material may involve other directional strains, mimicking a transverse (or non-longitudinal strain) that causes a birefringent reflectance peak splitting(200)

from different light polarisation and effective index, according to Gafsi et al. (201)

$$B = \frac{\left|n_{\parallel} - n_{\perp}\right|}{n_{eff}} = \frac{\left|\Delta n_y - \Delta n_x\right|}{n_{eff}} + B_0$$

where $\mathrm{n}_{\parallel}$, $\mathrm{n}_{\perp}$, n_y, and n_x represent indices for directions related to external force and the index changes due to different polarisation. n_{eff} is the base effective index prior to modification. Ther are necessary calibrations required to effectively deconvolute peak splitting that are detailed in several publications, and in Ref. (192) for calibration curves obtained for the cell at open circuit voltage (OCV). In summary, this method provides additional resolution in the analysis of in-situ stresses in longitudinal and transverse directions with reference to the FBG on ASSB electrodes during cycling.

Operando stress measurements using FBGs has significant potential to track chemico-mechanical processes inside electrodes and at their interfaces, both for probing fundamental questions on material behaviour during cycling and as a diagnostic toolset for new materials under various cycling conditions. This is important for ASSBs that rely on well-defined interfaces and tracking stress build up in general will require adaption of the technique to place FBG probes at optimum regions in any form factor cell that could benefit from accurate operando stress build up measurements. The key difference in the application of FBG sensing to battery systems compared to the other operando techniques discussed in this review is the incorporation of the probe inside the cell itself.

Technique	Operando Cell Setup	Capabilities	Limitations	Local Resolution
Raman Spectroscopy	One-sided: Pyrex window(99, 202) Quartz window(98) ECC-Opto-Std with Borosilicate window(104)	Phase detection Degree of disorder at molecular level Nanoparticle size Indication of degree of crystallinity	Applicable only to polarised species Interference to electrode signals due to electrolyte species	0.5 – 1 µm
FTIR Spectroscopy	ATR-FTIR cell based on: Single-crystal Si, Ge(114, 117) Diamond/ZnSe/Steel ATR module(116) Si wafer window(203) Diamond disk(204) KBr window(205)	Transmission measurements provide bulk information on bulk properties of electrode/electrolyte ATR provides high surface sensitivity measurements at the electrode/electrolyte interface	Applicable only to species with a net change in dipole moment Detectors can require cryogenic cooling - liquid nitrogen (e.g. MCT for mid-IR) and liquid helium (e.g. Si, Ge bolometers for far-IR) Requires computational processing via Fourier Transform	0.001 – 4 cm^{-1}
Optical Spectroscopy	Transmission/Reflectance: Flooded glass cell(188) Modified Swagelok Cell(206) “Coffee bag” cell with glass window(207)	Optical fingerprint monitoring Macroscopic stress evaluation Detection of changes to the photonic lattice parameters including interplanar spacing Indication of swelling and electrode material degradation Determination of degree of disorder	Requires highly ordered materials Attenuation of photonic response by cell components and electrolyte species Flooded cell can cause delamination electrolyte Reflectance mode require large angles which disobey Bragg-Snell model	0.3 nm

Fiber Bragg Grating (FBG) Sensors and Probes	FBG-embedded modified Swagelok cell(192, 193) FBG-embedded composite laminate(191, 194, 196)	Optical and calorimetric sensing Internal sensing of materials Access to stress-strain and mechanical properties High sensitivity Stable under aggressive cycling conditions	Highly dependent on form factor, specific fiber design for each battery	1 pm

Table 2.3. Novel cell designs and key characteristics for experimental optimisation in the application of operando optical spectroscopy techniques to battery systems.

2.7. Nuclear Magnetic Resonance Analyses of Mass Shifting in Battery Systems

Moving to the low energy end of the spectrum, radiofrequencies can also be used to assess battery performance. The performance of battery electrodes relies on the behaviour of electrons and ions within and in the vicinity of the material. Nuclear magnetic resonance (NMR) spectroscopy characterises the materials based on the electron density present by applying an external magnetic field of strength B_0 to measure the frequency at which atoms in the material achieve resonance. Magnets are rated by the radiofrequencies used to cause resonance between the target nuclei and the magnetic field. The resonant frequency of the nucleus relative to the applied field is known as the chemical shift, usually measured in parts per million (ppm). Electrons orbiting the nucleus naturally oppose B_0, referred to as shielding the nucleus, which determines the chemical shift. The method is useful for atoms with nonzero nuclear spin. External interactions refer to those which involve the nuclear spins (rotational movement of nucleus around its axis) and the magnetic field. Internal interactions determine the NMR spectra, dictating signal shift and line shape. These internal interactions are described in detail elsewhere.(45) NMR itself is not phase sensitive. For structure determination, NMR spectra must therefore be used with line shape analysis and known shift ranges.

NMR offers insights into particle sizes, crystal structure, surface changes, phase analysis, oxidation states of elements and electrochemical performance of battery materials. While XRD provides similar information for crystalline materials, NMR proves useful for amorphous materials also.(44) Given batteries consist of complex material systems under continuous

modification in charging and discharging, predictions of the properties of battery materials using theoretical approaches such as density functional theory(208) and Hartree Fock methods have been effective and useful predictors in concert with NMR experiments.(209, 210) The combination of NMR and diffraction methods can be extremely powerful, as the techniques provide short-range, local structure information and long-range information, respectively. Insight into crystal and electronic structure can be provided simultaneously. NMR proves useful regardless of the charge storage mechanism, given that alloying, conversion, and intercalation mode cathodes all involve significant structural changes and phase transformations during cycling.

Real-time, non-destructive NMR measurements are required to adequately assess the evolution of the battery during electrochemical cycling. For in-situ NMR measurements, self-relaxation processes are minimised, high chemical specificity can be achieved for both crystalline and amorphous materials, and both short-lived and metastable phases can be tracked. Ex-situ NMR can be used to streamline the in-situ experiments by selecting the relevant NMR parameters to study for well characterised materials. The in-situ approach has its limitations, it is performed under static conditions such that sample spinning is not an option. Therefore, cell design, hardware, detection, and analysis methods must be given far more thought.

In Key et al.,(211) a range of NMR techniques used to probe local structural changes during discharge of crystalline silicon in a working LIB are described. Figure 2.20 shows the stacked in-situ NMR spectra obtained, at a range of capacity levels, revealing the change in composition of the electrodes

at each SoC. The work outlines the benefits of using the combination of NMR and diffraction methods as a diagnostic tool for battery electrodes. Similarly, the advantages of using the combination of in-situ and ex-situ analysis are shown, along with the accompanying complications that arise in the setup of the required system. The data obtained provides the ability to streamline in-situ NMR measurements. The in-situ NMR measurements detected phases which were not observed in the ex-situ data, a clear indication that amorphous phases form during the cycling of Si electrodes in LIBs. Dynamic processes which are short lived or metastable and therefore not accessible via ex-situ methods are captured. While analysis can prove difficult due to the extremely short time scale of the interactions involved, NMR remains useful from nanosecond to sub-nanosecond time domains.

The key result here is that the combination of in-situ and ex-situ NMR with a knowledge of the structural and electrochemical processes at work provides a clear route to investigating the processes that occur in the vicinity of the electrodes in an LIB, especially processes related to the formation and passivation of the SEI layer. The requirement for a more sophisticated methodology design for in-situ measurements compared to traditional NMR measurements is evident, including the inclusion of a flexible electrochemical cell to facilitate the in-situ probe.

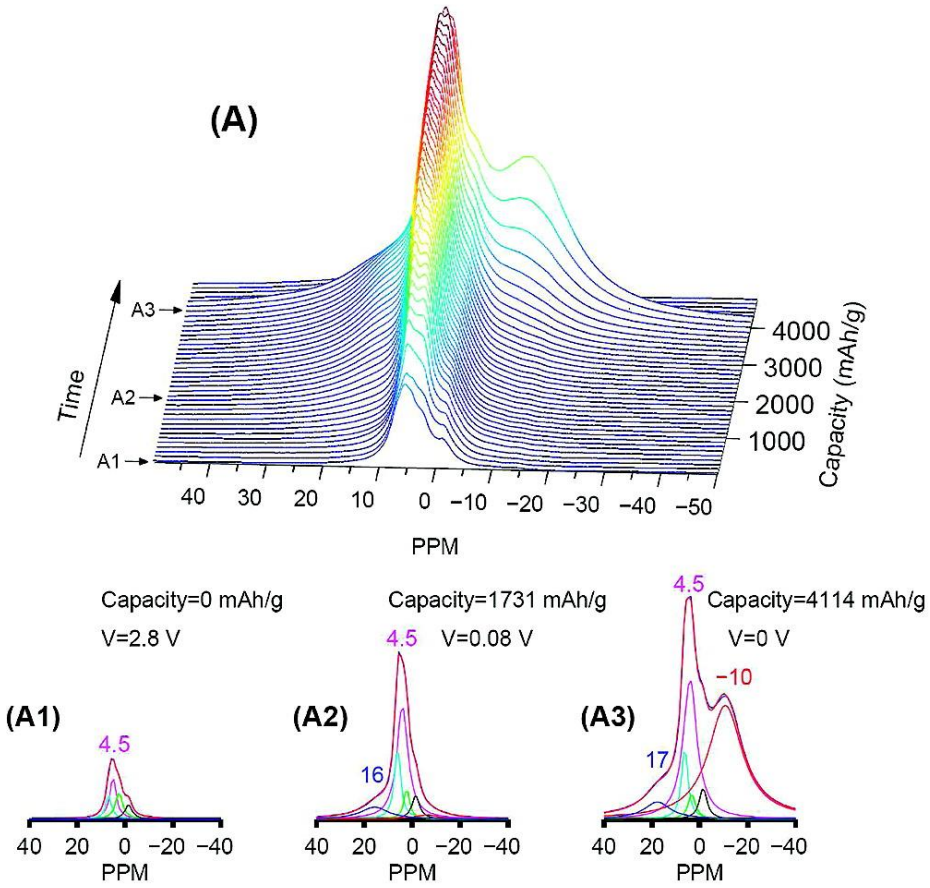


Figure 2.20. (A) Stacked plots of in-situ ^{7}Li static NMR spectra of the first discharge of an actual crystalline Si vs Li/Li+ battery (the colour bar shows the relative intensity scale for the spectra). (A1-A3) Deconvoluted spectra at various discharge capacity values of interest. Adapted from ref. (15). Copyright ACS 2009.

In applying NMR to battery materials, the interfaces between the electrodes and the species with which they react (e.g., electrolyte, SEI layer) have a significant impact on performance. Decomposition products are one of the primary factors which dictate ion transport through interfaces and the electrolyte, ultimately determining energy density. Interference in NMR spectra is often caused by dendrite formation, which can lead to short circuiting and battery failure. Efforts to combat these effects in various battery systems are widely researched.(212-215) This phenomenon occurs in Li and Na cells with metallic anodes during cycling. One of the limitations of NMR is that the

penetration of RF fields used to excite nuclear transitions is severely limited through metal samples because of an effect known as skin depth. Skin depth is usually an order of magnitude larger than dendrite thickness. Therefore, signals penetrate dendrites fully but appear constant relative to the signal of the bulk metal.(216) Identification of microstructural characteristics, growth mechanisms and contributory factors is required to minimise this interference during in-situ NMR experiments to provide a better insight into the evolution of the microstructures leading to electrode degradation.

Li metal batteries (LMBs) are being investigated with renewed interest for higher energy density future battery systems.(217-219) Li metal is well known to have the highest theoretical specific capacity of all Li-ion anodes and low negative potential. In LMBs, charging and discharging involves the deposition and stripping of Li metal for each process, respectively. Capacity retention, cycling stability and fire hazards are the key issues for in service LMBs, which can all be attributed to Li dendrite growth, but many examples of these batteries are deemed safe. Li dendrite growth and the factors that affect it for LMBs being investigated in new form factor cells or at non-standard temperature, or at higher charging rates can be difficult to accurately track and examine in real-time during battery operation. Figure 2.21 shows the stages of Li dendrite growth in tandem with SEI formation, the predominant mechanism leading to short circuiting in LMBs.



Figure 2.21. Li dendrite growth: Schematic depicting the SEI build up and dead Li formation at the electrode/electrolyte interface. Reproduced from ref. (220). Copyright ACS 2020.

Gunnarsdóttir et al. demonstrated an in-situ NMR metrology where an "anode-free" LMB setup was employed.(220) The typical Li metal anode was absent, meaning that Li was plated directly onto a bare Cu current collector from a $LiFePO_4$ cathode. The build-up of dead Li and the evolution of the SEI layer was tracked by in-situ NMR. While traditional performance analysis techniques detect only the capacity losses of the system, in-situ NMR can be used to deconvolute individual capacity drops to pinpoint their sources. In-situ NMR can detect the bulk magnetic susceptibility (BMS) shifts caused by Li metal and determine the location and environment of the sources of capacity losses by providing information on the density of surface coverage of the current collector in its various environments. In this study, the environment was varied using different electrolytes and coatings. SEI formation is of paramount importance during cycling of a battery, yet its evolution can either be key in optimising performance or detrimental to it. By monitoring the surface

coverage of the current collector, the effects of the SEI layer on performance can be determined.

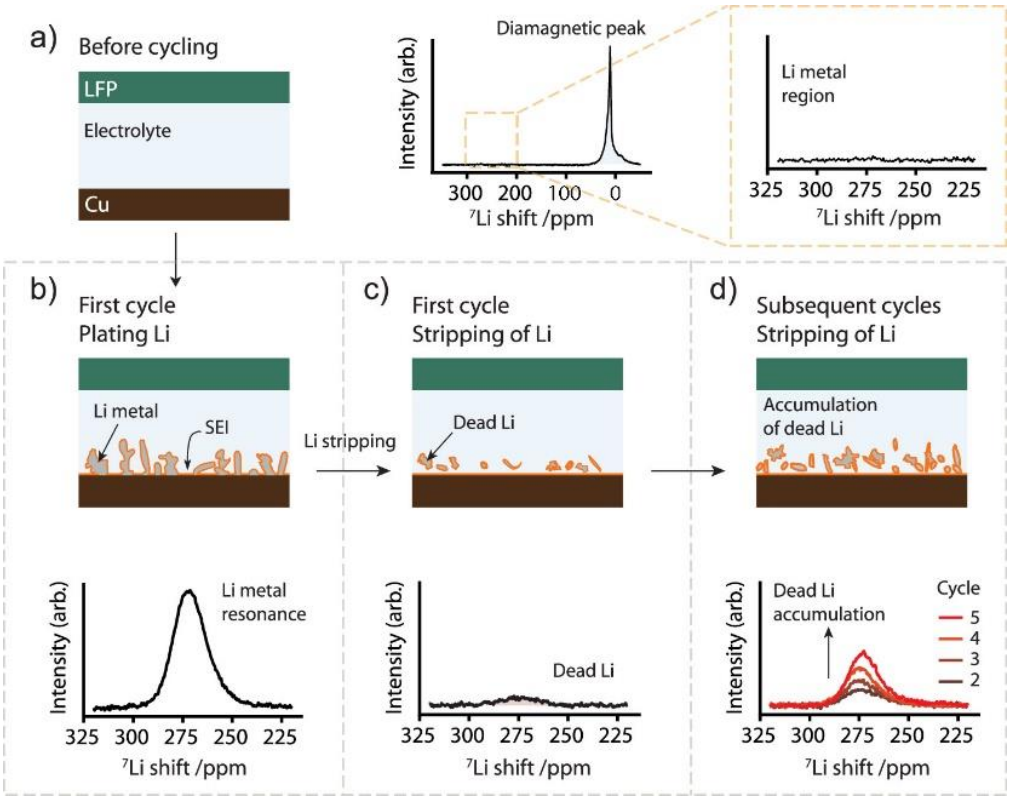


Figure 2.22. Schematic of the ^{7}Li in-situ NMR technique used to study dead Li formation and the resulting ^{7}Li NMR spectra. (a) The Cu-$LiFePO_4$ (LFP) cell before cycling and the corresponding ^{7}Li NMR spectrum showing the resonance of the diamagnetic Li (the SEI and Li+ ions) and the absence of the Li metal peak. (b) Charging the cell results in Li deposition, as shown in the ^{7}Li NMR spectrum of the Li metal region. (c) At the end of discharge, the Li metal signal can still be observed, which is attributed to dead Li. (d) Further cycling of the Cu−LFP cell results in an accumulation of dead Li over the next cycles (cycle 2−5), the intensity of the Li metal signal increasing at the end of stripping in each cycle. Adapted from ref. (220). Copyright ACS 2020.

Figure 2.22 (a) shows the Cu-$LiFePO_4$ cell before cycling, and the NMR spectrum shows the diamagnetic peak corresponding to the SEI and Li^+ ions, with the spectrum region associated with Li metal highlighted to show its absence. The schematics in Figure 2.22 (b-d) show the cell at different stages of cycling, providing an image of the accumulation of dead Li over time. The

NMR spectra associated with each stage are also shown. For a system with no dead Li deposited, there would be an absence of any peak for NMR spectra acquired after discharge, i.e., the stripping phase. The spectra clearly demonstrate the build-up of dead Li as the number of cycles increase. A continuation of this trend would lead inevitably to contact between anode and cathode, resulting in short circuit and system failure. The results of this study highlight the significant advantages in using in-situ NMR metrology to analyse battery degradation processes, in this case Li dendrite growth. The “anode-free” cell removed some of the complications of NMR methods for battery cells, like the issue of spacing between electrodes within the cell and effectively locating Li metal build-up. Potential solutions were also examined in the form of metal coatings, additives, and artificial SEI. Once again, in-situ NMR applied to the “anode-free” setup can be used to track the dead Li formation for each environment. Going forward, the versatility of this approach is evident. Small alterations can allow its extension to Li-S and Na metal batteries and operando studies. The fact that disassembly of the cell is not required means that the approach in this study can be added to the arsenal of non-destructive techniques for monitoring battery electrode degradation mechanisms in real time.

The geometry and composition of commercially used battery cells render many direct NMR methods ineffective in examining battery performance. The spacing between electrode layers and conductive casings prevent the penetration of the radiofrequencies required to induce nuclear transitions. In Pigliapochi *et al.,*(221) an ultrafast, inside-out magnetic resonance technique is used for the assessment of rechargeable cells. Here,

cell classification is performed via a single shot free induction decay (FID) NMR spectrum acquisition of the liquid compartments surrounding the cell.

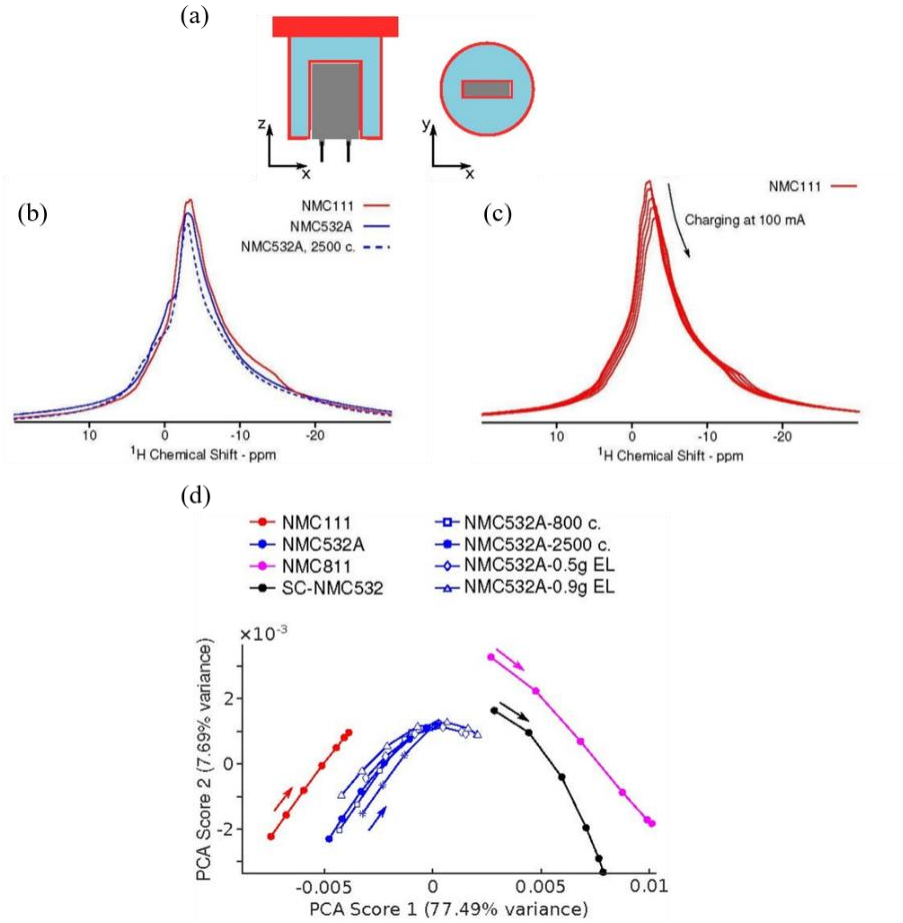


Figure 2.23. (a) Schematic of 3D-printed holder (red) used for ioMRI and NMR. The holder contains the cell (grey), which is surrounded by water compartment (light blue). The system is placed inside an NMR probe with the z-axis aligned with the static magnetic field. The vertical and horizontal cross sections are shown left and right, respectively. (b) ^{1}H NMR spectra taken at 2.5 V for cells containing, as cathode: NMC111 (red), NMC532A (solid blue) and NMC532A already undergone 2500 cycles prior to the MRI (dashed blue). (c) ^{1}H NMR spectra taken at intervals during charging of the cell containing NMC111 as cathode. The black arrow shows the direction of shift of the spectra as the cell undergoes charging. (d) Principal component analysis (PCA) performed on the ^{1}H NMR spectra of all the cells. Each arrow indicates the direction of the trend(s) of the corresponding colour as the cell is charged. Adapted with permission from ref. (221). Copyright Wiley 2020.

Changes in magnetic susceptibilities occur due to changing oxidation states in the electrode materials during charge and discharge. The method provides a non-invasive cell classification based on cathode material, volume of electrolyte and cycle life, while also presenting an overview of the ageing model of the system. A schematic of the operando cell design is shown in Figure 2.23 (a). The system was simply placed inside an NMR probe with its z axis aligned with the magnetic field. The cell was probed using inside-out magnetic resonance imaging (ioMRI), described in detail elsewhere,(222) prior to NMR measurements. However, there are limitations to the ioMRI approach.

Strongly magnetic materials, like those used as battery cathode materials, cause distortions in the magnetic imaging. The limitations of the ioMRI technique can be avoided using FID NMR spectroscopy.(223) Instead of obtaining a series of images, spectra are acquired in one fast, single-shot readout lasting less than a second. The speed of the technique allows access to the fast relaxation regime, negating the effects of large magnetic field gradients. Figure 2.23 (b) shows the ^{1}H NMR spectra obtained at 2.5V for the three cells of different cathode materials. The ^{1}H NMR spectra acquired at successive states of charge in one of the cells is shown in Figure 2.23 (c). The change in chemical shift and signal intensity due to lithiation during the charging cycle is indicated by the black arrow.

Principal component analysis (PCA) is used to classify groups of measurements based on the few strongest-contributing features of the dataset, which are the principal values, and is useful in the diagnosis of energy storage mechanisms.(224) The results from PCA applied to the ^{1}H NMR spectra acquired are presented in Figure 2.23 (d). A clear trajectory with

charging is observed for each cell. The trajectories of cells of the same cathode component and different electrolytes or cell age are grouped together (blue lines), while there is a significant difference between cells of different cathode components. The PCA analysis shows that cell classification based on cathode materials as a function of state of charge is an effective approach while electrolyte amount and cell age have little influence on the results. The ultrafast inside-out NMR technique is depicted as a fast, robust, non-destructive method for examining battery electrode materials in-situ. The versatility of the setup means that it can be extended to operando studies in the future. The applicability of in-situ NMR and MRI techniques to commercial cells has proven difficult to date, calling for novel adaptations to their methodology.

The application of NMR to battery materials proves powerful for determining particle dimensions, oxidation states of constituent elements, and changes at the surface. Its applicability to both crystalline and amorphous materials is useful, such as in cases where XRD has been used for phase detection and failed to capture the full picture due to the presence of non-crystalline phases, such as those corresponding to SEI species and intermediate phases which occur especially in conversion materials during cycling. For metallic materials, NMR provides the ability to spatially resolve areas in which build-up of dead Li (or Na, K, etc.) occurs. Its widespread incorporation for battery system analysis is limited by the difficult nature of cell design, with dimensions on an insufficient scale to accommodate the radiofrequency penetration that is required to induce nuclear transitions. In the case of NMR, the local resolution is directly proportional to the signal

acquisition duration, which determines the line width of the corresponding peaks.(225) Resolution is species dependent, where spectral regions of overlapping peaks prove difficult to deconvolute. Traditionally deconvolution can be simplified in cases where magic angle spinning (MAS) NMR can be used instead of its static counterpart. However, MAS NMR cannot be used for in-situ measurements of current battery technologies. For in-situ measurements, the spatial resolution is limited by the length of the radiofrequency detection coil inserted into the cell.(226) The non-destructive nature of NMR is a significant motivation for its application to sensitive, thin film battery materials, especially for the researcher concerned about beam damage inherent to electron microscopy and X-ray techniques.

2.8. Electrochemical-Acoustics – Listening to a Battery's Health

In recent years, the advantages of radiofrequencies have also been demonstrated using electrochemical-acoustic methods to monitor the properties of battery materials, particularly SoC and state of health (SoH). Most of the techniques discussed thus far involve the interaction of the material with a form of electromagnetic energy – X-rays, UV-vis range photons, and infrared light. One of the main disadvantages common between these techniques is their applicability to electrolytes and gaseous species due to their poor scattering properties.(141, 227) Acoustic measurements are obtained by applying a series of ultrasonic pulses to the system which can be monitored non-destructively in real-time. Evidence points towards a relationship between ultrasonic transmittance parameters and battery SoC/SoH.(176, 228, 229) Ultrasound transmission is highly sensitive to gas, porosity, and the

mechanical properties of materials. The general approach used to probe battery SoC includes examinations of the relationship between ultrasonic transmittance and the evolution of some of the key physical parameters of the materials.(108, 188, 230) Changes in the physical dynamics of the system affects the electrochemical activity in the cell and ultimately determines both SoC and SoH.

Operando acoustic time of flight (ToF) modelling and experiments are employed in Hsieh et al. to correlate structural changes to electrochemical performance.(231) The overarching advantages of the technique are in its simplicity and universal applicability. A combination of modelling and experimental measurements creates a framework relating the distribution of density within a battery system to its SoC and SoH. A representative battery stack used for modelling is shown in Figure 2.24 (a), with the same setup used for experimental measurements. The setup consists only of the battery and two transducers, one operating in pulse/listen mode and the other only in listen. Unlike the other techniques discussed in this review, the effectiveness of acoustic measurements is independent of the battery chemistry or form factor. The SoC-density relationship can be interrogated since density within the cell affects the speed of the penetrating ultrasonic waves. The speed of sound through a solid material is a function of the elastic modulus and density, given by the Newton-Laplace equation $c = \sqrt{\frac{E}{\rho}}$. Therefore, these two properties govern the speed of the ultrasonic waves which travel through each layer of battery material. A description of the computational model used to simulate the battery stack can be found elsewhere. Strong correlations between SoC and

distribution of density within the cell are shown. Furthermore, SoC-density correlations indicate underlying physical processes which occur in electrodes during cycling. A layer-by-layer examination describes mechanical degradation (and evolution) within the cell. Figure 2.24 (b)-(i) summarise the results of the study, with a clear correlation between the acoustic and electrochemical properties of the $LiCoO_2$/graphite pouch cell during galvanostatic cycling.

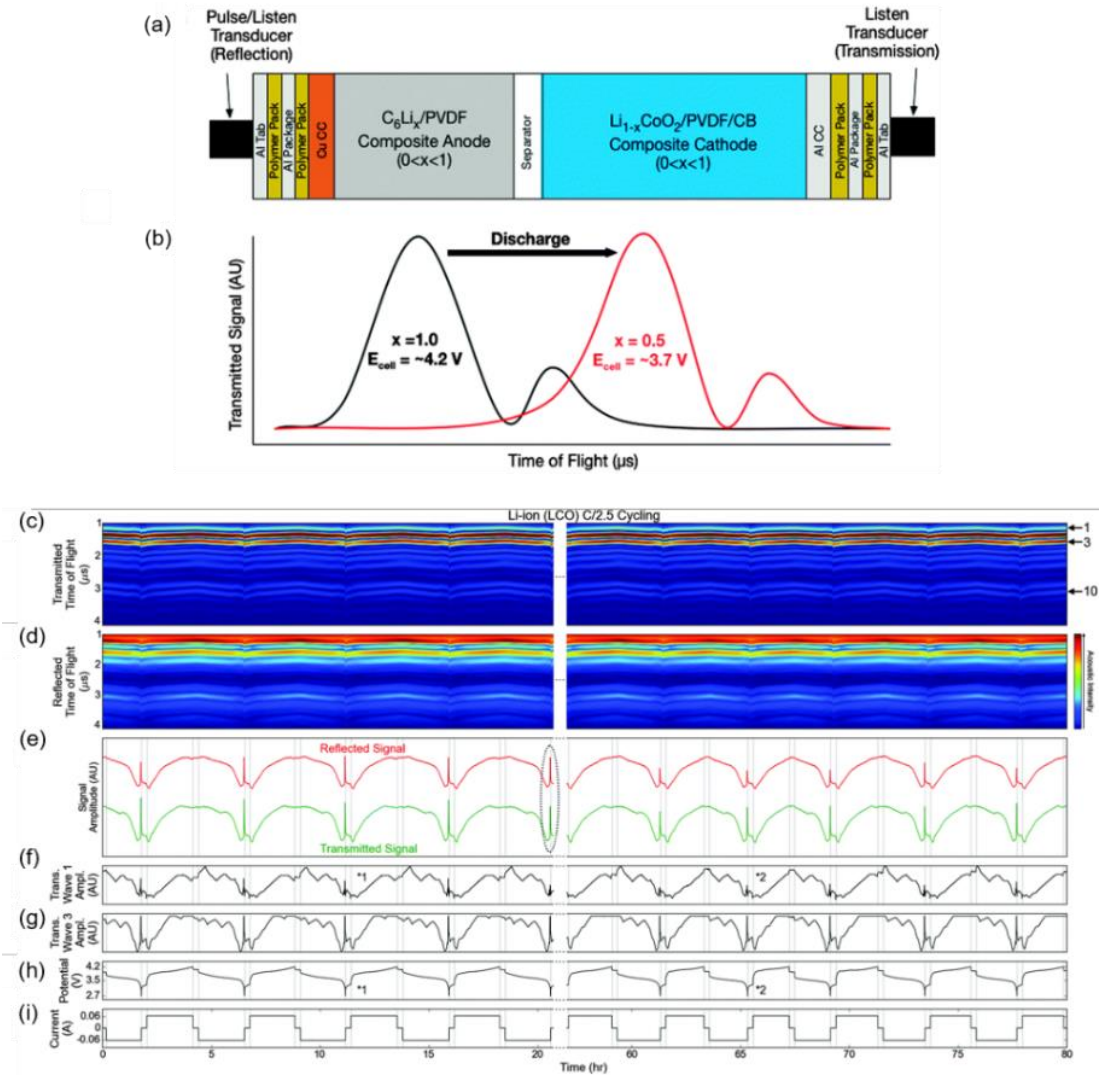


Figure 2.24. Ultrasonic probe of a representative battery. (a) Schematic representation of the battery stack used for acoustic modelling and experimental measurements, shown with packaging, current collector, electrode, separator layers and two acoustic transducers (b) Example illustration of the increase in time of flight (ToF) of the transmitted signal as a

Figure 2.24 (continued). function of SOC that occurs during discharge; this shift is a result of the changes in electrode densities as the SOC (i.e., Li content, x) changes. Acoustic behaviour of a $LiCoO_2$/graphite prismatic cell. (c), (d) ToF maps for transmission and reflection modes, respectively, (e) total reflected (red) and transmitted (green) signal amplitudes, (f), (g) traces for the amplitudes of transmitted waves 1 and 3, respectively, (h) cell potential, and (i) applied current as a function of cycling time. The vertical grey lines in panels (e)-(i) represent transitions between charge, discharge, and rest steps. Adapted from ref. (232). Copyright IOP Publishing 2020.

Figure 2.24 (e) shows the sum of all transmitted and reflected waves received by the transducers in green and red, respectively. As the battery is discharged, acoustic absorption increases, which results in a decrease in transmitted and reflected intensity. An exception occurs at end of discharge. The authors attribute this to the capacity-limited cathode. Near 0 % SoC (full discharge), $LiCoO_2$ undergoes a hexagonal-to-monoclinic phase transformation, which dramatically changes both the density and bulk modulus of the cathode, leading to a spike in both the transmitted and reflected acoustic intensities.

Cyclic voltammetry and differential capacity plots can provide an electrochemical fingerprint of a battery system. Light transmission and reflectance spectra can provide an optical fingerprint of battery electrode materials. Here, it is shown that ultrasonic measurements can provide an acoustic fingerprint of the battery system under analysis in real time using a simple methodology in a non-destructive fashion. The acoustic fingerprint is denoted by the ToF of the waves which occur in discrete materials based on the density within the cell. Change in lithiation and therefore SoC alter the acoustic fingerprint, changes which with further research can potentially be quantified based on the change in density and modulus of the material. Currently, there are significant limitations to the model. Many assumptions are

made, such as the exclusion of many known non-linear processes which occur during cycling, along with more cell layers.(233, 234) Beyond SoC, density changes indicate underlying physical processes affecting electrode degradation. ToF echo profiles and acoustic signal amplitudes shown as a function of cycle number are key indicators of battery SoC and SoH, indicating inter particle and intra particle stress and strain along with alterations to layer composition of the cell. Physical correlations for large-scale, complex, commercial batteries which have only been probed using high energy X-ray techniques to date are achieved. The method is a fraction of the cost of photonic analysis and negates the need for electrical contact.

Ultrasonic transmittance is particularly useful for detecting the wetting and “unwetting” of Li-ion cells as the presence or absence of the electrolyte at any given position has a significant effect on the ultrasonic transmission at that point. “Unwetting” refers to the swelling of an electrode stack to the point where there is insufficient electrolyte to completely fill the expanded pore space, a phenomenon which occurs as Li intercalation of IO electrodes occurs during LIB operation. Unlike the techniques discussed previously where initially the techniques are applied ex-situ and then the required adjustments (e.g., cell design) are made to obtain in-situ measurements, the ultrasonic transmission method is in-situ (and operando) by nature. In this case, the advancements that have been made to the analytical power of the technique have been in its spatial resolution. Earlier works employed a fixed-point method, where the ultrasonic transmittance was measured using a beam focused on a particular point or multiple successive points across the cell, providing results averaged over the area of the cell.(206, 235) These approaches resulted in a lack of

spatial resolution as the beam width was too wide to probe the structural features of the microscale structures which are formed and changed during cycling of a Li-ion cell. One route that has shown success is the use of acoustic measurements to identify defects within battery systems and use complementary techniques to analyse the properties of the defects. Robinson et al. used ultrasonic time-of-flight analysis to identify defects and SoH in a Li-ion pouch cell, by examining the acoustic transmission signal through the cell and X-Ray tomography was used to determine the location and scale of the defects.(236) Several studies have taken a similar approach, using ultrasonic transmittance measurements to probe a certain physical/structural change in the material which is then analysed using complementary techniques.(206)

A state-of-the-art approach to operando ultrasonic analysis of the Li-ion cells was taken in Deng et al., with an ultrasonic scanning method that employed a narrow beam with a diameter less than 1 mm which provided sub millimetre resolution. The beam was scanned across the cell with a position control accuracy of 0.2 mm.(237) Here, complementary techniques were not required. Figure 2.25 (a) and (b) show a schematic and photograph of the setup used for the ultrasonic scanning of electrolyte wetting and “unwetting” in a Li-ion pouch cell.(41) Gassing, and ‘‘unwetting’’ can be observed in aged cells, which helps to explain their loss in capacity after extended testing. A full map of the ultrasonic transmittance throughout the cell is shown in Figure 2.25 (c). The ultrasonic scanning technique developed here is cheap, fast, non-destructive and can be applied to large pouch and prismatic cells to monitor the degradation of Li-ion cells on an industrial scale.

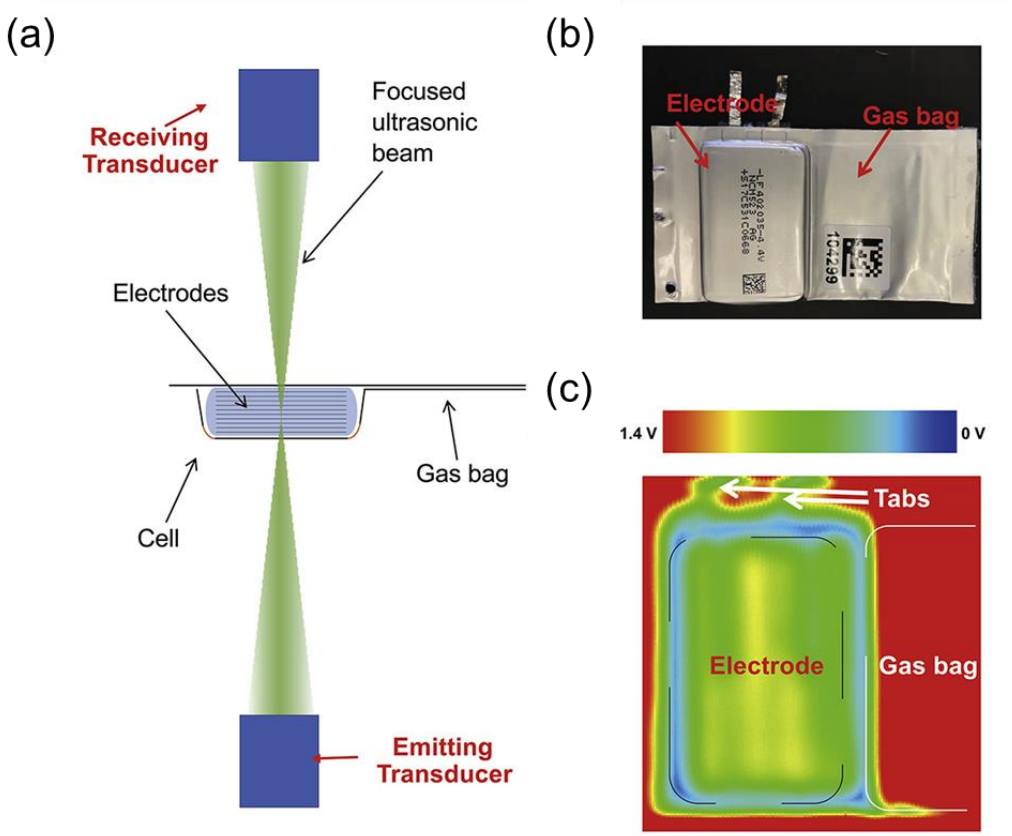


Figure 2.25. (a) Schematic of ultrasonic transmission setup showing path of focused beam. (b) Photograph of pouch cell and its main components. (c) Ultrasonic transmission image of the pouch cell overlapped on the optical photo. Adapted from ref. (45). Copyright Joule 2020.

Ultrasonic transmittance measurements can be used to monitor the electrochemical-acoustic behaviour and the underlying physical processes can be interrogated in real-time using a cheap, simple, non-destructive method that can be integrated easily into electric vehicles and mobile devices. Acoustic monitoring lacks the ability to resolve microstructural electrode features due to the relatively large radiofrequencies employed. While the method doesn't compete with the power of some of the higher energy techniques, acoustic measurements constitute a valuable addition to the arsenal of the battery analyst on the lower end of the energy spectrum, providing the ability to listen

to a battery's health during operation. The power instead lies in the simplicity of the approach. Non-destructive in nature, measurements can be acquired without requiring state-of-the-art cell designs or cell disassembly. Insight into the degree of wetting within is of major importance to experimental-phase cell methodologies, and new materials, where the structural specifications result in an ambiguity surrounding the extent to which the electrolyte infiltrates the corresponding electrode materials.

Technique	Operando Cell Setup	Capabilities	Limitations	Local Resolution
Nuclear Magnetic Resonance (NMR) Imaging	Bellcore-type flat bag cell(238-241) Swagelok-type cylindrical plastic cell capsule(242)	Particle sizes Surface changes Elemental oxidation states Applicable to amorphous materials Spatial resolution of dead Li build-up	Skin depth effect Dendrite interference Radiofrequency penetration difficult due to cell components dimensions Resolution limited by radiofrequency detection coil	Spatial: <1 cm(226)
Electrochemical-Acoustic Time-of-Flight (ToF)	Pouch cell(45, 234, 243-245) Cylindrical cell(231) AA alkaline cell(231)	Shifting of mass within cell Detection of “unwetting” of electrode materials Monitoring of electrolyte gassing Applicable to any battery chemistry or form factor Intraparticle and interparticle stress and strain Performance without electrical contact	Inapplicable to resolution of microstructural features More detailed model required to decouple individual events	Temporal: 3 ns – 20 ns Spatial: < 1 mm

Table 2.4. Summary of the application of state-of-the-art operando techniques based on low energy radio wave penetration of battery systems.

2.9. Battery Operation in a Dynamic Service Environment – Building a Sensor Network

While operando analysis of individual cells and their components provides information on battery performance, it is also necessary to examine batteries under dynamic conditions. Operando measurements tend to be performed under optimal conditions in a lab-based setting. Often, batteries are used as components of larger battery pack systems. In Li et al.,(246) Li-ion battery monitoring was performed operando using a sensor-based network. The network was used to examine the effects of vibration and impact on battery performance during cycling, to provide a simulation of the conditions the system may experience during transport. The relationships of both temperature variance and deformation to capacity degradation during cycling in various dynamic environments are established. The network identifies critical points during cycling where high heat generation and stress accumulation may lead to thermal runaway and potential explosion. The comparison between single cell and battery pack performance is also explored.

In Figure 2.26, the operando testing platform used for (a) the vibration test and (b) the impact test of the LIBs is shown. An electromagnet shaker was used to simulate vibration, while a drop hammer simulated impact. In the sensor network, capacity degradation was measured using the internal resistance temperature detector (RTD) and eddy current sensor. Vibration and impact testing investigated the changes in battery capacity over the typical service life of 500 cycles. The testing results showed capacity retention immediately after impact, with gradual capacity degradation observed after

continuous cycling. Low momentum impact can release compressive stress in the electrodes, while high momentum impacts can cause severe cracking, each leading to degradation and capacity loss. The evidence indicates that dynamic loading has little effect on battery performance in the short term, but repeated stress leads to electrode degradation and battery failure.

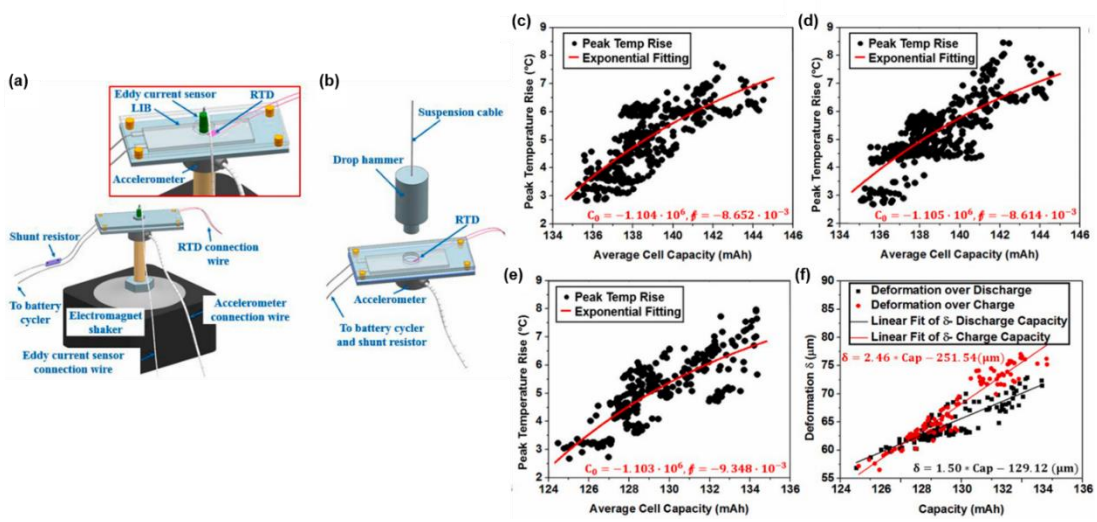


Figure 2.26. Operando testing platform for LIBs: (a) setup for operando vibration test, and (b) setup for operando impact test analysis. Relation between maximum temperature increase and capacity of (c) cell 1, (d) cell 2 and (e) cell 3. Relation between maximum deformation and capacity of cell 3. Adapted from ref. (246). Copyright Elsevier B.V. 2020.

Cell deterioration and the role of electrode degradation is explored in this work by examining the relationships between capacity and two of the key physical properties which affect it, temperature change and deformation, for both a single cell and two-cell pack. In Figure 2.26 (c)-(e), the temperature-capacity relationship is shown for each of the three cells. The relationship provides an indirect method to measure temperature, eliminating the requirement for dedicated temperature monitoring, reducing the number of components consuming power in the network and reducing cost. However, for a multi-cell battery, the effects of adjacent cells must also be considered.

Figure 2.26 (f) shows the deformation-capacity relationship. Deformation measurements provide information on structural changes to the cell. Following the theme of this review, the study links structural changes to the electrochemical processes which occur during cycling, via operando analysis. For the sensor network designed here, deformation indicates the level of stress accumulation during service which can lead to dendrite formation causing internal short circuits. The evidence shows greater deformation occurs during charge than during discharge, which causes the cell to swell over its cycle life. The overall deformation growth can be attributed to several factors. These factors can be broken down into two categories, gas generation and electrode thickness change. By mapping deformation to electrode thickness change, the role of electrode degradation to cell performance can be established. The sensor network can not only detect degradation but identify and quantify its source. Here, the results show that deformation is greater than thickness change, which occurs only in the graphite anode and not the LCO cathode. The results demonstrate that anode degradation and gas generation (due primarily to electrolyte decomposition), are the key factors leading to deformation of the cell.

As the inevitable move towards renewable energy gains momentum, energy storage requirements mean that battery performance assessment methods must not fall behind. The use of a sensor network as described above which can pinpoint performance issues in a multi-cell configuration can support the employment of battery systems at the grid level, a key player in the move towards global decarbonisation. The methods outlined in this short review highlight how many cross-disciplinary studies are now being conducted to

benefit the electric future, from materials choice and abundance, to long term high performance battery response, while in parallel gaining better understanding on issues and safety concerns from new battery chemistry and designs to detailed microstructure, interface and localised reactions that govern, control, improve, and impede safe, efficient cyclic charging and discharge over a long lifetime.

2.10. Conclusions and outlook

Many of the achievements using operando XRD, NMR and synchrotron techniques(247) have provided useful capabilities and new insights in terms of operando detail and understanding of critical processes in batteries and electrochemical materials science. However, they do not readily translate into real-time monitoring of batteries in the field because of the nature of the infrastructural requirements. These methods do provide very detailed and powerful ways of assessing material and cell-chemistry behaviour in real time. Methods that will allow detection, in real time, of the complex combination of intended chemical and electrochemical processes, and of the panoply of side reactions that significantly affect long-term performance will be useful and complement synchrotron-based methods when used for material prediction, screening and safety diagnostics. This will allow the material science, chemistry, electrochemistry, and battery communities to optimise cycling regimes or identify failure mechanisms more rapidly in emerging technologies.

Battery history can then be determined, and a health 'check-up' be performed, allowing appropriate pricing and insurance for a battery as it enters

its second-life application. Grid and transport demonstration projects and battery tests are already in progress to link traditional electrochemical responses (such as current, voltage and impedance) with test routines appropriate to the technology and produce the 'big data' needed to extract new correlations and, ultimately, predict future performance. Current examples at the time of writing are large scale European projects under the Battery2030+ initiative that is focused on real-time, passive, and other methods to monitor battery performance, safety, and cell health. An inside-the-battery-material analogue of today's battery management systems would prove useful too. Deriving useful information from the thousands of batteries used commercially via data-driven consumer apps and coordinated mapping of testing procedures from lab-based tests of new systems are ways being investigated now to obtain a big-data map of all that affect batteries and battery components. The details of these larger scale, forward looking initiatives are outside the scope of this review and the reader is directed to available internet resources on these initiatives(248-254). Diagnostics are required that can couple electronic with chemical traceability and can identify key reactions that are critical to both short- and long-term cell failure.

These methods will be vital for Na-ion, solid state batteries and related battery formulations, as well as many electrochemical systems where solid-solution interfaces are common and where dynamic processes in materials control and affect the nature of their response and behaviour. Li-ion technologies are now proven from data to in principle power an EV for a ‘million miles’, a reference to seminal work by Dahn and co-workers(255) where

crystalline NMC532 cathodes and balanced artificial graphite cell were demonstrated. The cells used in that study were never turned off and are still cycling at the time of writing to many tens of thousands of cycles within the optimised voltage window. The same group have also demonstrated that an ionic liquid electrolyte and choice voltage window can allow similar cells to run for effectively more than a century at 25 °C, and state of the art stability and longevity at extremely high (~70 °C and higher) temperatures.(256) As Na-ion make inroads to be the next replacement for applications where Li-ion is critical now, screening, prediction and real-time analysis will be essential in its future. Safety matters will always be obviously important and leveraging many of these techniques as predictive or real-time monitoring methods in test and also in commercial battery systems with communication functionality to the user will be key components that help battery technology users, such as EV drivers, to better understand the battery and its health, as much as has been learned by users of ICE equivalents.

Ultimately, big-data analysis and prediction of battery behaviour and new materials, together with large-scale high resolution operando methods with built-in analytical sensors in consumer batteries will form a trifecta of analysis that can help to optimise existing and future battery use and development.

2.11. References

1. M. S. Whittingham, *Chemical reviews*, **114**, 11414 (2014).
2. Y. Li, Q. Zhou, S. Weng, F. Ding, X. Qi, J. Lu, Y. Li, X. Zhang, X. Rong, Y. Lu, X. Wang, R. Xiao, H. Li, X. Huang, L. Chen and Y.-S. Hu, *Nature Energy* (2022).
3. B. Yin, S. Liang, D. Yu, B. Cheng, I. L. Egun, J. Lin, X. Xie, H. Shao, H. He and A. Pan, *Advanced Materials*, **33**, 2100808 (2021).
4. M. A. Rahman, X. Wang and C. Wen, *Journal of The Electrochemical Society*, **160**, A1759 (2013).
5. L. Ma, T. Yu, E. Tzoganakis, K. Amine, T. Wu, Z. Chen and J. Lu, *Advanced Energy Materials*, **8**, 1800348 (2018).
6. Y. X. Ren, L. Zeng, H. R. Jiang, W. Q. Ruan, Q. Chen and T. S. Zhao, *Nature Communications*, **10**, 3249 (2019).
7. Z. Shen, X. Jin, J. Tian, M. Li, Y. Yuan, S. Zhang, S. Fang, X. Fan, W. Xu, H. Lu, J. Lu and H. Zhang, *Nature Catalysis* (2022).
8. Y. Liang, H. Dong, D. Aurbach and Y. Yao, *Nature Energy*, **5**, 646 (2020).
9. D. Chao, W. Zhou, F. Xie, C. Ye, H. Li, M. Jaroniec and S.-Z. Qiao, *Science Advances*, **6**, eaba4098 (2020).
10. C. Zhu, R. E. Usiskin, Y. Yu and J. Maier, *Science*, **358**, eaao2808 (2017).
11. O. Pecher, J. Carretero-González, K. J. Griffith and C. P. Grey, *Chemistry of Materials*, **29**, 213 (2017).
12. M. Armand and J. Tarascon, *Nature*, **414**, 359 (2001).
13. E. Pomerantseva, F. Bonaccorso, X. Feng, Y. Cui and Y. Gogotsi, *Science*, **366**, eaan8285 (2019).
14. N. Nitta, F. Wu, J. T. Lee and G. Yushin, *Materials today*, **18**, 252 (2015).
15. B. Key, R. Bhattacharyya, M. Morcrette, V. Seznéc, J.-M. Tarascon and C. P. Grey, *Journal of the American Chemical Society*, **131**, 9239 (2009).
16. R. Bhattacharyya, B. Key, H. Chen, A. Best, A. Hollenkamp and C. Grey, *Nature materials*, **9**, 504 (2010).
17. V. K. Peterson and L. Stievano, *Batteries & Supercaps*, **4**, 1789 (2021).
18. Y. Wu and N. Liu, *Chem*, **4**, 438 (2018).
19. L. Mai, M. Yan and Y. Zhao, *Nature*, **546**, 469 (2017).
20. F. Blanc, M. Leskes and C. P. Grey, *Acc. Chem. Res.*, **46**, 1952 (2013).
21. S. Chandrashekar, N. M. Trease, H. J. Chang, L. S. Du, C. P. Grey and A. Jerschow, *Nat. Mater.*, **11**, 311 (2012).
22. M. Sathiya, M. Sathiya, M. Sathiya, M. Sathiya, M. Sathiya and M. Sathiya, *Nat. Commun.* , **6**, 6276 (2015).
23. D. X. Liu, L. Cao and A. C. Co, *Chem. Mater.*, **28**, 556 (2016).
24. D. X. Liu and A. C. Co, *J. Am. Chem. Soc.*, **138**, 231 (2016).
25. D. X. Liu, J. Wang, P. Ke, J. Qiu, M. Canova, L. Cao and A. C. Co, *Angew. Chem. Int. Ed.*, **53**, 9498 (2014).
26. F. Wang, F. Wang, F. Wang, F. Wang, F. Wang and F. Wang, *Nat. Commun.*, **3**, 1201 (2012).

27. J. Y. Huang, L. Zhong, C. M. Wang, J. P. Sullivan, W. Xu, L. Q. Zhang, S. X. Mao, N. S. Hudak, X. H. Liu, A. Subramanian, H. Fan, L. Qi, A. Kushima and J. Li, *Science*, **330**, 1515 (2010).
28. S. C. Chao, S. C. Chao, S. C. Chao, S. C. Chao, S. C. Chao and S. C. Chao, *Electrochem. Commun.*, **12**, 234 (2010).
29. A. Ulvestad, A. Singer, J. N. Clark, H. M. Cho, J. W. Kim, R. Harder, J. Maser, Y. S. Meng and O. G. Shpyrko, *Science*, **348**, 6241 (2015).
30. A. Molinari, P. M. Leufke, C. Reitz, S. Dasgupta, R. Witte, R. Kruk and H. Hahn, *Nat. Commun.*, **8**, 15339 (2017).
31. C. Reitz, P. M. Leufke, R. Schneider, H. Hahn and T. Brezesinski, *Chem. Mater.*, **26**, 5745 (2014).
32. S.-H. Kim, S. Antonov, X. Zhou, L. T. Stephenson, C. Jung, A. A. El-Zoka, D. K. Schreiber, M. Conroy and B. Gault, *Journal of Materials Chemistry A*, **10**, 4926 (2022).
33. A. C. Marschilok, A. M. Bruck, A. Abraham, C. A. Stackhouse, K. J. Takeuchi, E. S. Takeuchi, M. Croft and J. W. Gallaway, (2020).
34. W. Zhu, D. Liu, A. Paolella, C. Gagnon, V. Gariépy, A. Vijh and K. Zaghib, *Frontiers in Energy Research*, **6** (2018).
35. Y. Xie, H. Wang, G. Xu, J. Wang, H. Sheng, Z. Chen, Y. Ren, C.-J. Sun, J. Wen, J. Wang, D. J. Miller, J. Lu, K. Amine and Z.-F. Ma, *Advanced Energy Materials*, **6**, 1601306 (2016).
36. X.-M. Zheng, J.-H. You, J.-J. Fan, G.-P. Tu, W.-Q. Rong, W.-J. Li, Y.-X. Wang, S. Tao, P.-Y. Zhang, S.-Y. Zhang, S.-Y. Shen, J.-T. Li, L. Huang and S.-G. Sun, *Nano Energy*, **77**, 105123 (2020).
37. J. Zhang, L. Lai, H. Wang, M. Chen and Z. X. Shen, *Materials Today Energy*, **21**, 100747 (2021).
38. Y. Yan, C. Cheng, L. Zhang, Y. Li and J. Lu, *Advanced Energy Materials*, **9**, 1900148 (2019).
39. Y.-C. Chien, A. S. Menon, W. R. Brant, M. J. Lacey and D. Brandell, *The Journal of Physical Chemistry C*, **126**, 2971 (2022).
40. J. B. Robinson, M. Maier, G. Alster, T. Compton, D. J. L. Brett and P. R. Shearing, *Physical Chemistry Chemical Physics*, **21**, 6354 (2019).
41. K. Kirshenbaum, D. Bock, C.-Y. Lee, Z. Zhong, K. Takeuchi, A. Marschilok and E. Takeuchi, *Science*, **347**, 149 (2015).
42. R. D. Schmidt and J. Sakamoto, *Journal of Power Sources*, **324**, 126 (2016).
43. W. Chang, C. Bommier, T. Fair, J. Yeung, S. Patil and D. Steingart, *Journal of The Electrochemical Society*, **167**, 090503 (2020).
44. Z. Deng, Z. Huang, Y. Shen, Y. Huang, H. Ding, A. Luscombe, M. Johnson, J. E. Harlow, R. Gauthier and J. R. Dahn, *Joule*, **4**, 2017 (2020).
45. H. Liu, F. C. Strobridge, O. J. Borkiewicz, K. M. Wiaderek, K. W. Chapman, P. J. Chupas and C. P. Grey, *Science*, **344**, 1252817 (2014).
46. X. Lu, A. Bertei, D. P. Finegan, C. Tan, S. R. Daemi, J. S. Weaving, K. B. O'Regan, T. M. M. Heenan, G. Hinds, E. Kendrick, D. J. L. Brett and P. R. Shearing, *Nature Communications*, **11**, 2079 (2020).
47. X. Lu, S. R. Daemi, A. Bertei, M. D. R. Kok, K. B. O'Regan, L. Rasha, J. Park, G. Hinds, E. Kendrick, D. J. L. Brett and P. R. Shearing, *Joule*, **4**, 2746 (2020).

48. J. Scharf, M. Chouchane, D. P. Finegan, B. Lu, C. Redquest, M.-c. Kim, W. Yao, A. A. Franco, D. Gostovic, Z. Liu, M. Riccio, F. Zelenka, J.-M. Doux and Y. S. Meng, *Nature Nanotechnology* (2022).
49. J. Scharf, L. Yin, C. Redquest, R. Liu, X. L. Quinn, J. Ortega, X. Wei, J. Wang, J.-M. Doux and Y. S. Meng, *Advanced Energy Materials*, **11**, 2101327 (2021).
50. O. J. Borkiewicz, B. Shyam, K. M. Wiaderek, C. Kurtz, P. J. Chupas and K. W. Chapman, *Journal of Applied Crystallography*, **45**, 1261 (2012).
51. H. Liu, P. K. Allan, O. J. Borkiewicz, C. Kurtz, C. P. Grey, K. W. Chapman and P. J. Chupas, *Journal of Applied Crystallography*, **49**, 1665 (2016).
52. Y.-N. Zhou, J.-L. Yue, E. Hu, H. Li, L. Gu, K.-W. Nam, S.-M. Bak, X. Yu, J. Liu, J. Bai, E. Dooryhee, Z.-W. Fu and X.-Q. Yang, *Advanced Energy Materials*, **6**, 1600597 (2016).
53. Z. Yang, L. Trahey, Y. Ren, M. K. Y. Chan, C. Lin, J. Okasinski and M. M. Thackeray, *Journal of Materials Chemistry A*, **3**, 7389 (2015).
54. M. M. Storm, R. E. Johnsen, R. Younesi and P. Norby, *Journal of Materials Chemistry A*, **3**, 3113 (2015).
55. S. Waluś, C. Barchasz, R. Bouchet, J.-C. Leprêtre, J.-F. Colin, J.-F. Martin, E. Elkaïm, C. Baehtz and F. Alloin, *Advanced Energy Materials*, **5**, 1500165 (2015).
56. K. P. C. Yao, J. S. Okasinski, K. Kalaga, I. A. Shkrob and D. P. Abraham, *Energy & Environmental Science*, **12**, 656 (2019).
57. X. H. Liu, Y. Liu, A. Kushima, S. Zhang, T. Zhu, J. Li and J. Y. Huang, *Advanced Energy Materials*, **2**, 722 (2012).
58. M. T. McDowell, I. Ryu, S. W. Lee, C. Wang, W. D. Nix and Y. Cui, *Advanced Materials*, **24**, 6034 (2012).
59. S. Basak, K. Dzieciol, Y. E. Durmus, H. Tempel, H. Kungl, C. George, J. Mayer and R.-A. Eichel, *Chemical Physics Reviews*, **3**, 031303 (2022).
60. Z. Zeng, W.-I. Liang, H.-G. Liao, H. L. Xin, Y.-H. Chu and H. Zheng, *Nano Letters*, **14**, 1745 (2014).
61. M. E. Holtz, Y. Yu, D. Gunceler, J. Gao, R. Sundararaman, K. A. Schwarz, T. A. Arias, H. D. Abruña and D. A. Muller, *Nano Letters*, **14**, 1453 (2014).
62. M. Gu, L. R. Parent, B. L. Mehdi, R. R. Unocic, M. T. McDowell, R. L. Sacci, W. Xu, J. G. Connell, P. Xu, P. Abellan, X. Chen, Y. Zhang, D. E. Perea, J. E. Evans, L. J. Lauhon, J.-G. Zhang, J. Liu, N. D. Browning, Y. Cui, I. Arslan and C.-M. Wang, *Nano Letters*, **13**, 6106 (2013).
63. F. Wu and N. Yao, *Nano Energy*, **11**, 196 (2015).
64. H.-W. Lee, Y. Li and Y. Cui, *Current Opinion in Chemical Engineering*, **12**, 37 (2016).
65. K. A. Taylor and R. M. Glaeser, *Science*, **186**, 1036 (1974).
66. X. Wang, Y. Li and Y. S. Meng, *Joule*, **2**, 2225 (2018).
67. X. Wang, M. Zhang, J. Alvarado, S. Wang, M. Sina, B. Lu, J. Bouwer, W. Xu, J. Xiao, J.-G. Zhang, J. Liu and Y. S. Meng, *Nano Letters*, **17**, 7606 (2017).
68. Y. Li, Y. Li, A. Pei, K. Yan, Y. Sun, C.-L. Wu, L.-M. Joubert, R. Chin, A. L. Koh, Y. Yu, J. Perrino, B. Butz, S. Chu and Y. Cui, *Science*, **358**, 506 (2017).

69. D. Aurbach, Y. Ein-Ely and A. Zaban, *Journal of The Electrochemical Society*, **141**, L1 (1994).
70. R. F. Ziesche, T. Arlt, D. P. Finegan, T. M. M. Heenan, A. Tengattini, D. Baum, N. Kardjilov, H. Markötter, I. Manke, W. Kockelmann, D. J. L. Brett and P. R. Shearing, *Nature Communications*, **11**, 777 (2020).
71. *Nature Reviews Methods Primers*, **1**, 52 (2021).
72. A. N. Chiaramonti, L. Miaja-Avila, P. T. Blanchard, D. R. Diercks, B. P. Gorman and N. A. Sanford, *MRS Advances*, **4**, 2367 (2019).
73. Z. Peng, F. Vurpillot, P.-P. Choi, Y. Li, D. Raabe and B. Gault, *Ultramicroscopy*, **189**, 54 (2018).
74. D. N. Seidman, *Annual Review of Materials Research*, **37**, 127 (2007).
75. T. T. Tsong, *Surface Science*, **85**, 1 (1979).
76. B. Gault, A. La Fontaine, M. P. Moody, S. P. Ringer and E. A. Marquis, *Ultramicroscopy*, **110**, 1215 (2010).
77. S. K. Sundaram and E. Mazur, *Nature Materials*, **1**, 217 (2002).
78. J. Houard, A. Vella, F. Vurpillot and B. Deconihout, *Physical Review B*, **84**, 033405 (2011).
79. M. Müller, D. Saxey, G. Smith and B. Gault, *Ultramicroscopy*, **111**, 487 (2011).
80. I. E. McCarroll, P. A. J. Bagot, A. Devaraj, D. E. Perea and J. M. Cairney, *Materials Today Advances*, **7**, 100090 (2020).
81. A. Devaraj, C. Szymanski, P. Yan, C. M. Wang, V. Murgesan, J. M. Zheng, J. Zhang, T. Tyliszczak and S. Thevuthasan, *Microscopy and Microanalysis*, **21**, 685 (2015).
82. B. Gault and J. D. Poplawsky, *Nature Communications*, **12**, 3740 (2021).
83. D. Santhanagopalan, D. K. Schreiber, D. E. Perea, R. L. Martens, Y. Janssen, P. Khalifah and Y. S. Meng, *Ultramicroscopy*, **148**, 57 (2015).
84. A. Devaraj, R. Colby, W. P. Hess, D. E. Perea and S. Thevuthasan, *The Journal of Physical Chemistry Letters*, **4**, 993 (2013).
85. Y. Zhang, J. A. Alarco, A. S. Best, G. A. Snook, P. C. Talbot and J. Y. Nerkar, *RSC Adv*, **9**, 1134 (2019).
86. C. Dette, M. A. Pérez-Osorio, C. S. Kley, P. Punke, C. E. Patrick, P. Jacobson, F. Giustino, S. J. Jung and K. Kern, *Nano Lett*, **14**, 6533 (2014).
87. X. H. Liu, S. Huang, S. T. Picraux, J. Li, T. Zhu and J. Y. Huang, *Nano Letters*, **11**, 3991 (2011).
88. S. Lee, Y. Oshima, E. Hosono, H. Zhou, K. Kim, H. M. Chang, R. Kanno and K. Takayanagi, *ACS Nano*, **9**, 626 (2015).
89. Y. Gong, J. Zhang, L. Jiang, J.-A. Shi, Q. Zhang, Z. Yang, D. Zou, J. Wang, X. Yu, R. Xiao, Y.-S. Hu, L. Gu, H. Li and L. Chen, *Journal of the American Chemical Society*, **139**, 4274 (2017).
90. J. Maier, B. Pfeiffer, C. A. Volkert and C. Nowak, *Energy Technology*, **4**, 1565 (2016).
91. L. Meyer, N. Saqib and J. Porter, *Journal of The Electrochemical Society*, **168**, 090561 (2021).
92. V. Stancovski and S. Badilescu, *Journal of Applied Electrochemistry*, **44**, 23 (2014).
93. P. Jiang, J. F. Bertone, K. S. Hwang and V. L. Colvin, *Chemistry of Materials*, **11**, 2132 (1999).

94. E. Armstrong, D. McNulty, H. Geaney and C. O'Dwyer, *ACS Applied Materials & Interfaces*, **7**, 27006 (2015).
95. L. Mai, Y. Dong, L. Xu and C. Han, *Nano Letters*, **10**, 4273 (2010).
96. Y. Akita, M. Segawa, H. Munakata and K. Kanamura, *Journal of Power Sources*, **239**, 175 (2013).
97. M. J. Christian and M. Alain, *AIMS Materials Science*, **5**, 650 (2018).
98. H. Nakagawa, Y. Domi, T. Doi, M. Ochida, S. Tsubouchi, T. Yamanaka, T. Abe and Z. Ogumi, *Journal of Power Sources*, **206**, 320 (2012).
99. W. Zhu, A. Paolella, C. S. Kim, D. Liu, Z. Feng, C. Gagnon, J. Trottier, A. Vijh, A. Guerfi, A. Mauger, C. M. Julien, M. Armand and K. Zaghib, *Sustainable Energy & Fuels*, **1**, 737 (2017).
100. Z. Wei, A. Salehi, G. Lin, J. Hu, X. Jin, E. Agar and F. Liu, *Journal of Power Sources*, **449**, 227361 (2020).
101. Z. Gao, H. Sun, L. Fu, F. Ye, Y. Zhang, W. Luo and Y. Huang, *Advanced Materials*, **30**, 1705702 (2018).
102. S. Randau, D. A. Weber, O. Kötz, R. Koerver, P. Braun, A. Weber, E. Ivers-Tiffée, T. Adermann, J. Kulisch, W. G. Zeier, F. H. Richter and J. Janek, *Nature Energy*, **5**, 259 (2020).
103. X. Yao, D. Liu, C. Wang, P. Long, G. Peng, Y.-S. Hu, H. Li, L. Chen and X. Xu, *Nano Letters*, **16**, 7148 (2016).
104. Y. Zhou, C. Doerrer, J. Kasemchainan, P. G. Bruce, M. Pasta and L. J. Hardwick, *Batteries & Supercaps*, **3**, 647 (2020).
105. Y. Matsuda, N. Kuwata, T. Okawa, A. K. Dorai, O. Kamishima and J. Kawamura, *Solid State Ionics*, **335**, 7 (2019).
106. Y. Deng, S. Dong, Z. Li, H. Jiang, X. Zhang and X. Ji, *Small Methods*, **2**, 1700332 (2018).
107. D. Liu, Z. Shadike, R. Lin, K. Qian, H. Li, K. Li, S. Wang, Q. Yu, M. Liu, S. Ganapathy, X. Qin, Q.-H. Yang, M. Wagemaker, F. Kang, X.-Q. Yang and B. Li, *Advanced Materials*, **31**, 1806620 (2019).
108. G. Collins, E. Armstrong, D. McNulty, S. O'Hanlon, H. Geaney and C. O'Dwyer, *Science and Technology of Advanced Materials*, **17**, 563 (2016).
109. D. McNulty, E. Carroll and C. O'Dwyer, *Advanced Energy Materials*, **7**, 1602291 (2017).
110. E. Armstrong and C. O'Dwyer, *Journal of Materials Chemistry C*, **3**, 6109 (2015).
111. G. Mayonado, S. Mian, V. Robbiano and F. Cacialli, *Investigation Of The Bragg-Snell Law In PhCs* (2015).
112. J.-L. Xu, K. V. Thomas, Z. Luo and A. A. Gowen, *TrAC Trends in Analytical Chemistry*, **119**, 115629 (2019).
113. A. Götz, R. Nikzad-Langerodi, Y. Staedler, A. Bellaire and J. Saukel, *Spectrochimica Acta Part A: Molecular and Biomolecular Spectroscopy*, **224**, 117460 (2020).
114. J. Grdadolnik, *Acta Chimica Slovenica*, **49**, 631 (2002).
115. F. Shi, P. N. Ross, G. A. Somorjai and K. Komvopoulos, *The Journal of Physical Chemistry C*, **121**, 14476 (2017).
116. S. G. Kazarian and K. L. Chan, *Analyst*, **138**, 1940 (2013).
117. C. Marino, A. Boulaoued, J. Fullenwarth, D. Maurin, N. Louvain, J.-L. Bantignies, L. Stievano and L. Monconduit, *The Journal of Physical Chemistry C*, **121**, 26598 (2017).

118. D. Alves Dalla Corte, G. Caillon, C. Jordy, J.-N. Chazalviel, M. Rosso and F. Ozanam, *Advanced Energy Materials*, **6**, 1501768 (2016).
119. W. Ren, X. Chen and C. Zhao, *Advanced Energy Materials*, **8**, 1801413 (2018).
120. S. A. Freunberger, Y. Chen, N. E. Drewett, L. J. Hardwick, F. Bardé and P. G. Bruce, *Angewandte Chemie International Edition*, **50**, 8609 (2011).
121. J. Manuel, T. Salguero and R. P. Ramasamy, *Journal of Applied Electrochemistry*, **49**, 529 (2019).
122. T. Köhler, J. Hanzig and V. Koroteev, *Physical Sciences Reviews*, **4** (2019).
123. D. McNulty, H. Geaney, E. Armstrong and C. O'Dwyer, *Journal of Materials Chemistry A*, **4**, 4448 (2016).
124. S. Chiluwal, A. M. Rao and R. Podila, *Nanotechnology Reviews*, **10**, 1993 (2021).
125. C. O'Dwyer, *Advanced Materials*, **28**, 5681 (2016).
126. V. N. Astratov, Y. A. Vlasov, O. Z. Karimov, A. A. Kaplyanskii, Y. G. Musikhin, N. A. Bert, V. N. Bogomolov and A. V. Prokofiev, *Physics Letters A*, **222**, 349 (1996).
127. K. Busch and S. John, *Physical Review E*, **58**, 3896 (1998).
128. C. Cheng, A. Scherer, R.-C. Tyan, Y. Fainman, G. Witzgall and E. Yablonovitch, *Journal of vacuum science & technology. B, Microelectronics and nanometer structures: processing, measurement, and phenomena: an official journal of the American Vacuum Society*, **15** (2004).
129. D. Gaillot and T. Yamashita, *Phys. Rev. B*, **72** (2005).
130. S. A. Asher, J. M. Weissman, A. Tikhonov, R. D. Coalson and R. Kesavamoorthy, *Physical Review E*, **69**, 066619 (2004).
131. V. Golubev, *Phys. Rev. B*, **72** (2005).
132. W. Wu, M. Wang, J. Ma, Y. Cao and Y. Deng, *Advanced Electronic Materials*, **4**, 1800185 (2018).
133. T. Kuno, Y. Matsumura, K. Nakabayashi and M. Atobe, *Angewandte Chemie International Edition*, **55**, 2503 (2016).
134. S.-L. Kuai, G. Bader and P. V. Ashrit, *Applied Physics Letters*, **86**, 221110 (2005).
135. G. Collins, E. Armstrong, D. McNulty, S. O'Hanlon, H. Geaney and C. O'Dwyer, *Sci. Tech. Adv. Mater.*, **17**, 563 (2016).
136. D. McNulty, H. Geaney and C. O'Dwyer, *Sci. Rep.*, **7**, 42263 (2017).
137. D. McNulty, H. Geaney, E. Carroll, S. Garvey, A. Lonergan and C. O'Dwyer, *Materials Research Express*, **4**, 025011 (2017).
138. A. Esmanski and G. A. Ozin, *Advanced Functional Materials*, **19**, 1999 (2009).
139. J.-H. Kim, S. H. Kang, K. Zhu, J. Y. Kim, N. R. Neale and A. J. Frank, *Chemical Communications*, **47**, 5214 (2011).
140. B. Ding, M. Pemble, A. Korovin, U. Peschel and S. Romanov, *Phys. Rev. B*, **82** (2010).
141. Z.-Y. Li and Z.-Q. Zhang, *Physical Review B*, **62**, 1516 (2000).
142. A. Lonergan, D. McNulty and C. O'Dwyer, *Journal of Applied Physics*, **124**, 095106 (2018).
143. S. Romanov, H. Yates, M. Pemble and R. De La Rue, *Journal of Physics: Condensed Matter*, **12**, 8221 (2000).

144. S. G. Romanov, A. V. Fokin, V. Y. Butko, N. P. Johnson, H. M. Yates, M. E. Pemble and C. M. S. Torres, in *CLEO '97., Summaries of Papers Presented at the Conference on Lasers and Electro-Optics*, p. 527 (1997).
145. R. K. Cersonsky, J. Antonaglia, B. D. Dice and S. C. Glotzer, *Nature Communications*, **12**, 2543 (2021).
146. K. Busch and S. John, *Phys. Rev. Lett.*, **83**, 967 (1999).
147. Y. Nishijima, K. Ueno, S. Juodkazis, V. Mizeikis, H. Misawa, T. Tanimura and K. Maeda, *Optics Express*, **15**, 12979 (2007).
148. K. R. Phillips, N. Vogel, Y. Hu, M. Kolle, C. C. Perry and J. Aizenberg, *Chem. Mater.*, **26**, 1622 (2014).
149. M. Lanata, M. Cherchi, A. Zappettini, S. M. Pietralunga and M. Martinelli, *Opt. Mater.*, **17**, 11 (2001).
150. Y. Meng, F. Liu, M. M. Umair, B. Ju, S. Zhang and B. Tang, *Advanced Optical Materials*, **6**, 1701351 (2018).
151. E. Armstrong and C. O'Dwyer, *J. Mater. Chem. C*, **3**, 6109 (2015).
152. H. Chen, R. Lou, Y. Chen, L. Chen, J. Lu and Q. Dong, *Drug Delivery*, **24**, 775 (2017).
153. S. Kim, A. N. Mitropoulos, J. D. Spitzberg, D. L. Kaplan and F. G. Omenetto, *Opt. Express*, **21**, 8897 (2013).
154. W. Chen, Z. Meng, M. Xue and J. Shea Kenneth, Molecular imprinted PhC for sensing of biomolecules, in *Molecular Imprinting*, p. 1 (2016).
155. W. S. Lee, T. Kang, S.-H. Kim and J. Jeong, *Sensors (Basel, Switzerland)*, **18**, 307 (2018).
156. Y. S. Zhang, C. Zhu and Y. Xia, *Adv. Mater.*, **29**, 1701115 (2017).
157. C. López, *Adv. Mater.*, **15**, 1679 (2003).
158. S. Amrehn, X. Wu, C. Schumacher and T. Wagner, *physica status solidi (a)*, **212**, 1266 (2015).
159. M. Danaie and B. Kiani, *Photonics and Nanostructures - Fundamentals and Applications*, **31**, 89 (2018).
160. A. Cumbo, B. Lorber, P. F. X. Corvini, W. Meier and P. Shahgaldian, *Nature Communications*, **4**, 1503 (2013).
161. A. Chutinan, N. P. Kherani and S. Zukotynski, *Optics Express*, **17**, 8871 (2009).
162. K. Xie, M. Guo and H. Huang, *Journal of Materials Chemistry C*, **3**, 10665 (2015).
163. Y. Yu, Y. Yu, Y. Yu, Y. Yu, Y. Yu and Y. Yu, *Nano Lett.*, **15**, 4282 (2015).
164. H. Liu, H. Liu, H. Liu, H. Liu, H. Liu and H. Liu, *Science*, **344**, 1 (2014).
165. F. C. Strobridge, F. C. Strobridge, F. C. Strobridge, F. C. Strobridge, F. C. Strobridge and F. C. Strobridge, *Chem. Mater.* , **27**, 2374 (2015).
166. A. Senyshyn, M. J. Mühlbauer, K. Nikolowski, T. Pirling and E. H., *J. Power Sources*, **203**, 126 (2012).
167. K. Ogata, K. Ogata, K. Ogata, K. Ogata, K. Ogata and K. Ogata, *Nat. Commun.* , **5**, 3217 (2014).
168. B. R. Long, M. K. Y. Chan, J. P. Greeley and A. A. Gewirth, *The Journal of Physical Chemistry C*, **115**, 18916 (2011).
169. L. Mai, M. Yan and Y. Zhao, *Nature*, **546**, 469 (2017).
170. K. Hongyou, T. Hattori, Y. Nagai, T. Tanaka, H. Nii and K. Shoda, *Journal of Power Sources*, **243**, 72 (2013).
171. A. Vu, Y. Q. Qian and A. Stein, *Adv. Energy Mater.* , **2**, 1056 (2012).

172. E. Armstrong, M. Osiak, H. Geaney, C. Glynn and C. O'Dwyer, *CrystEngComm*, **16**, 10804 (2014).
173. M. J. Armstrong, D. M. Burke, T. Gabriel, C. O'Regan, C. O'Dwyer, N. Petkov and J. D. Holmes, *J. Mater. Chem. A* (2013).
174. C. O'Dwyer, V. Lavayen, D. A. Tanner, S. B. Newcomb, E. Benavente, G. Gonzalez and C. M. Sotomayor Torres, *Adv. Funct. Mater.*, **19**, 1736 (2009).
175. P. Ladpli, F. Kopsaftopoulos, R. Nardari and F.-K. Chang, *Battery charge and health state monitoring via ultrasonic guided-wave-based methods using built-in piezoelectric transducers*, SPIE (2017).
176. F. Wang, L. Feng, Y. Qin, T. Zhao, H. Luo and J. Zhu, *Journal of Materials Chemistry C*, **7**, 11972 (2019).
177. L. Mishchenko, B. Hatton, M. Kolle and J. Aizenberg, *Small*, **8**, 1904 (2012).
178. P. V. Braun, *Chem. Mater.*, **26**, 277 (2013).
179. E. Armstrong, W. Khunsin, M. Osiak, M. Blömker, C. M. S. Torres and C. O'Dwyer, *Small*, **10**, 1895 (2014).
180. C. O'Dwyer, M. Szachowicz, G. Visimberga, V. Lavayen, S. B. Newcomb and C. M. S. Torres, *Nat. Nanotech.*, **4**, 239 (2009).
181. M. Osiak, W. Khunsin, E. Armstrong, T. Kennedy, C. M. S. Torres, K. M. Ryan and C. O'Dwyer, *Nanotechnology*, **24**, 065401 (2013).
182. W. Zhang, M. Anaya, G. Lozano, M. E. Calvo, M. B. Johnston, H. Míguez and H. J. Snaith, *Nano Letters* (2015).
183. A. Ghannoum, R. C. Norris, K. Iyer, L. Zdravkova, A. Yu and P. Nieva, *ACS Applied Materials & Interfaces*, **8**, 18763 (2016).
184. A. Ghannoum and P. Nieva, *Journal of Energy Storage*, **28**, 101233 (2020).
185. J. Hedman, D. Nilebo, E. Larsson Langhammer and F. Björefors, *ChemSusChem*, **13**, 5731 (2020).
186. D. Krotkov, D. Schneier, S. Menkin, Y. Horowitz, E. Peled, D. Golodnitsky and S. Fleischer, *Batteries & Supercaps*, **5**, e202100183 (2022).
187. A. Navid and L. Pilon, *Thin Solid Films*, **516**, 4159 (2008).
188. N. J. Hutchinson, T. Coquil, A. Navid and L. Pilon, *Thin Solid Films*, **518**, 2141 (2010).
189. A. Lonergan, C. Hu and C. O'Dwyer, *Physical Review Materials*, **4** (2020).
190. M. E. Layani-Tzadka, D. Krotkov, E. Tirosh, G. Markovich and S. Fleischer, *Nanotechnology*, **30**, 215702 (2019).
191. K. S. C. Kuang, R. Kenny, M. P. Whelan, W. J. Cantwell and P. R. Chalker, *Composites Science and Technology*, **61**, 1379 (2001).
192. L. Albero Blanquer, F. Marchini, J. R. Seitz, N. Daher, F. Bétermier, J. Huang, C. Gervillié and J.-M. Tarascon, *Nature Communications*, **13**, 1153 (2022).
193. J. Huang, L. Albero Blanquer, J. Bonefacino, E. R. Logan, D. Alves Dalla Corte, C. Delacourt, B. M. Gallant, S. T. Boles, J. R. Dahn, H.-Y. Tam and J.-M. Tarascon, *Nature Energy*, **5**, 674 (2020).
194. J. A. Guemes and J. M. Menéndez, *Composites Science and Technology*, **62**, 959 (2002).
195. A. J. Louli, L. D. Ellis and J. R. Dahn, *Joule*, **3**, 745 (2019).

196. C. J. Bae, A. Manandhar, P. Kiesel and A. Raghavan, *Energy technology*, **4**, 851 (2016).
197. Y. D. Su, Y. Preger, H. Burroughs, C. Sun and P. R. Ohodnicki, *Sensors*, **21**, 1397 (2021).
198. X. Cheng and M. Pecht, *Energies*, **10**, 591 (2017).
199. A. Bertholds and R. Dandliker, *Journal of lightwave technology*, **6**, 17 (1988).
200. Y. Wang, B. Yun, N. Chen and Y. Cui, *Measurement Science and Technology*, **17**, 939 (2006).
201. R. Gafsi and M. A. El-Sherif, *Optical fiber technology*, **6**, 299 (2000).
202. M. Inaba, H. Yoshida and Z. Ogumi, *Journal of The Electrochemical Society - J ELECTROCHEM SOC*, **143**, 2572 (1996).
203. A. Vizintin, J. Bitenc, A. Kopač Lautar, K. Pirnat, J. Grdadolnik, J. Stare, A. Randon-Vitanova and R. Dominko, *Nature Communications*, **9**, 661 (2018).
204. M. Matsui, S. Deguchi, H. Kuwata and N. Imanishi, *Electrochemistry*, **83**, 874 (2015).
205. R. Sharabi, E. Markevich, V. Borgel, G. Salitra, D. Aurbach, G. Semrau and M. A. Schmidt, *Electrochemical and Solid-State Letters*, **13**, A32 (2010).
206. A. Ghannoum, K. Iyer, P. Nieva and A. Khajepour, in *2016 IEEE SENSORS*, p. 1 (2016).
207. M. Patel, R. Demir-Cakan, M. Morcrette, J.-M. Tarascon, M. Gaberscek and R. Dominko, *ChemSusChem*, **6** (2013).
208. K. Yue, C. Zhai, S. Gu, Y. He, J. Yeo and G. Zhou, *Electrochimica Acta*, **368**, 137535 (2021).
209. P. Lanz, C. Villevieille and P. Novak, *Electrochimica Acta*, **109**, 426 (2013).
210. T. Gross, L. Giebeler and C. Hess, *Review of Scientific Instruments*, **84**, 073109 (2013).
211. M. Inaba, Y. Iriyama, Z. Ogumi, Y. Todzuka and A. Tasaka, *Journal of Raman Spectroscopy*, **28**, 613 (1997).
212. K. Shen, Z. Wang, X. Bi, Y. Ying, D. Zhang, C. Jin, G. Hou, H. Cao, L. Wu, G. Zheng, Y. Tang, X. Tao and J. Lu, *Advanced Energy Materials*, **9**, 1900260 (2019).
213. X. Xu, S. Wang, H. Wang, B. Xu, C. Hu, Y. Jin, J. Liu and H. Yan, *Journal of Energy Storage*, **13**, 387 (2017).
214. F. Wu, Y.-X. Yuan, X.-B. Cheng, Y. Bai, Y. Li, C. Wu and Q. Zhang, *Energy Storage Materials*, **15**, 148 (2018).
215. L. Kong, Y. Xing and M. G. Pecht, *IEEE Access*, **6**, 8387 (2018).
216. Y. Wu, C. Zhang, Y. Yuan, Z. Wang, W. Shao, H. Wang and X. Xu, *Langmuir*, **29**, 14017 (2013).
217. X.-B. Cheng, R. Zhang, C.-Z. Zhao and Q. Zhang, *Chemical Reviews*, **117**, 10403 (2017).
218. J. Liu, Z. Bao, Y. Cui, E. J. Dufek, J. B. Goodenough, P. Khalifah, Q. Li, B. Y. Liaw, P. Liu, A. Manthiram, Y. S. Meng, V. R. Subramanian, M. F. Toney, V. V. Viswanathan, M. S. Whittingham, J. Xiao, W. Xu, J. Yang, X.-Q. Yang and J.-G. Zhang, *Nature Energy*, **4**, 180 (2019).
219. M. D. Tikekar, S. Choudhury, Z. Tu and L. A. Archer, *Nature Energy*, **1**, 16114 (2016).

220. A. B. Gunnarsdóttir, C. V. Amanchukwu, S. Menkin and C. P. Grey, *Journal of the American Chemical Society*, **142**, 20814 (2020).
221. R. Pigliapochi, S. Benders, E. V. Silletta, S. L. Glazier, E. Lee, J. Dahn and A. Jerschow, *Batteries & Supercaps*, **4**, 322 (2021).
222. A. J. Ilott, M. Mohammadi, C. M. Schauerman, M. J. Ganter and A. Jerschow, *Nature Communications*, **9**, 1776 (2018).
223. A. L. Sukstanskii and D. A. Yablonskiy, *Journal of Magnetic Resonance*, **151**, 107 (2001).
224. E. Banguero, A. Correcher, Á. Pérez-Navarro, E. García and A. Aristizabal, *Renewable Energy*, **146**, 2438 (2020).
225. S. Tikole, V. Jaravine, V. Y. Orekhov and P. Güntert, *PLoS One*, **8**, e68567 (2013).
226. J.-H. Chen, H. Zhang, S. M. Althaus and M. Boudjatit, *Fuel*, **297**, 120777 (2021).
227. G. E. Möhl, E. Metwalli and P. Müller-Buschbaum, *ACS Energy Letters*, **3**, 1525 (2018).
228. G. Subramania, R. Biswas, K. Constant, M. M. Sigalas and K. M. Ho, *Physical Review B*, **63**, 235111 (2001).
229. D. McNulty, A. Lonergan, S. O'Hanlon and C. O'Dwyer, *Solid State Ionics*, **314**, 195 (2018).
230. V. Roscher and K. Riemschneider, *IEEE Transactions on Instrumentation and Measurement*, **67**, 735 (2018).
231. A. G. Hsieh, S. Bhadra, B. J. Hertzberg, P. J. Gjeltema, A. Goy, J. W. Fleischer and D. A. Steingart, *Energy & Environmental Science*, **8**, 1569 (2015).
232. D. A. Steingart, Without sound and fury, signifying something: acoustics and batteries, in *Instrumentation and Measurement*, Physics World (2020).
233. J. B. Robinson, M. Pham, M. D. R. Kok, T. M. M. Heenan, D. J. L. Brett and P. R. Shearing, *Journal of Power Sources*, **444**, 227318 (2019).
234. W. Chang, R. Mohr, A. Kim, A. Raj, G. Davies, K. Denner, J. H. Park and D. Steingart, *Journal of Materials Chemistry A*, **8**, 16624 (2020).
235. H.-S. Kitzerow, H. Matthias, S. L. Schweizer, H. M. van Driel and R. B. Wehrspohn, *Advances in Optical Technologies*, **2008**, 12 (2008).
236. R. Norris, K. Iyer, V. Chabot, P. Nieva, A. Yu, A. Khajepour and J. Wang, *Multi-band reflectance spectroscopy of carbonaceous Li iron phosphate battery electrodes versus state of charge*, SPIE (2014).
237. A. Messica, A. Greenstein and A. Katzir, *Applied Optics*, **35**, 2274 (1996).
238. J. M. Tarascon, A. S. Gozdz, C. Schmutz, F. Shokoohi and P. C. Warren, *Solid State Ionics*, **86-88**, 49 (1996).
239. M. Letellier, F. Chevallier, C. Clinard, E. Frackowiak, J.-N. Rouzaud, F. Béguin, M. Morcrette and J.-M. Tarascon, *The Journal of Chemical Physics*, **118**, 6038 (2003).
240. F. Chevallier, M. Letellier, M. Morcrette, J. M. Tarascon, E. Frackowiak, J. N. Rouzaud and F. Béguin, *Electrochemical and Solid-State Letters*, **6**, A225 (2003).
241. M. Letellier, F. Chevallier, F. Béguin, E. Frackowiak and J.-N. Rouzaud, *Journal of Physics and Chemistry of Solids*, **65**, 245 (2004).

242. F. Poli, J. S. Kshetrimayum, L. Monconduit and M. Letellier, *Electrochemistry Communications*, **13**, 1293 (2011).
243. G. Davies, K. W. Knehr, B. Van Tassell, T. Hodson, S. Biswas, A. G. Hsieh and D. A. Steingart, *Journal of The Electrochemical Society*, **164**, A2746 (2017).
244. C. Bommier, W. Chang, Y. Lu, J. Yeung, G. Davies, R. Mohr, M. Williams and D. Steingart, *Cell Reports Physical Science*, **1**, 100035 (2020).
245. L. Gold, T. Bach, W. Virsik, A. Schmitt, J. Müller, T. E. M. Staab and G. Sextl, *Journal of Power Sources*, **343**, 536 (2017).
246. B. Li, C. M. Jones, T. E. Adams and V. Tomar, *Journal of Power Sources*, **486**, 229349 (2021).
247. J. McBreen, *J. Solid State Electrochem.* , **13**, 1051 (2009).
248. J. Amici, P. Asinari, E. Ayerbe, P. Barboux, P. Bayle-Guillemaud, R. J. Behm, M. Berecibar, E. Berg, A. Bhowmik, S. Bodoardo, I. E. Castelli, I. Cekic-Laskovic, R. Christensen, S. Clark, R. Diehm, R. Dominko, M. Fichtner, A. A. Franco, A. Grimaud, N. Guillet, M. Hahlin, S. Hartmann, V. Heiries, K. Hermansson, A. Heuer, S. Jana, L. Jabbour, J. Kallo, A. Latz, H. Lorrmann, O. M. Løvvik, S. Lyonnard, M. Meeus, E. Paillard, S. Perraud, T. Placke, C. Punckt, O. Raccurt, J. Ruhland, E. Sheridan, H. Stein, J.-M. Tarascon, V. Trapp, T. Vegge, M. Weil, W. Wenzel, M. Winter, A. Wolf and K. Edström, *Advanced Energy Materials*, **12**, 2102785 (2022).
249. D. Atkins, E. Ayerbe, A. Benayad, F. G. Capone, E. Capria, I. E. Castelli, I. Cekic-Laskovic, R. Ciria, L. Dudy, K. Edström, M. R. Johnson, H. Li, J. M. G. Lastra, M. L. De Souza, V. Meunier, M. Morcrette, H. Reichert, P. Simon, J.-P. Rueff, J. Sottmann, W. Wenzel and A. Grimaud, *Advanced Energy Materials*, **12**, 2102687 (2022).
250. D. Atkins, E. Capria, K. Edström, T. Famprikis, A. Grimaud, Q. Jacquet, M. Johnson, A. Matic, P. Norby, H. Reichert, J.-P. Rueff, C. Villevieille, M. Wagemaker and S. Lyonnard, *Advanced Energy Materials*, **12**, 2102694 (2022).
251. A. Benayad, D. Diddens, A. Heuer, A. N. Krishnamoorthy, M. Maiti, F. L. Cras, M. Legallais, F. Rahmanian, Y. Shin, H. Stein, M. Winter, C. Wölke, P. Yan and I. Cekic-Laskovic, *Advanced Energy Materials*, **12**, 2102678 (2022).
252. A. Bhowmik, M. Berecibar, M. Casas-Cabanas, G. Csanyi, R. Dominko, K. Hermansson, M. R. Palacin, H. S. Stein and T. Vegge, *Advanced Energy Materials*, **12**, 2102698 (2022).
253. M. Fichtner, K. Edström, E. Ayerbe, M. Berecibar, A. Bhowmik, I. E. Castelli, S. Clark, R. Dominko, M. Erakca, A. A. Franco, A. Grimaud, B. Horstmann, A. Latz, H. Lorrmann, M. Meeus, R. Narayan, F. Pammer, J. Ruhland, H. Stein, T. Vegge and M. Weil, *Advanced Energy Materials*, **12**, 2102904 (2022).
254. J. Schaarschmidt, J. Yuan, T. Strunk, I. Kondov, S. P. Huber, G. Pizzi, L. Kahle, F. T. Bölle, I. E. Castelli, T. Vegge, F. Hanke, T. Hickel, J. Neugebauer, C. R. C. Rêgo and W. Wenzel, *Advanced Energy Materials*, **12**, 2102638 (2022).
255. J. E. Harlow, X. Ma, J. Li, E. Logan, Y. Liu, N. Zhang, L. Ma, S. L. Glazier, M. M. E. Cormier, M. Genovese, S. Buteau, A. Cameron, J. E. Stark and J. R. Dahn, *Journal of The Electrochemical Society*, **166**, A3031 (2019).

256. C. P. Aiken, E. R. Logan, A. Eldesoky, H. Hebecker, J. M. Oxner, J. E. Harlow, M. Metzger and J. R. Dahn, *Journal of The Electrochemical Society*, **169**, 050512 (2022).

Chapter 3

Experimental

3.1. Introduction

All experimental methods used throughout the research included in this thesis are summarised in the following chapter. In the subsequent chapters, experimental details specific to each study are outlined. Experimental methods are broken down into four primary sections: (1) Sample preparation: All steps taken to prepare samples used either as standalone materials for characterisation, or implementation as battery electrodes. (2) Cell preparation: Electrolyte preparation for Li-ion and Na-ion batteries, and the range of cell assemblies used for battery performance testing are detailed. (3) Structural characterisation: Methods used to probe the structure of materials including microscopy, optical, and compositional analysis. (4) Electrochemical characterisation: Details of all methods used to probe battery performance.

3.2. Sample Preparation

3.2.1. Substrate Preparation

In Chapters 4-5, sodalime glass coated with a conductive layer of fluorine-doped tin oxide (FTO), purchased from Solaronix SA, was used as the substrate for opal formation. Substrates of thickness 2.2 mm were cut to dimensions of 10 mm x 25 mm. In Chapter 6, the substrates used were stainless-steel 316L disks with 15.5 mm diameter and 0.2 mm thickness. For the results in Chapter 7, two substrates were prepared. (1) The same stainless-steel disks from previous chapters were punched to a diameter of 10 mm to ensure compatibility with the associated cell. (2) A 6 mm Cu mesh disk was punched from Cu foil. Prior to opal formation, all substrates were

sonicated in acetone (reagent grade 99.5%; SigmaAldrich), followed by sonication in isopropyl alcohol (reagent grade 99.5%; Sigma-Aldrich) and finally sonicated in deionised water. A Novascan PSD Pro Series digital UV-ozone system was used to maximise hydrophilicity of the surface of the substrates immediately prior to opal template formation for a duration of 1 h for FTO glass, and 30 minutes for the stainless-steel and Cu mesh. UV-ozone treatment duration was chosen based on the hydrophobicity of each substrate, indicate by their respective water contact angles.

3.2.2. Evaporation-Induced Self-Assembly of Opals

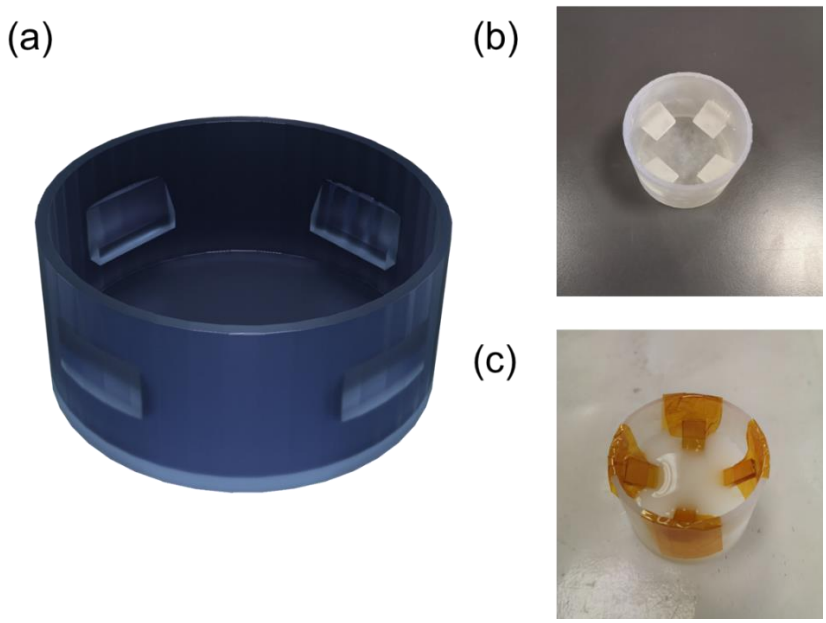


Figure 3.1. (a) Schematic and (b) photograph of the 3D printed beaker used during the EISA process. (c) Photograph of the 3D printed beaker prepared with samples fixed in position and sphere solution added.

For the work included in Chapters 4-5, 3D printed polymer beakers were formed from Formlabs Clear Photoreactive Resin using a Formlabs Form 2 stereolithography (SLA) printer. Figure 3.1 (a) and (b) show a schematic and

photograph of one of the finished beakers, respectively. Once printed, each beaker was sonicated in IPA for 10 minutes followed by curing for 10 minutes.

Next, all beakers were cleaned using the same sonication process described previously, followed by treatment in a Novascan PSD Pro Series digital UV-Ozone system for 1 h to maximise surface hydrophilicity. Substrates were then taped to the inside of the beaker as shown in Figure 3.1 (c). The polymer beakers were designed with substrate rests on the inside of the beaker at a tilt angle of 30 ° to aid the assembly process. Once the substrates were firmly in place, dilutions of the polystyrene (PS) sphere solutions were prepared. Aqueous solutions of PS and de-ionised water were prepared based on the desired concentration for each experiment. The total volume of the aqueous solution was determined based on the height of the beaker at which the exposed surfaces of the substrates were immersed. A 1 mL pipette was used to add the PS solution to the beaker. Beakers containing the diluted sphere suspensions were placed on a hot plate that was pre-heated to ~30 °C to 33 °C and left in place for 36 - 48 h as evaporation-induced self-assembly (EISA) occurred. Once the solution in each beaker had been completely evaporated the beakers were removed from the hot plate. Next, the substrates were removed from their respective beakers and left to dry in an inert atmosphere at room temperature.

In Chapters 6-7, EISA was performed under different conditions. Glass vials with diameter 20 mm were used instead of the 3D printed beakers. Stainless steel 316L substrates were taped to the inside of the glass vials immediately after UV-ozone treatment and an aqueous sphere suspension

was added with a concentration between 0.1-0.2 %. Instead of a hot plate, evaporation was induced using a Binder convection oven at temperatures of 60-70 °C. While a much higher evaporation temperature was used for the steel substrates, the smaller diameter of the glass vials resulted in a greatly reduced exposed solution surface area compared to the larger 3D printer beakers used for the FTO glass substrates described previously. Evaporation times were similar for both methodologies despite a significant difference in evaporation temperature. Experimental trial and error demonstrated that this adaptation greatly improved the quality of opal templates grown on stainless steel and lead to superior IOs.

3.2.3. IO Formation by Template Infiltration

IOs were formed via infiltration of the opal templates by metal alkoxide precursors. Upon infiltration, the precursor fills the unoccupied space within the opal specimens. Simultaneously, a typical sol-gel process occurs. The metal alkoxide in alcohol solution first hydrolyses upon contact with water in the air. Next, the hydrolysed metal alkoxide forms a polymer through the condensation of hydroxyl groups and further crosslinking and branching.

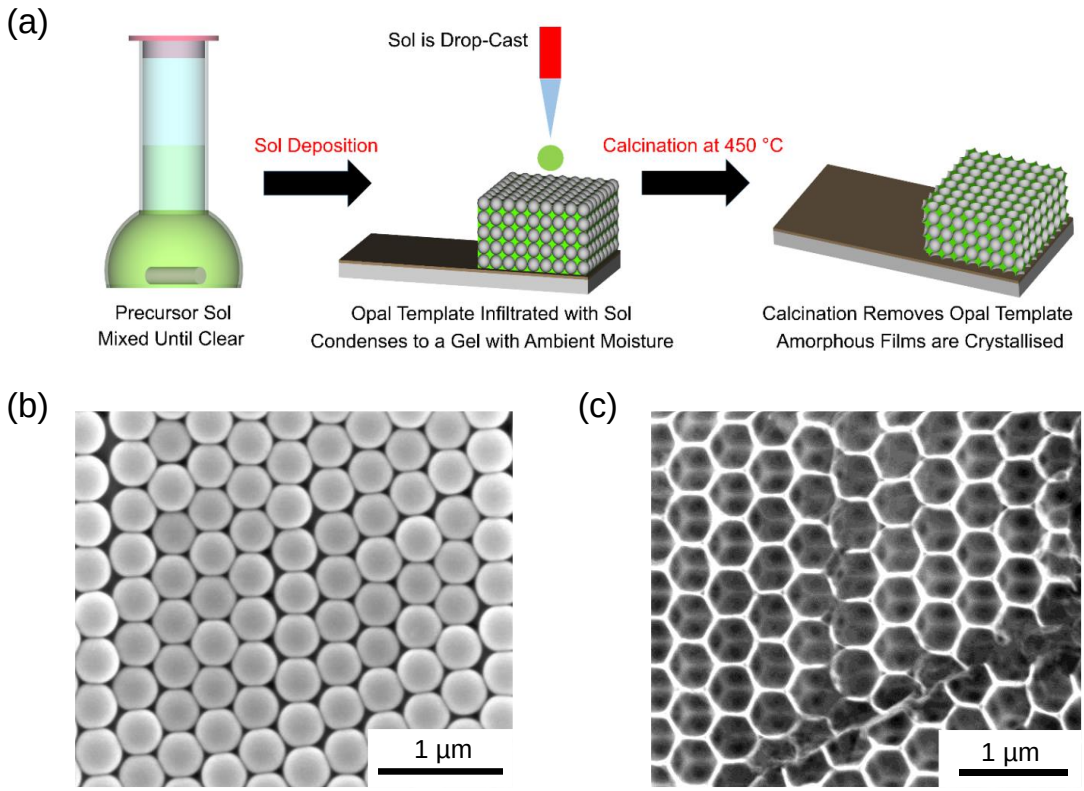


Figure 3.2. (a) Schematic of sol-gel process depicting the infiltration of opal template with metal alkoxide precursor and calcination to form IO. (b) SEM image of opal template prior to infiltration. (c) SEM image of IO after infiltration and calcination.

For each IO, the precursor was added either dropwise using a 1 mL syringe, or a measured volume using a micropipette. After infiltration, the precursor underwent the described sol-gel process to form an amorphous metal oxide gel. Next, infiltrated templates were left to dry at 70 °C in a Binder convection oven for 20 minutes. Following drying, calcination was performed at 450 °C in air, which simultaneously burned the PS opal template and crystallised the amorphous metal oxide gel. For the SnO_2 IOs investigated in Chapter 6, the chosen precursor was $SnCl_2.H_2O$ Mixed with IPA to a 0.1 M

concentration. For the TiO_2 IOs examined in Chapter 7, $TiCl_4$.2THF was mixed with IPA to a 0.1 M concentration.

3.2.4. Electrode Washing

For postmortem SEM image acquisition, electrode washing was required. First, a volume of the associated electrolyte solvent was prepared. Next, cells were disassembled, and the electrodes removed inside the glovebox. Each electrode was then immersed in solvent for 30 s, this was repeated twice. The electrodes were then left to dry at room temperature overnight. Here, electrodes removed from Li-ion and Na-ion cells were washed in DMC and PC, respectively.

3.2.5. Sputter Coating

In some cases, metal coatings were formed on opals prior to SEM imaging via physical vapour deposition. SEM image resolution is strongly affected by the electrical conductivity of the target specimen. Specimens with low conductivity, such as the PS opals described in Chapters 4-5 can result in charging, which causes beam drift. Other advantages include reduced microscope beam damage, increased thermal conduction, improved secondary electron emission, and reduced beam penetration with improved edge resolution.

Sputter deposition occurs when a glow discharge is formed between a cathode and anode using an appropriate inert gas like Argon. The cathode material acts as the target, while the specimen destined for coating is positioned at the anode. The applied potential difference (on the order of 1 kV) creates an electric field which causes the gas to breakdown into positive ions,

known as a plasma. The heavier ions are accelerated towards the negative cathode which is eroded. Simultaneously, the electrons are released from the cathode which give rise to excitation and ionisation collisions with argon gas atoms, followed by a decay back to ground state with emission of light, causing a glow discharge. The eroded cathode particles are then sputtered onto the surface of the specimen to form a thin coating.

A Quorum 150T S magnetron sputtering system was used for magnetron sputter coating in all cases. A removable metal disc target with a thickness of 0.1 mm and diameter 57 mm was used for nickel deposition to a thickness of ~ 20 nm. The target was purchased from Ted Pella Inc. and featured a material purity of 99.99%. A quartz oscillator film thickness monitor was used to select nominal thickness. All metals were sputtered under an inert gas of high purity to ensure that the gas molecules did not react with the sputtered metal particles. Argon (> 99.995 % purity) was used as the sputtering gas. Cleaning of the target surface prior to film deposition was allowed by a target shutter in the sputter coater assembly. Cleaning is particularly important in the case of oxidising metal targets.

3.3. Cell Preparation

3.3.1. Electrolyte Preparation

The electrolyte used for all Li-ion cells was 1 M Li hexafluorophosphate ($LiPF_6$) in a 1:1 mixture (v/v) of ethylene carbonate (EC) and dimethyl carbonate (DMC). The electrolyte used for all Na-ion cells was 1 M Na perchlorate ($NaClO_4$) in propylene carbonate (PC) with a 5 wt % fluoroethylene carbonate (FEC) additive to stabilise the SEI layer.

3.3.2. Electrode Preparation

In Chapter 6, SnO_2 IO electrodes were prepared using the template infiltration procedure outlined previously on 15 mm stainless steel substrates. In Chapter 7, three different electrodes were used. (1) TiO_2 IO electrodes were prepared using the same template infiltration procedure outlined previously, on 10 mm stainless steel substrates. (2) Commercial NMC-622 disks on Al foil. Received as 15 mm in diameter, punched to 10 mm diameter for compatibility with the PAT-Cell-Opto-10. (3) TiO_2 electrodes were prepared via a traditional slurry coating procedure. The slurries were obtained by mixing the TiO_2 active material, conductive carbon (Super-P) and Na carboxymethyl cellulose (CMC) binders in the mass ratio of 8:1:1. First, the CMC binder was dissolved into deionised water by stirring for 4-8 hours at room temperature. Second, the TiO_2 active material and conductive carbon (Super-P) were ground by an agate mortar and pestle for 20-30 minutes before adding to the mixture. The slurry mixture was coated on the Cu mesh (a diameter of 6 mm) after stirring overnight for 12 hours. The obtained electrodes were first dried in a vacuum oven at 80 °C for 12 h before assembling the cell.

3.3.3. Cell Assembly

Two cell configurations were used in Chapters 6-8. (1) EL Cell PAT cells (ECC1–01–0012-A/L, 18 mm diameter, 0.65 mm thickness) operated as half-cells. (2) CR2032 coin cells (SS304, 20 mm diameter, 3.2 mm thickness prior to crimping).

3.3.4. Operando Cell Assembly

Operando techniques, as described extensively throughout the literature review in Chapter 2, can be used to monitor changes to the electrode and electrolyte during battery cycling. A prerequisite for successful operando measurements is the design of a suitable operando cell. For electromagnetic probes such as XRD, FTIR, Raman, and optical spectroscopy, a spectroelectrochemical cell is required, where light penetration is permitted by an optical window. The chosen window material depends on the frequency of incident radiation. Sapphire or quartz are the most commonly window materials used for penetration by optical wavelengths.(1) Accessing the active electrode material with incident radiation is challenging. Typically, four configurations are used: transmission, ATR, one-sided, and transverse. The configuration used depends on the nature of the electrode stack.(2)

(a) (b)



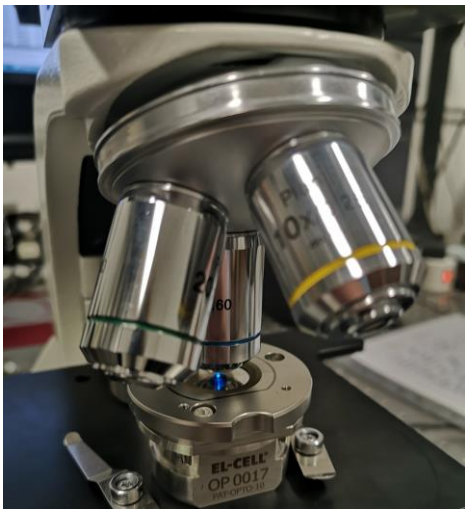
(c)



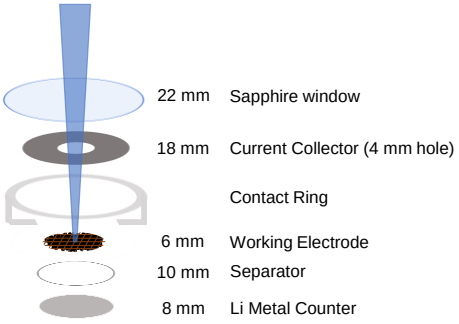
Figure 3.3. Photographs of EL Cell PAT cells used for battery performance testing (a) Opened PAT cell (b) PAT Cell clipped into PAT-Clamp for connection to potentiostat. (c) PAT cells clipped into docking station inside temperature-controlled oven connected to potentiostat.

Typical electrochemical cell designs are “face-to-face”, with each electrode facing each other. For two-sided electrodes, access to the active material by the incident probe is straightforward. For one-sided electrodes, the substrate blocks access to the active material. In the literature, various adaptations can be made to the electrode, including the use of a mesh so that light can be transmitted directly through the substrate.(3, 4)

(a)



(b)



(c)

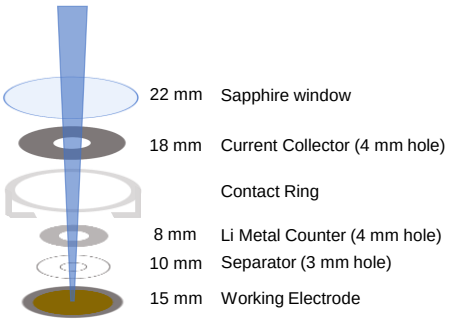


Figure 3.4. (a) Assembled PAT-Cell-Opto-10 under microscope in preparation for alignment with Raman laser. (b) Electrode stack configuration 1: Regular face-to-face setup with active material of working electrode coated on a Cu mesh substrate in upper electrode position placed “face-down”. (c) Electrode stack configuration 2: “Ring-system” face-to-face setup with active material coated on either aluminium foil or a stainless-steel disk in lower electrode position placed “face-down”.

In Chapter 7, the spectroelectrochemical cell used for operando Raman spectroscopy measurements was the EL-Cell Pat-Cell-Opto-10, shown in Figure 3.4 (a) with a sapphire window (22 mm diameter, 0.3 mm thickness). Two electrode stack configurations were used: (1) Regular face-to-face electrode stack, shown in Figure 3.4 (b): This consisted of from bottom to top Li metal counter electrode (8 mm diameter), Whatman GF/A separator (10 mm), 20-30 µL $LiPF_6$-based electrolyte prepared es described previously working electrode (6 mm diameter), nanoparticulate anatase TiO_2 slurry on Cu mesh substrate. (2) A 'ring system' face-to-face electrode stack, shown in Figure 3.4 (c). This consisted of from bottom to top the working electrode (10 mm diameter) either NMC on Al foil substrate or TiO_2 IO on stainless steel substrate, Whatman GF/A separator (10 mm diameter with a 3 mm diameter hole punched in the center), 10-20 µL $LiPF_6$-based electrolyte prepared as described previously, Li metal counter electrode (8 mm diameter with 4 mm diameter hole punched in the center), contact ring around the electrode stack creating connection between the counter electrode and electrode contact pins, and a holed current collector placed on top of the ring.

The primary concern for operando Raman measurements is providing direct access for the Raman laser beam to the active electrode material and the electrode stack must be adapted correctly. For electrode stack configuration (1), access to the active material of the working electrode is provided by the Cu mesh substrate, positioned "face-down" as the upper electrode. The coated active material fills the gaps between the mesh, and simultaneous electrolyte infiltration and Raman beam penetration is achieved.

Electrode stack configuration (2) is used for one-sided electrodes, where access to the active material is prevented by the solid substrate. Here, the orientation of the electrode stack is reversed, and the working material is positioned as the lower electrode “face-up”. The ring system allows the Raman laser beam to propagate directly through to the active material of the working electrode.

3.4. Structural Characterisation Methods

3.4.1. Scanning Electron Microscopy

In scanning electron microscopy (SEM), a focused beam of relatively high energy electrons (2-40 kV) is raster scanned across the sample surface under high vacuum. The intensity of the detected signal is combined with the position of the beam to produce an image. Inelastic collisions between the incident beam and the atoms within the material cause secondary electrons (SEs) to be released from the material surface which are collected by the detector and a magnified image of the surface is produced.(5) The secondary electrons are utilised to fluoresce a scintillating material on the detector face, analogous to a cathode ray tube using phosphorus to fluoresce on a television screen. The fluoresced material is then translated to an electronic signal using a photomultiplier tube.

A range of other signals are produced including back-scattered electrons, X-rays, and transmitted electrons, but SE mode is the most common method of detection. SEs have a small mean free path in solids due to their low energy, meaning that they can only escape from the top few nanometres of the material surface. SEM is therefore most useful for topographical

characterisation. The strong localisation of the signal from SEs on impact of the incident beam can provide high image resolution of below 1 nm.(6) SEM images yield a three-dimensional appearance due to the large depth of field caused by the narrow incident electron beam and magnification of over 250 times that of the limit of the most efficient light microscopes can be achieved for a resolution of up to ~ 200 nm. The maximum resolution of conventional microscopy is proportional to the wavelength of light. By using a high energy beam of electrons instead, the resolution is enhanced due to the small de Broglie wavelength of electrons, which is inversely proportional to the accelerating voltage of the electrons.

The large depth of field proves particularly advantageous for opals, where the characteristic large peak to peak roughness significantly limits the resolution of other microscopy techniques, such as atomic force microscopy (AFM). The teardrop-shaped interaction volume of the specimen ranges from 100 nm to 5 µm into the surface and depends on several factors including the kinetic energy of the electron, accelerating voltage, and the density of the specimen.(7)

SEM is also commonly performed in backscattered electron (BSE) mode. BSEs are not generated in the sample but are incident electrons which have been elastically scattered within the specimen and reach the detector to create an image. The number of backscattered electrons depends on the atomic number of the element from which they are ejected. The greater scattering of heavier elements produces brighter images, while lighter

elements produce darker images. BSE mode can therefore be used for contrast between areas of different chemical compositions.

SEM analysis was performed using two instruments. An FEI Quanta 650 SEM with accelerating voltages of 10 kV to 30 kV was used for imaging in Chapters 4-5. Prior to imaging, an incision was made along the length of each sample using a thin blade so that the cross section could be imaged for thickness measurements. For Chapters 6-8, SEM analysis was carried out using a Zeiss Supra 40 high resolution SEM at an accelerating voltage of 2 kV to 10 kV.

3.4.2. Transmission Electron Microscopy

Transmission electron microscopy (TEM) is used to elucidate the morphology of nanostructured materials which cannot be resolved using SEM. Rather than raster scanning the specimen surface, the beam penetrates through the specimen to create an image, which is magnified and focused onto an imaging plate. Acceleration voltages of the electron beams are in the range of 100 kV to 300 kV, providing resolution on the order of 3.9 to 1.3 pm, corresponding to wavelengths far smaller than a single atom.(8) High-resolution TEM images allow phase identification by revealing the spacings between atomic lattice fringes. Like SEM, TEM can be operated in several modes, such as conventional TEM imaging, scanning TEM (STEM) imaging, and diffraction.(9) Each provides a different kind of information based on the contrast which is detected. These contrasts include mass-thickness, atomic number, crystallographic structure, and orientation (diffraction). TEM can therefore generate a plethora of nanoscale and atomic scale information, revealing

surface topology, elemental composition, phase identification, crystallographic orientation, and bonding environment.

TEM analysis was conducted using a JEOL JEM-2100 TEM operating at 200 kV to investigate structural parameters at the nanoscale. Bright and dark-field TEM images, HRTEM images at atomic resolution and electron diffraction analysis were obtained and included in Chapters 6.

3.4.3. Electron Diffraction Spectroscopy

The direction of an electron beam incident on a specimen changes due to interactions with the atoms in the form of elastic scattering. These changes can be detected using TEM and a corresponding diffraction pattern created. While X-rays and neutrons are scattered based on electron density and atomic nuclei, respectively, electrons are scattered due to interactions with bots. Given the tiny size of electrons, their “wavelike” behaviour can be measured.

Electron diffraction patterns are a result of Fraunhofer (far-field) diffraction and are a map of the directions of the electron waves leaving the sample.(10) Favoured directions appear brightly as points of high intensity and other directions appear dark. For a single crystal, electron diffraction patterns appear as a series of dots, while for a polycrystalline material, such as the IOs examined in this work, the patterns are formed as a superposition of the individual patterns of each crystal, forming a series of concentric rings. Electron diffraction can therefore be used to evaluate crystallinity. Consequently, the crystallographic dimensions can be measured by calculating the spacings between the rings.

For the results presented in Chapter 6, the JEOL JEM-2100 TEM was operated in diffraction mode to generate electron diffraction information on the pure SnO_2 IOs and SnO_2-TiO_2 IO composites.

3.4.4. Optical Transmission Spectroscopy

PhC materials, such as the opals and IOs used in this work, demonstrate unique behaviour when exposed to light at optical wavelengths due to their periodicity. Each PhC has an optical fingerprint based on the dimensions of its lattice. If the incident light is on the same order as the lattice parameters of the crystal, a mixture of coherent Bragg diffraction and refraction results in the formation of the PBG (PBG).(11) Transmission spectroscopy can be used to probe this optical fingerprint and determine the nature of the PBG, along with any other optical interactions which may occur. An array of optical information can be extracted from transmission spectra and provide insight into the contributing phenomena.

In Chapters 4-5, transmission spectra were used extensively to evaluate the optical properties of opals and extract information about crystal structure using the Bragg-Snell law. Specific details can be found in 4.3.1, 4.3.3, and 5.3.1. The light source used for optical transmission measurements was a tungsten-halogen lamp with an operating wavelength range of 400-2200 nm, purchased from Thorlabs Inc.

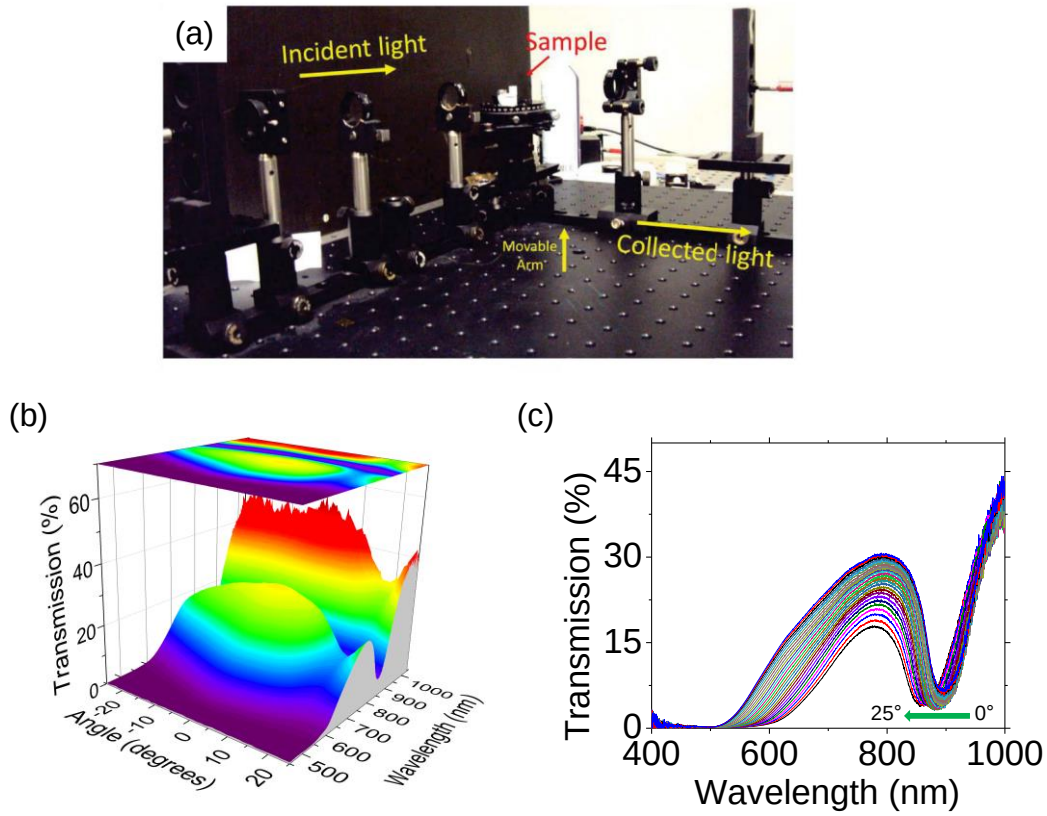


Figure 3.5. (a) Photograph of spectroscopy setup. (b) 3D angle-resolved transmission spectrum of an opal PhC. (c) Typical angle-resolved transmission spectra of opal PhC. Green arrow indicates blue shift of PBG as incident angle is increased from 0° to 25°.

Transmission measurements were recorded using an Ocean Optics UV-visible spectrometer (USB2000 + VIS-NIR-ES) with an operational range of 350-1000 nm and a Ocena Ocean NIR spectrometer (NIRQuest512-2.5) with an operational range of 900 nm to 2500 nm. Adjustments to the incidence angle for transmission measurements was enabled by a motorised rotational stage (ELL8; Thorlabs Inc.).

3.4.5. Raman Spectroscopy

For Raman active molecules, peaks appear according to the active Raman modes caused by the inelastic scattering of photons. The energy shifts caused

by interactions of the laser light with molecular vibrations, phonons and other excitations result in Raman shift. The magnitude of the Raman shift is correlated to the polarizability of the electrons in the molecule. Photons from the incident laser excites molecules into a virtual energy state before a photon is emitted. The inelastic nature of the scattering changes the rotational and/or vibrational energy state of the target specimen. The scattering of the emitted photons to lower and higher energy states correspond to Stokes and anti-Stokes shifts, respectively.

Phase changes can be detected based on the evolution of the peaks. There are four primary spectral evolutions which appear: Appearance of a new band, change in band profile, change in band intensity, and shift of vibrational mode.(12) Raman laser excitation wavelength influences Raman band intensity because the radiated power of an oscillating dipole I is related to the laser wavelength λ as $I \sim \lambda^{-4}$.(13) Choice of Raman laser excitation wavelength is a compromise between maximising signal to noise ratio (SNR) which is favoured by shorter wavelengths, and minimising fluorescence background such that masking of the Raman signal provided by the target specimen is prevented, which is favoured by longer wavelengths. Similarly, laser specific power is a balancing act between the reliable SNR provided at higher power and the avoidance of laser-induced sample transformations which is more likely at lower specific powers. Typical ranges used lie between 0.01 and 1 $mW/\mu m^2$.(14)

All Raman spectroscopy experiments were carried out using a Renishaw InVia Raman Spectrometer with a 30 mW Ar^+ laser at 532 nm

excitation with a laser power in the 2-30 mW range. The beam was focused using a 40x objective lens and collected using a RenCam CCD camera. Measurements obtained from conventional Raman spectroscopy of bare electrode materials are included in Chapter 6. The materials analysed were SnO_2 IOs with a mass of 0.2 to 0.7 mg on stainless steel disk substrate.

In Chapter 7, operando Raman spectroscopy measurements were performed using the spectroelectrochemical cell described in section 3.3.4 under the same laser conditions as the previous two chapters, except for a higher laser power of 50-60 mW to combat any attenuation of the beam by the components of the spectroelectrochemical cell. The electrode materials analysed were a TiO_2 IO on 10 mm stainless steel disk with a mass of 0.1-0.2 mg, nanoparticulate TiO_2 slurry with a mass of 0.2 – 0.3 mg on Cu mesh, and a commercial NMC622 slurry with a mass of 67.5 mg on Al foil. It is noteworthy here that the mass of the NMC622 electrode was markedly higher than the other electrodes used. For the TiO_2 IO, the macroporosity of the IO structure corresponds to a low filling factor which resulted in a relatively low mass per unit area. For the TiO_2 slurry, the gaps within the Cu mesh also resulted in low relative mass per unit area. For the NMC622 slurry, a uniform coating covered the entire area of the Al foil substrate. The electrolyte under Raman excitation was $LiPF_6$ in 1:1 EC:DMC in all three cases. Background subtraction was performed by creating a baseline for each spectrum using the 2^{nd} derivative function in OriginPro and subtracting from the raw spectra.

3.4.6. X-Ray Photoelectron Spectroscopy

X-Ray photoelectron spectroscopy (XPS) is a fundamental technique used for the quantitative analysis of elemental compositions and chemical states at the surface of a specimen, X-rays typically penetrate to a depth of 0.5-10 nm below the surface.(15) Spectra are obtained by irradiating the target material with X-rays and measuring the resulting electrons which are released due to the photoelectric effect with a specific kinetic energy that is later translated to binding energy.(16) The quantum character of the kinetic energy leads to an energy band distribution associated with the electronic structure of the atom. This ultimately allows identification of the elements present at the surface. Binding energy reveals two primary forms of information. First, elemental composition based on the close relationship between electronic structure and the number of protons in an atom. Second, oxidation states present, given that the binding energy is directly proportional to the oxidation state. Lower oxidation states cause shifts of core level spectra to higher kinetic energies. The resolution in terms of distinguishing between atoms of slightly different chemical shifts is limited primarily by linewidth and lifetime of the incident photon, along with the lifetime and width of the initial energy level.(17)

In Chapter 6, X-ray photoelectron spectroscopy (XPS) was performed using a Kratos AXIS ULTRA spectrometer with a detection limit of < 0.1 at %, ~1 mm^2 detection area, analysis depth of ~10 nm to determine the binding energies between the core electrons occurring in the SnO_2 IO material. Survey scans were recorded with a step size of 1.0 eV, dwell time of 50 ms, and pass energy of 160 eV and 20 eV for narrow spectral regions. Core level scans were

acquired with a step size of 0.05 eV, dwell time of 100 ms, and pass energy of 20 eV averaged over 10 scans with an analysis nominal area of ~220 μm^2. A non-monochromated Al Kα X-ray source at 300 W power was used for all scans. Data was processed using CasaXPS software where a Shirley background correction was employed, and peaks were fitted to Voigt profiles. Both Au 4f and C 1s were examined as references, with care taken to ensure that referencing to literature spectra and databases spectra (e.g. NIST XPS database) are consistent.

3.4.7. X-Ray Diffraction

X-ray diffraction (XRD) is useful for examining the crystalline structure of materials. Given the periodic structure of the components of crystalline material (atoms, ions or molecules), diffraction of scattered X-rays can occur. Interference of scattered X-rays is either constructive or destructive, and the detector only reads out a signal at angles at which constructive interference occurs. X-rays are scattered from different planes of the target specimen and each travel a different optical path length. The path length depends on the interplanar spacing d of the specimen and the angle θ of the incident X-ray beam. These are related to the wavelength λ of the incident X-ray beam by Bragg's law: $n\lambda = 2d\sin\theta$.

XRD can be performed using three primary scanning types based on the geometry of the goniometer. The goniometer is comprised of the sample holder, detector arm and associated gearing. The scan type is based on the movement of the elements of the goniometer, namely the sample holder and detector arm. The first is a 2θ scan, also known as glancing/grazing incident

XRD. Here, X-ray incident angle is fixed (<1 degree) and the detector scans over 2θ. The second type is θ:2θ Here, the sample is fixed, X-ray tube rotates at θ/min while the detector rotates at 2θ/min. The third type is ω:2θ and is used for measurements obtained in this thesis. Here, the detector scans at 2θ/min and the sample is tilted at ω/min.

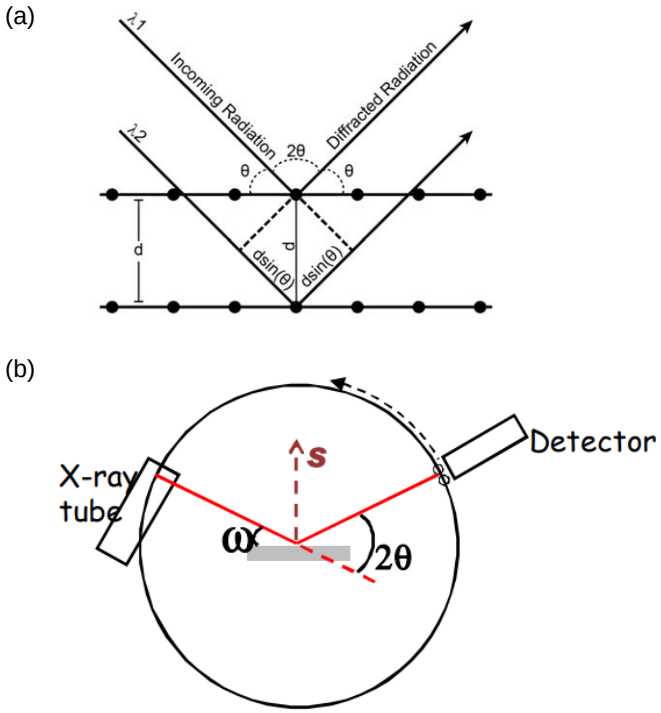


Figure 3.6. (a) Schematic depicting the concept of XRD which demonstrates the origin of Bragg's Law. (b) Schematic of typical XRD instrument setup that illlustrates the geometry of the goniometer, highlighting the sample tilt direction over angle ω and detector rotation direction over 2θ. s is the diffraction vector.

XRD spectra are presented as a series of lines formed due to the incident radiation generated by the anode of the diffractometer versus the angle of reflection (*2θ*). Cu is typically used as anode material and the corresponding series of lines are called K_α, corresponding to the transition from the 2p to 1s orbital, and K_β, corresponding to the transition between 3p and 1s orbital in Cu. All atoms have unique XRD spectra based on their *d*-

spacings and the crystallographic planes from which the X-rays are scattered. Matching the lines from each spectrum with spectra from an appropriate XRD database allows identification of the unknown crystalline specimen. In this work, all reference spectra were taken from the Joint Committee on Powder Diffraction Standards.

XRD measurements were performed using a PANalytical X'Pert PRO PW3050 diffractometer with a Cu anode, Kα radiation with wavelength λ = 0.15406 nm, operating voltage 40 kV, current 20 mA, fixed divergence slit of 0.38 mm in ω:2θ mode with scan resolutions for both ω and 2θ of 0.0001°, sample height (z displacement) of 9.142 mm. Specific details on the calculations performed using XRD measurements to determine crystallographic d-spacings can be found in section 6.2.2 of Chapter 6 for SnO_2 IOs.

3.5. Electrochemical Characterisation Methods

All electrochemical measurements were conducted using a multichannel BioLogic VSP Potentiostat/Galvanostat.

3.5.1. Cyclic Voltammetry

Cyclic voltammetry (CV) is a potentiodynamic technique used to detect the electrochemical mechanism of an electrode material over a given voltage range. CV reveals the potentials at which each redox reaction contributes to the current response and determines the reversibility of these reactions. Often, it is employed simply to test the stability of the cell prior to cycling. The

electrode potential is ramped with a linear potential sweep for the working electrode against a counter electrode as shown in Figure 3.7 (a).

A CV scan consists of a negative and positive linear sweep which are known as the cathodic and anodic scans, respectively. Reduction peaks are elucidated during the cathodic scan while oxidation peaks are obtained during the anodic scan as illustrated in Figure 3.7 (b). Peak potentials are helpful for determining the types of reaction which occurs. For battery systems that take advantage of multiple types of electron transfer, such as the conversion/alloying electrodes examined in Chapters 6, peak potential is particularly helpful in distinguishing the point at which each process occurs. The magnitudes of the associated peak currents are proportional to the scan rate. The relative peak currents from each reaction can be used to predict the relative contributions of each reaction to the capacity that will be delivered to the system during galvanostatic cycling. The schematic in Figure 3.7 (c) illustrates the detection of peak potentials and currents.

The key benefits of CV measurements arise from the role of scan rate, which is the rate of change of voltage with time (usually measured as mV s^{-1}). While perfectly reversible redox processes are independent of scan rate, quasi-reversible and irreversible processes are a function of scan rate. The differences in the CV response for each of the three processes are shown in Figure 3.7 (d). In battery systems, there is a polarisation overpotential and a voltage hysteresis (peak separation shift) is observed, and the associated reactions are not perfectly reversible. Voltage hysteresis intensifies with scan rate,(18) a fact that can be taken advantage of to analyse the reversibility of

the reactions which occur during each voltage sweep. The dependence of the peak currents for each redox reaction on scan rate can be expressed using the Randles-Sevcik equation.(19)

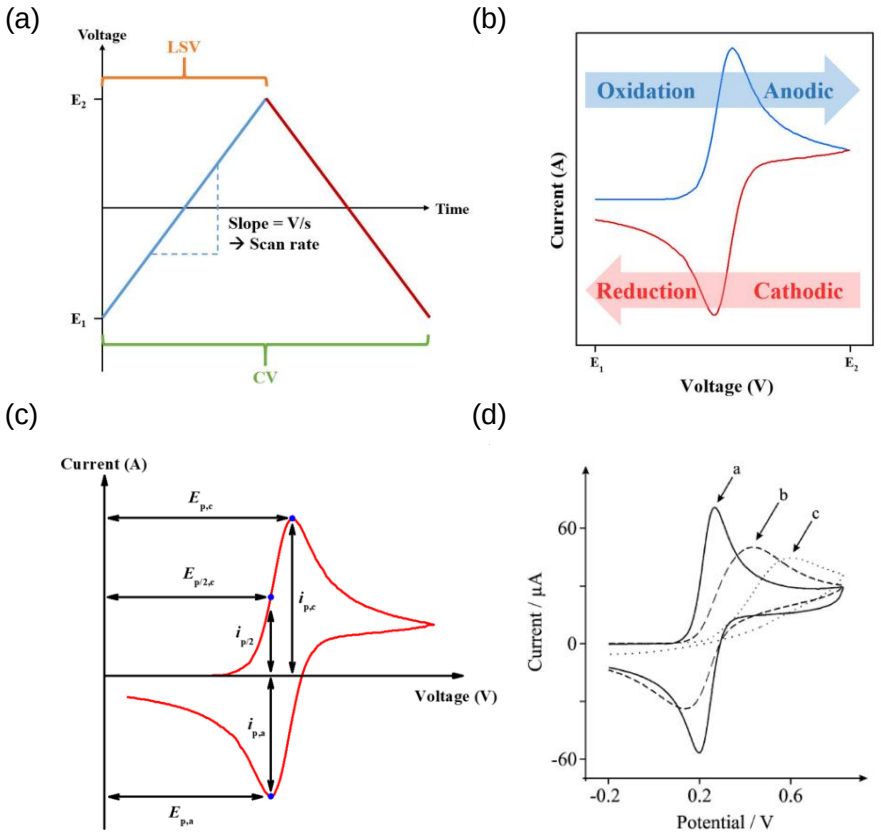


Figure 3.7. Schematics showing basic principles of cyclic voltammetry. (a) Voltage-time profile for linear sweep (LSV) and cyclic voltammetry (CV). (b Typical CV curve indicating oxidation and reduction directions. (c) CV curve highlighting the most informative points quantities, peak currents, and potentials. (d) Contrast of CV curves for different types of electron transfer: a – reversible, b – quasi-reversible and c – irreversible.(19)

For secondary (rechargeable) batteries, CV scans for cathode materials are typically initiated in the positive direction, due to their pre-lithiated nature while anode materials are typically scanned first in the negative direction. For Li-ion (Na-ion) batteries, lithiation (sodiation) occurs during the cathodic scan while delithiation (desodiation) occurs during the anodic scan.

CV measurements were performed in Chapters 6-7. In Chapter 6, fixed rate measurements were performed at 0.1 mV s^{-1}. CV response as a function of scan rate was also examined at each scan rate increasing incrementally from 0.05 mV s^{-1} to 5 mV s^{-1}. During scans, coin cells and PAT cells were operated as half cells, where Li metal and Na metal were used as coupled reference and counter electrodes for the Li-ion and Na-ion systems, respectively. The PAT cells were operated under temperature control, in a BINDER convection oven at 24 °C. In Chapter 6, the voltage range chosen was 0.01 V to 3 V, corresponding to the range where the redox reactions associated with SnO_2 occur, and is within the electrochemical stability window of the Li-ion and Na-ion electrolytes used, the details of which are provided in 6.2.3.

In Chapter 7, CV was performed using the spectroelectrochemical cell described in section 3.3.4 at scan rates of 0.05 mV s^{-1} and 0.1 mV s^{-1}. Low scan rates are typically used for operando Raman measurements, to cause a more uniform reaction between electrode and electrolyte throughout the active material and improve the probability that changes to Raman spectra will be detected. Potential ranges were from 1 V to 3 V for TiO_2, and 2.8 V to 4.3 V for NMC.

3.5.2. Galvanostatic Cycling

Galvanostatic cycling is the first tool used by a battery chemist to evaluate battery performance. The battery is charged and discharged at constant current over a specific voltage range for a certain number of cycles. The voltage window is chosen based on the electrochemical window, the potential

range in which the electrolyte is stable and neither oxidised nor reduced.(20) A plethora of electrochemical information can be extracted from the resulting data. The specific capacity of the battery is examined by constructing capacity-voltage profiles. Capacity retention is examined by plotting the maximum charge and discharge capacities as a function of cycle number. Coulombic efficiency can be evaluated by comparing the maximum discharge and charge capacities at each cycle. In a Li-ion battery, Coulombic efficiency is measured as the ratio of delithitation capacity to lithiation capacity. In a full-cell, Coulombic efficiency is calculated differently depending on whether the calculations are anode or cathode-based. For the anode, lithiation corresponds to the charge portion of the cycle. For the cathode, lithiation corresponds to the discharge portion of each cycle. For the half-cells, such as those employed throughout this thesis, the working electrode acts as cathode, and lithiation always corresponds to the discharge portion of each cycle. The same considerations apply for Coulombic efficiency calculation in Na-ion system related to sodiation and desodiation. Coulombic efficiency is highly dependent on the quality of the SEI layer.(21)

Rate capability testing involves galvanostatic cycling of a battery for a certain number of cycles for a range of applied currents. The applied current determines the rate of charge and discharge of the battery. Typically, a low specific current is applied for a chosen number of cycles and is then ramped up to successively higher specific currents for the same number of cycles at each one. Capacity retention typically decreases with each increase in rate and the tests evaluate the extent of this decrease. The last stage of a rate test

usually involves applying the initial low specific current of the first stage. Given that extensive structural and electrochemical changes occur throughout the rate testing, this last step examines the extent to which these changes have irreversibly degraded the performance of the system. This is particularly useful for systems in which significant electrode volume expansion occurs, which is the case for SnO_2.

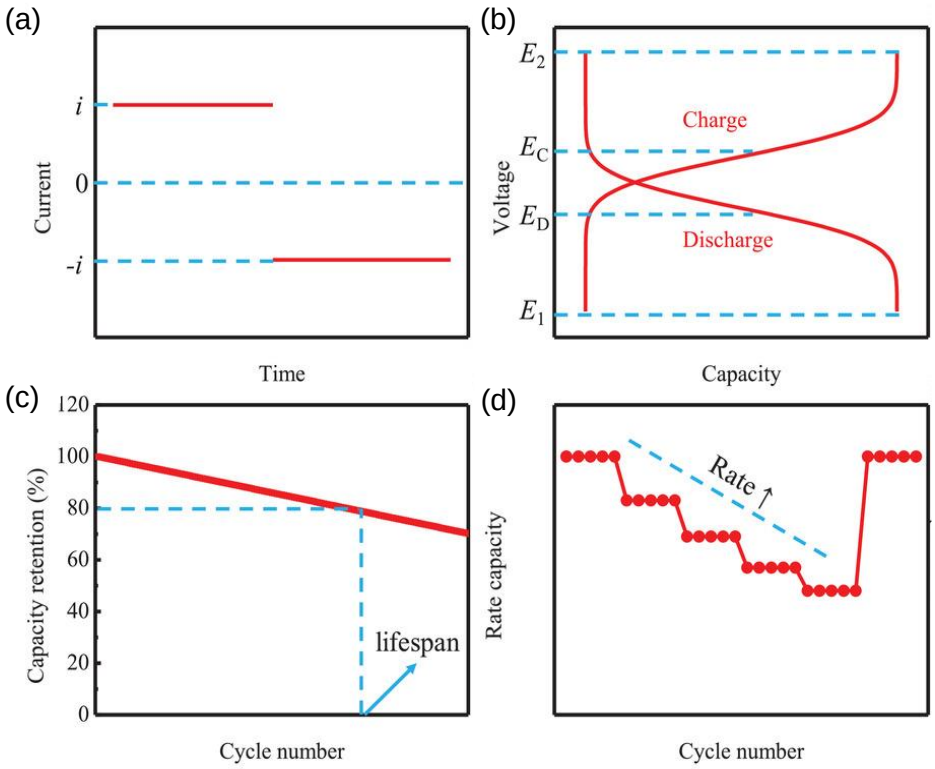


Figure 3.8. Schematics depicting results generated from typical galvanostatic cycling of batteries. (a) Applied current profile. (b) Charge-discharge curve showing voltage response vs capacity. (c) Cycling stability, capacity retention over battery lifetime. (d) Typical rate test showing change in capacity at each rate as a function of cycle number.(22)

In Chapter 6, the results from galvanostatic cycling of SnO_2 IO are shown in the form of charge-discharge curves, capacity-cycle profiles, and rate capability tests. Details on cell configurations were outlined in section 3.3. In

Chapter 7, the galvanostatic cycling results used in the operando Raman spectroscopy examination of several electrode materials and the associated electrolyte evolutions are demonstrated. The same representations of the data are used as the previous chapters, along with chronoamperometry. All galvanostatic results are used in tandem with the associated Raman spectra to correlate electrochemical responses to atomic-scale structural changes and electrolyte phase transitions. The electrode materials and cell configuration used were outlined in section 3.3.4.

3.5.3. Differential Capacity Analysis

Differential capacity plots (DCPs) are generated by the numerical differentiation of a galvanostatic cycling profile (voltage vs charge) as shown in Figure 3.9 (a). Direct differentiation results in a differential voltage (dV/dQ) plot as shown in Figure 3.9 (b). Discharge data is multiplied by -1 for visual clarity, as is the convention. DCPs (also referred to differential charge plots in the literature) are the reciprocal of differential voltage plots and can be obtained by transposing the axes of the galvanostatic cycling profiles (to charge vs voltage) and performing the differentiation. Figure 3.9 (c) shows a typical DCP, the reciprocal of Figure 3.9 (b) represented as voltage vs dQ/dV and is the representation used for all differential analysis included in this thesis. Once again, the differentiated discharge data is multiplied by -1, in line with the convention.

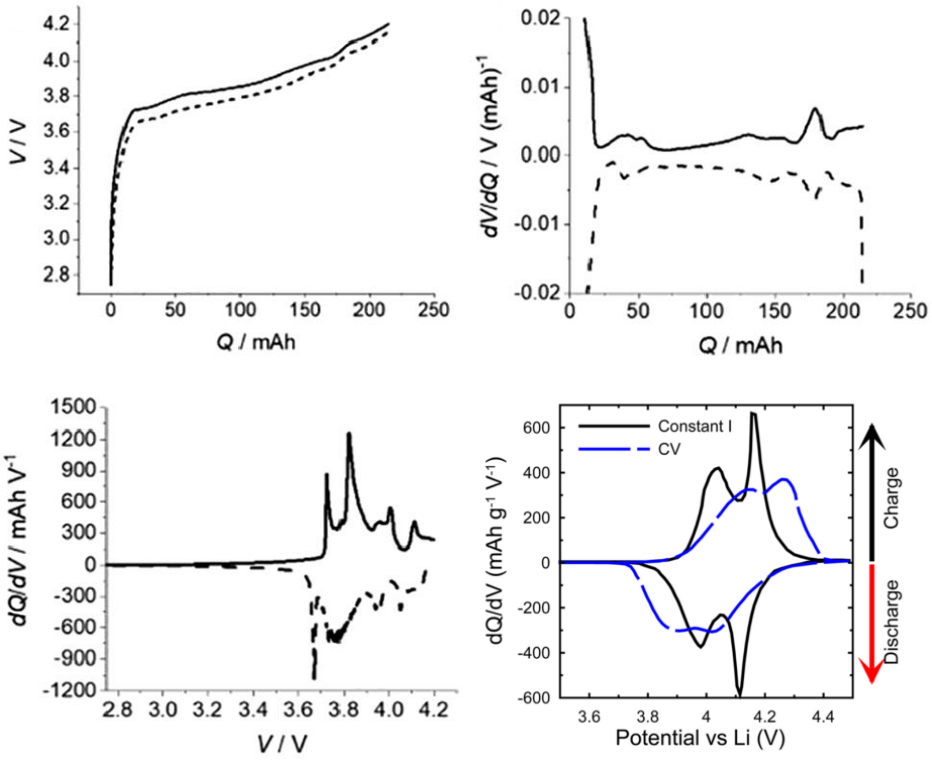


Figure 3.9. (a) Typical charge-discharge curve from galvanostatic cycling. (b) Differential voltage calculated as the first derivative of (a). (c) Differential capacity, calculated as the reciprocal of (b). (d) Comparison of typical differential capacity and cyclic voltammetry curves.(23)

In a charge storage material, the incremental charge dQ is passed from one electrode to another due to the incremental voltage change dV. In Li-ion and Na-ion batteries, as voltage changes charge is transferred by the transfer of mass into the electrode by insertion, conversion to a new material or alloying to form a new Li/Na compound. Each process results in a plateau in the charge-discharge curves. Similarly, phase changes during charge transfer process causes further plateaus which can appear as subtle inflections. The main benefit of DCPs is the conversion of these inflections to pronounced peaks and plateaus which are far more visually informative.

CV curves and DCPs are often used interchangeably, as much of the same information can be extracted from both, such as the relative voltage changes and current responses of the various redox processes which can occur. Figure 3.9 (d) illustrates the similarity between the two techniques. However, unlike CV, DCPs do not contain rate information.(24) In this thesis, half-cells are used in all cases, which is important given that there are several additional considerations required in performing differential analysis on full cells. Such as the fact that while the voltage of each electrode contributes linearly, the stored differential capacity does not.

In Chapter 6, DCPs are constructed from the differentiation of the galvanostatic cycling performed for rate capability testing of the SnO_2 IO anode in both Li-ion and Na-ion half cells. The differential capacities at a range of specific currents from 25 mA g^{-1} to 450 mA g^{-1} are examined for both chemistries.

3.6. References

1. A. Grant and C. O'Dwyer, *Applied Physics Reviews*, **10** (2023).
2. L. Meyer, N. Saqib and J. Porter, *Journal of The Electrochemical Society*, **168**, 090561 (2021).
3. A. J. Merryweather, Q. Jacquet, S. P. Emge, C. Schnedermann, A. Rao and C. P. Grey, *Nature Materials*, **21**, 1306 (2022).
4. A. J. Merryweather, C. Schnedermann, Q. Jacquet, C. P. Grey and A. Rao, *Nature*, **594**, 522 (2021).
5. W. Zhou, R. Apkarian, Z. L. Wang and D. Joy, in *Scanning Microscopy for Nanotechnology: Techniques and Applications*, W. Zhou and Z. L. Wang Editors, p. 1, Springer New York, New York, NY (2007).
6. K. de Haan, Z. S. Ballard, Y. Rivenson, Y. Wu and A. Ozcan, *Scientific Reports*, **9**, 12050 (2019).
7. B. J. Inkson, in *Materials Characterization Using Nondestructive Evaluation (NDE) Methods*, G. Hübschen, I. Altpeter, R. Tschuncky and H.-G. Herrmann Editors, p. 17, Woodhead Publishing (2016).
8. M. Winey, J. B. Meehl, E. T. O'Toole and J. Thomas H. Giddings, *Molecular Biology of the Cell*, **25**, 319 (2014).
9. M. Varela, A. R. Lupini, K. v. Benthem, A. Y. Borisevich, M. F. Chisholm, N. Shibata, E. Abe and S. J. Pennycook, *Annual Review of Materials Research*, **35**, 539 (2005).
10. M. Gemmi, E. Mugnaioli, T. E. Gorelik, U. Kolb, L. Palatinus, P. Boullay, S. Hovmöller and J. P. Abrahams, *ACS Central Science*, **5**, 1315 (2019).
11. J. D. Joannopoulos, S. G. Johnson, J. N. Winn and R. D. Meade, *Photonic Crystals: Molding the Flow of Light*, Princeton University Press (2008).
12. C. Julien and A. Mauger, *AIMS Materials Science*, **5**, 650 (2018).
13. D. Chen, X. Xiong, B. Zhao, M. A. Mahmoud, M. A. El-Sayed and M. Liu, *Advanced Science*, **3**, 1500433 (2016).
14. E. Flores, P. Novák and E. J. Berg, *Frontiers in Energy Research*, **6** (2018).
15. F. A. Stevie and C. L. Donley, *Journal of Vacuum Science & Technology A*, **38** (2020).
16. C. S. Fadley, *Journal of Electron Spectroscopy and Related Phenomena*, **178-179**, 2 (2010).
17. M. C. Biesinger, C. Brown, J. R. Mycroft, R. D. Davidson and N. S. McIntyre, *Surface and Interface Analysis*, **36**, 1550 (2004).
18. X. Pu, D. Zhao, C. Fu, Z. Chen, S. Cao, C. Wang and Y. Cao, *Angewandte Chemie International Edition*, **60**, 21310 (2021).
19. T. Kim, W. Choi, H.-C. Shin, J.-Y. Choi, J. M. Kim, M.-S. Park and W.-S. Yoon, *J. Electrochem. Sci. Technol*, **11**, 14 (2020).
20. C. F. N. Marchiori, R. P. Carvalho, M. Ebadi, D. Brandell and C. M. Araujo, *Chemistry of Materials*, **32**, 7237 (2020).
21. A. J. Smith, J. C. Burns and J. R. Dahn, *Electrochemical and Solid-State Letters*, **13**, A177 (2010).
22. X. Yang and A. L. Rogach, *Advanced Energy Materials*, **9**, 1900747 (2019).

23. J. Z. Olson, C. M. López and E. J. F. Dickinson, *Chemistry of Materials*, **35**, 1487 (2023).
24. M. S. Palagonia, C. Erinmwingbovo, D. Brogioli and F. La Mantia, *Journal of Electroanalytical Chemistry*, **847**, 113170 (2019).

Chapter 4

Thickness Control of Dispersion in Opal PhCs

Adapted from: A. Grant, A. Lonergan and C. O'Dwyer, Thickness control of dispersion in opal photonic crystals, Optical Materials, 142, 114053 (2023). DOI: 10.1016/j.optmat.2023.114053.

Abstract

Opals are naturally occurring PhCs which can be formed easily using low-cost self-assembly methods. While the optical behaviour of opals has received significant attention for several decades, there is limited information on the effect of crystal thickness on the optical properties they display. Here, the relationship between volume fraction and crystal thickness is established with an evaporation-induced self-assembly (EISA) method of formation. The extent to which thickness can be used to manipulate the optical properties of the crystals is explored, focusing on the change in the PBG. Microscopical structural characterisation and angle-resolved transmission spectroscopy are used to examine the quality of the PhCs formed using different volume fractions of PS spheres, with thicknesses up to 37 layers grown from volume fractions of 0.125%. This work provides a direct correlation between sphere solution volume fraction and crystal thickness, and the associated optical fingerprint of opal PhCs. Maximum thickness is examined, which is shown to converge to a narrow range over several evaporation rates. We identify the criteria required to achieve thickness control in relatively fast evaporation induced self-assembly while maintaining structural quality, and the change to the spectroscopic signature of the (111) stopband and higher order (220) reflections, under conditions where less ordered PhCs are formed.

4.1 Introduction

For researchers interested in perfecting colloidal crystal growth, maximising structural quality requires optimisation of an array of environmental conditions.(1-6) Bottom-up self-assembly methods such as dip coating,(7) spin coating,(8) Langmuir Blodgett deposition,(9) electromagnetic-induced self-assembly,(10) and evaporation-induced self-assembly (EISA) are simple and cost effective, but difficult to control due to their spontaneous nature. As has been demonstrated, colloidal crystal films involving silica or polymeric spheres as opal, suffer from localised regions of disorder, layer-on-layer registry changes that affect long range order, and cracking from various forces during drying. There have been attempts to control these issues recently.(11-13)

There have been approaches that allow 2D colloidal crystals to form from a single layer of spheres, showing diffraction grating reflection characteristics.(14) More recently, 2D colloidal crystal and opals were shown to be transferred to more useful (and often complex or problematic substrates) by capillary transfer to give very high quality coatings useful for application.(15) A key advantage of many of these approaches is fast growth of potentially ultra-thick colloidal crystals, or the formation of functional films with required or useful optical properties, on substrates that are best for the application. The requirements for high crystal quality are now well established, directed primarily by the appropriate sample volume fraction, evaporation rate, and electrostatic compatibility between sample and substrate. However, some key

questions remain. Under what conditions and to what extent can crystal thickness be directed while maintaining overall structural quality?

Knowing the factors that influence colloidal crystal growth of opal PhCs from relatively simple solution-based evaporation methods is important.(16) These amenable PhCs are well known to manipulate photons, like the manipulation of electrons by the atomic lattice.(17-19) Consisting of periodic dielectric material, the structure can be designed to inhibit light propagation in specific directions, providing the ability to tune the frequencies which are allowed to propagate, with a range of potential applications in fields such as optics and optoelectronics,(20) energy storage,(21, 22) and sensors for environmental monitoring, biomedicine and food preservation.(23) A PhC can also be designed such that light propagation is inhibited in all directions at specific frequencies, and crystal or film quality is important here, to minimise scattering and dispersion losses, for example. The omnidirectional PBG (PBG) of a 3D PhC is derived from Maxwell's equations.(24)

Perfectly ordered self-assembled opals can be constructed entirely by repetition of the face-centered cubic (FCC) unit cell, the most thermodynamically favourable packing arrangement of crystalline spheres.(25) For an ideal opal, the FCC unit cell is repeated with the spheres stacked in the direction normal to the lattice plane described by the miller indices (111).(26, 27) The wavelength-dependent structural colour observed in opals can be approximated well by the Bragg-Snell law that results from an extension of the dispersion relations.(28)

Despite a tendency towards (111) FCC stacking during opal self-assembly, defective areas are inevitable. Stacking faults are most common, and usually occur in the (100) crystallographic direction. Surface SEM images can be used to distinguish between the two stacking arrangements. Planes corresponding to the (111) and (100) directions are observed as hexagonal and square patterns, respectively. A host of other stacking arrangements are possible, but more difficult to detect.(29) In optical transmission spectra, (111) stacking arrangements are observed as the primary transmission dip constituting the PBG of the opal. Stacking faults such as in the (100) direction occur as transmission dips with a significantly lower depth relative to the PBG towards the higher energy region of the spectrum.

Forms of disorder which significantly affect the optical spectra of opals include grain boundaries, defects, and dislocations of unit cells and polydispersity. These processes lead to a range of scattering regimes, each of which impacts the intensity profile of the optical spectra depending on the frequency range under consideration.(30) While there is very often a statistically quantifiable average variance in sphere diameter, the standard deviation must be minimal to prevent destruction of the spectral shape of the PBG in a high-quality colloidal opal film as it has been shown that polydispersity and displacements of unit cells determine scattering loss in 3D PhCs.(31) Such deviations from perfect periodicity cause exponential attenuation of the coherent beams, the propagation of which generate the PBG. The attenuation affects the mean free path, also known as the extinction length. After propagation over this length the coherent light beams are

converted to a diffuse glow which impacts the associated optical spectra and prevents the application of such materials in any photonic integrated circuit.(32) It is instructive to know how the factors of the growth such as colloid concentration, bath temperature and thus the crystallization or evaporation rate, and final thickness, affect degree of order.

We use EISA to study the spectroscopic signature of the PBG in opals films. Both order and thickness can be controlled primarily by the sphere solution volume fraction and evaporation rate. Previous research indicates that faster evaporation rates can result in earlier onset crystallisation, which causes a more disordered surface structure.(33) On the other hand, higher kinetic energy provided at these faster rates mean that the spheres can explore more favourable lattice sites, leading to a greater overall tendency towards FCC packing. Maximal crystal quality and thickness control is achieved through the selection of the optimal evaporation rate and volume fraction combination.

Here, we establish the relationship between volume fraction and opal thickness at three evaporation rates formed using EISA. In tandem with electron microscopy, we characterize the degree of order in successively thicker films up to 37 layers by examining the modification to dispersion using angle-resolved transmission spectra with Bragg-Snell analysis. Lastly, the assembly conditions under which the crystals can no longer be characterised using traditional Bragg-Snell analysis applied to the PBG are identified.

4.2. Experimental

4.2.1. Materials and Substrate Preparation

Colloidal solutions of PS spheres in 2.5 % (w/v) aqueous suspension with diameters of 370 nm and 500 nm were purchased from Polysciences Inc. The sphere suspension possessed a net negative charge due to functionalization using a sulfate ester during formation to aid in self-assembly. The substrates used were fluorine-doped tin oxide (FTO)-coated soda-lime glass purchased from Solaronix SA. Glass of thickness 2.2 mm was cut into pieces with dimensions 10 × 25 mm^2. The conductive layer of the pieces consisted of a thin FTO layer followed by a thin SiO_2 layer (each layer ~20 nm) followed by a thicker FTO layer (~300 nm). The conductive layer rested upon a glass substrate. All substrates were cleaned using the same process: Successive sonication in acetone (reagent grade 99.5%; Sigma Aldrich), isopropyl alcohol (reagent grade 99.5%; Sigma Aldrich) and de-ionized water, each for 5 minutes. All cleaned samples were dried at room temperature in an inert atmosphere. Kapton tape was used to cover the back of the substrate and partially cover the surface of the substrate such that an exposed surface of 10 × 10 mm^2 remained. This ensured colloidal crystal formation occurred only on the desired surface area. The samples were treated in a Novascan PSD Pro Series digital UV-ozone system for 1 h to maximise hydrophilicity of the surface of the substrates immediately prior to PhC formation.

4.2.2. Evaporation-Induced Self-Assembly

Opals were formed using EISA. FTO glass substrates were immersed in a diluted PS sphere solution with volume fractions in the range of 0.025% to 0.125 % which were placed on a hot plate at a constant temperature between 28 °C and 34 °C. Once the sphere solution was evaporated fully, the substrates were removed and left to dry in inert atmosphere at room temperature. To ensure consistent EISA of the colloidal films at a well-defined angle, we used Vat polymerisation 3D printing to create beakers that were formed from photopolymerised poly(methyl methacrylate)-based resin using a Formlabs Form 2 stereolithography printer. Further details are provided in the Supplementary material, Figure S4.1. All beakers were cleaned using the same sonication process described above, followed by UV-ozone treatment for 1 h. The diameter of each beaker was 6 cm and substrate rests were positioned at an angle of 30 ° to the beaker walls.

4.2.3. Microscopy and Spectroscopy

All microscopy was performed using a FEI Quanta 650 SEM at accelerating voltages of 10 kV to 30 kV. Prior to imaging, an incision was made along the length of each sample using a thin blade so that the cross-section could be imaged for thickness measurements and were then sputtered using an ATC Orion–5–UHV sputtering system to increase conductivity and improve grounding of the sample. Gold coating on non-conductive PS spheres was carried out using a Quorum 150T S magnetron sputtering system. Sputtering samples reduced charging effects, namely electron diffusion and beam drift,(34) allowing better contrast and feature definition. For a thickness line

measurement L, the actual thickness is calculated according to $T = L/\cos(45°) = L\sqrt{2}$. Thickness measurements were enabled by tilting the stage on which the sample lay parallel to the surface at an angle of 45°. For each sample, several thickness measurements were obtained and the mean values in each case used as data points to establish the volume fraction-thickness relationship.

Angle-resolved transmission spectra were used to characterise colloidal opal films. The light source was a tungsten-halogen lamp with an operating wavelength range of 400–2200 nm. Transmission measurements were recorded using a UV-visible spectrometer (USB2000 + VIS-NIR-ES) with an operational range of 350–1000 nm and a NIR spectrometer (NIRQuest512-2.5) with an operational range of 900 nm to 2500 nm, both from Ocean Optics Inc. Adjustments to the incident angle for transmission measurements was enabled by a motorized rotational stage (ELL8; Thorlabs Inc.).

4.3. Results and Discussion

4.3.1. Volume Fraction-Thickness Relationship

Several colloidal opal films were grown using the EISA method in a range of sphere solutions and at several temperatures. The relationship between sphere solution volume fraction and opal thickness is shown in Figure 4.1 (a) for the three temperatures investigated. The evaporation times were approximately 24 h, 36 h, and 48 h for temperatures of 34°C, 31 °C, and 28 °C, respectively. The cross-sectional SEM images used for all thickness measurements are shown in Figure S4.2.

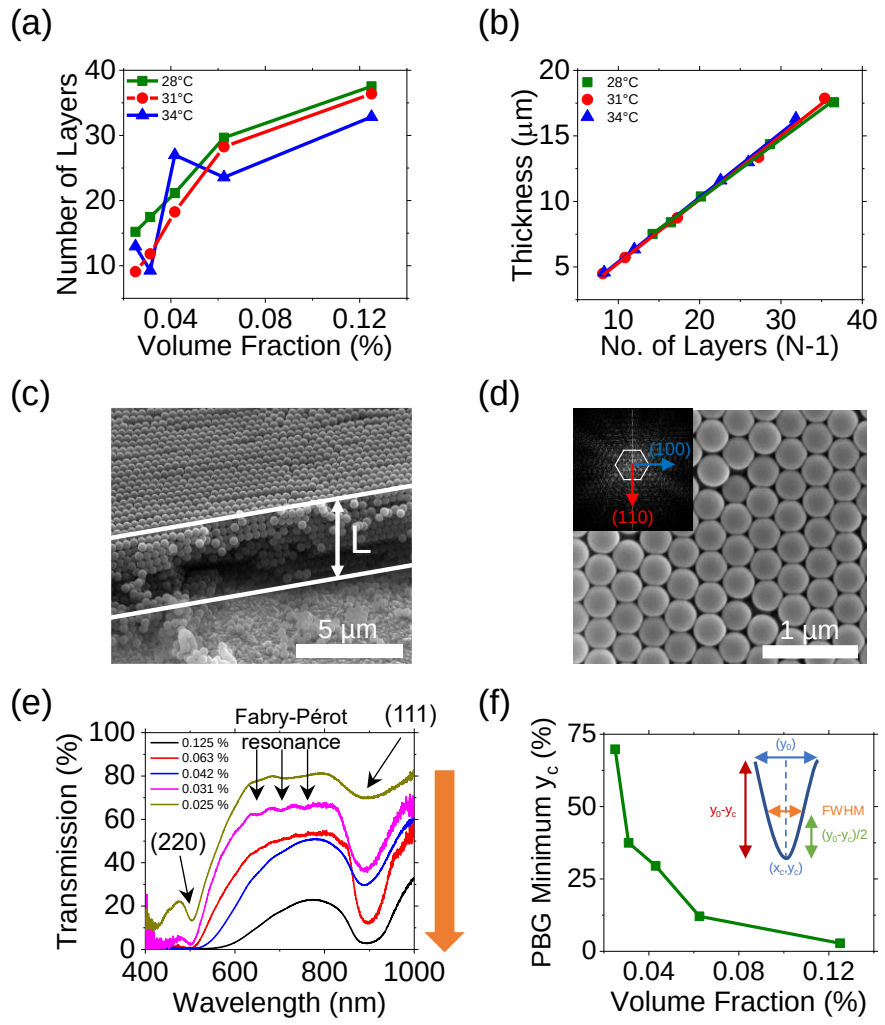


Figure 4.1. (a) Volume fraction-thickness relationship for opals grown from PS sphere solutions of five volume fractions at three evaporation temperatures. (b) Number of opal layers calculated using Eq. 4.1 as a function of measured sample thickness for samples formed under all investigated conditions. (c) Cross-sectional SEM image of representative opal demonstrating thickness measurement. (d) Plan view SEM image of surface of an opal grown from a volume fraction of 0.125 % at 28 °C. Inset: FFT with 2D hexagonal symmetry, the (100) and (110) directions labelled corresponding to the Γ-X and Γ-L directions of a 2D hexagonal lattice. (e) Transmission spectra obtained at normal incidence for opals grown from all five volume fractions at 28 °C. (f) Transmission intensity at the PBG centre as a function of volume fraction for all opals grown at 28 °C . Inset: Schematic illustrating the defining parameters of spectral transmission dips.

At all three temperatures, large crystal thicknesses for each volume fraction are achieved relative to those observed in the literature. In general,

slower evaporation rates provide time for the self-assembly process and stacking of layers to continue at each point along the direction of evaporation flux. Excluding two outlier cases, the two lowest volume fractions grown at 34 °C, crystal thickness for each volume fraction at a given temperature is larger than the equivalent volume fraction at a higher temperature. Measured opal thicknesses range from a minimum of ~4.5 μm (9 layers) to a maximum of ~17.9 μm (37 layers). The investigated temperature range is narrow at only 6 °C, yet the evaporation time of the assembly process at the lowest temperature of 28 °C is twice that at the highest of 34 °C. A relatively small change in temperature significantly affects the speed of colloidal self-assembly for the system used here.

For the majority of EISA experiments found in the literature, small sphere solution surface areas are incorporated to minimise convective air flow and allow slow evaporation rates at higher temperatures of 60 – 80 °C.(35, 36) In our experiments evaporation occurs over relatively large solution surface areas. Given that molecules contained in a liquid evaporate at the gas-liquid interface,(37) evaporation rate is proportional to the exposed surface area of the solution during the assembly process. To provide context, in one study, the EISA process was performed at 65 °C over a period of 1-2 days. In our experiments, the EISA process was performed at 28-34 °C over 1-2 days. Crystal growth occurs at a significantly lower temperature. The comparatively large surface area is helpful to both crystal quality and thickness. The result of our methodology is the assembly of multi-layered crystals of large thicknesses up to 37 layers for comparatively low volume fractions relative to the literature

with a high level of order above a minimum evaporation rate and volume fraction combination.(38, 39)

While a general increase in thickness as a function of volume fraction is observed for each temperature, the increase is not linear (Figure 4.1(a)). The height, *h* of an opal sphere stack can alternatively be estimated using a simple geometric approach such as

$$h = D + (N-1)\sqrt{\frac{3}{2}}D \tag{4.1}$$

where *D* is the PS sphere diameter and *N* is the number of opal layers. Figure 4.1 (b) shows a scatter plot of measured thickness as a function of *N-1*, calculated using Eq. 4.1 for all films grown for each sphere solution volume fraction at each of the three evaporation temperatures. The lines correspond to the line of best fit for each dataset. Comparison of the parameters obtained from the line of best fit in tandem with Eq. 4.1 with measured experimental data determines the accuracy of the approach in predicting crystal thickness and sphere diameter. Based on Eq. 4.1, the *y*-axis intercept from each line of best fit can be approximated as the average opal sphere diameter D. The slope of the line approximates the interplanar spacing $d = \sqrt{\frac{3}{2}}D$ of the opals based on FCC stacking in the [111] direction, a stacking arrangement that is proven dominant based on the Bragg-Snell analysis of spectral data provided in Figure S4.3.

Calculations of average sphere diameter *D* and average interplanar spacing *d* at each evaporation temperature using Eq. 4.1 were performed. The

calculated and corresponding experimentally measured values are included in Table S4.1. For the interplanar spacing *d* at the higher two evaporation temperatures, there is clear agreement, with a relative difference of less than 1% between measured and values calculated from the slope of the lines of best fit. For the lowest evaporation temperature, there is a relative difference of 6 %. For the average sphere diameter *D*, the relative difference between experimental measurements and calculations using the *y* intercepts of the lines of best fit in order from highest to lowest evaporation temperature is 11%, 10%, and 163%. For the higher two temperatures the approximation is relatively accurate. For the lowest temperature, the approximation is completely inaccurate. The accuracy of the approximation of sphere diameter D using the y intercept of Eq. 4.1 can be further analysed by an examination of the practical considerations of each value. In Eq. 4.1, the quantity *N* corresponds to the number of opal layers. The *y* axis in Figure 4.1 (b) corresponds to (*N* - 1). Therefore, at the *y* intercept where *N* - 1 = 0, *N* = 1 opal layer. Practically, 1 opal layer should be equal to the opal sphere diameter. For the two higher evaporation temperature datasets, the approximations are practically realistic to approximately 10% of the measured average sphere diameter. For the lowest temperature, applying Eq. 4.1 to the linear fit in Figure 4.1 (b) is inaccurate and this approach is not applicable. The inaccuracy of the data corresponding to the highest evaporation temperature in Figure 4.1 (b) can be attributed to the two outlier points corresponding to the two lowest volume fractions which indicates this evaporation rate is too fast to achieve thickness control below a volume fraction of 0.063%.

In Figure 4.1 (c), a cross-sectional SEM image of a representative opal sample is shown, illustrating the approach used to obtain thickness measurements. A plan view SEM image of another representative opal is provided in Figure 4.1 (d), demonstrating the order at the surface of the sample. The inset shows the corresponding FFT image, emphasising the hexagonal surface symmetry. The [100] and [110] directions are highlighted, given that opal layer growth occurs perpendicular to the (111) plane of an FCC lattice.

Optical transmission spectra for opals grown from all five volume fractions at an evaporation temperature of 28 °C and an incident angle range of 0–25 ° are shown in Figure 4.1 (e). The primary transmission dip formed from light interaction with the (111) FCC lattice plane is observed in each case, corresponding to the PBG of each opal. As will be discussed later, opals grown at higher volume fraction show a stronger transmission suppression at ~500 nm corresponding to the (220) planes of the PhC.(40)

While stacking faults along the (111) direction are the most common defects in artificial opals, the optical properties are unaffected at low energies such as those close to the PBG. Disorder in the form of grain boundaries, point defects, and dislocations affect the optical properties in two ways depending on whether the considered spectral region lies outside the PBG, or is contained within. Outside the PBG, light propagation becomes diffuse in a cone around the zero order beam.(41) Such diffuse scattering is observed here in the form of Fabry-Perot resonances close to the blue edge of the PBG at the three lower volume fractions, but is suppressed for the two highest.

Inside the stopband region, there is an interplay between the coherent Bragg scattering which forms the stopband and incoherent diffuse scattering which leads to enhanced diffuse intensity for frequencies near the edges of the stopband. This enhanced diffuse intensity at the stopband edges degrades the amplitude of the transmission dip and is observed in optical spectra as attenuation of the PBG. Examination of stopband attenuation for crystals of equivalent thickness can be used to indicate the magnitude of diffuse scattering. Here, the optical spectra are presented for a range of different thicknesses, so other scattering regimes must be considered when interpreting the evolution of the optical spectra.

Figure 4.1 (f) shows the measured transmission intensity y_c at the central frequency x_c at normal incidence of the PBG for opals grown at an evaporation temperature of 28 °C as a function of sphere solution volume fraction. An exponential decay in y_c as a function of volume fraction (and thereby thickness) occurs. While order is sufficiently high for each of the corresponding opals such that the PBG is preserved, each additional layer of spheres enhances scattering, which reduces the intensity of transmitted light resulting in a reduction of the PBG minimum y_c. Data for opals formed at 31 °C and 34 °C are shown in the supplementary material, Figure S4.1. The full optical transmission spectra under all investigated conditions are provided in the supplementary material, Figure S4.4.

The opals examined here can be considered periodic-on-average, based on the SEM imaging and Bragg-Snell analysis performed. The optical spectra of such crystals can be interpreted as the result of four primary

mechanisms – Anderson localisation, absorption, incoherent diffuse scattering, and Bragg diffraction.(42) The effective refractive index of the opals grown here can be approximated using the Drude model based on a two-material system of PS spheres and air in an FCC geometry, resulting in n_{eff} = 1.46. Anderson localisation typically requires a much higher refractive index contrast to cause complete localisation and any significant impact on the optical properties are unlikely here.(43) Absorption in the considered spectral range for PS can be considered negligible. Therefore, the remaining considerations are coherent Bragg scattering and incoherent diffuse scattering.

For a system with a low refractive index contrast such as artificial opals, it is the (111) close-packed layers of the FCC lattice which provide the greatest contribution to the observed diffraction in the form of the PBG. While decay in transmission intensity occurs with thickness, attenuation of the corresponding stopband, is expected to be enhanced with thickness due to an increase in diffuse scattering. Simultaneously, an increase in the effect of the Bragg diffraction regime is expected with thickness, acting to enhance the depth of the PBG. In the spectra, the PBG attenuation fluctuates while intensity at the stopband center (y_c) decreases exponentially. Nevertheless, the central wavelength of the PBG (x_c) sees little change between spectra at all investigated thicknesses, indicating that the crystals possess a low concentration of disordered sites. The trade-off between coherent Bragg diffraction and incoherent diffuse scattering is therefore the defining factor in the optical properties observed. While diffuse scattering is particularly evident

near the blue edge of the PBG, where Fabry-Perot resonances are present, coherent Bragg diffraction occurs in a sufficient vein that the PBG retains its spectral shape.

For a perfectly periodic system, the optical spectra are expected to evolve with thickness as an attenuation of the stopband which is formed by coherent Bragg diffraction, while frequencies outside the stopband remain close to the incident value.(44) Here, the spectra evolve such that an increase in the diffuse scattering background due to thickness-induced disorder attenuates transmitted intensity at all frequencies, while the disorder is sufficiently low that the Bragg diffraction regime remains dominant, evident in the integrity of the spectral shape of the PBG at all thicknesses.

4.3.2. Opal Thickness Control

Formation of opal PhCs where the thickness can be controlled is particularly useful when it is to be used as a template for IO formation and the myriad of applications stemming from those structures. Applications based on the opals themselves also require good control of film formation, especially for rapid crystallisation and recent efforts have shown that higher concentrations of sphere solutions are required for fast, high quality film formation during the drying phase.(45) Past works have examined the relationship between colloidal crystal thickness and volume fraction during vertical self-assembly.(46, 47) However, a detailed examination of the maximum thickness which can be achieved by these methods, and the conditions under which these thicknesses can be achieved is needed.

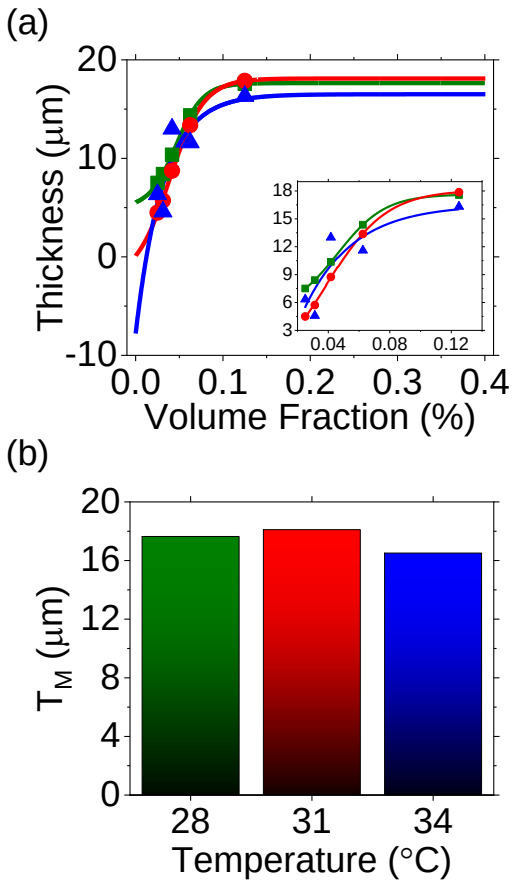


Figure 4.2. (a) Thickness volume fraction relationship for each evaporation temperature with sigmoidal Boltzmann fit function applied to an extended volume fraction range of 0 – 0.4%. Inset: Boltzmann function applied to volume fraction range of 0.025 – 0.125% as per experimental measurements. (b) Maximum thickness T_M for opals grown at each evaporation temperature based on the Boltzmann function.

In Figure 4.2 (a), results from the investigations of opal thickness as a function of volume fraction at each evaporation temperature are shown. The values are fitted with the sigmoidal Boltzmann growth function

$$y = \frac{A_1 - A_2}{1 + e^{\frac{x - x_0}{dx}}} + A_2 \tag{4.2}$$

where y is overall opal thickness, A_1 and A_2 are opal thickness minimum and maximum values, respectively, x is sphere solution volume fraction, x_0 is sphere solution volume fraction at $(A_1 + A_2)/2$, and dx is volume fraction interval

constant. The domain of the fit is extended beyond the experimental volume fraction range to 0 – 0.4% to predict the observed thicknesses at very low volume fractions, and maximum thicknesses at high volume fractions. While we observe some scatter in the change in overall thickness at 34 °C owing to the formation of more defective layers in the opal stack at faster evaporation rates, the data indicate a cut-off thickness of ~18 μm for samples grown at each rate, using nominally 370 nm PS spheres over the investigated volume fraction range. At temperatures below 34 °C where the fit is well-behaved, the trend indicates that the colloidal crystal formation occurs sufficiently fast at a solution volume fraction of 0.125% to limit film thickening beyond 37 layers of spheres. Practically, at a volume fraction of 0%, crystal thickness must be zero. For the median evaporation temperature of 31 °C, crystal thickness at 0% from the fit is 0.11 μm and less than the thickness of a single sphere, indicating that the asymmetric sigmoidal function is a reasonably good fit. For the other two temperatures, the fit is far from zero at low volume fractions. In all three cases, the plateau of the fit is very close to the experimentally observed maximum.

For opals grown by EISA, thickness is affected by a myriad of conditions including meniscus shape, substrate tilt angle, relative humidity, and sphere size. However, the two most dominant contributing factors are volume fraction and evaporation rate. For the experiments reported here, the maximum volume fraction of 0.125% was chosen at all three evaporation rates since a breakdown in the self-assembly process was observed for higher volume fractions. In Figure 4.2 (b), the maximum thickness (T_M) at each evaporation rate based on the sigmoidal Boltzmann fits are shown. The largest thickness

is observed at the median temperature of 31 °C, which appears to correspond to the optimal evaporation rate for maximising thickness while maintaining crystal order at a particular volume fraction. The minimum occurs at the highest temperature of 34 °C. This is the expected result, given that it corresponds to the fastest evaporation rate. For the slowest evaporation rate at a temperature of 28 °C, the sigmoidal fit is good at median to high volume fractions. A deviation from the expected thickness at low volume fractions is expected based on the deviation of the corresponding data from the expected crystal order based on the Bragg-Snell model, which is discussed in the subsequent section. The relatively large magnitude of the T_M values relative to the literature can be attributed to the experimental growth conditions, particularly the employment of the large sphere solution surface areas which allow the use of lower evaporation temperature that result in a more stable assembly process.

4.3.3. Accuracy of Bragg-Snell Model Under Investigated Conditions

For highly ordered opals, the reflected wavelengths can be approximated using the Bragg-Snell model. The extent to which each opal obeys the model can be determined using Bragg-Snell plots based on the corresponding angle-resolved transmission spectra. Each plot can be constructed using

$$\lambda_{\mathrm{hkl}}^2 = \frac{4d_{\mathrm{hkl}}^2}{m^2} n_{\mathrm{eff}}^2 - \frac{4d_{\mathrm{hkl}}^2}{m^2} \sin^2 \theta \tag{4.3}$$

where λ_{hkl} represents the central wavelength of the (111) transmission dip, which constitutes the PBG. The extent to which each plot can be approximated by a linear fit indicates the accuracy of the model.

Figure 4.3 (a) depicts the agreement between measured average sphere diameter D_{meas} and the sphere diameter calculated using Eq. 4.3 for opals grown under all five volume fractions at each evaporation temperature. The difference for each set of conditions is plotted as a function of the adjusted R^2 value of the associated Bragg-Snell plots. From examination of the figure, the data can be split into two distinct groups. The first are grouped closely together, with a minimum adjusted R^2 value of 0.98 and maximum difference $|D_{\mathrm{meas}} - D_{\mathrm{BS}}|$ of 52 nm, representing a relative difference based on the average sphere diameter for opals grown under all investigated conditions $\Delta D = |D_{\mathrm{meas}} - D_{\mathrm{BS}}|/D_{\mathrm{avg}}$ of ~13 %. Measured values are in close agreement with those calculated, demonstrating the accuracy of Eq. 4.3 to model the structure of all opals grown, and the high level of order they possess.

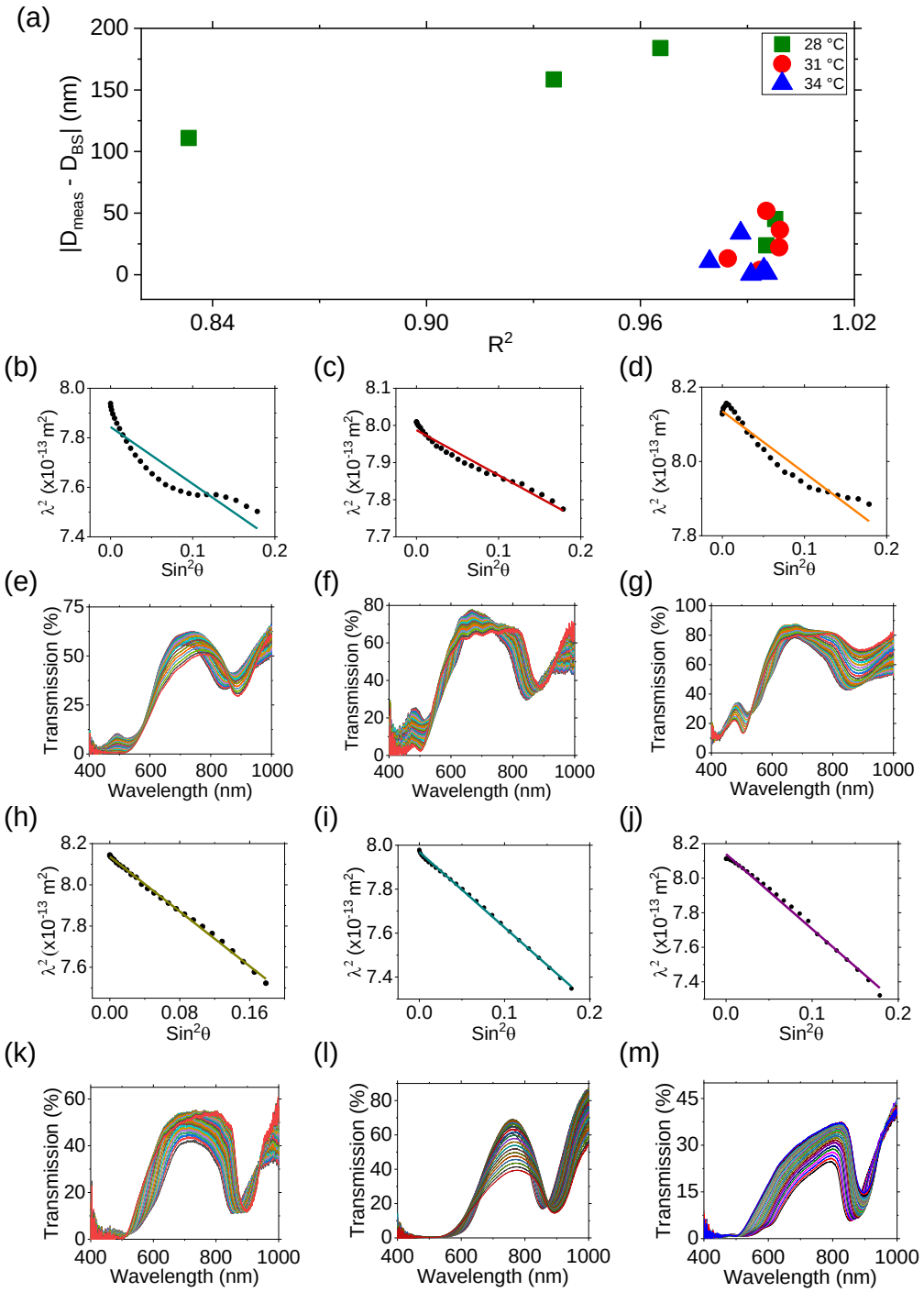


Figure 4.3. (a) Agreement between experimentally measured sphere diameters and those calculated according to Eq. 4.3 as a function of the R^2 value of the corresponding linear fits for opals grown from all five volume fractions at each of the three evaporation rates. (b)-(d) Bragg-Snell plots based on the central frequencies of the primary transmission dips observed in the transmission spectra for opals grown by EISA at an evaporation temperature of 28 °C from sphere solution volume fractions of 0.063% 0.042%, and 0.025% respectively, the three outlier cases for which the Bragg-Snell relationship breakdown occurs.

Figure 4.3 (continued). (e)-(g) Corresponding transmission spectra obtained in the incident angle range of 0 – 25° relative to the normal to the (111) plane of an FCC lattice. Bragg-Snell plots for opals grown at evaporation temperatures and volume fractions of (h) 28 °C, 0.031%, (i) 31 °C, 0.042%, (j) 34 °C, 0.025% for three example cases which demonstrate strong agreement with the Bragg-Snell relationship. (k)-(m). Corresponding transmission spectra for the incident angle range of 0 – 25° relative to the normal to the (111) plane of an FCC lattice.

The second group are the three outliers, which show a significant deviation from the model based on Eq. 4.3. For these three sets of conditions, the adjusted R^2 values range from 0.83 – 0.97, while the minimum $|D_{\mathrm{meas}} - D_{\mathrm{BS}}|$ is 111 nm, representing a relative difference ΔD of ~28%. Figure 4.3 (b)-(d) show the Bragg-Snell plots associated with the three outliers, the opals grown at an evaporation temperature of 28 °C, at the three lowest volume fractions, decreasing in order as 0.042%, 0.031%, and 0.025%. A benefit of constructing Bragg-Snell plots is the ability to directly extract the structural parameters of the corresponding crystal such as interplanar spacing and sphere diameter. The fact that the breakdown in the approximation based on Eq. 4.3 occurs only for these three sets of conditions indicates that the lower evaporation rate limit for which opals of a sufficient order such that (111) FCC symmetry is achieved is reached here at an evaporation temperature of 28 °C and volume fraction of 0.042%.

In Figure 4.3 (e)-(g), optical transmission spectra are shown for an incident angle range of 0 – 25°. The primary transmission dip corresponding to the PBG is observed in all cases. From examination of the spectra, we see the order of these opals deviates from the expected structural order. We

observe the appearance of higher order transmission dips from the (220) planes at ~500 nm for all three cases. The most common forms of disorder in the self-assembly of opals are stacking faults.(48-51) While Eq. 4.3 can be used to calculate the structural parameters of opals based on the (111) transmission dip, it can be used in tandem with Eq. S4.1, provided in the Supplementary material, to predict structural parameters based on lattice planes of alternative plane orientations. Based on these optical spectra, it appears that below the lower evaporation rate limit for these three lowest volume fractions, breakdown in characteristic (111) FCC symmetry begins and the opal is better able to transmit blue light, after suppression of transmission from the photonic bands associated with the (220) planes in these samples.

In the high-energy region of the spectrum ($a/\lambda > 1$, where $a = 563$ nm here based on an average measured sphere diameter of 398 nm), multiple Bragg diffraction by several families takes place and the associated Bragg scattering processes are enhanced. While diffraction from the (220) plane dominates the high energy region, the increase in transmitted blue light is symptomatic of the presence of additional stacking faults.(52) The increase is most pronounced at high incidence angles, which is unsurprising given that stacking faults in the (111) direction have little effect on the optical properties of the crystal, and it is stacking faults in alternative directions which are detected by transmission spectra obtained at angles other than normal incidence.

Another noteworthy aspect of these spectra is that while the PBG is present, there is a clear attenuation of the depth of spectral transmission dips

compared to spectra from all other conditions, and a general widening of the PBG occurs. The amplitude of radiation incident on a PhC attenuates rapidly with propagation distance such that the FWHM of the stopband experiences an exponential decay with thickness below the critical thickness, which can be derived using the scalar wave approximation (SWA) and is found elsewhere to be 13 layers for a silica/air colloidal crystal with silica sphere diameters of ~342 nm,(53-55) close in size to the PS opals in this work with an experimentally measured average diameter in the range of 384 – 412 nm (see Figure S4.5 and S4.6). For colloidal crystals ranging from single layer to the critical thickness, a narrowing of the stopband occurs similar to the Debye-Scherrer effect in small crystallites and the narrowing of the stopband is inversely proportional to the number of lattice planes.(56) However, past the point of critical thickness, the narrowing of the stopband saturates. Broadening of the stopband occurs due to disorder in various forms including inhomogeneous thickness and domains corresponding to alternative lattice planes.(57) For the opals analysed here, thickness ranges from a minimum of 10 layers to a maximum of 37 layers. Even crystals of minimum thickness approach the critical value. The broadening of the FWHM is evident as volume fraction and crystal thickness increase, indicative of the inevitable appearance of disordered sites which occurs in the self-assembly process. Light which propagates in these regions of disorder becomes diffuse from scattering, broadening the width of the corresponding stopband.(48)

For comparison, Bragg-Snell plots and transmission spectra corresponding to three of the well-behaved cases are shown in Figure 4.3 (h)-

(m). For the Bragg-Snell plots, the quality of the linear fit is evident. The transmission spectra show no evidence of higher energy blue photon transmission increases at energies higher than the transmission dip from (220) planes, indicating better overall order. The PBG is also of greater depth and a more well-defined spectral shape, meaning that the structures are dominated by the characteristic (111) symmetry of opals with a consistent and well-defined refractive index contrast throughout the structure, and no Fano resonance or Mie scattering effects are obvious(58). Branching of the dispersion and overlapping of a PBG from the (111) planes and the (200) planes has been reported previously, and results in curvature of the Bragg-Snell plots(59). In those cases, a specific reflection from the (200) planes was evident due to the high angle spectra of 45° and higher, and no branching of the dispersion and emergence of alternative reflections were seen at lower angle such as we observe. In a separate study, double peaked PBG were linked to stacking faults, but in our case the second dip is located in a separate part of the overall spectrum, and only observed when the volume fraction/temperature pairing forms less than perfect opal films.

The two factors which primarily govern opal order and thickness are sphere solution volume fraction and evaporation rate. While slower evaporation rates tend to facilitate increased crystal thickness, the corresponding volume fraction must be sufficient to prevent spreading of local sphere arrangements such that stacking faults, dislocations and non-close packed arrays are formed. In areas where such disorder occurs, a breakdown in FCC symmetry means that the corresponding crystal deviates from the

traditional Bragg-Snell analysis model based on stacking in the (111) direction and show enhanced blue photon transmission after the higher order band gap from (220) planes. For our experiments, an evaporation temperature of 28 °C and volume fraction of 0.042% stands as the critical minimum of this pair of conditions below which the opals lose their characteristic order. For researchers interested in nanostructured IO battery electrodes (60-62) or structured porous materials for sensing electro-photo-catalysis or supports, or for a range of other applications, control of the quality and thickness of the opal template material has a defining impact on the final IO structure.(63, 64)

4.4. Conclusions

The criteria required for thickness control of opal PhCs while simultaneously maintaining a high level of order have been demonstrated here for a range of volume fractions and evaporation rates grown using EISA for thicknesses up to 37 layers of PS spheres. The effect of order and thickness on their associated optical fingerprints are captured experimentally using angle-resolved transmission spectra. The order of each crystal is quantified by the extent to which each opal can be approximated using the Bragg-Snell model for the (111) reflection from an FCC lattice, which constitutes the omnidirectional PBG. SEM measurements are used to directly compare measured structural parameters to those predicted by the Bragg-Snell model. Over the broad range of conditions investigated, those that result in a breakdown in the stacking of an ideal opal are revealed. Furthermore, the maximum thicknesses that can be achieved under the investigated conditions

of volume fraction and temperature/evaporation rate are identified. The investigation also demonstrates the extent to which the PBG and other spectral features can be used to assess the degree of (dis)order, structural parameter extraction, and crystal thickness in opal film growth.

4.5. Appendix: Supplementary Material

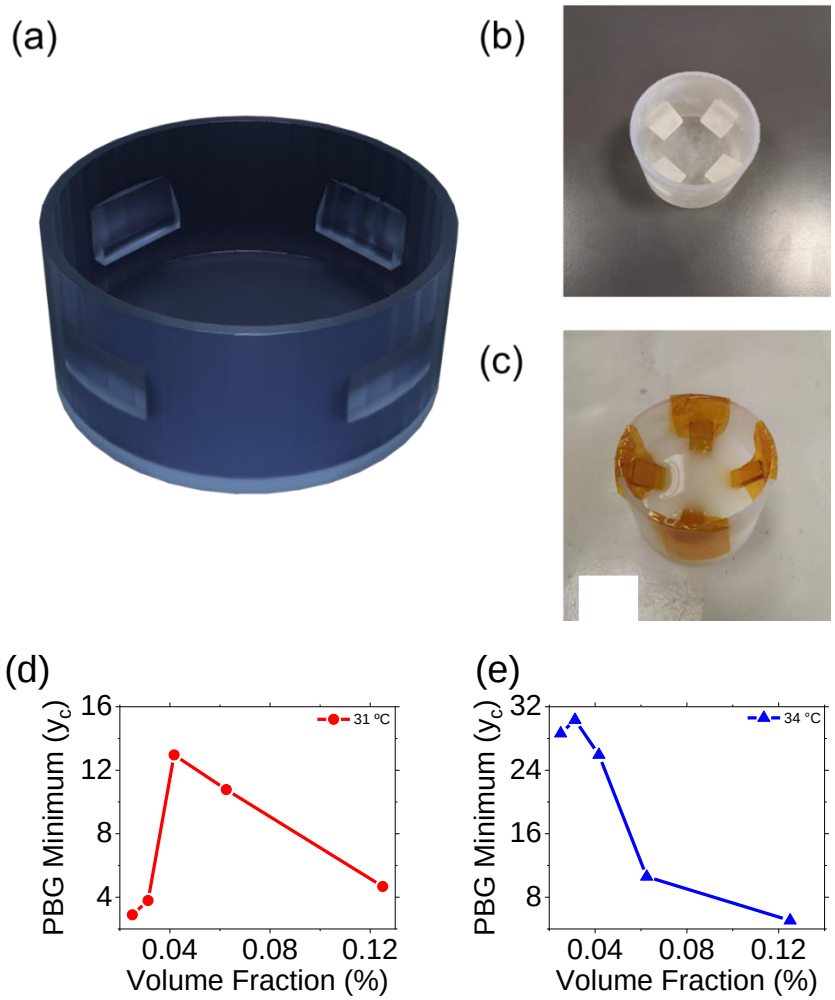


Figure S4.1. SLA 3D printed beaker designed with substrate rests at an angle of 30 ° to the vertical used for opal growth by EISA. (a) 3D rendered image of beaker. (b) Photograph of beaker. (c) Photograph depicting FTO substrates immersed in PS sphere solution inside beaker. (d) Intensity of central PBG frequency as a function of sphere solution volume fraction for opals grown using EISA at evaporation temperatures of 31 °C and 34 °C.

Figure S4.1 shows the 3D printed polymer beakers that were formed from Formlabs Clear Photoreactive Resin using a Formlabs Form 2 stereolithography (SLA) printer. All beakers were cleaned using the same sonication process described above, followed by UV-ozone treatment for 1 h. The diameter of each beaker was 6 cm and substrate rests were orientated at

an angle of 30 ° to the beaker walls. Figure S4.1 (d) and (e) show the relationship between volume fraction and the transmission intensity at the central PBG frequency at normal incidence for opals grown at evaporation temperatures of 31 °C and 34 °C, respectively.

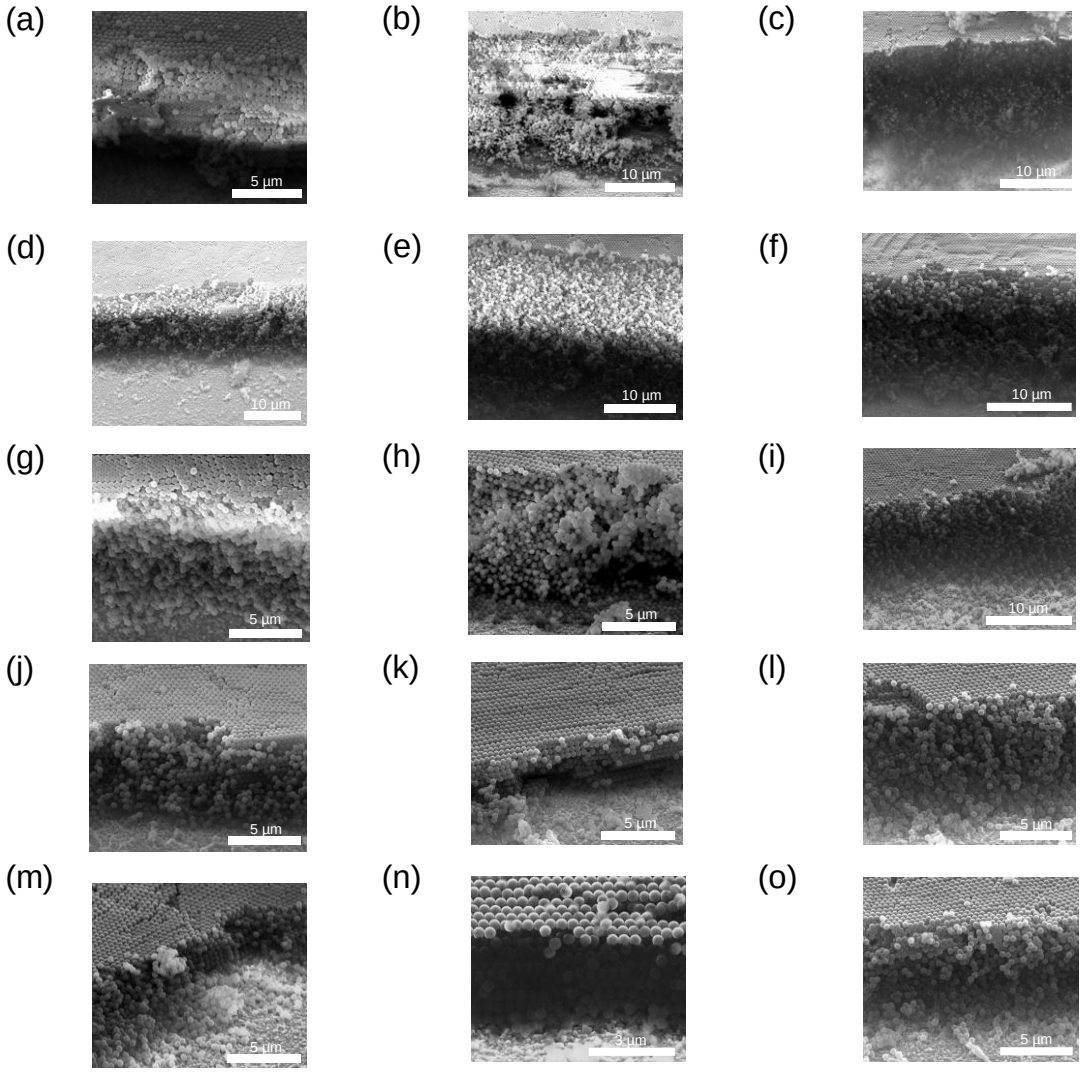


Figure S4.2. Cross-sectional SEM images of opals as examples used for thickness measurements provided to establish relationship with volume fraction. Evaporation temperatures are 28 °C, 31 °C, 34 °C, increasing from columns 1-3. Sphere solution volume fractions: (a)-(c) 0.025 %, (d)-(f) 0.0625 % (g)-(i) 0.042 %, (j)-(l) 0.031 %, (m)-(o) 0.025 %.

A general trend of decreasing PBG minimum occurs as a function of volume fraction for both temperatures. At 31 °C the outliers at low volume fraction significantly affect the trend. For 34 °C, the trend is similar to that observed for the slowest evaporation at 28 °C case.

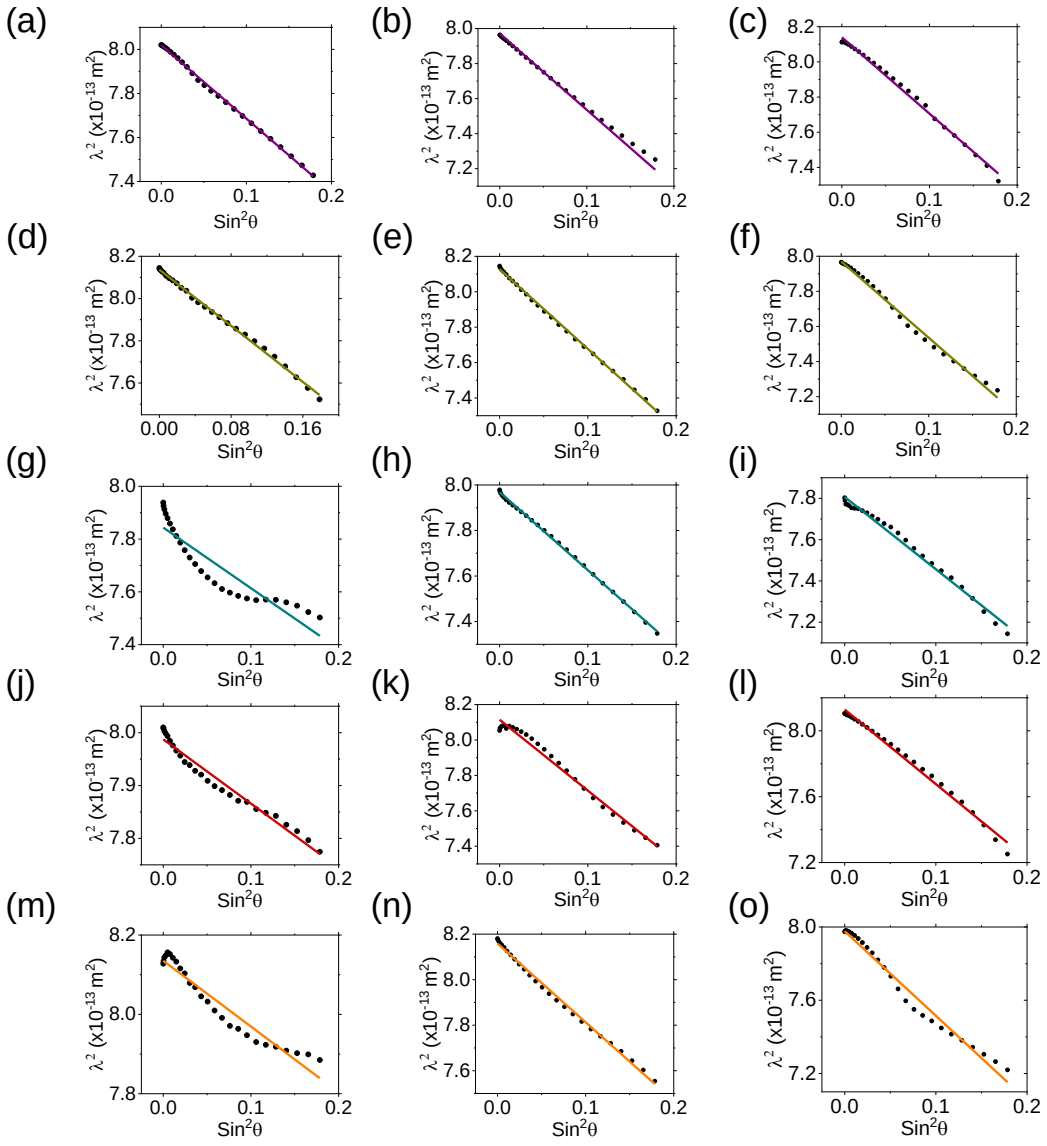


Figure S4.3. Bragg-Snell plots based on the central frequency of the primary transmission dip observed in the optical spectra of opals obtained in the incident angle range of 0-25 °. Evaporation temperatures are 28 °C, 31 °C, 34 °C, increasing from columns 1-3. Sphere solution volume fractions: (a)-(c) 0.125%, (d)-(f) 0.063% (g)-(i) 0.042%, (j)-(l) 0.031%, (m)-(o) 0.025%.

Figure S4.2 shows sample SEM images which were used as contributions to calculations of the thickness measurements used as data points in Figure 4.3 (a) of the main text. All opals were sputtered with Nickel with a total sputtering thickness of 20 nm prior to imaging to enhance resolution and reduce charging effects.

Temp (°C)	D_{meas} (nm)	$D_{Eq.\ 4.1}$ (nm)	$\Delta D/D_{Meas}$ (%)	d_{Meas} (nm)	$d_{Eq.\ 4.1}$ (nm)	$\Delta d/d_{Meas}$ (%)
28	398.2	1046	162.68	487.69	457	6.29
31	400	439	9.75	489.9	486	0.8
34	405.2	451	11.3	496.27	493	0.66

Table S4.1. Comparison of experimental measurements and calculations using Eq. 4.1 for opal sphere diameters and interplanar spacings at each evaporation rate.

In Figure S4.3, Bragg-Snell plots are provided under all investigated evaporation temperatures and volume fractions. Each data point in a Bragg-Snell plot is determined based on the square of the central wavelength of the PBG as a function of the square of the sine of the incident angle of the PBG. The central wavelength of the PBG is defined as the wavelength at which the minimum transmission intensity value of the (111) transmission dip in the associated transmission spectrum occurs. The incident angle is defined relative to the normal to the (111) plane of an FCC lattice. The incident angle range investigated was 0-25°. The extent to which each plot can be approximated by a linear fit indicates the dominance of the (111) FCC symmetry and can be used to determine the structural quality of each opal, quantified in this study using the adjusted R^2 value.

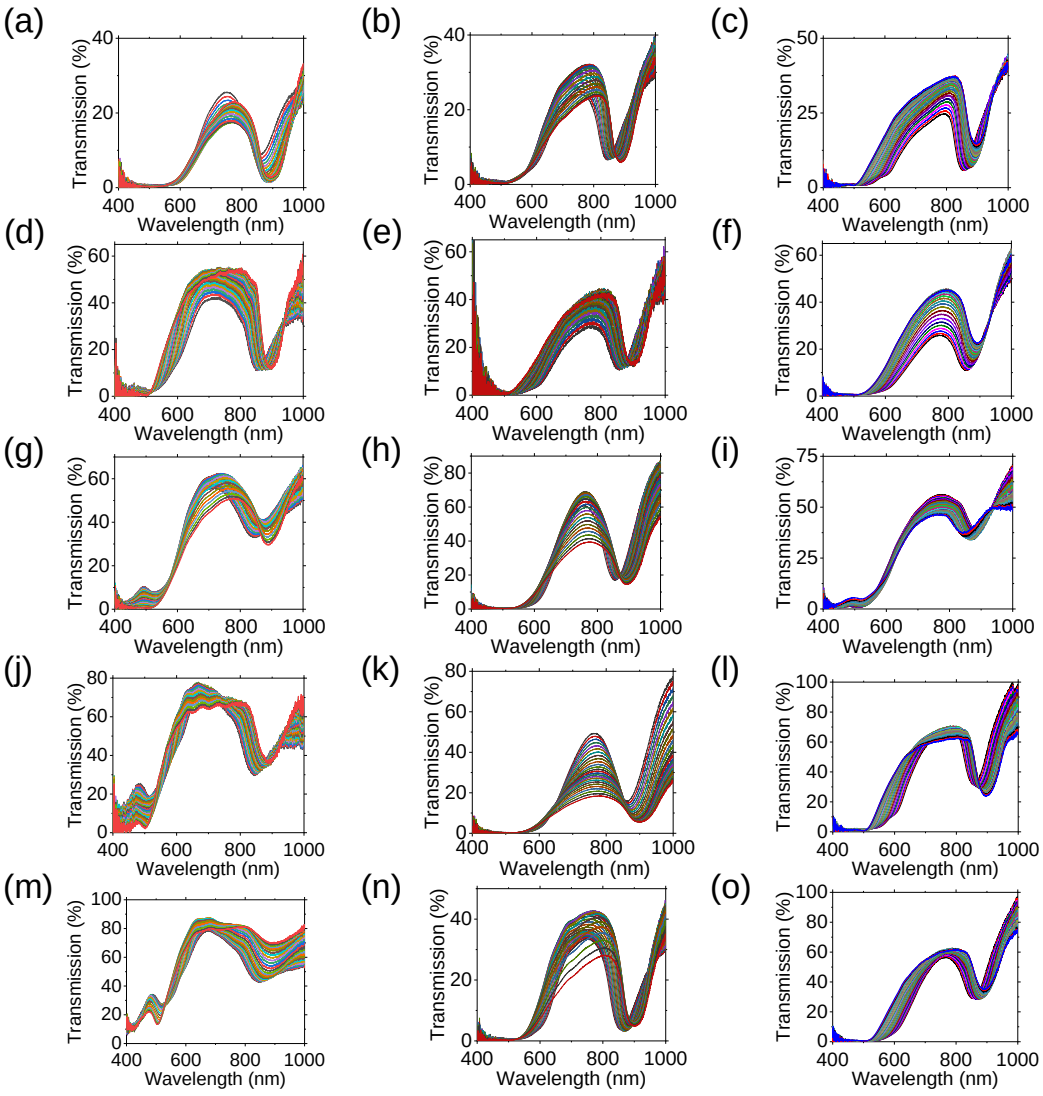


Figure S4.4. Transmission spectra of opals obtained in the incident angle range of 0-25 ° relative to the normal to the (111) plane of an FCC lattice. Evaporation temperatures are 28 °C, 31 °C, 34 °C, increasing from columns 1-3. Sphere solution volume fractions: (a)-(c) 0.125%, (d)-(f) 0.063% (g)-(i) 0.042%, (j)-(l) 0.031%, (m)-(o) 0.025%.

Table S4.1 shows a comparison of the structural parameters of sphere diameter and interplanar spacing from experimental measurements and based on calculations using the geometric approach in Eq. 4.1. Calculated sphere diameter $D_{\text{Eq. 4.1}}$ was obtained from the y-intercept of the linear fits applied to each dataset in Figure 4.1 (b) of the main text. The calculated interplanar

spacing was equated to the slope of each linear fit, where $D_{\text{Eq. 4.1}} = \sqrt{\frac{3}{2}}\mathrm{D}$. Good agreement between data occurs at the higher two temperatures, while the lowest temperature shows a significant contrast in results.

Transmission spectra for opals grown under all investigated volume fractions and evaporation rates in the incident angle range of 0 – 25° are shown in Figure S4.2. In all cases, the primary stopband corresponding to the PBG (PBG) is observed. The PBG is blue shifted as incident angle increases. Transmission level at the center of the PBG decreases with increasing volume fraction and hence thickness.

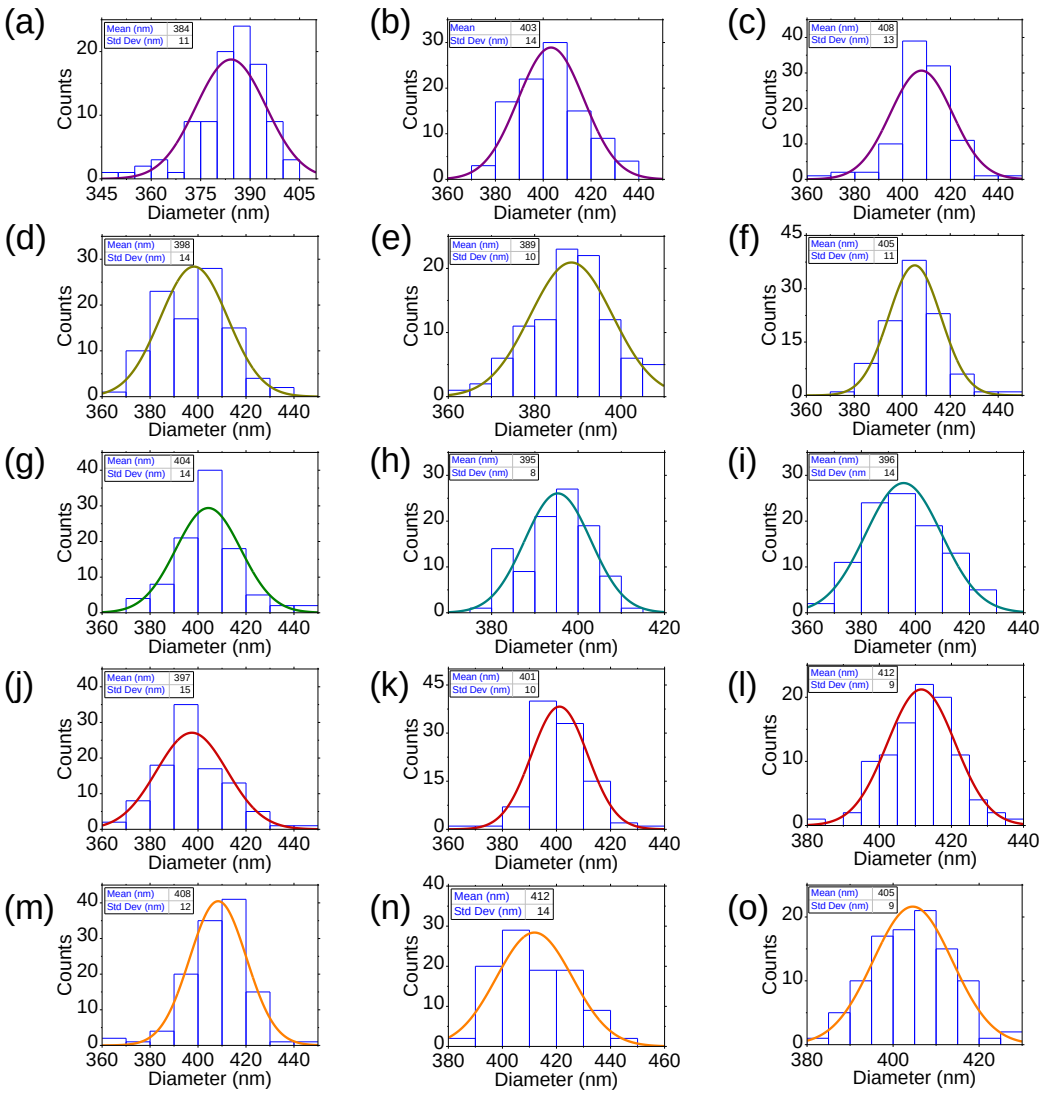


Figure S4.5. Size distributions for opals grown from sphere solutions with a nominal sphere diameter of 370 nm. Evaporation temperatures are 28 °C, 31 °C, 34 °C, increasing from columns 1-3. Sphere solution volume fractions: (a)-(c) 0.125%, (d)-(f) 0.063% (g)-(i) 0.042%, (j)-(l) 0.031%, (m)-(o) 0.025%.

Thickness measurements were obtained using cross-sectional SEM images. The mathematical method used to determine the actual thickness is shown in Figure S4.6 (a), out detailed in the Experimental section of the main text. A sample image is shown as an example in Figure S4.6 (b). The white lines depict where the line measurement *L* was determined.

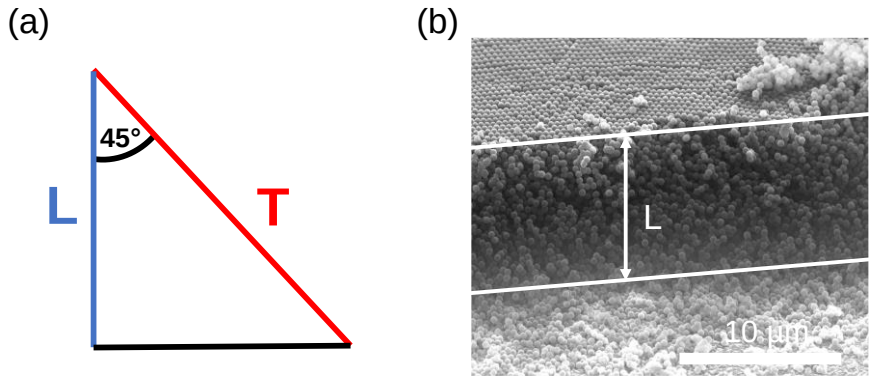


Figure S4.6. (a) Schematic of the determination of opal thickness. (b) Sample cross-sectional SEM image illustrating the method used to acquire thickness measurements.

Experimental detection of the PBG, along with any other stopbands which occur in a PhC, can be performed across the full range of the electromagnetic spectrum. Photonic stopbands commonly refer to frequencies from the UV to IR range. However, the iridescent colours characteristic of PhCs can only be observed if the stopbands occur in the visible region of the spectrum which is 380 nm – 740 nm.(65) Analysis shows that there is little change in the position of the PBG for opals formed under each set of conditions which can be attributed to their ordered nature and the narrow size distributions. For opals grown here from sphere solutions with a nominal diameter of 370 nm, the PBG lies between 890 nm and 901 nm at normal incidence, corresponding to the near-IR region of the electromagnetic spectrum. A stopband in this range can make no contribution to the observed colour in the visible range. Instead, the structural colour of the samples can be explained using Bragg-Snell theory for second order reflections.

While the FCC dominant stacking arrangement causing the (111) transmission dip which forms the PBG is evident throughout this work, secondary Bragg reflections can also be observed in transmission spectra acquired. A sharp increase in transmission can be observed at ~ 485 nm, following higher order transmission dips from the (220) planes. Here, the secondary transmission dips are fully formed only for the two lowest volume fractions with a central wavelength of ~ 500 nm. For the three higher volume fractions, the dips are suppressed. We evaluate the transmission dips for low volume fractions as the result of secondary Bragg reflections due to the most common form of disorder observed in opals, which are stacking faults. We evaluate the disappearance of the transmission dips at higher volume fractions to the attenuation of propagating light in this frequency range as a function of crystal thickness like that experienced by the primary Bragg reflection which constitutes the PBG.

Calculations in the main text have been performed only for reflected frequencies based on growth perpendicular to the (111) plane of an FCC lattice. Secondary Bragg reflections are a result of the interaction of propagating light with alternative lattice planes. Consequently, a correct model for secondary Bragg reflections must incorporate the orientation of the corresponding lattice plane to the (111) lattice plane. The angle α between two such planes defined by the miller indices ($h_1k_1l_1$) and ($h_2k_2l_2$) can be calculated using

$$\alpha = \cos^{-1}\left(\frac{h_1h_2 + k_1k_2 + l_1l_2}{\sqrt{h_1^2 + k_1^2 + l_1^2}\sqrt{h_2^2 + k_2^2 + l_2^2}}\right) \quad \text{(S4.1)}$$

The relation above must be incorporated for planes orientated at an angle to the (111) plane. However, the predicted (220) reflection lies parallel to the (111) plane. Artefacts corresponding to allowed Bragg reflections in the (200), (220), (311), and (400) directions may also be observed for self-assembled opals, especially at low incidence angles.(49, 66, 67), but are not observed in the spectral range for our samples.

4.6. References

1. A. B. Rao, J. Shaw, A. Neophytou, D. Morphew, F. Sciortino, R. L. Johnston and D. Chakrabarti, *ACS Nano*, **14**, 5348 (2020).
2. N. Vogel, M. Retsch, C.-A. Fustin, A. del Campo and U. Jonas, *Chemical Reviews*, **115**, 6265 (2015).
3. D. J. Norris, E. G. Arlinghaus, L. Meng, R. Heiny and L. E. Scriven, *Advanced Materials*, **16**, 1393 (2004).
4. C. López, *Advanced Materials*, **15**, 1679 (2003).
5. A. Stein, B. E. Wilson and S. G. Rudisill, *Chemical Society Reviews*, **42**, 2763 (2013).
6. J. Aizenberg, D. A. Muller, J. L. Grazul and D. R. Hamann, *Science*, **299**, 1205 (2003).
7. C. J. Brinker, G. C. Frye, A. J. Hurd and C. S. Ashley, *Thin Solid Films*, **201**, 97 (1991).
8. Y. Lu, R. Ganguli, C. A. Drewien, M. T. Anderson, C. J. Brinker, W. Gong, Y. Guo, H. Soyez, B. Dunn, M. H. Huang and J. I. Zink, *Nature*, **389**, 364 (1997).
9. M. Bardosova, M. E. Pemble, I. M. Povey and R. H. Tredgold, *Advanced Materials*, **22**, 3104 (2010).
10. G. Singh, H. Chan, T. Udayabhaskararao, E. Gelman, D. Peddis, A. Baskin, G. Leitus, P. Král and R. Klajn, *Faraday Discussions*, **181**, 403 (2015).
11. K. R. Phillips, T. Shirman, E. Shirman, A. V. Shneidman, T. M. Kay and J. Aizenberg, *Adv Mater*, **30**, e1706329 (2018).
12. B. Hatton, L. Mishchenko, S. Davis, K. H. Sandhage and J. Aizenberg, *Proceedings of the National Academy of Sciences*, **107**, 10354 (2010).
13. J. E. S. v. d. Hoeven, A. V. Shneidman, N. J. Nicolas and J. Aizenberg, *Accounts of Chemical Research*, **55**, 1809 (2022).
14. E. Armstrong, M. Osiak, H. Geaney, C. Glynn and C. O'Dwyer, *CrystEngComm*, **16**, 10804 (2014).
15. J. Ma, J. M. Kim, M. J. Hoque, K. J. Thompson, S. Nam, D. G. Cahill and N. Miljkovic, *Nano Letters*, **21**, 9983 (2021).
16. Y. Kim, A. A. Shah and M. J. Solomon, *Nature Communications*, **5**, 3676 (2014).
17. E. Yablonovitch, *Physical Review Letters*, **58**, 2059 (1987).
18. S. John, *Physical Review Letters*, **58**, 2486 (1987).
19. J. V. Sanders, *Nature*, **204**, 1151 (1964).
20. M. I. Shalaev, W. Walasik, A. Tsukernik, Y. Xu and N. M. Litchinitser, *Nature Nanotechnology*, **14**, 31 (2019).
21. S. Lin, M. K. Shafique, Z. Cai, J. Xiao, Y. Chen, Y. Wang and X. Hu, *ACS Nano*, **13**, 13037 (2019).
22. J. Yu, J. Lei, L. Wang, J. Zhang and Y. Liu, *Journal of Alloys and Compounds*, **769**, 740 (2018).
23. J. Hou, M. Li and Y. Song, *Nano Today*, **22**, 132 (2018).
24. E. Armstrong and C. O'Dwyer, *Journal of Materials Chemistry C*, **3**, 6109 (2015).
25. L. V. Woodcock, *Nature*, **385**, 141 (1997).
26. E. Armstrong, W. Khunsin, M. Osiak, M. Blömker, C. M. S. Torres and C. O'Dwyer, *Small*, **10**, 1895 (2014).

27. W. Khunsin, A. Amann, G. Kocher-Oberlehner, S. G. Romanov, S. Pullteap, H. C. Seat, E. P. O'Reilly, R. Zentel and C. M. Sotomayor Torres, *Advanced Functional Materials*, **22**, 1812 (2012).
28. C. I. Aguirre, E. Reguera and A. Stein, *Advanced Functional Materials*, **20**, 2565 (2010).
29. P. D. García, J. F. Galisteo-López and C. López, *Applied Physics Letters*, **87** (2005).
30. V. N. Astratov, A. M. Adawi, S. Fricker, M. S. Skolnick, D. M. Whittaker and P. N. Pusey, *Physical Review B*, **66**, 165215 (2002).
31. A. F. Koenderink, A. Lagendijk and W. L. Vos, *Physical Review B*, **72**, 153102 (2005).
32. P. D. García, S. Smolka, S. Stobbe and P. Lodahl, *Physical Review B*, **82**, 165103 (2010).
33. Y.-H. Ye, F. LeBlanc, A. Haché and V.-V. Truong, *Applied Physics Letters*, **78**, 52 (2001).
34. N. Duy Duc, T. Jean-Herve, A. Mohamed and S. Patrick, in *Proc.SPIE* (2018).
35. J. H. Han, A. V. Shneidman, D. Y. Kim, N. J. Nicolas, J. E. S. van der Hoeven, M. Aizenberg and J. Aizenberg, *Angewandte Chemie International Edition*, **61**, e202111048 (2022).
36. A. Galukhin, D. Bolmatenkov, A. Emelianova, I. Zharov and G. Y. Gor, *Langmuir*, **35**, 2230 (2019).
37. A. A. S. Gonçalves and M. Jaroniec, *J Colloid Interface Sci*, **537**, 725 (2019).
38. S. Wong, V. Kitaev and G. A. Ozin, *J Am Chem Soc*, **125**, 15589 (2003).
39. S.-H. Kim, S. Y. Lee, S.-M. Yang and G.-R. Yi, *NPG Asia Materials*, **3**, 25 (2011).
40. M. V. Rybin, A. V. Baryshev, A. B. Khanikaev, M. Inoue, K. B. Samusev, A. V. Sel'kin, G. Yushin and M. F. Limonov, *Physical Review B*, **77**, 205106 (2008).
41. J. F. Galisteo-López, E. Palacios-Lidón, E. Castillo-Martínez and C. López, *Physical Review B*, **68**, 115109 (2003).
42. Y. A. Vlasov, M. A. Kaliteevski and V. V. Nikolaev, *Physical Review B*, **60**, 1555 (1999).
43. S. H. Abrandabadi, A. Anvari and R. S. Bonabi, *Physica B: Condensed Matter*, **649**, 414499 (2023).
44. J. D. Joannopoulos, P. R. Villeneuve and S. Fan, *Nature*, **386**, 143 (1997).
45. G. T.H. Tran, M. Koike, T. Uchikoshi and H. Fudouzi, *Langmuir*, **36**, 10683 (2020).
46. P. Jiang, J. F. Bertone, K. S. Hwang and V. L. Colvin, *Chemistry of Materials*, **11**, 2132 (1999).
47. S.-L. Kuai, X.-F. Hu, A. Haché and V.-V. Truong, *Journal of Crystal Growth*, **267**, 317 (2004).
48. T. Turiv, I. Lazo, A. Brodin, B. I. Lev, V. Reiffenrath, V. G. Nazarenko and O. D. Lavrentovich, *Science*, **342**, 1351 (2013).
49. J. P. Hoogenboom, D. Derks, P. Vergeer and A. v. Blaaderen, *The Journal of Chemical Physics*, **117**, 11320 (2002).

50. X. Checoury, S. Enoch, C. Lopez and A. Blanco, *Applied Physics Letters*, **90**, 161131 (2007).
51. T. Liu, B. VanSaders, S. C. Glotzer and M. J. Solomon, *ACS Applied Materials & Interfaces*, **12**, 9842 (2020).
52. L. C. Andreani, A. Balestreri, J. F. Galisteo-López, M. Galli, M. Patrini, E. Descrovi, A. Chiodoni, F. Giorgis, L. Pallavidino and F. Geobaldo, *Physical Review B*, **78**, 205304 (2008).
53. P. Schall, I. Cohen, D. A. Weitz and F. Spaepen, *Science*, **305**, 1944 (2004).
54. D. M. Mittleman, J. F. Bertone, P. Jiang, K. S. Hwang and V. L. Colvin, *The Journal of Chemical Physics*, **111**, 345 (1999).
55. S. Venkatesh, P. Jiang and B. Jiang, *Langmuir*, **23**, 8231 (2007).
56. J. F. Bertone, P. Jiang, K. S. Hwang, D. M. Mittleman and V. L. Colvin, *Physical Review Letters*, **83**, 300 (1999).
57. H. W. Nho and T. H. Yoon, *Scientific Reports*, **7**, 12424 (2017).
58. M. V. Rybin, A. B. Khanikaev, M. Inoue, K. B. Samusev, M. J. Steel, G. Yushin and M. F. Limonov, *Physical Review Letters*, **103**, 023901 (2009).
59. S. G. Romanov, T. Maka, C. M. Sotomayor Torres, M. Müller, R. Zentel, D. Cassagne, J. Manzanares-Martinez and C. Jouanin, *Physical Review E*, **63**, 056603 (2001).
60. C. O'Dwyer, *Advanced Materials*, **28**, 5681 (2016).
61. G. Collins, E. Armstrong, D. McNulty, S. O'Hanlon, H. Geaney and C. O'Dwyer, *Science and Technology of Advanced Materials*, **17**, 563 (2016).
62. D. McNulty, A. Lonergan, S. O'Hanlon and C. O'Dwyer, *Solid State Ionics*, **314**, 195 (2018).
63. A. Lonergan, D. McNulty and C. O'Dwyer, *Journal of Applied Physics*, **124**, 095106 (2018).
64. A. Lonergan and C. O'Dwyer, *Advanced Materials Technologies*, **n/a**, 2201410.
65. N. Vogel, S. Utech, G. T. England, T. Shirman, K. R. Phillips, N. Koay, I. B. Burgess, M. Kolle, D. A. Weitz and J. Aizenberg, *Proceedings of the National Academy of Sciences*, **112**, 10845 (2015).
66. J. Hilhorst, J. Wolters and A. Petukhov, *CrystEngComm*, **12** (2010).
67. E. Vekris, V. Kitaev, D. D. Perovic, J. S. Aitchison and G. A. Ozin, *Advanced Materials*, **20**, 1110 (2008).

Chapter 5

Asymmetric Optical Response of Thickness Graded Opal PhCs

Adapted from: Grant, A.; O'Dwyer, C. Asymmetrical Optical Response of Opal Photonic Crystals with Graded Thickness. ECS Advances 2023, 2 (4), 043501. DOI: 10.1149/2754-2734/ad0cd4.

Abstract

The influence of thickness gradient and structural order on the spectral response of opal PhCs (PhCs) grown by evaporation-induced self-assembly (EISA) are presented. SEM imaging and angle resolved optical transmission spectroscopy are used to investigate the evolution of the PBG along a thickness gradient for opals grown from five different colloidal sphere concentrations at two different evaporation rates. The degradation of structural order along the thickness gradient is demonstrated, the occurrence of which attenuates the PBG with the thinning of the opal film and results in asymmetrical angle-resolved transmission spectra. The asymmetry becomes more pronounced for opals grown from lower volume fractions, where secondary Bragg reflections also appear at low incident angles.

5.1. Introduction

Opals are a type of PhC which exhibit striking colours determined by their structure. The optical response of PhCs originates from the periodic refractive index contrast within the crystal, which can be implemented by using materials of alternating refractive index.(1-3) Further tuning of the optical response of these PhCs can be realised by forming structures with graded refractive index.(4) The contrast depends on both the materials used, and the path length which light propagates through each medium. The graded index can be designed by changing the thickness of the individual layers or the dimension of the unit cell from which the crystal is constructed.(5-7) Our recent work investigates how opal thickness can be controlled using volume fraction and evaporation rate and the impact of thickness on their associated optical fingerprints.(8) The observed colours are a result of the wavelengths reflected from each crystal, caused by an interplay between coherent Bragg diffraction and incoherent diffuse scattering that form the PBG (PBG).(9, 10) Extensive reviews of the characteristics which underpin these structures, and their applications are provided elsewhere.(11, 12)

In top-down fabrication methods where compounds are formed layer by layer, these graded thickness PhCs can be designed easily in 1D, 2D and 3D.(13-15) In this case, the thickness gradient is parallel to the growth direction that induces a graded refractive index contrast which shifts the position of the PBG. The value of such materials has been demonstrated in applications such as waveguides,(16, 17) biosensors,(18) optical switches and filters,(19, 20) along with templates for microporous and macroporous

materials.(21) In these applications, the benefit of the thickness gradient is primarily in its consequence on the optical response, where the frequency of the photonic stopbands associated with the crystal is tuned based on thickness.

Bottom-up self-assembly methods are simple and cost-effective in the formation of PhCs. However, structural control is difficult, given that assembly proceeds spontaneously. Here, we show that opal PhCs formed by EISA demonstrate a natural thickness gradient, analogous to the “coffee-ring” effect.(22) The gradient in this case is perpendicular to the growth direction, following the direction of evaporation flux.

The result is regions of uniform localised thickness parallel to the growth direction. As a result, spectra acquired at any point are formed from light propagating through uniform thickness, so the gradient does not affect the frequency of the PBG. Instead, we investigate the effects of the thickness gradient on intensity of the transmitted light. We show that the thickness gradient results in a predictable optical response, and angle-resolved transmission spectra are used in tandem with cross-sectional SEM imaging to map the effects of the gradient on the optical fingerprint of opals grown under a range of volume fractions at two different evaporation rates. Furthermore, SEM imaging shows that structural order is progressively reduced along the gradient, which attenuates the PBG (PBG). 3D transmission spectra provide unique optical fingerprints for opals PhCs grown under a range of conditions, all of which demonstrate an asymmetry caused by attenuation of the PBG at regions of least thickness.

5.2. Experimental

5.2.1. Materials and Substrate Preparation

Colloidal solutions of PS spheres in 2.5 % (w/v) aqueous suspension with a nominal diameter of 370 nm were purchased from Polysciences Inc. The sphere suspension possessed a net negative charge due to functionalisation using a sulfate ester during formation to aid in self-assembly. The substrates used were fluorine-doped tin oxide (FTO)-coated soda-lime glass purchased from Solaronix SA. Glass of thickness 2.2 mm was cut into pieces with dimensions 10 × 25 mm^2. The conductive layer of the pieces consisted of a thin FTO layer followed by a thin SiO_2 layer (each layer ~20 nm) followed by a thicker FTO layer (~300 nm), all deposited on a borosilicate glass substrate. All substrates were cleaned using the same process: Successive sonication in acetone (reagent grade 99.5%; Sigma Aldrich), isopropyl alcohol (reagent grade 99.5%; Sigma Aldrich) and de-ionised water, each for 5 minutes. All cleaned samples were dried at room temperature in an inert atmosphere. Kapton tape was used to cover the back of the substrate and partially cover the surface of the substrate such that an exposed front surface of 10 × 10 mm^2 remained. This ensured colloidal crystal formation occurred only on the desired surface area. The samples were treated in a Novascan PSD Pro Series digital UV-ozone system for 1 h to maximise hydrophilicity of the surface of the substrates immediately prior to PhC formation.

5.2.2. Evaporation-Induced Self-Assembly

Opals were formed using evaporation-induced self-assembly. FTO glass substrates were immersed in a diluted PS sphere solution with volume

fractions in the range of 0.025% to 0.125 % which were placed on a hot plate at a constant temperature between 28 °C and 34 °C. Once the sphere solution was evaporated fully, the substrates were removed and left to dry in inert atmosphere at room temperature. To ensure consistent EISA of the colloidal films at a well-defined angle, we used Vat polymerisation 3D printing to create beakers that were formed from photopolymerised poly(methyl methacrylate)-based resin using a Formlabs Form 2 stereolithography printer. All beakers were cleaned using the same sonication process described above, followed by UV-ozone treatment for 1 h. The diameter of each beaker was 6 cm and substrate rests were positioned at an angle of 30° to the beaker walls.

5.2.3. Microscopy and Spectroscopy

All microscopy was performed using a FEI Quanta 650 SEM at accelerating voltages of 10 kV – 30 kV. Prior to imaging, an incision was made along the length of each sample using a thin blade so that the cross-section could be imaged for thickness measurements. Sputter coating on non-conductive PS spheres was carried out using a Quorum 150T S magnetron sputtering system. Sputtering samples reduced charging effects, namely electron diffusion and beam drift, allowing better contrast and feature definition. For a thickness line measurement L, the actual thickness is calculated according to $T = L/\cos 45° = L\sqrt{2}$. Thickness measurements were enabled by tilting the sample stage parallel to the surface at an angle of 45°. For each sample, several thickness measurements were obtained and the mean values in each case used as data points to establish the volume fraction-thickness relationship.

Angle-resolved transmission spectra were used to characterise colloidal opal films. The light source was a tungsten-halogen lamp with an operating wavelength range of 400 to 2200 nm. Transmission measurements were recorded using a UV-visible spectrometer (USB2000+ VIS-NIR-ES) with an operational range of 350 to 1000 nm and a NIR spectrometer (NIRQuest512-2.5) with an operational range of 900 nm to 2500 nm, both from Ocean Optics Inc. Spectra were acquired for an incident angle range of -25° to 25° with a full spectrum recorded for each 1° increment in angle. The integration time was 100 s averaged over 25 scans. Adjustments to the rotation of the sample were made using a motorised rotational stage (ELL8; Thorlabs Inc.) which rotated the sample while the incident beam and detector arm remained fixed. For all measurements, the sample was placed on its side (25 mm^2 side) and angle displacement occurred perpendicular to the direction of the thickness gradient, opposite to the direction of evaporation flux during growth, corresponding to a small region at either side of the normal.

5.3. Results and Discussion

The central wavelength of a photonic stopband can be calculated using the Bragg-Snell law:(23)

$$\lambda_{hkl} = \frac{2d_{hkl}}{m}\sqrt{n_{eff}^2 - \sin^2\theta} \tag{5.1}$$

The PBG is the primary stopband of an opal and is formed due to Bragg reflections from the (111) plane of an FCC lattice. The interplanar spacing, d_{111} is between adjacent (111) planes and can be calculated as 0.816*D*, where *D* is the average opal sphere diameter. The effective refractive index n_{eff} can

be calculated using the Drude model for a two-material system and θ is the incident angle relative to the (111) FCC lattice plane.(24) First order resonance is assumed (m = 1). A perfectly ordered opal consists of layers of spheres stacked in the [111] direction of an FCC lattice. For a given incident angle, the central wavelength of the photonic stopband is dependent only on interplanar spacing and refractive index contrast.

For all opals examined here, the average sphere diameter is ~400 nm and remains relatively constant. Average sphere diameters for each opal were calculated from over 100 measurements and the maximum standard deviation for any opal examined is 14 nm. Therefore, any shift in the PBG is caused primarily by the effective refractive index, which is dependent on the constituent media within the material and the stacking arrangement of these media. All opals here consist of PS spheres and the air which fills the voids between them. Therefore, PBG shift can occur if the stacking arrangement deviates from a perfectly ordered FCC lattice stacked normal to the (111) plane. Its position is unaffected by crystal thickness.

Figure 5.1 illustrates the effect of structural order and thickness on the optical transmission spectra for opals grown from a range of volume fractions by EISA at an evaporation temperature of 34 ºC. The photograph in Figure 5.1 (a) shows the opal from which the SEM images were acquired. The red arrow indicates the direction along which angle-resolved transmission spectra were acquired. The incident angle range chosen was from -25º, corresponding to the edge of the sample near the tail of the red arrow, to 25º, corresponding to

a location near the head of the red arrow. Incident angles are relative to the normal to the (111) FCC lattice plane.

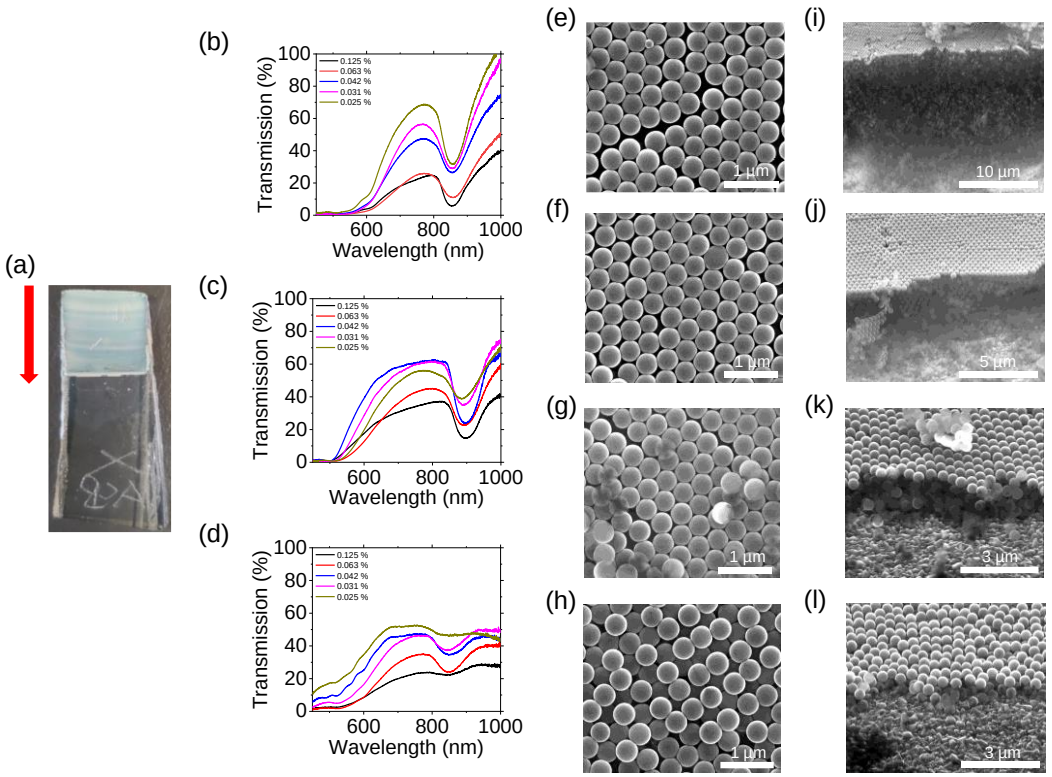


Figure 5.1. Optical and structural characterisation of opals grown by EISA at an evaporation temperature of 34 ºC. (a) Photograph of opal sample. Opal thickness decreases in the direction of the red arrow. Optical transmission spectra for five opals, denoted by their volume fractions from 0.025 % to 0.125 %. (b) Spectra obtained at an angle of -25º, corresponding to a location near the tail of the red arrow. (c) Spectra obtained at normal incidence, near the centre of the sample. (d) Spectra obtained at an angle of 25º, at a location near the head of the red arrow. (e)-(g) SEM images obtained normal to the stacking direction at four positions along the direction of the red arrow shown in (a). (i)-(l) Corresponding cross-sectional SEM images obtained at four positions along the direction of the red arrow in (a) captured at an angle of 45º to the stacking direction.

Figure 5.1 (b), (c), and (d) were acquired for opals of five volume fractions at an angle of -25º, 0º, and 25º, respectively. Our recent work investigates the evolution of the optical spectra for opals grown from these five volume fractions at normal incidence. Crystal thickness increases with volume

fraction. For the investigated volume fraction range investigated of 0.025 % to 0.125 %, crystal thickness from 4.6 μm (9 layers) to 16.3 μm (33 layers). Moving from high to low volume fractions, we observe in Figure 5.1 some key changes to the PBG. As volume fraction and hence thickness decreases, the PBG is attenuated and its depth is progressively reduced, transmission at the centre decreases and the band broadens. Due to the thickness gradient, the same changes occur for each given volume fraction as spectra are acquired along this direction, evident in the spectra at each of the three locations probed for the spectra in Figure 5.1 (b)-(d).

There is little observable change in the central wavelength of the PBG between all volume fractions in Figure 5.1 (b) and (c), indicating a high degree of order at these locations. In Figure 5.1 (d), the central wavelength of the PBG varies, indicative of a higher concentration of disordered sites. In Figure 5.1 (e)-(h), plan view SEM images are presented in the order of the locations at which they were acquired along the red arrow. The cross-sectional SEM images in Figure 5.1 (i)-(l) are presented in the same order. Both order and thickness of the opal decrease in this direction along the sample. The plan view SEM images show that there is a significant difference in stacking order along the direction of the red arrow, opposite to the direction of evaporation flux. While in Figures 5.1 (e) and (f), there is clear FCC symmetry with some disordered domains, Figures 5.1 (g)–(h) show more disorder with numerous defects and non-close-packed arrays. The thinning of the opal film toward the evaporation line is illustrated by the cross-sectional SEM images in Figures 5.1 (i)–(l) from a maximum of over 30 layers to a single layer.

Transmitted intensity exponentially decays with crystal thickness.(25) The transmission spectra measured here for all volume fractions show an increase in transmission intensity across the investigated spectral region at locations along the thickness gradient toward the terminating evaporation line. In transmission spectra, disorder presents as increased transmission around the stopband frequencies, with a background of decreased transmission for frequencies outside the stopband, resulting in an attenuation of the PBG.(26) The PBG is well defined and of greatest depth at the region of greatest thickness, while the PBG is attenuated for all volume fractions for the three sets of spectra obtained along the negative thickness gradient. The increase in disorder this direction is shown clearly by the plan view SEM images.

Figure 5.2 shows angle-resolved transmission spectra for a range of incident angles from -25 º to 25º, relative to the normal to the plane of incidence for opals grown at an evaporation temperature of 34 ºC. Even though just a few degrees higher in temperature, this has been shown to have a dramatic effect on the rate of evaporation and opal formation by EISA. The spectra from these samples are presented in order of decreasing volume fraction (and hence thickness) from Figures 5.2 (a)–(e). Considering the dispersion relation for the (111) Bragg reflection for an FCC lattice, the opals are well-behaved for all volume fractions at this evaporation rate. The PBG is easily identified by the overhead colormaps as a thin band of lower transmission intensity towards the red edge of the investigated spectral region with a central wavelength at normal incidence occurring from 893–901 nm. The most notable aspects of

these spectra are in the asymmetry in both transmission intensity and width of the PBG which is caused by the thickness gradient of the samples.

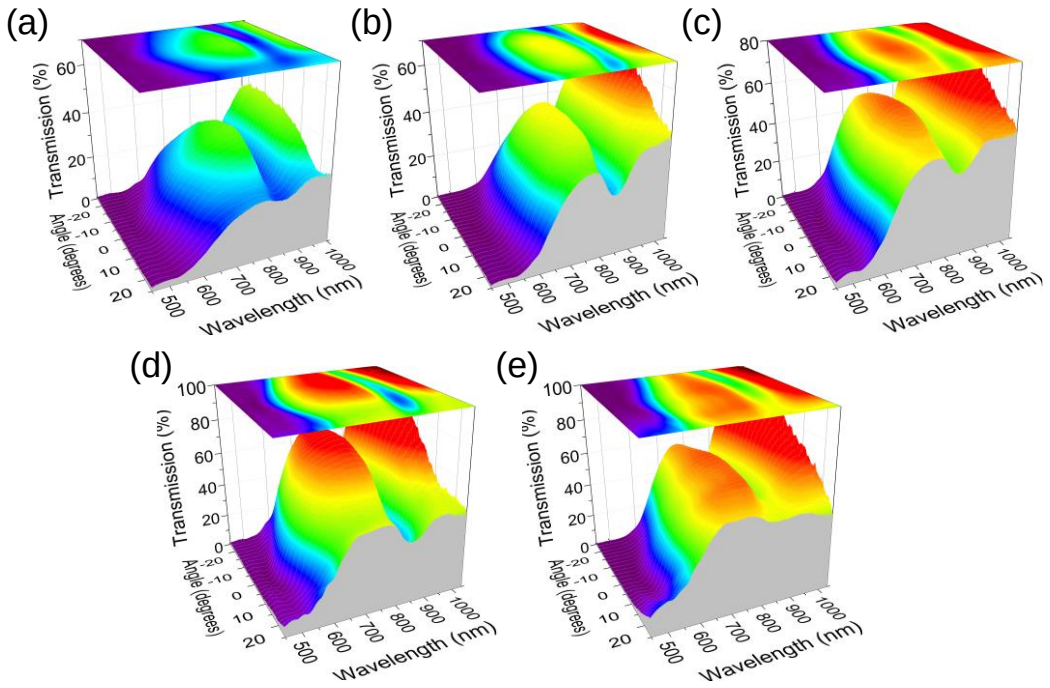


Figure 5.2. Angle-resolved transmission spectra showing the variation of optical transmission as a function of angle of incidence and wavelength, for opals grown by EISA at 34 ºC. The spectra correspond to transmission intensity for a range of volume fractions of (a) 0.125 %, (b) 0.063 %, (c) 0.042 %, (d) 0.031 %, and (e) 0.025 % at a range of incident angles from -25º to 25º. Corresponding 2D color maps overhead show the degree of symmetry in the angle-resolved response of EISA grown opals. The colors are linked to transmission intensity.

In angle-resolved transmission spectra, the curvature of the bands associated with the PBG are important and this contrast is linked to the degree of order. Based on the Bragg-Snell law, the frequency of the PBG changes with incident angle and higher angles result in a blue shift of the PBG. In the angle-resolved spectra for these five volume fractions the PBG central wavelength is blue-shifted at -25º, where thickness and order are maximum,

to between 853 nm and 858 nm, which is in good agreement with the Bragg-Snell model. At +25° the PBG central wavelength is further shifted to between 845 nm and 849 nm, which is not in agreement with the Bragg-Snell model, and this deviation is caused by the gradient in thickness and order. The optical response due to the thickness gradient can be clearly observed by the change in color maps for each volume fraction. The band associated with the PBG increases from the low intensity blue color to green from Figure 5.2 (a)-(e), while the frequencies in the vicinity of the PBG increase from green to red color. Increased transmission is a direct result of reduced close-packed order and thinner opal film regions.

The optical response in opals changes at high incident angles, where spectra typically begin to deviate from the Bragg-Snell law. The differences tend to be most pronounced in the high-energy region ($\sqrt{2}D/\lambda > 1$) where Bragg diffraction by several crystallographic plane families occurs.(27-29) Under this range of conditions, secondary transmission dips appear for high negative incident angles (-25º to 10º) at locations where thickness is minimal. In our case, the secondary transmission dip observed at ~517 nm at -25º and is associated with the (220) Bragg reflection of an FCC lattice.(30) While some of the other Bragg reflections associated with transmission in opals only occur at incident angles outside the range investigated in this work, there is an absence of any transmission dips associated with reflection from the $(11\bar{1})$ and (200) planes, which are expected to appear at energies between those of the (111) and (220) bands.(31-33)

Angle-resolved transmission spectra of opal PhCs performed in other studies have shown that these materials exhibit a highly symmetrical spectral fingerprint over a broad incident angle range up to ±45º due to their thickness uniformity.(34) Elsewhere, the evolution of the PBG and overall spectral response for samples with two uniform thicknesses of 15 µm and 25 µm using angle-resolved reflectance spectra over an incident angle range of ±60º were interrogated.(35) Similar effects were evident, with an attenuation of the PBG and increased reflectance at its edges along with greater reflectance at the higher energy side of the spectra due to interactions with lattice planes other than the [111] family.

The typical approach used to acquire angle-resolved transmission/reflectance measurements is to change the incident angle by rotation of the incident beam or detector arm such that all measurements are obtained at a fixed point on the sample. Here, it is the sample that is rotated using the motorised rotation stage such that the angle-resolved transmission measurements interrogate a small region on either side of the absolute normal. Accordingly, the beam interaction area on the sample moves acutely along the direction in which both thickness and order decrease. The asymmetry in the spectra arises from the attenuation of the PBG along this direction. Given that the incident angle increases along the thickness gradient towards the thinner regions, the asymmetry is always observed with lower transmission and well defined spectral features on the negative side of the normal (where the thickness and order are reduced), and an attenuation of the same spectral features on the positive side.

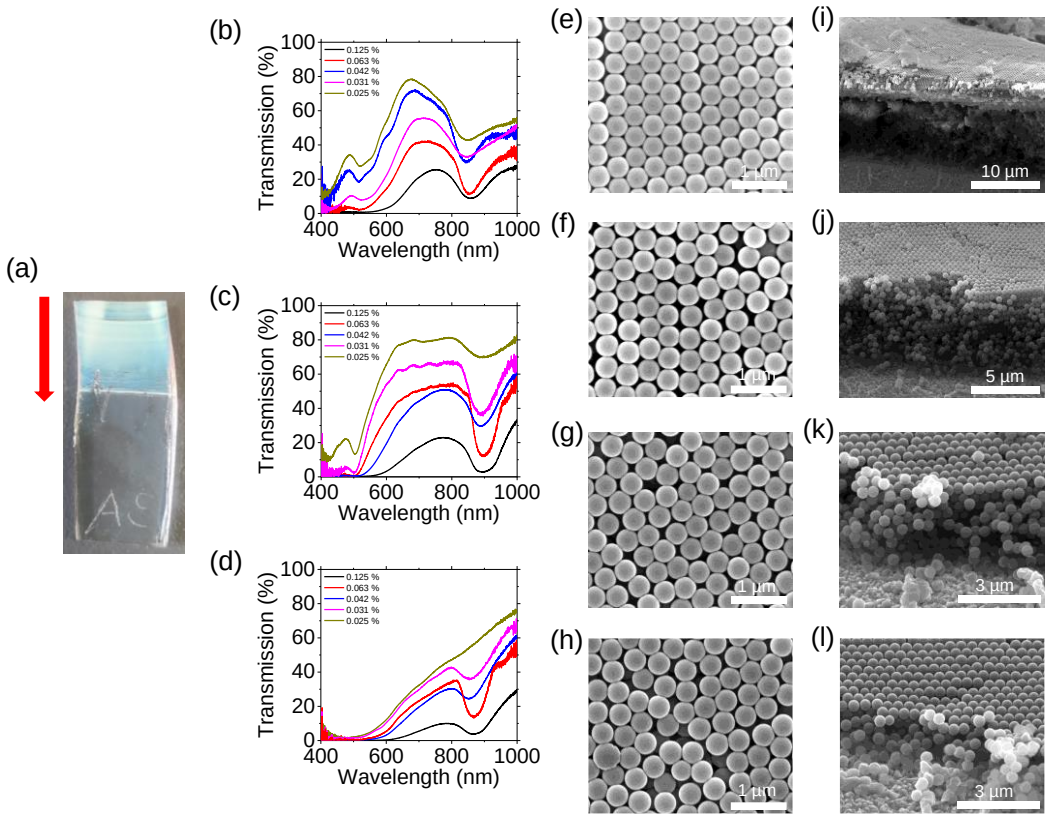


Figure 5.3. Optical and structural characterisation of opals grown by EISA at an evaporation temperature of 28 ºC. (a) Photograph of opal sample. Opal thickness decreases in the direction of the red arrow. Optical transmission spectra for five opals, denoted by their volume fractions from 0.025 % to 0.125 %. (b) Spectra obtained at a sample angle of -25º, corresponding to a location near the tail of the arrow. (c) Spectra obtained at normal incidence, near the centre of the sample. (d) Spectra obtained at an angle of 25º, at a location near the head of the arrow. (e)-(g) SEM images obtained normal to the stacking direction at four positions along the direction of the red arrow shown in (a). (i)-(l) Cross-sectional SEM images obtained at four positions along the direction of the red arrow in (a) captured at an angle of 45º to the stacking direction.

Figure 5.3 shows the optical and structural characterisation of opals grown at an evaporation temperature of 28 ºC, corresponding to an evaporation time measured to be twice as long as the previous evaporation temperature of 34 ºC. The transmission spectra for opals grown from all five volume fractions obtained at incident angles of -25º, 0º, and 25º are shown in Figure 5.3 (b), (c), and (d), respectively. For the same range of volume

fractions from 0.025 % to 0.125 %, crystal thickness increases from 7.5 μm (15 layers) to 17.5 μm (37 layers). The spectra are notably different from their counterparts grown at 34 ºC. At normal incidence, the low energy side of the spectrum follows the expected shape of a well-defined PBG and a transmission intensity which decreases as a function of volume fraction and hence thickness. At the high negative incidence of -25º, the PBG is blue-shifted as expected based on the Bragg-Snell law. Like the opals grown at 34 ºC, secondary transmission dips associated with the (220) reflection from an FCC lattice occur at ~517 nm at -25º. In this case these (220) dips are present and most well-defined at normal incidence, occurring at ~503 nm. While the PBG is blue shifted by incident angle based on the Bragg-Snell law for reflection from a (111) FCC lattice plane, the secondary reflection is red-shifted given that the frequency of the secondary stopband occurs due to reflection from the (220) plane. Reflections from alternative planes require adaptations to be made to the Bragg-Snell law. These adaptations are to account for the change in incident angle due to the consideration of an alternative lattice plane. The actual incident angle is then the sum of the angle measured between the incident beam and the normal to the sample surface, and the angle between the plane of reflection and the (111) plane which can be calculated using Eq. 4.1. The appearance of the stopband from -25º to normal incidence indicates that at an evaporation temperature of 28 ºC, there is a high concentration of stacking faults in the form of planes orientated in the (220) direction. At 25º, the spectra correspond to the location of least thickness and the (220) dips are absent. The combination of increased disorder and

minimum thickness severely attenuates the PBG and suppresses transmission in the blue region of the spectrum.

There is a significant increase in transmission intensity in the spectral region between the primary and secondary transmission dips, where Fabry-Pérot resonances in ordered FCC assemblies are normally found and we see that the edges of the PBG are attenuated on the lower energy red side resulting in a highly asymmetric PBG. The spectra obtained at high positive incidence of 25º show a well-defined PBG at the two highest volume fractions. As shown by our previous work, the PBG is highly attenuated at the three lowest volume fractions at this evaporation temperature, leading to the conclusion that this evaporation rate-volume fraction combination is the limit below which a breakdown in FCC symmetry for opals grown by EISA occurs.

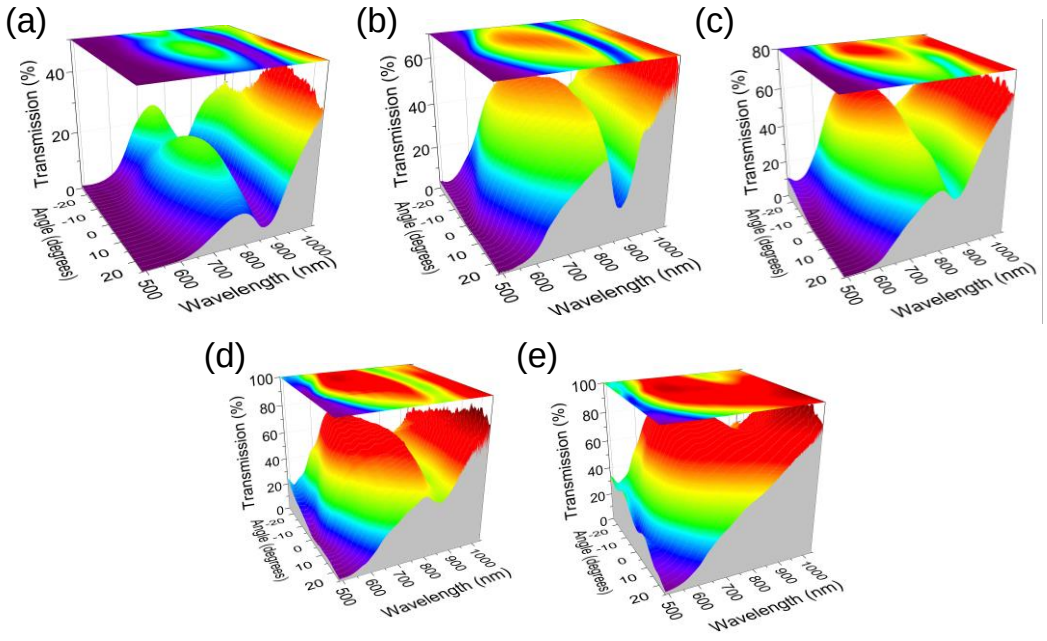


Figure 5.4. Angle-resolved transmission spectra of opals grown by EISA at 28 ºC for a range of concentrations of (a) 0.125 %, (b) 0.063 %, (c) 0.042 %, (d) 0.031 %, and (e) 0.025 % at a range of incident angles from -25º to 25º with corresponding 2D color maps of transmission intensity overhead.

For opals grown at 34 ºC, for the spectra acquired at the thickest region at higher negative incidence, there was high transmittance at the red side of the PBG, resulting in a red-skewed PBG for all volume fractions. In the 28 ºC case, the opposite occurs and a blue-skewed PBG occurs, particularly for the two lowest volume fractions. It appears that these crystals are better able to transmit blue light. Diffuse transmittance is also evident between the PBG and the secondary stopband, presenting in the form of Fabry-Perot resonances.(36)

Figures 5.4 (a)-(e) show the angle-resolved transmission spectra in order of increasing volume fraction from 0.025 % to 0.125 %. The FWHM of the PBG is broadest and of lowest transmission intensity at the largest volume fraction of 0.125 %. Transmission at the PBG increases with volume fraction as expected. Like the 34 ºC case, there is an asymmetry in the spectral window at the PBG, which becomes particularly pronounced at lower volume fractions. Unlike the 34 ºC case, the complete breakdown of FCC symmetry at the lowest volume fraction at higher positive angles of incidence is evident in Figure 5.4 (e), particularly in the 2D colour map which is saturated fully in red color (higher light transmission) as the PBG band disappears for all angles except those of highest negative incidence angles.

The secondary transmission dip corresponding to the (220) reflection of the FCC lattice is most evident from -25º to 0º for the two lowest volume fractions. The (220) dip can also be distinguished from -25º to 10º at the median volume fraction of 0.042 % in Figure 5.4 (c). In all cases the gradient to thinner opal films influences transmission across the full spectral region.

Nevertheless, the spectral shape of the PBG is well defined for all except the three lowest volume fractions. Even in the unfavourable conditions, larger thickness does not attenuate the PBG, and the PBG is best defined in the regions of maximum thickness. It is the decrease in structural order that causes attenuation and the regions of low thickness tend to form non-close packed arrays, defective areas, and dislocations, which significantly disrupt their associated spectral fingerprints.

5.4. Conclusions

Opals grown here by EISA demonstrate a thickness gradient along which stacking order decreases. This results in a reduction of the contrast and reflectivity of the PBG and is observed within the interaction beam waist of an opal film that is rotated between -25 and + 25º about the normal. Angle-resolved transmission spectra reveal a clear asymmetry in the spectral response of the PhC and the PBG spectral window. This asymmetry is a result of the thickness gradient and becomes particularly pronounced at low volume fractions of PS sphere used to grow the opal films. While the PBG is known to shift due to thickness at fixed angle, we have shown how the change in transmission intensity occurs in films where the PBG remains fixed in ordered regions and a spectral shift happens in more disordered regions. The influence on the overall spectra is very sensitive to thickness and order changes when the sample film is rotated. The spectra for all opals examined here demonstrate a similar trend, with a clearly defined PBG where thickness and order are greatest, and an attenuated PBG where thickness and order are minimal. Secondary Bragg reflections typically occur at high incident angles

but are shown here to appear at low incident angles where growth conditions are unfavourable for highly ordered, thicker opal films.

Changes to thickness and structure are common in many methods of opal PhC growth and this work highlights the care needed in assessing the angular dependence of the PBG either side of the normal and the overall transmission response, particularly when ordered periodicity is critical for the study or application. Changes in thickness and order that occur at the evaporation line during EISA, or the drying line for dip coating or other coating methods, affect order and this degree of order is shown to be sensitive to evaporation rate and the resulting thickness of the opal film either side of the normal to the incident light.

5.5. References

1. E. Yablonovitch, *Physical Review Letters*, **58**, 2059 (1987).
2. S. John, *Physical Review Letters*, **58**, 2486 (1987).
3. J. D. Joannopoulos, P. R. Villeneuve and S. Fan, *Nature*, **386**, 143 (1997).
4. H. Kurt and D. S. Citrin, *Opt. Express*, **15**, 1240 (2007).
5. E. Armstrong, W. Khunsin, M. Osiak, M. Blömker, C. M. S. Torres and C. O'Dwyer, *Small*, **10**, 1895 (2014).
6. A. Stein and R. C. Schroden, *Current Opinion in Solid State and Materials Science*, **5**, 553 (2001).
7. A. Arsenault, D. Puzzo, I. Manners and G. Ozin, *Nature Photonics*, **1**, 468 (2007).
8. A. Grant, A. Lonergan and C. O'Dwyer, *Optical Materials*, **142**, 114053 (2023).
9. Y. A. Vlasov, V. N. Astratov, O. Z. Karimov, A. A. Kaplyanskii, V. N. Bogomolov and A. V. Prokofiev, *Physical Review B*, **55**, R13357 (1997).
10. S. G. Johnson and J. D. Joannopoulos, *Applied Physics Letters*, **77**, 3490 (2000).
11. E. Armstrong and C. O'Dwyer, *Journal of Materials Chemistry C*, **3**, 6109 (2015).
12. A. Lonergan and C. O'Dwyer, *Advanced Materials Technologies*, **8**, 2201410 (2023).
13. A. E. Schedl, I. Howell, J. J. Watkins and H.-W. Schmidt, *Macromolecular Rapid Communications*, **41**, 2000069 (2020).
14. F. Gaufillet and É. Akmansoy, *Optics Communications*, **285**, 2638 (2012).
15. H. Ding, C. Liu, B. Ye, F. Fu, H. Wang, Y. Zhao and Z. Gu, *ACS Applied Materials & Interfaces*, **8**, 6796 (2016).
16. P. S. J. Russell, *J. Lightwave Technol.*, **24**, 4729 (2006).
17. W. Liu, H. Liu, X. Sun and F. Zhang, *Photonics*, **10**, 781 (2023).
18. Z. Xie, K. Cao, Y. Zhao, L. Bai, H. Gu, H. Xu and Z.-Z. Gu, *Advanced Materials*, **26**, 2413 (2014).
19. Y.-J. Lee and P. V. Braun, *Advanced Materials*, **15**, 563 (2003).
20. Y.-J. Lee, S. A. Pruzinsky and P. V. Braun, *Langmuir*, **20**, 3096 (2004).
21. Y. S. Zhang, C. Zhu and Y. Xia, *Adv Mater*, **29** (2017).
22. Z. Xie, L. Li, P. Liu, F. Zheng, L. Guo, Y. Zhao, L. Jin, T. Li and Z. Gu, *Small*, **11**, 926 (2015).
23. A. Lonergan, D. McNulty and C. O'Dwyer, *Journal of Applied Physics*, **124** (2018).
24. A. Lonergan, C. Hu and C. O'Dwyer, *Physical Review Materials*, **4**, 065201 (2020).
25. C. Luo, S. G. Johnson, J. D. Joannopoulos and J. B. Pendry, *Physical Review B*, **68**, 045115 (2003).
26. J. F. Galisteo-López, E. Palacios-Lidón, E. Castillo-Martínez and C. López, *Physical Review B*, **68**, 115109 (2003).
27. L. C. Andreani, A. Balestreri, J. F. Galisteo-López, M. Galli, M. Patrini, E. Descrovi, A. Chiodoni, F. Giorgis, L. Pallavidino and F. Geobaldo, *Physical Review B*, **78**, 205304 (2008).

28. M. Golosovsky, Y. Neve-Oz and D. Davidov, *Physical Review B*, **71**, 195105 (2005).
29. H. Míguez, V. Kitaev and G. A. Ozin, *Applied Physics Letters*, **84**, 1239 (2004).
30. B. Ding, M. E. Pemble, A. V. Korovin, U. Peschel and S. G. Romanov, *Physical Review B*, **82**, 035119 (2010).
31. R. C. Schroden, M. Al-Daous, C. F. Blanford and A. Stein, *Chemistry of Materials*, **14**, 3305 (2002).
32. A. Balestreri, L. C. Andreani and M. Agio, *Physical Review E*, **74**, 036603 (2006).
33. C. I. Aguirre, E. Reguera and A. Stein, *Advanced Functional Materials*, **20**, 2565 (2010).
34. B. Ding, M. Pemble, A. Korovin, U. Peschel and S. Romanov, *Applied Physics A*, **103**, 889 (2011).
35. M. Muldarisnur, I. Popa and F. Marlow, *Physical Review B*, **86**, 024105 (2012).
36. S. G. Romanov, T. Maka, C. M. Sotomayor Torres, M. Müller, R. Zentel, D. Cassagne, J. Manzanares-Martinez and C. Jouanin, *Physical Review E*, **63**, 056603 (2001).

Chapter 6

Comparing Cycling and Rate Response of SnO_2 Macroporous Anodes in Li-ion and Na-ion Batteries

Adapted from: Grant, A.; Carroll, A.; Zhang, Y.; Gulzar, U.; Ahad, S. A.; Geaney, H.; O'Dwyer, C. Comparing Cycling and Rate Response of SnO2 Macroporous Anodes in Lithium-Ion and Sodium-Ion Batteries. Journal of The Electrochemical Society 2023, 170 (12), 120505. DOI: 10.1149/1945-7111/ad0ff5.

Abstract

Tin oxide (SnO_2) is a useful anode material due to its high capacity (1493 mAh g^{-1} and 1378 mAh g^{-1} vs Li/Li^+ and vs Na/Na^+, respectively) and natural abundance (tin is one of the thirty most abundant elements on earth). Unfortunately, only moderate electrical conductivity and significant volume expansion of up to 300 % for Li-ion, and as much as 520% for Na-ion can occur. Here, we use an ordered macroporous interconnected IO (IO) architectures to enhance rate capability, structural integrity, and gravimetric capacity, without conductive additives and binders. Excellent capacity retention is shown during cycling vs Na/Na^+ relative to Li/Li^+. Cyclic voltammetry (CV) analysis, galvanostatic cycling, and differential capacity analysis extracted from rate performance testing evidence the irreversibility of the oxidation of metallic Sn to SnO_2 during charge. This behavior allows for a very stable electrode during cycling at various rates. A stable voltage profile and rate performance is demonstrated for both systems. In a Na-ion half-cell, the SnO_2 retained >76% capacity after 100 cycles, and a similar retention after rate testing.

6.1. Introduction

Li-ion battery chemistries dominate the commercial range of energy storage systems available due to superior energy density, lifetime, and stability compared to other chemistries. The ethical issues surrounding cobalt, one of the key components of Li-ion battery cathodes, have been well documented.(1) Li reserves are finite, and the current high demand is growing rapidly during the transition to a green energy future. Issues related to ethics and safety also surround the mining of Li.(2, 3) Alternative systems must be considered including Li sulfur,(4, 5) redox-flow,(6, 7) potassium-ion,(8, 9) and aluminium-ion.(10) Possibly the most promising substitute is Na-ion. Na lies in the top ten most abundant elements on earth and can be easily extracted by isolating seawater (Na chloride) and performing electrolysis when in its cooled, molten form. Given that graphite has maintained its status as the gold standard anode material for Li-ion systems, battery research has been dominated by efforts to maximise the performance of cathode materials, the limiting factor for energy density.

However, there is a dramatic drop in the capacity provided by graphite anodes in Na-ion systems. Many reports show an experimental discharge capacity of 35 mAh g^{-1} in Na-ion systems compared to the 335 mAh g^{-1} which can be achieved in Li-ion systems. Intercalation efficiency of alkali-ions in graphite can be evaluated by the formation energy of the corresponding intercalation compound. The two contributions to this formation energy are: (1) structural deformation energy and (2) binding energy.(11, 12) Structural deformation energy corresponds to the energy required to expand the spacing

between graphitic layers to accommodate ions. As a result, structural deformation energy is minimum for Li relative to the other alkali ions and this energy contribution increases along the Alkali metal group. However, the binding energy contribution does not follow the same trend. Na requires a much higher binding energy than Li, yet the binding energy of potassium is the minimum of the three. The binding energy is a direct consequence of the interaction between the *p*–orbitals of the carbon atoms of graphite and the active ions.(13) Review of the binding energies of the three alkali ions with carbon shows that Na requires the maximum energy, due to the least overlap with carbon in its sp^2 hybridised state. By obtaining the sum of the two energy contributions, the overall formation energy is minimum for Li, and a maximum for Na.(12, 14)

Fortunately, there are alternatives to intercalation materials, such as those which follow conversion(15) and alloying mechanisms.(16) The intercalation mode mechanism of charge transfer employed by graphite involves the shuttling of ions in and out of openings within the host structure. When conversion materials undergo electrochemical cycling, the active ions are inserted into nanosized binary compounds denoted by MX (M for transition metals such as Fe, Cu, Co, etc. and X for O, S, F, etc.) which results in the reduction of M cations to M^0 and the formation of LiX or NaX for Li-ion and Na-ion batteries, respectively. The microstructures suffer great changes and are usually associated with the recrystallisation of active materials.(17) The alloy mechanism proceeds by direct bonding between the inserted active ion and the host element A (A for Si, Sn, Ge, etc.) leading to the formation of Li-A and

Na-A alloys for Li-ion and Na-ion batteries, respectively.(18) The motivation for alloy materials for Li-ion batteries is based on the massive theoretical capacity of Li metal (3860 mAh g^{-1}), but many of these materials are associated with serious safety issues. For Na-ion batteries, Na metal also demonstrates high capacity (1166 mAh g^{-1}), but is highly reactive, yielding yet greater safety concerns. Li and Na alloys can be used which take advantage of the high capacities of each metal while maximising safety. In general, charge storage is directed so differently between the three mechanisms that there are distinct contrasts between the resultant capacity and morphology of the electrode.

Dual storage mechanism materials exist, known as conversion/alloy materials. These deliver high capacities but can suffer from significant issues such as large volume expansion,(19) mechanical brittleness, and unwanted side reactions with Na-based electrolytes.(20) The associated issues mean that experimentally, a wide range of novel adaptations and manipulations of the materials are introduced to improve performance.

One conversion-alloy material with potential for high performance in Na-ion systems is tin oxide (SnO_2), which provides a theoretical capacity of 1378 mAh g^{-1} and is highly sustainable, appearing in nature as the mineral cassiterite which can be mined from alluvium and placer deposits at seabeds(21) and processed without the high CO_2 emissions of graphite.(22, 23) SnO_2 is notorious for its volume expansion, up to 300% in a Li-ion system.(24-26) Unsurprisingly, volume expansion is further enhanced in Na-ion systems, up to 520%.(27-29) In the literature, efforts to improve

performance of SnO_2-based materials for Na-ion, and in fact Li-ion systems, appear in two primary forms: nanostructure design to buffer volume expansion and carbon-based nanocomposites to improve electronic conductivity. Typically, pure SnO_2 nanostructures for Li-ion and Na-ion batteries are designed with specific morphologies such as nanorods and nanotubes by involved methods like hydrothermal synthesis and electrospinning. Carbonaceous nanocomposites are often of complex designs such as hollow(29-31) or yolk-shell structures,(32-35) along with the embedding of SnO_2 nanoparticles into carbon or the encapsulation of SnO_2 nanostructures by carbon in forms such as graphene,(36-38) reduced graphene oxide (RGO),(39-42) and carbon nanotubes (CNTs),(43-46) among others. These complexities prompt an alternative approach.

IOs can be formed simply by colloidal self-assembly of a parent opal template, followed by infiltration by a metal alkoxide precursor and calcination of the template to form the IO. Detailed information on self-assembly of the opal template(47, 48) and subsequent IO preparation is provided elsewhere.(49-51) IOs consist of a macroporous, interconnected network with periodicity in three dimensions, usually a metallic or metal oxide material.(52-56) A type of PhC, they possess the ability to reflect wavelengths determined by the refractive index contrast and periodicity of the material.(57, 58) There are multiple benefits to their use as battery electrodes, and some trade-offs.(59, 60) Porosity provides high surface area to volume ratio. The interconnectivity removes the need for conductive additives/binders, which mitigates to a limited degree, the reduced volumetric mass loading of the

porous material. For conversion-alloy materials such as SnO_2, significant volume expansion is a characteristic issue faced during electrochemical cycling. The macroporosity of IOs provides excellent tolerance for such volume expansion. While mesoporous materials provide a similar tolerance for volume expansion and a higher surface area to volume ratio, the smaller pore size can adversely affect rate capability, inhibiting Li-ion (or Na-ion) flux into the electrode. The IOs studied in this work are formed as islands of interconnected material, each contacted to the underlying current collector. While the growth of crack-free IOs using evaporation coassembly methods has been performed elsewhere,(61-64) the cracks between islands in the IOs studied here provide a good environment for electrolyte soakage. For materials like SnO_2 which suffer from such dramatic volume expansion, potential effects like pore collapse and delamination can be localised to the area covered by the specific island of material. The primary motivation for the use of IOs here, lies in their charging and discharging rate capability. Thin pore walls consisting of an agglomeration of the active nanoparticles result in short ion diffusion distances, the limiting factor for rate performance.(65)

Here, structural analysis and electrochemical characterisation provide a comparative study of the behaviour of macroporous SnO_2 anode materials in Li-ion and Na-ion systems. We show these electrodes provide good capacity retention for the Na-ion system and we use analyses from cyclic voltammetry (CV), galvanostatic cycling and differential capacity to define and compare the nature of the reactions of macroporous SnO_2 with Li and Na during charging and discharging. Finally, the rate performance of the macroporous SnO_2 show

excellent cyclability and capacity recovery, particularly for the Na-ion case. Comparing the SnO_2 anodes in Li-ion and Na-ion systems simultaneously reveals the underlying causes underpinning the contrast in the response between the two systems.

6.2. Experimental

6.2.1. Preparation of SnO_2 IOs

Colloidal solutions of PS spheres in 2.5% (w/v) aqueous suspension with a nominal diameter of 510 nm were purchased from Polysciences Inc. The sphere suspension possessed a net negative charge due to functionalisation using a sulfate ester during formation to aid in self-assembly. The substrates used 316L stainless steel with a 15.5 mm diameter and 0.2 mm thickness. All substrates were cleaned using the same process: Successive sonication in acetone (reagent grade 99.5%; Sigma Aldrich), isopropyl alcohol (reagent grade 99.5%; Sigma Aldrich) and de-ionised water, each for 5 minutes. All cleaned samples were dried at room temperature in an inert atmosphere. The samples were treated in a Novascan PSD Pro Series digital UV-ozone system for 1 h to maximise hydrophilicity of the surface of the substrates immediately prior to opal template formation.

Opal templates were formed using evaporation-induced self-assembly where first the substrates were immersed in a diluted PS sphere solution with volume fractions in the range of 0.1% to 0.2% which were placed inside a Binder convection oven at temperatures between 55 – 60 °C for ~ 24 h. Once

the sphere solution was evaporated fully, the substrates were removed and left to dry in inert atmosphere at room temperature.

SnO_2 IOs were formed via infiltration of the opal template with a $SnCl_2$ precursor by drop casting followed by calcination at 450 °C in air for 1 h to oxidise and crystallise the material. The $SnCl_2$ complex used was a 0.1 M solution of tin (II) chloride dihydrate ($SnCl_2.2H_2O$, 98%; Sigma-Aldrich).

6.2.2. Materials Analysis

All scanning electron microscope (SEM) imaging was performed using a Zeiss Supra 40 high-resolution SEM at an accelerating voltage of 2 kV. SEM images and feature dimensions were analysed using ImageJ software. Transmission electron microscopy (TEM) combined with electron diffraction analysis was conducted using a JEOL JEM-2100F TEM operating at 200 kV to investigate structural parameters at the nanoscale. X-ray photoelectron spectroscopy (XPS) was performed using a Kratos AXIS ULTRA spectrometer with a detection limit of < 0.1 at %, ~1 mm^2 detection area, analysis depth of ~ 10 nm to determine the energy required to remove core electrons from their electron shells in the corresponding atoms or ions, known as the binding energy. Raman spectroscopy was performed with a Renishaw InVia Raman Spectrometer using a 30 mW Ar-ion laser under 532 nm excitation. The beam was focused onto the samples using a 50× objective lens and spectra were collected using a RenCam CCD camera. X-ray diffraction (XRD) measurements were performed using a Phillips Xpert PW3050 diffractometer with a Cu anode, Kα radiation with wavelength λ = 0.15406 nm, operating voltage 40 kV, current 20 mA.

6.2.3. Cell Assembly

Two cell configurations were used for Li-ion and Na-ion testing. (1) El-Cell PAT cells (ECC1–01–0012-A/L, 18 mm diameter, 0.65 mm thickness) operated as half-cells. (2) CR2032 coin cells (SS304, 20 mm diameter, 3.2mm thickness prior to crimping). The separators used in all cells were glass microfiber Whatman Grade GF/A cut to size.

Li-ion cells: The working electrode was an SnO_2 IO on stainless steel substrate, Li metal counter electrode, and 1 M solution of Li hexafluorophosphate ($LiPF_6$) in a 1:1 (v/v) mixture of ethylene carbonate: dimethyl carbonate (SigmaAldrich, battery grade), and no additives or binders were used.

Na-ion cells: The same configuration was used apart from a Na metal counter electrode and electrolyte which consisted of 1 M Na perchlorate ($NaClO_4$, AlfaAesar, $\geqslant$99%) in propylene carbonate (PC, $C_4H_6O_3$, SigmaAldrich, 99.7%). 5% fluoroethylene carbonate ($C_3H_3FO_3$, AlfaAesar, $\geqslant$99%) additive was used.

6.2.4. Electrochemical Characterisation

All electrochemical tests were conducted on a multichannel BioLogic VSP Potentiostat/Galvanostat. Electrodes were examined using cyclic voltammetry (CV) and constant current (galvanostatic) potentiometry. The details of potentials, applied currents, scan rates or voltage ranges are provided in the captions to each relevant figure.

Differential capacity analysis was performed on the galvanostatic rate testing data, where current density was ramped in four steps from 50-450 mAh g^{-1}, followed by a final step at 50 mAh g^{-1} for 20 cycles at each rate. From the capacity-voltage data, the discharge and charge stages were segregated at all rates. Numerical differentiation was performed on the discharges and charges for both the Li-ion and Na-ion cells to obtain dV/dQ, with the reciprocal taken to generate differential capacity (dQ/dV) data. Differential capacity plots (DCPs) were constructed as a plot of voltage versus cycle number vs differential capacity. A total of four DCPs corresponding to the discharge and charge profiles for the Li-ion and Na-ion systems were formed with an appropriate colour scale applied based on the differential capacity range observed.

6.3. Results and Discussion

6.3.1. Structure of macroporous SnO_2 electrode material

The details of the three-dimensional interconnected macroporous architecture of the SnO_2 IOs are demonstrated by scanning electron microscope (SEM) images in Figure 6.1. IOs grown from calcination of opal templates infilled with a sol-gel precursor, results in multi-layered islands of IO material as shown in Figure 6.1 (a). Throughout these IO samples, the islands consist of highly ordered, “honeycomb” layers of interconnected SnO_2, dominated by face-centered cubic (FCC) symmetry, evident in the higher magnification SEM images in Figure 6.1 (b) and (c). Growth of the opal template occurs perpendicular to the (111) plane of the FCC lattice.(66) The cross-sectional SEM image in Figure 6.1 (d), obtained at an angle of 30°, shows that the

honeycomb structure is continuous in three dimensions, rather than just the surface.

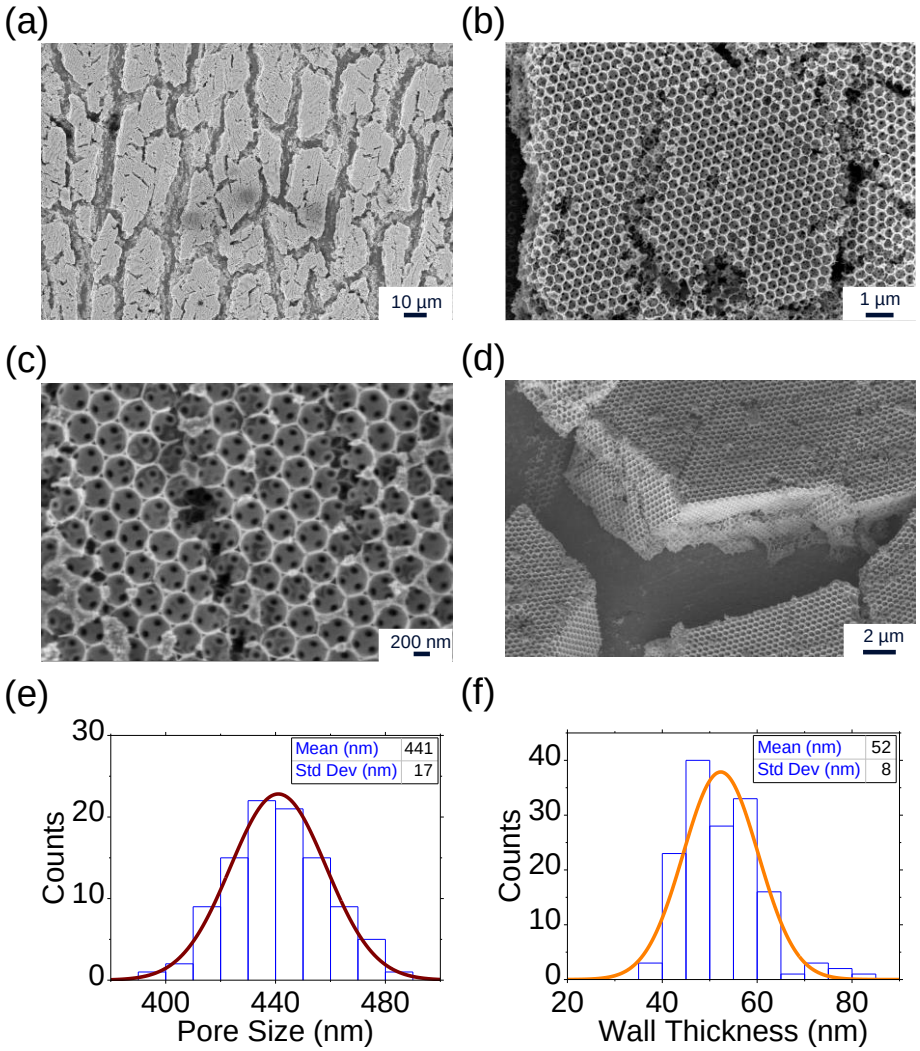


Figure 6.1. (a)-(c) Planview SEM images of SnO_2 IO at various levels of magnification. (d) Cross-sectional SEM image at a tilt angle of 30°. (e) Pore size distribution of SnO_2 IO obtained from SEM images. (f) Pore wall thickness distribution obtained from SEM images.

The SnO_2 IO pore size is also a direct consequence of the sphere diameter of the parent opal. Shrinkage occurs upon calcination of infiltrated opals. Here, the IO pore size distribution is shown in Figure 6.1 (e), with a mean diameter D of ~441 nm based on a parent opal template with a nominal sphere diameter of 510 nm. This macroporosity results in a high surface are

to volume ratio, while adequate space is provided for optimal electrolyte infiltration. The specific surface area can be approximated based on the calculated average macropore diameter assuming the IO has perfect FCC symmetry and neglecting the micropores and mesopores within the IO walls. Each FCC unit cell contains 4 macropores and the volume of each unit cell can be approximated as a^3, where the lattice parameter a = $D\sqrt{2}$. The surface area per unit volume can then be found by multiplying the surface area per unit cell by the number of unit cells per unit volume, resulting in a specific surface area per unit volume of 10.05 m^2/cm^3. The specific surface area per unit mass can be calculated based on the density of SnO_2 (6.95 g/cm^2)(67) and the volume fraction of SnO_2 material of a perfectly ordered FCC IO (0.26 %) as 5.56 m^2/g. Both calculated values are in good agreement with reports for IO structured metal oxide materials in the literature.(68, 69)

Figure 6.1 (f) shows the size distribution of the IO walls. One of the principal motivations for IO use as battery electrode materials, is the ability of interconnected macroporous materials to show excellent rate capability compared to dense or compact materials. The rate performance is a consequence of the thin IO pore walls in an electrolyte-soaked electrode, with a mean value of ~52 nm. Additional SEM images are provided in Figure S6.1 of the Supplementary Material.

Bright-field transmission electron microscopy (TEM) images in Figure 6.2 (a)-(c) show the morphology of the IO pores. For a structure dominated by FCC symmetry, contact points between layers occur as octahedral and tetrahedral interstitial sites, indicated in Figure 6.2 (a). These sites arise from

the ABC stacking arrangement of each layer. Each FCC unit cell of the porous SnO_2 material consists of eight tetrahedral and four octahedral sites all connected with walls of SnO_2. The symmetry of the IO is a direct consequence of the parent opal template. While these IOs have been considered as the direct inverse of their parent opal templates in the literature, recent work from our group has revealed that a slight deviation occurs from the symmetry of the template. The proposed explanation for this deviation is due to a reported tendency for preferential filling of the tetrahedral sites (orange circles in Figure 6.2 (a)) before the octahedral sites (red circles in Figure 6.2 (a)) during infiltration of the opal template.(70) While this slight deviation in symmetry has a pronounced impact on the photonic character of the IOs, there is no reported evidence that this impacts the electrochemical performance of the material.

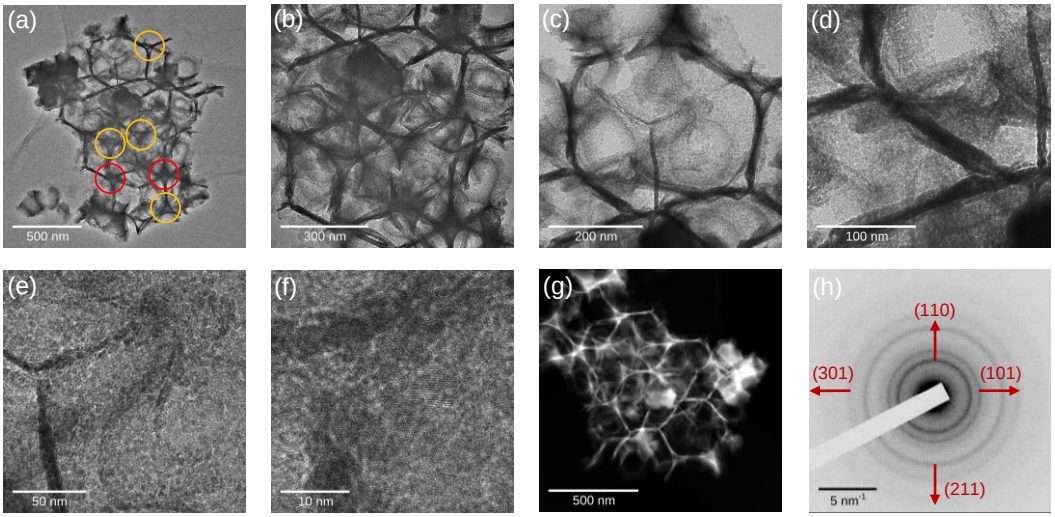


Figure 6.2. (a)-(d) TEM images of SnO_2 IO at various levels of magnification. Red circles: Octahedral sites. Orange circles: Tetrahedral sites. (e)-(f) HRTEM images showing configuration of nanoparticles within the pore walls and the fringes of the SnO_2 lattice. (g) STEM image of SnO_2 IO. (h) Electron diffraction pattern of SnO_2 IO with indexed lattice planes.

Figure 6.2 (e) and (f) show high resolution transmission electron microscope (HRTEM) images of the crystalline SnO_2 nanoparticles that

comprise the IO walls. Scanning transmission electron microscope (STEM) images of the SnO_2 IO are shown in Figure 6.2 (f)(g), focusing on the surface of the IO structure. Further TEM images are provided in Figure S6.2 of the Supplementary Material.

While the HRTEM images are not of a sufficient resolution to accurately measure the d-spacings between lattice fringes, the electron diffraction pattern in Figure 6.2 (h) provides the same information. The concentric rings demonstrate the highly ordered, polycrystalline structure of the SnO_2 IO. The low index lattice planes are identified by red arrows. Based on the radii of the indexed rings, the measured d-spacing of the atomic planes of the SnO_2 IO is 0.33 nm, in good agreement with the theoretical value for the (110) lattice plane of tetragonal SnO_2.(71, 72) The remaining measured d-spacings are 0.26 nm, 0.17 nm, and 0.14 nm, associated with the (101), (211), and (301) lattice planes, respectively.

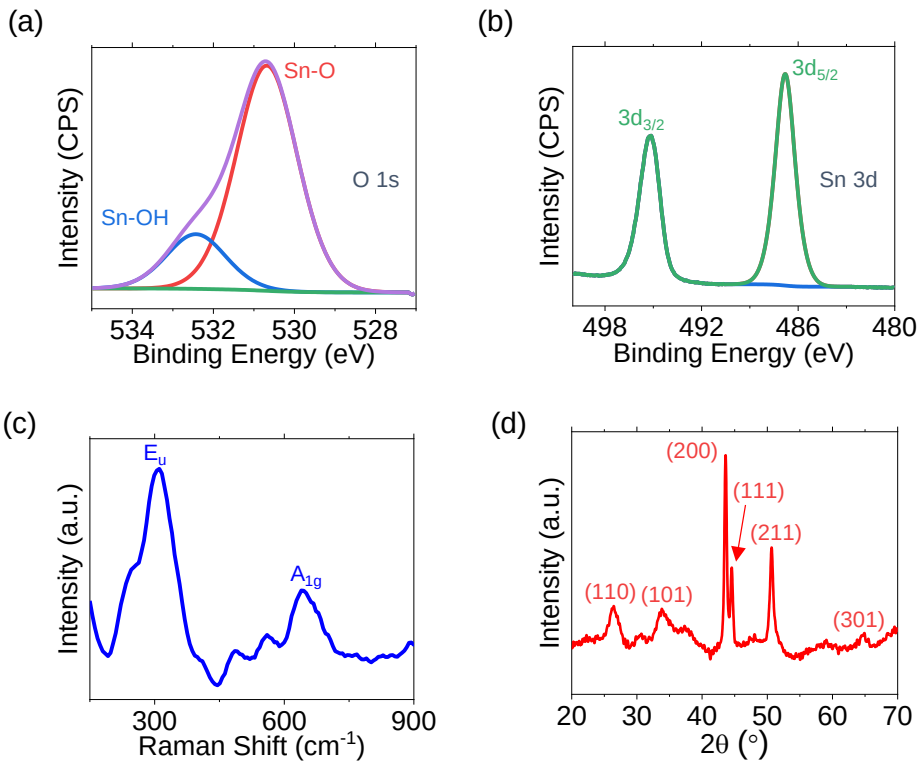


Figure 6.3. XPS core-level photoemission spectra of the (a) O 1s region and (b) Sn 3d region for a SnO_2 IO. (c) Raman scattering spectrum of SnO_2 IO. (d) XRD spectrum of SnO_2 IO showing reflections associated with tetragonal SnO_2.

Figure 6.3 (a) shows obtained X-ray photoelectron spectroscopy (XPS) measurements for SnO_2 IO samples corresponding to the O 1s core-levels in SnO_2. The strong photoemission observed at 530.7 eV is in good agreement with values in the literature corresponding to the O 1s core level electrons of SnO_2.(73) A weaker peak is observed at 532.4 eV which, based on reports, is caused by the multiplicity of the adsorbed hydroxyl species at the material surface.(74) Figure 6.3 (b) shows the XPS spectrum corresponding to the Sn 3d region. For the 3d core-level region, peaks occur at 495.24 eV and 486.77, corresponding to the binding energies of Sn $3d_{3/2}$ and Sn $3d_{5/2}$,(75) respectively. The doublet photoemission confirms the formation of Sn^{4+} and thus the presence of SnO_2. The associated Raman scattering spectrum is

shown in Figure 6.3 (c). Two primary peaks are observed at ~643 cm^{-1} and ~312 cm^{-1}. The prior is the characteristic A_{1g} band of SnO_2, which appears due to expansion and contraction of the Sn-O bond.(76, 77) The latter is ascribed to the E_u band, which is indicative of amorphous or nanocrystalline character, arising due to the nanoparticulate nature of the SnO_2 IO.(78) The X-Ray diffraction spectrum in Figure 6.3 (d) suggests that the nanocrystallites within the IO pore walls exist in the characteristic tetragonal SnO_2 phase with space group *P42/mnm* with two SnO_2 molecules per unit cell.(79) The calculated d-spacing for the SnO_2 IO based on the observed (110) reflection is 0.34 nm, in good agreement with the value of 0.33 nm calculated previously from the electron diffraction pattern. The d-spacings from all observed reflections were calculated and used to determine the lattice parameters of tetragonal SnO_2 as $a \approx 0.47$ nm and $c \approx 0.32$ nm which agree with values reported in the literature for nanoparticulate SnO_2.(80-82)

6.3.2. Voltammetric comparison in Li-ion and Na-ion cells

Cyclic voltammetry (CV) experiments were conducted at a scan rate of 0.1 mV s^{-1} in a voltage window of 0.01 V to 3.0 V vs Li^+/Li and vs Na^+/Na for Li/SnO_2 and Na/SnO_2 half cells, respectively. The results for the first five cycles are shown in Figure 6.4 (a) and (b). Based on previous reports, the reversible redox conversion process between SnO_2 and metallic Sn in a Li-ion system proceeds as follows:(83)

$$SnO_2 + 2Li^+ + 2e^- \leftrightarrow SnO + Li_2O \quad (6.1)$$

$$SnO + 2Li^+ + 2e^- \leftrightarrow Sn + Li_2O \quad (6.2)$$

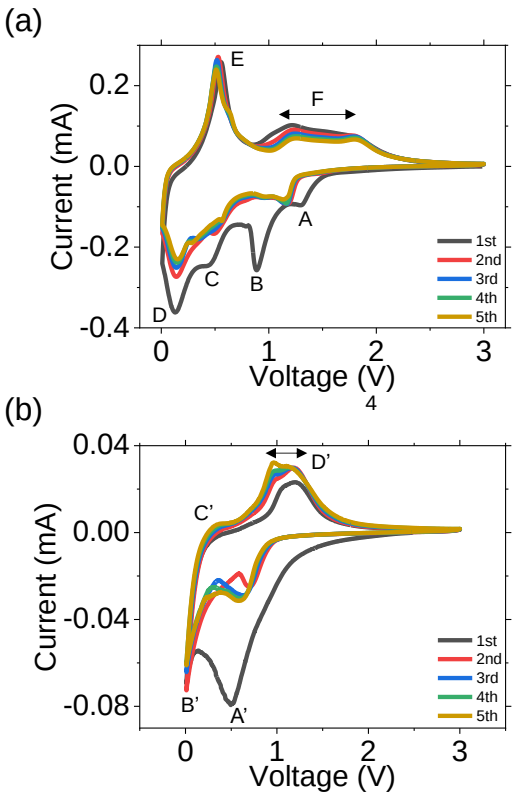


Figure 6.4. Cyclic voltammetry curves obtained over 5 cycles for SnO_2 IO in a (a) Li-ion system and (b) a Na-ion system in a potential window of 0.01 V to 3.0 V at a scan rate of 0.1 mV s^{-1}. The electrode was initially swept from 3.0 V to 0.01 V in each case.

In the first cathodic scan of the Li-ion system shown in Figure 6.4 (a), peak A is observed at 1.31 V, indicative of the onset of the reduction process of SnO_2 to metallic Sn.(32) This grows to form a distinct peak in the second scan at 1.18 V which is incrementally shifted with subsequent scans ending at 1.13 V for the fifth. Peak B at 0.89 V is attributed to the formation of the SEI layer.(84) The onset of the alloying mechanism is indicated by peak C at 0. 41 V and the strongest, broad peak of the first cathodic scan occurs at 0.13 V (peak D), corresponding to the maximum current response of the alloying mechanism of metallic Sn with Li to form nanoparticulate Li_xSn as below:(85)

$$Sn + \chi Li^+ + \chi e^- \leftrightarrow Li_\chi Sn, (0 \leq \chi \leq 4.4) \quad (6.3)$$

For the alloying peak, the current response decreases significantly for the second scan while only a minor decrease occurs in those that follow. There is slight change in the potential, with the peak centre shifted only from 0.14 V and 0.15 V from the second to the fifth scan. Minor current responses and additional smaller peaks are observed in the vicinity of the broad alloying peak after the first scan, indicating a more progressive alloying regime as cycling continues.(86)

In the anodic portion of the CV scans for the Li-ion system, the strong, relatively narrow peak E occurs for all five cycles due to the dealloying process of $Li_\chi Sn$ back to metallic Sn. In the first anodic scan, the peak is centred at 0.56 V and gradually shifts towards lower potentials for each cycle. The peak current increases for the second scan before decreasing incrementally for subsequent scans as expected. Peak F corresponds to the oxidation of metallic Sn to SnO_2 which occurs at 1.22 V in the first anodic scan and shifts to slightly higher potentials for the following scans. The large width of the peak indicates that like the alloying process, oxidation from metallic Sn to SnO_2 is progressive, even for the first cycle in this case. The peak width increases with each scan.

In Figure 6.4 (b), the electrochemical response of SnO_2 in the Na-ion system is illustrated. While the reaction steps are similar to the Li-ion case, the reversibility of the reaction is significantly limited in a Na-ion system.(87) Such irreversibility reduces capacity, given that the total capacity delivered is the

sum of the capacities delivered by the Sn redox and Sn-Na alloying processes. Based on the literature, the conversion process proceeds as follows:(88)

$$SnO_2 + 4Na^+ + 4e^- \leftrightarrow Sn + 2Na_2O \quad (6.4)$$

In the first cathodic scan, a steep current gradient begins at ~1.23 V and forms the largest peak A' at 0.51 V, which represents the reduction of SnO_2 to metallic Sn. An absence in any discernible peak representative of SEI formation is noted, which is expected to appear at ~0.4 V based on previous reports.(89) The initial conversion process to form metallic Sn causes significant structural changes in the presence of Na. The electrolyte species are susceptible to decomposition, catalysed by the reduced Sn nanoparticles.(90) While electrolyte decomposition is problematic in both Li-ion and Na-ion systems, Na-based electrolytes are relatively unstable.(91) Wang and coworkers reported peaks between 0.6 V and 0.1 V associated with irreversible decomposition of the electrolyte during the first cathodic scan for their SnO_2/MWCNT nanocomposite Na-ion batteries.(46) The reported difficulties in controlling SEI species for these Na-ion batteries prompted the use in this work of FEC as a stabilisation additive. The current gradient between ~1.23 V and 0.51 V, caused by localised phase changes, possible effects due to volume expansion, electrolyte decomposition and unstable SEI species masks any peak related to SEI formation and reaches a maximum where the rate of conversion to metallic Sn is highest at 0.51 V. For the second cathodic scan, the current is significantly lower and shifted to a higher voltage of 0.7 V. For subsequent scans, the current response increases, and the peaks are shifted to incrementally lower voltages. The trend indicates that conversion

of the SnO_2 nanoparticles to metallic Sn occurs gradually throughout the structure during the first few cycles.

Peak B' occurs sharply at 0.01 V in the first cathodic scan and can be attributed to the alloying of metallic Sn with Na to form amorphous $Na_\chi Sn$ nanoparticles dispersed in an Na_2O matrix as below:(92)

$$Sn + \chi Na^+ + \chi e^- \leftrightarrow Na_\chi Sn, (0 \leq \chi \leq 3.75) \quad (6.5)$$

When χ is 3.75, $Na_\chi Sn$ crystallises into the final discharge product, $Na_{15}Sn_4$. Unlike the peak associated with reduction of SnO_2 to metallic Sn, the magnitude of the alloying peak current sees little change through the five cycles examined and there is a negligible voltage shift. There is a stark contrast in the relative peak currents between the reduction and alloying processes in the first cycle compared to all subsequent cycles. The reduction peak current is greater by a multiple of three than the alloying peak during the first cathodic scan. For the following scans, the situation is reversed, and the alloying peak current is greater by a multiple of two than the reduction peak current. The results show that while the alloying regime provides the dominant capacity contribution throughout the lifetime of the cell, the conversion of SnO_2 to metallic Sn dominates the first cycle. Volume expansion is maximal during the first cathodic scan. This step, which includes both a significant structural change to the entirety of electrode material that undergoes an uptake of Na ions, and a distinct chemical reaction which forms a new compound from which the energy of the system is extracted, heavily influences the performance of the system throughout subsequent cycles.

An additional insertion reaction has been found during the beginning of the first discharge process by Wang and co-workers which proceeds as follows:(93)

$$Na^{+} + SnO_2 \leftrightarrow NaSnO_2 \qquad (6.6)$$

However, there is no current response in the first cathodic scan to indicate such insertion has taken place here. Occurrence of the insertion reaction significantly enhances capacity above that provided by the conversion and alloying reactions, but the galvanostatic cycling results in the following section show no evidence of such additional capacity.

During the first anodic scan, there is an absence of any discernible peak corresponding to the dealloying mechanism of Na_XSn_4. However, a positive current gradient begins at ~0.31 V (point C'), which indicates the beginning of the dealloying process. The positive current gradient continues from this point up to the distinct peak D' at 1.21 V, indicative of the oxidation process of metallic Sn to SnO_2, so it is difficult to determine the point at which dealloying ceases and oxidation begins. Like the Li-ion case, peak D' is broad and indicates a gradual oxidation process. The low current response, combined with reports from the literature strongly suggests that neither process nears completion.(94, 95) The difficulties related to detection of the dealloying mechanism can be understood based on work by Ghu et al. in 2013.(96) The failure mechanism of nanowire SnO_2 in Na-ion batteries was probed using in-situ TEM. It was found that during the alloying mechanism where Na_XSn is formed, massive structural change causing volume expansion of over 100% (its contribution to a possible volume expansion of 520 % throughout cycling)

occurs. Simultaneously, a Na_2O matrix is formed, surrounding the Na_XSn particles. The matrix then acts as an impediment to the dealloying process. When dealloying does occur, vacancies arise which lead to a disconnected network within the electrode. In the subsequent scans, the sharp peak at 1.21 V broadens to form a doublet peak, with maxima at 1.1 V and 0.96 V for the fifth cycle. The broad, doublet peak indicates a two-step oxidation process after the first cycle, like the equivalent oxidation process in the Li-ion system.

These CV results demonstrate distinct differences in the electrochemical processes that govern the current response from an SnO_2 anode in Li-ion and Na-ion systems, which can be summarised by three main points. (1) Overall current response: For the Na-ion system, the magnitude of the current during each CV scan is much lower, where all peak currents associated with both conversion and alloying processes are greater by multiples for the Li-ion system. Low charge flow is often a result of low conductivity, indicating that a large proportion of active material remains unused, and the associated reactions are incomplete.(97) (2) Lithiation versus sodiation: Broad, well-defined peaks are observed for all processes over the 5 cycles investigated for the Li-ion system. For the Na-ion system, not all the peaks are clearly defined, with some of the expected current responses such as SEI formation undetected. The contrast indicates a more efficient, progressive lithiation relative to sodiation, despite that sodiation speed has been reported as ~20× lower than that of lithiation.(89) More efficient charge flow in the Li-ion system results in greater usage of the active material, and a more uniform lithiation process. While the sodiation speed is slower, its

utilisation of less active material means that sharp current responses, as seen for the alloying process, occur due to more instantaneous sodiation in localised areas rather than a gradual mechanism throughout the entire electrode. (3) Impact of first CV scan: For the Li-ion system, each CV scan demonstrates the same set of peaks, except for those related to SEI formation in the first scan. Peak currents decrease incrementally, with slight voltage shifts as expected. For the Na-ion system, there is a stark contrast between the first scan and all subsequent scans. Considerable volume expansion and unstable electrolyte evolution is assumed to occur during the first scan, and the associated peak currents are not representative of the subsequent behaviour of the system. Following this first scan, the curves follow a much more stable pattern, with incrementally lower peak currents and slight voltage shifts as in the Li-ion case.

6.3.3. Galvanostatic cycling comparison in Li and Na half cells

The response of SnO_2 IOs in Li-ion and Na-ion half cells is demonstrated here using the galvanostatic cycling results presented in Figure 6.5 at a current density of 50 mA g^{-1} in both cases.(98) The calculations of the theoretical capacities for SnO_2 is based on the sum of the capacities of conversion and alloying charge storage mechanisms in each system.

For the alloying reaction in a Li-ion system based on the maximum molar ratio of 4.4 during conversion as per equation 6.3 the theoretical capacity is 782 mAh g^{-1}. The equivalent calculation for the Na-ion system, based on a molar ratio of 3.75 during conversion, results in a theoretical capacity of 667 mAh g^{-1}. In both systems, the conversion reactions result in a

capacity of 711 mAh g^{-1}. The total theoretical capacity for the Li-ion and Na-ion systems are 1493 mAh g^{-1} and 1378 mAh g^{-1}, respectively.

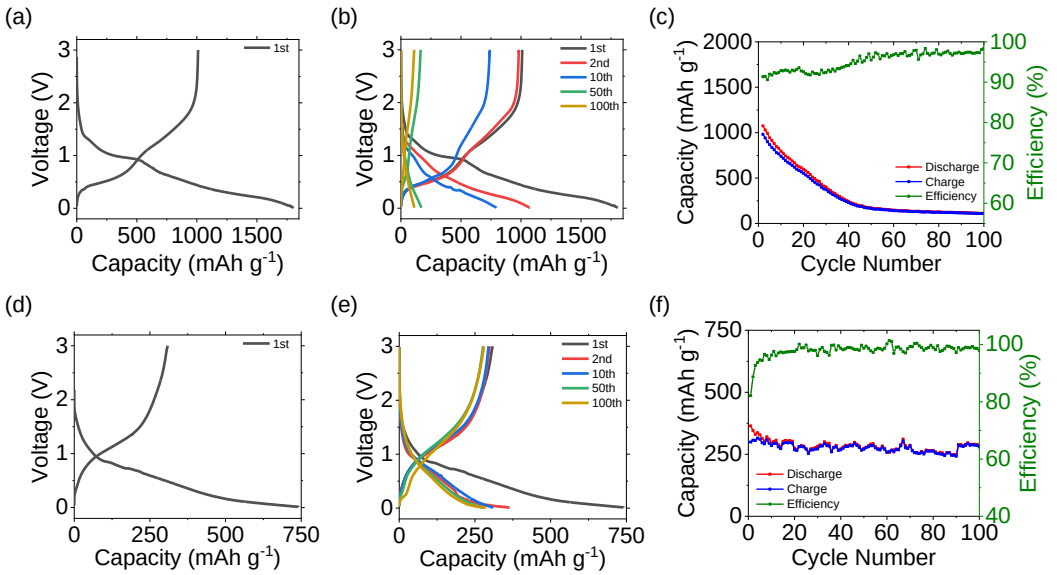


Figure 6.5. Galvanostatic cycling for a SnO_2 IO in a Li-ion half-cell at a specific current of 50 mA g^{-1} showing (a) charge and discharge voltage profiles for first cycle, (b) a range of select charge discharge profiles up to the 100th cycle and (c) specific capacity and coulombic efficiency (CE) as a function of cycle number. Galvanostatic cycling results for a SnO_2 IO in a Na-ion half-cell at a specific current of 50 mA g^{-1} showing (d) charge and discharge voltage profiles for first cycle, (e) a range of select charge discharge profiles like the Li-ion half-cell and (f) specific capacity and coulombic efficiency as a function of cycle number.

Figure 6.5 (a) shows the capacity-voltage profile for the first cycle in the Li-ion system. The current density of 50 mA g^{-1} corresponds to a C-rate of 0.033 C, based on a theoretical maximum for 1C = 1493 mA g^{-1}, corresponding to the sum of the theoretical capacities delivered by the reduction to metallic Sn, and the formation of the $Li_{4.4}Sn$ alloy. The first discharge capacity is 1806 mAh g^{-1}. Above the theoretical value, this additional capacity can be attributed to the formation of the SEI layer on the IO surface, along with the formation of quasi-reversible Li_2O from SnO_2 nanoparticles.(99) The voltage plateau of the first discharge begins just above 1 V as expected based on the CV results,

where the onset of the reduction mechanism begins. The plateau is further enhanced below 0.5 V, where alloying begins. Figure 6.5 (b) shows the evolution of the capacity-voltage profiles for select cycles up to the 100th cycle. A significant drop in capacity for the 2nd cycle is observed as expected, with a value of 1075 mAh g^{-1}, which is below the theoretical capacity. While in the first cycle capacity above the theoretical is provided by the energy related to SEI formation, the drop below the theoretical for the second cycle is a result of irreversible capacity loss from the initial reduction and alloying processes, along with volume expansion of the electrode material and unwanted side reactions with SEI species.

In Figure 6.5 (c), the maximum specific capacities for the discharge and charge of each cycle, along with the Coulombic efficiency (CE) for the Li-ion system are shown. The most notable aspect of these results is the relatively poor capacity retention. Most of the capacity is lost in the first 40 cycles, and the capacity stabilises considerably after 60 cycles. The discharge capacity at the 100th cycle is 112 mAh g^{-1}. The continued stability at this capacity level up to 250 cycles is demonstrated in Figure S6.3. Low initial CE is a symptom of the large initial irreversible capacity due to large volume expansion of SnO_2 upon Li uptake.(100) While an initial low CE is typical of SnO_2 anodes,(101) the value remains low for the first 40 cycles, where the most dramatic loss in capacity occurs, an atypical trend as the CE usually stabilises in early stage cycling, indicating that during the first 40 cycles, the rate of Li insertion is affected at a far greater rate than its removal. The value then increases and stabilises to a value of 98% at 60 cycles.

The first discharge for the Na-ion system, shown in Figure 6.5 (d), is 741 mAh g^{-1}. The value is considerably lower than the theoretical capacity of 1378 mAh g^{-1} predicted by Faraday's law, which is the sum of the capacities delivered by the reduction to metallic Sn and the formation of the $Na_{3.75}Sn$ alloy. However, it is representative of the first discharge capacities reported in the literature for SnO_2 anodes in Na-ion systems.(102) Given that the difference between the theoretical and practical capacity of SnO_2 in Na-ion systems is well established, more accurate C-rate calculations can be performed here if based on the nominal capacity of 667 mAh g^{-1} . The current density of 50 mA g^{-1} corresponds to 0.075 C based on 1C = 667 mA g^{-1}. In Figure 6.5 (e), the second discharge capacity is 364 mAh g^{-1}. The large irreversible capacity loss here is again attributed to SEI formation, along with the irreversibility that has been documented in both the initial conversion and alloying reactions for SnO_2 vs Na/Na^+. The voltage plateaus occur at a slightly lower voltage than the Li-ion case, starting at about 1 V with the reduction of SnO_2 to metallic Sn. A second increase in the plateau is observed below 0.1 V, attributed to the alloying reaction of metallic Sn to form the Na_xSn phase. Figure 6.5 (f) shows the maximum specific capacities for the discharge and charge for each cycle, along with the CE for the Na-ion system. Like the Li-ion system, the initial value is indicative of SEI formation which tends to prevent Na^+ insertion at a greater rate than its removal. However, the value stabilises at 20 cycles and does not drop below 96% past this point. While the capacity of the second cycle is approximately half that of the Li-ion system, the capacity retention is significantly better. The capacity of the 100th cycle is ~280 mAh g^{-1}, representing a total loss from the 2nd to the 100th cycle of only 85 mAh g^{-1}, a

capacity retention of 76.6%. The impressive capacity retention of the SnO_2 IO in the Na-ion system is one of the key results of this work.

6.3.4. Comparing rate capability in Li- and Na-ion cells

Figure 6.6 (a) shows the results from macroporous SnO_2 IO rate performance testing for a Li-ion system. Figure 6.6 (b) shows the capacity-voltage profiles for select cycles performed prior to rate testing to demonstrate the initial capacities reached. The profiles in Figure 6.6 (c) correspond to cycles during maximum rate testing at 450 mA g^{-1}. Figure 6.6 (d) shows profiles from the last stage of rate testing where the current density was reduced back to the initial testing value of 50 mA g^{-1} to evaluate the ability of the electrode to recover some of the capacity not accessed at higher rates. Comparison of the capacity achieved at low current density in the initial and final stages of rate testing is indicative of the extent to which the electrode has been degraded.

The initial discharge capacity during rate testing at 50 mA g^{-1} is ~900 mAh g^{-1}. The initial discharge capacity during the last stage of rate testing when returned to 50 mA g^{-1} is ~660 mAh g^{-1}, representing a capacity retention of ~73%. For comparison, one study reported SnO_2 nanotubes which demonstrated a capacity retention of ~52% after rate performance testing for 50 cycles.(103) Our rate performance results are similar to those reported previously in our group for an SnO_2 anode tested in a Li-ion system.(104)

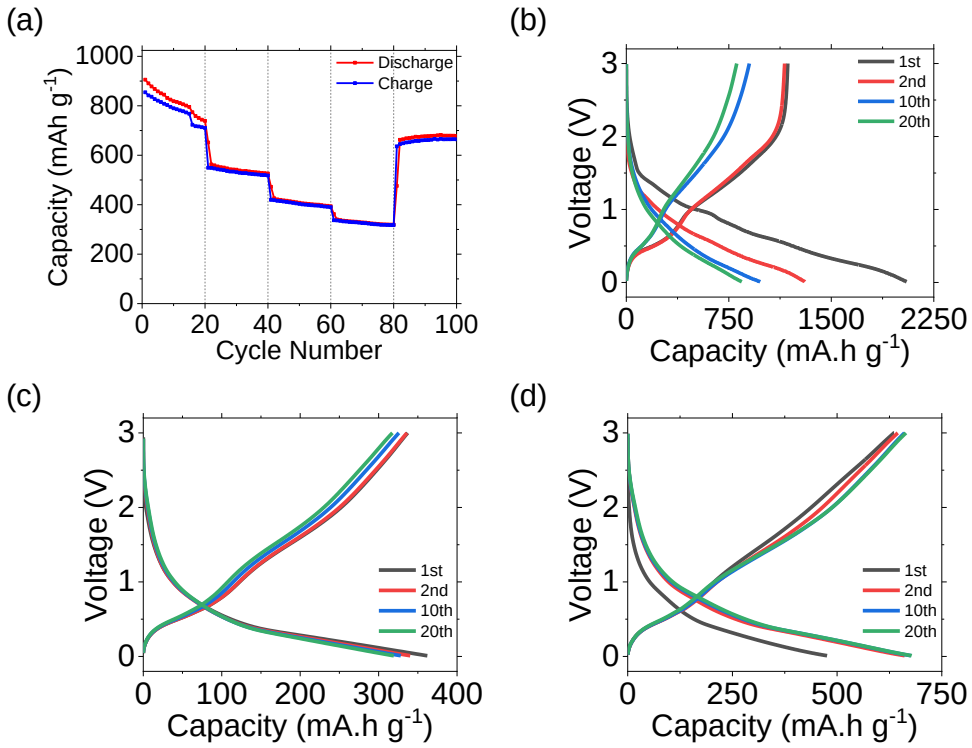


Figure 6.6. (a) Rate capability testing of SnO_2 IO in Li-ion system. Galvanostatic cycling curves (b) for initial specific settling current of 50 mA g^{-1} prior to the rate test, (c) maximum specific current applied during rate test of 450 mA g^{-1}, and (d) charging and discharging at a final current of 50 mA g^{-1}.

While there is a significant reduction in the capacity during the 10 cycles at the first rate of 50 mA g^{-1}, it stabilises from the second rate. The capacity reduces with each increase in current density as expected. The capacity recovery after maximum rate cycling is at the higher end of values reported in the literature.(105, 106) From the capacity-voltage profiles, those in Figure 6.6 (b) demonstrate the expected shape based on the conversion and alloying reactions of SnO_2 in a Li-ion system. In Figure 6.6 (c) and (d), the curves are attenuated relative to those corresponding to the initial rate, indicating that the reactions are inhibited from reaching completion particularly at voltages above 1 V.

Figure 6.7 (a) shows rate performance testing results for a SnO_2 IO in a Na-ion system. The current densities used for rate testing are identical to those used for the Li-ion system. A total of 20 cycles at 25 mA g^{-1} were performed prior to rate testing and the associated charge-discharge curves are shown in Figure 6.7 (b). Low initial current densities are used for most reports in the literature for pure SnO_2 anodes in Na-ion systems.(30, 107) The low current densities are due to the significant volume expansion typical of the conversion and alloying reactions between SnO_2 and Na/Na^+. For alkali-ion batteries, the beginning of any cycling regime corresponds to the most vulnerable stage and the system typically only stabilises after the first few cycles.(108, 109) The initial discharge capacity for the rate test is ~400 mA g^{-1}. From the rate performance data, there are two key findings. Firstly, efficient cyclability is evident. Stable capacities are observed for each rate with a gradual decrease in capacity as current density increases, reaching a minimum of 150 mAh g^{-1} at the highest rate of 450 mA g^{-1}. The associated charge-discharge curves are shown in Figure 6.7 (c) which further emphasise the stability in that their shape is retained with a strong plateau during discharge still observed just below 1 V. Second, for the final rate where current density is lowered back to 50 mA g^{-1}, the system demonstrates excellent capacity recovery to 298 mAh g^{-1}. The associated charge-discharge curves are shown in Figure 6.7 (d). The capacity retention of the system after the rate performance test over the 100 total cycles is ~74%.

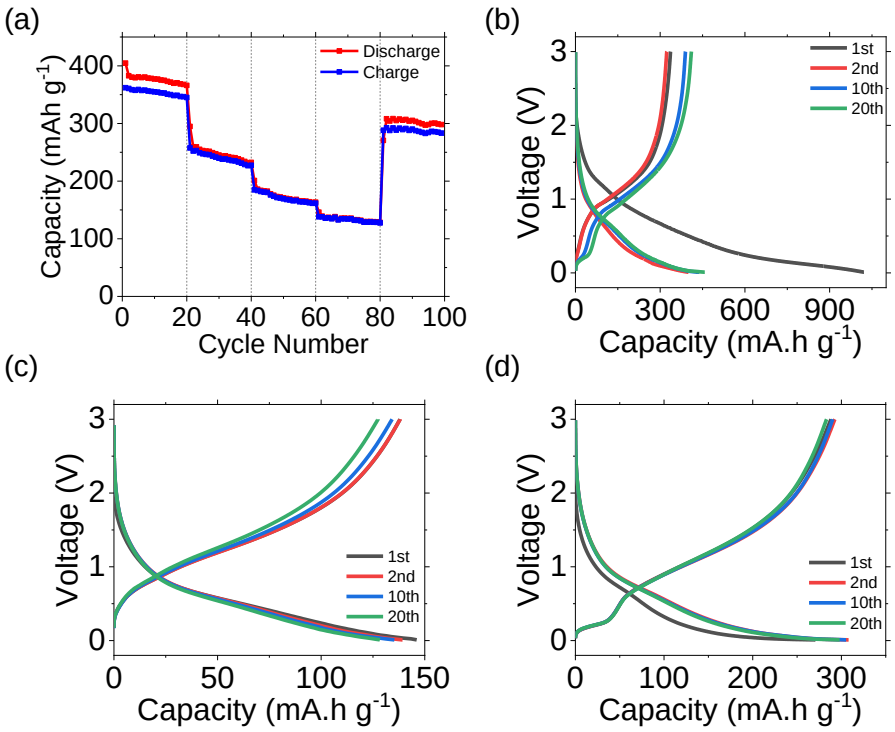


Figure 6.7. (a) Rate capability testing of SnO_2 IO in Na-ion system. Galvanostatic cycling curves (b) for initial specific settling current of 25 mA g^{-1} prior to rate test, (c) maximum specific current applied during rate test of 450 mA g^{-1}, and (d) final current of 50 mA g^{-1}.

The rate capability of SnO_2 IO anodes has been demonstrated here for both Li-ion and Na-ion systems. For Na-ion systems, the capacity values and stability at higher specific currents match or exceed many previous reports on purely nanostructured SnO_2 anodes,(110, 111) and even with reports of more conductive carbonaceous SnO_2 nanocomposites.(112-114) Table S6.1 of the Supplementary Material provides a breakdown of the retained capacities for a range of pure SnO_2 nanostructures and carbonaceous SnO_2 nanocomposites after rate performance testing compared to the SnO_2 IOs investigated in this work.

6.3.5. Reversibility of conversion between SnO_2 and metallic Sn

The conversion and alloying mechanisms dominate charge delivery for SnO_2 in both Li-ion and Na-ion systems. The peaks associated with these mechanisms are evident in the CVs, as shown earlier for a fixed scan rate of 0.1 mV s^{-1}. For a perfectly reversible system, the potentials at which these peaks occur remain unchanged, irrespective of the scan rate applied. One of the ways to distinguish between reversible, quasi-reversible and irreversible processes is by examining the change to the CVs with scan rate. Li^+ and Na^+ intercalation reactions tend to follow quasi-reversible processes, where peak potential shift to higher values with an increase of scan rate due to overpotential.(115) The conversion reactions between SnO_2 and both Li^+ and Na^+ follows a similar trend. However, the conversion mechanism of SnO_2 in Na-ion batteries has been documented as less reversible. Figure 6.8 (a) and (b) show CVs for a range of scan rates from 0.05 mV s^{-1} to 5 mV s^{-1} for the Li-ion and Na-ion systems, respectively. These results were obtained after five cycles at a fixed scan rate of 0.1 mV s^{-1}. CV scans obtained within the same range of scan rates without any prior fixed rate scanning are provided in Figure S6.4 of the Supplementary Material. The overall current response increases as a function of scan rate as expected. The irreversibility of the oxidation and reduction mechanisms can be quantified by the peak separation (ΔV_{conv}) between the oxidation peak potential ($V_{p,a}$) during the anodic scan, and the reduction peak potential ($V_{p,c}$) during the cathodic scan. Figure 6.8 (c) shows ΔV_{conv} as a function of scan rate for the Li-ion and Na-ion systems. At scan rates below 0.25 mV s^{-1}, peak separation is minimal. Above this, the peak

separation for the Na-ion system is more than double that of the Li-ion system, indicating greater irreversibility for the Na-ion system.

The reactions which govern the peak currents in a battery system are a sum of the contributions of Faradaic (diffusive) and non-Faradaic (capacitive) processes.(116) The relationship between the magnitude of observed peak currents and the scan rate (v) can be described by the Randles-Sevcik equation and used to quantify the diffusive and capacitive contributions to peak current at a specific potential.(115) For a capacitive-driven process, the associated current response is proportional to v. For a diffusion-driven process, the current response is proportional to $v^{1/2}$. The current associated with the oxidation ($I_{p,a}$) and reduction ($I_{p,c}$) peaks are shown as a function of ($v^{1/2}$) for the Li-ion system in Figure 6.8 (d). Figure 6.8 (e) shows the same two relationships for the Na-ion system. For any battery system, diffusive currents should exceed capacitive currents. Ion transport can be described by a mechanistic three-step process, where diffusion acts as the rate-limiting step.(117) One of the primary benefits of the IO morphology is the provision of excellent opportunities for efficient ion diffusion through the thin pore walls.

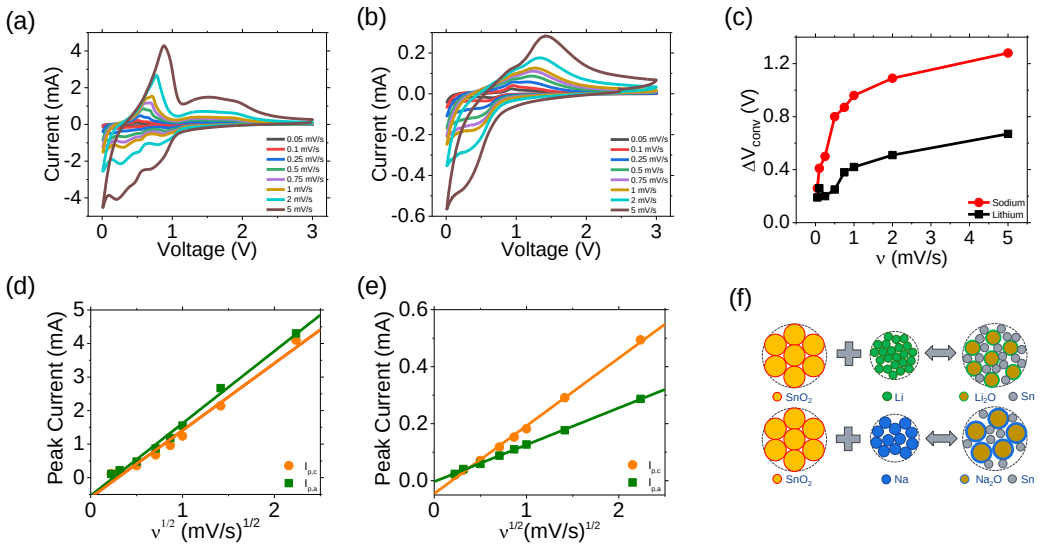


Figure 6.8. Cyclic voltammetry for a range of scan rates from 0.05 mVs^{-1} to 5 mVs^{-1} for a SnO_2 IO (a) vs Li/Li^+ and (b) vs Na/Na^+. (c) Potential separation between oxidation and reduction peaks as a function of scan rate for the Li-ion and Na-ion systems. (d) Peak current response as a function of the square root of scan rate for the anodic oxidation ($I_{p,a}$) and cathodic reduction ($I_{p,c}$) reactions in the (d) Li-ion system and (e) Na-ion system. The lines are linear fits to each data set. (f) Visual representation of the conversion reactions between SnO_2 and metallic Sn in both the Li-ion and Na-ion systems.

The poor linear fits in Figure 6.8 (d) show that diffusive current contribution is much lower than expected for the Li-ion system. The excellent agreement of the linear fits in Figure 6.8 (e) show that the total current for the Na-ion system is dominated by the diffusive contribution. Clearly, a greater buildup of capacitive current occurs in the Li-ion system, a potential cause of the rapid capacity degradation and instability in the first 40 cycles observed earlier for galvanostatic cycling in the Li-ion system. Buildup of capacitive current in battery systems occurs when ion diffusion through the electrode material is impeded. While diffusive currents occur due to imparted energy from the electrochemical reactions which occur at the electrode/electrolyte interface as ions transfer from the liquid to solid phase, capacitive currents occur when ions are accumulated in front of the electrode akin to the buildup

of charge on the plate of a capacitor. The generated current is an unwanted physical process with no electrochemical relevance. Capacitive currents in IOs are indicative of degradation of the IO structure which likely occurs when massive capacities are delivered and volume expansion occurs during early stage cycling in the Li-ion system that is evident in the galvanostatic curves shown previously. The excellent approximation of the $v^{1/2}$ quantity for the peak current in the Na-ion system stipulates that the conversion reactions between SnO_2 and Sn are diffusion driven.(118)

Furthermore, valuable insight into the rate performance of the Na-ion system can be gleaned from direct comparison of the rate of change of the anodic and cathodic peak currents. Examination of Figure 6.8 (e) shows that the rate of change of $I_{p,c}$ as a function of scan rate is far greater than $I_{p,a}$ for scan rates above 1 mV s^{-1}. The contrast suggests that the degree of cathodic reduction of SnO_2 to metallic Sn takes place at a greater rate than the reverse process, anodic oxidation of SnO_2 to Sn. A study by Ding et al. in 2014 reported the presence of unreacted β-Sn, surrounded by amorphous Na_xSn, alluding to a potential explanation for the irreversibility of the oxidation process. As cycling continues, the amount of unreacted Sn increases. The impediment caused by the surrounding amorphous Na_xSn alloy prevents its partaking in the oxidation process back to SnO_2.(119) While irreversibility proves advantageous here, those interested in its regulation can consult previous work on improving electrochemical performance of nanoparticulate SnO_2 anodes by tailoring oxygen vacancy.(120)

A visual representation of the conversion between SnO_2 and metallic Sn in both Li-ion and Na-ion systems is shown by the schematic in Figure 6.8 (f). The conversion reaction involves the reversible formation and decomposition of an associated metal oxide, which acts as a “buffer matrix” for relieving volume change and improves cycling stability in which the metallic Sn particles are embedded.(121) This model describes the situation in the ~50 nm thick walls that comprise the electrolyte-soaked IO structure. Nevertheless, the matrix induces large voltage hysteresis due to sluggish reaction kinetics. The size of the metal oxide nanoparticles also impacts the insertion and removal of Sn particles to and from the matrix as conversion proceeds. The smaller Li_2O nanoparticles permit easier movement of Sn nanoparticles in and out of the matrix for the Li-ion system while the opposite is true for the larger Na_2O nanoparticles.

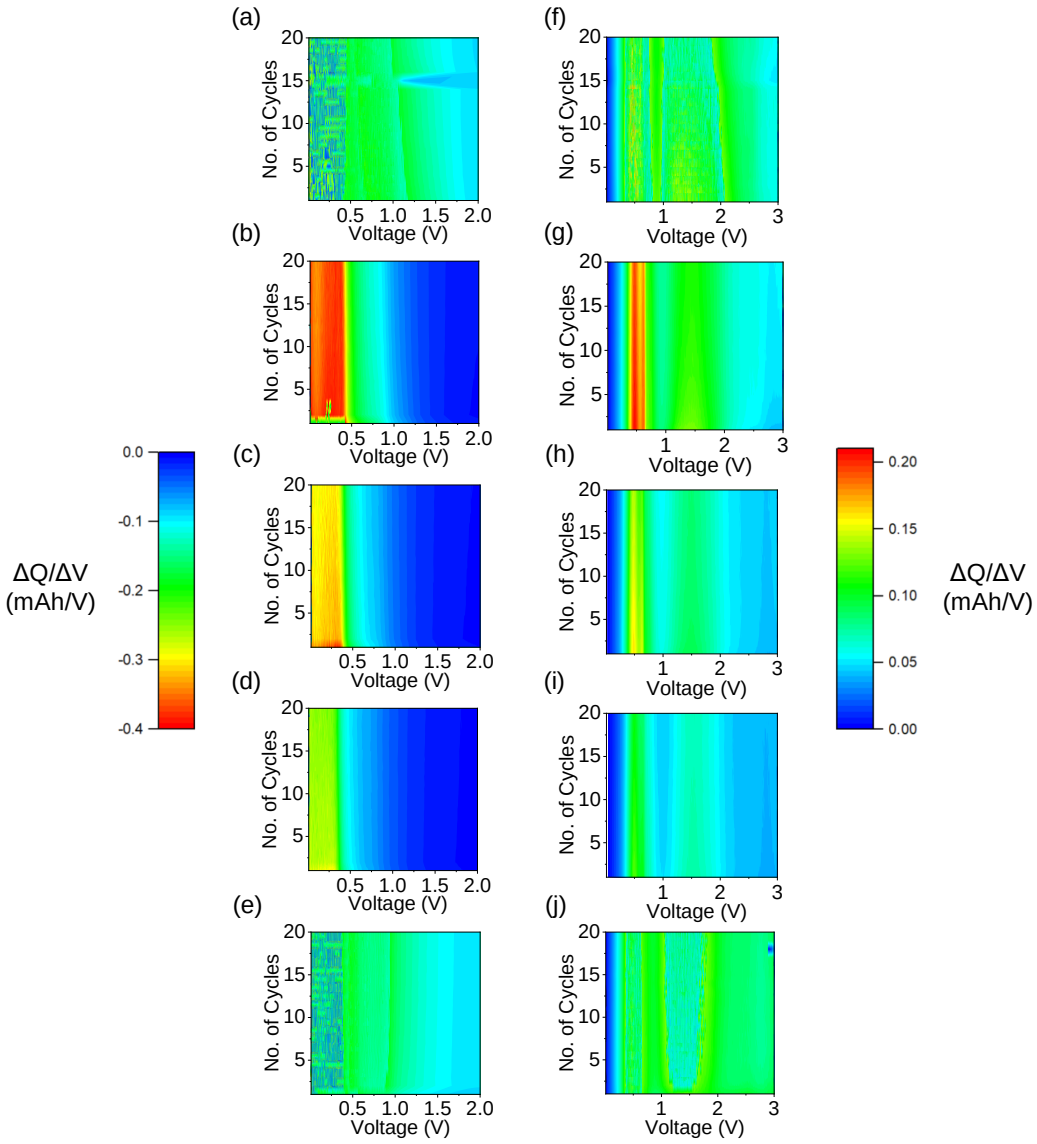


Figure 6.9. Differential capacity colour maps obtained from rate capability testing of the SnO_2 IO in the Li-ion system at current densities presented in the following order from top to bottom: 50 mA g^{-1}, 150 mA g^{-1}, 300 mA g^{-1}, 450 mA g^{-1}, 50 mA g^{-1}, generated from discharges (a)-(e) and charges (f)-(j). Colour bars associated with discharges and charges positioned left and right, respectively.

Consequently, an aggregation of elemental (Sn) particles can occur which leads to a less reversible Na-ion conversion reaction.(122) Additionally, intrinsic kinetic limitation of the sodiation reaction as a result of poor Na-ion diffusion and low electronic conductivity of the intermediate reaction products in SnO_2 has been proposed.(123)

In Figure 6.9 (a)-(e), differential capacity plots (DCPs) are shown corresponding to the discharges from the previously presented rate performance testing of the SnO_2 IO anode in a Li-ion system. Figure 6.9 (f)-(j) shows the equivalent DCPs for the corresponding charge profiles. The DCPs are presented in the order of current densities used for rate testing. An evident trend in both the discharges and charges is in the similarities between the initial and final rates, both at a current density of 50 mA g^{-1}. Likewise, there is a similarity between the three DCPs at higher currents, 150 mA g^{-1}, 300 mA g^{-1}, and 450 mA g^{-1}.

For the discharges, the DCPs are shown for a reduced voltage range, as little change was observed above 2 V. As voltage is swept downwards from 2 V, there is a positive gradient in differential capacity to 0.5 V as conversion of SnO_2 to metallic Sn takes place. A mosaic pattern is observed below 0.5 V as alloying begins, a result of the progressive alloying regime to form Li_XSn. The same regime was described earlier in the CV analysis section, where it presented as a major alloying peak at 0.01 V with other lower intensity peaks in its vicinity. The mosaic pattern indicates that the capacity delivered by the alloying reaction varies in magnitude between cycles here. There is little to no gradient between the conversion and alloying reactions, their contributions are on the same order of magnitude at this stage. Interestingly, the DCP corresponding to the final rate at the same current density of 50 mA g^{-1} in Figure 6.9 (e) follows an almost identical pattern.

For discharges at the higher current densities in Figure 6.9 (b)-(d), each of the three DCPs follows a similar pattern, with three distinct stages. (1) 2 V

– 1 V: A blue region at the three rates, minimal capacity change, no major electrochemical reactions take place here. (2) 1 V – 0.5 V: Increased differential capacity designated by green at 150 mA g^{-1}, narrows and diminishes towards blue for the two highest rates. (3) 0.5 V – 0.01 V: Maximum differential capacity illustrated by a vibrant red region at 150 mA g^{-1}, with some fluctuations observed for the first three cycles at this rate. From the diminishing of the two lower voltage regions in the DCPs, a reduction in capacity from the reduction and alloying processes occurs for each increase in rate, in line with the literature.(124) The narrowing shows that each increase in rate results in much sharper reduction and alloying processes.

For the charges, the initial and final rates are also similar. In both cases, there is no capacity change below 0.2 V as expected. Above 0.2 V, the DCP are predominantly green with intermediate capacity, a mosaic pattern observed up to 2 V, and maxima occurring mainly around 0.5 V and 1 V. At the second rate of 150 mA g^{-1}, a thin red region occurs at about 0.5 V, corresponding to the dealloying regime. From 0.65 V – 2 V, a green band appears associated with gradual oxidation of Sn to SnO_2. Much like the initial and final rates, it is unclear here where dealloying ends and oxidation begins. As the rate increases to 300 mA g^{-1} and 450 mA g^{-1}, the separation between dealloying and oxidation bands becomes clearer. Simultaneously, the differential capacity of each band decreases. The alloying band diminishes from red to orange and the oxidation band from green towards blue.

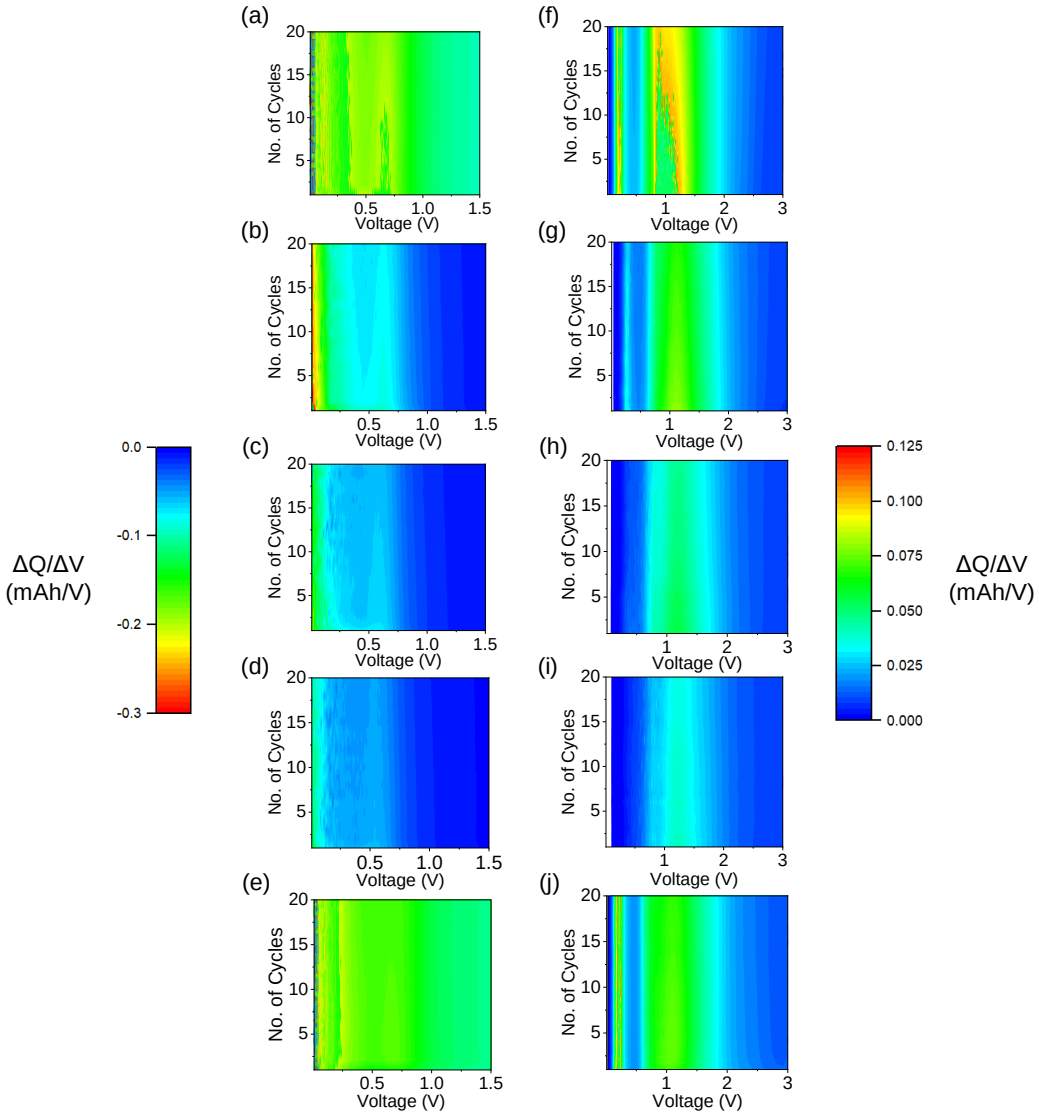


Figure 6.10. Differential capacity colour maps obtained from rate capability testing of the SnO_2 IO in the Na-ion system at current densities presented in the following order from top to bottom: 50 mA g^{-1}, 150 mA g^{-1}, 300 mA g^{-1}, 450 mA g^{-1}, 50 mA g^{-1}, generated from discharges (a)-(e) and charges (f)-(j). Colour bars associated with discharges and charges positioned left and right, respectively.

DCPs obtained from rate testing of the Na-ion system presented previously are shown in Figure 6.10 in the same order as the Li-ion case. Once again, for the discharges, DCPs obtained from the initial and final rate tests exhibit similar behaviour, while DCPs from the three higher current densities follow their own pattern. Unlike the Li-ion system, the charges exhibit similar

behaviour at all five rate testing steps. The initial and final rate DCPs are predominantly green. For the initial rate, regions of increased differential capacity occur as yellow bands. A wide band yellow band occurs between 0.4 V and 0.75 V, associated with the reduction process. At lower voltages, there are regions of varying differential capacity between cycles, with maxima close to 0.01 V where alloying occurs. Unlike the Li-ion case, the separation between reduction and alloying regimes can be detected for the initial rate. In the final rate, the separation is less clear. However, a thin yellow band occurs at 0.5 V, indicative of a more instantaneous reduction process, since there is far less active SnO_2 to be reduced in the system because of the irreversibility of the oxidation process suggested by our earlier CV analysis.

DCPs for discharges at the three higher rates show a positive differential capacity gradient consisting of three primary stages, like the Li-ion case. For the Na-ion system at the second rate of 150 mA g^{-1}, a dark blue band above 0.75 V designates the region where there is an absence of any of the primary electrochemical reactions which contribute to battery capacity. A light blue band between 0.75 V and 0.1 V designates the progressive reduction process. As cycling continues, a split in the centre of this band appears and grows, indicating the formation of a doublet peak, which suggests a two-step reduction process. At 300 mA g^{-1} and 450 mA g^{-1}, the three bands associated with the same three stages during discharge remain, diminishing in intensity with each increase in rate.

For the charges, a clearer separation between processes is observed for all rates. At the initial and final rates, a thin, red-orange band occurs at ~0.2

V, associated with the dealloying regime. For the second rate of 150 mA g^{-1}, the dealloying band diminishes to green. For the two highest rates of 300 mA g^{-1} and 450 mA g^{-1}, the dealloying band is absent, suggesting a minimal dealloying charge contribution. Earlier CV analysis demonstrated the difficulty in detection of the dealloying process. Its detection here suggests that an initial stabilisation period, such as the 20 cycles used here prior to rate testing, creates more favourable conditions for the dealloying process to occur.

A clearly separated green band occurs from 0.8 V to 2 V, where progressive oxidation occurs. Oxidation is clearly at a maximum between 0.8 V and 0.125 V, thin red bands appear initially at each of these potentials, before the width of each band grows gradually until they meet to form a wider band at 16 cycles. At the final rate, the system returns to similar behaviour as the initial rate. The thin dealloying peak returns. For the oxidation process, the red bands do not return, and a wide green band signifies the gradual oxidation of Sn to form SnO_2. The lower differential capacity is expected here as the irreversibility of the reaction compounds with cycle time.(125) The oxidation peak remains but diminishes in intensity and width with each increase in rate.

The differential capacity analysis performed on the rate performance testing for the SnO_2 IO in both Li-ion and Na-ion systems provide a comparative overview of how the electrochemical mechanisms vary with current density (rate), revealing some key insights. (1) In both systems, there is sufficient cycling stability such that after applying current densities at a range of higher rates, each system returns to baseline, and their electrochemical mechanisms are not disrupted. (2) At higher rates (150 mA g^{-1} – 450 mA g^{-1}),

DCPs can be split into three distinct regions, alloying, conversion, and inactive. At these rates, the separation between alloying and conversion mechanisms is clearest, albeit that the intensity of the bands for the two capacity contributing mechanisms diminish in both width and intensity as current density is increased. (3) Despite that the DCPs at the final rate show a return to similar behaviour as the initial rate in both systems, there is a clear contrast in the band associated with the oxidation reaction for the charges in the Na-ion system, designated by the disappearance of the orange-red bands which appears at the initial rate as two separate thin bands and grow to form a single wide band. The absence of this peak at the final rate supports our earlier hypothesis concerning the irreversibility of the oxidation reaction of metallic Sn to SnO_2 during charge in the Na-ion system. The irreversibility was shown earlier to increase with scan rate and shown here to increase with current density.

6.4. Conclusions

A comprehensive comparison of the electrochemical response and rate behaviour of macroporous SnO_2 IO anodes in both Li-ion and Na-ion batteries, showed how such nanostructures are beneficial particularly for Na-ion systems. Voltammetry at a fixed scan rate of 0.1 mV s^{-1} revealed that while both systems are governed by similar electrochemical reactions, the current responses in the Na-ion system are much lower, indicating incomplete reactions and unused active material. While the initial capacity is much higher in the Li-ion system than the Na-ion system, galvanostatic cycling results demonstrate that cycling stability is greater in the Na-ion system, resulting in

superior capacity retention of 76.6%, while the Li-ion system experienced dramatic capacity loss in the first 40 cycles.

The CV scan rate analysis stipulates that the conversion reaction is less reversible in the Na-ion system than the Li-ion system. Irreversibility of a reaction that provides a substantial contribution to the capacity delivered by the battery is typically considered an adverse effect, draining the capacity of the battery over time. However, conversion reactions are well documented to cause significant volume expansion, particularly in SnO_2. The results throughout this work indicate that while this irreversibility may lead to a certain capacity loss, the associated reduction in the extent of the conversion reaction mitigates volume expansion and preserves the structural integrity of the electrode. Furthermore, given the rate of reduction to metallic Sn exceeds the rate of the reverse oxidation reaction, as cycling continues, the system cycles with a progressively greater amount of metallic Sn, which improves electrical conductivity.

One of the primary motivations for the use of macroporous IOs in any binder-less, additive-free battery electrode is the short ion diffusion distances provided by the thin pore walls, which have been shown to improve rate performance. The rate performance of the SnO_2 IOs in the Na-ion system demonstrated here is commensurate with a wide variety of pure SnO_2 nanostructured electrodes reported in the literature. At the highest rate of 450 mA g^{-1}, the capacity retained is 150 mAh g^{-1}. The capacity recovery to 300 mAh g^{-1} at the last stage of rate testing indicates limited electrode degradation.

Differential capacity analysis of these rate tests gave further insight into the nature of the response at different rates.

6.5. Appendix: Supplementary Material

In Figure S6.1, additional SEM images of an SnO_2 IO are provided to those shown in the main text. Figure S1 (a) and (b) show other areas of the IO where FCC symmetry continues to dominate. Defects are present in some areas. Figure S6.1 (c) and (d) show further images of the cross section, showing that the FCC symmetry is present not only at the surface, but throughout the bulk of the sample. Figure S6.1 (e) and (f) show the islands of IO material, with cracks providing opportune routes for electrolyte soakage.

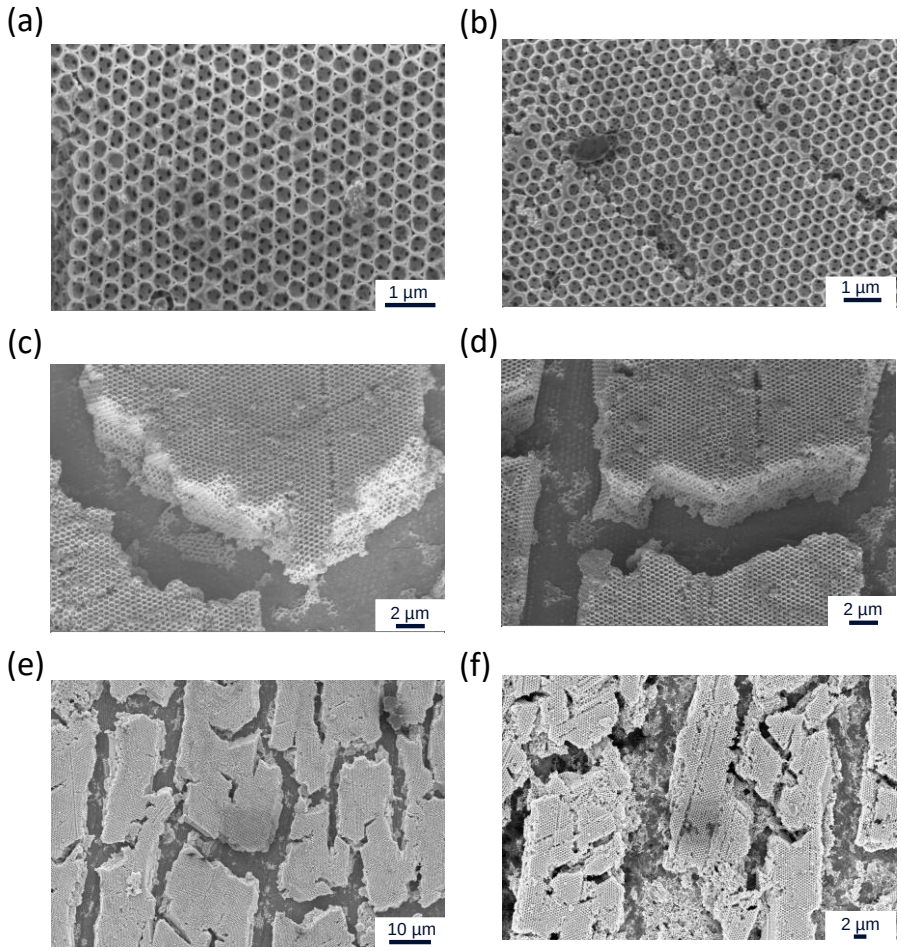


Figure S6.1: Additional SEM images of an SnO_2 IO to those shown in the main text. (a), (b) Planview, provides overview of porous network with honeycomb pattern. (c), (d) Cross-sectional, obtained at a stage tilt angle of 30°. (e), (f) Planview, provides overview of island of IO material.

Additional TEM images to the main text are shown in Figure S6.2, with different fragments of the IO sample at a resolution of 300 nm in Fig S6.2 (a)-(c). Fig S6.2 (d) shows a magnification of the IO wall at 100 nm resolution.

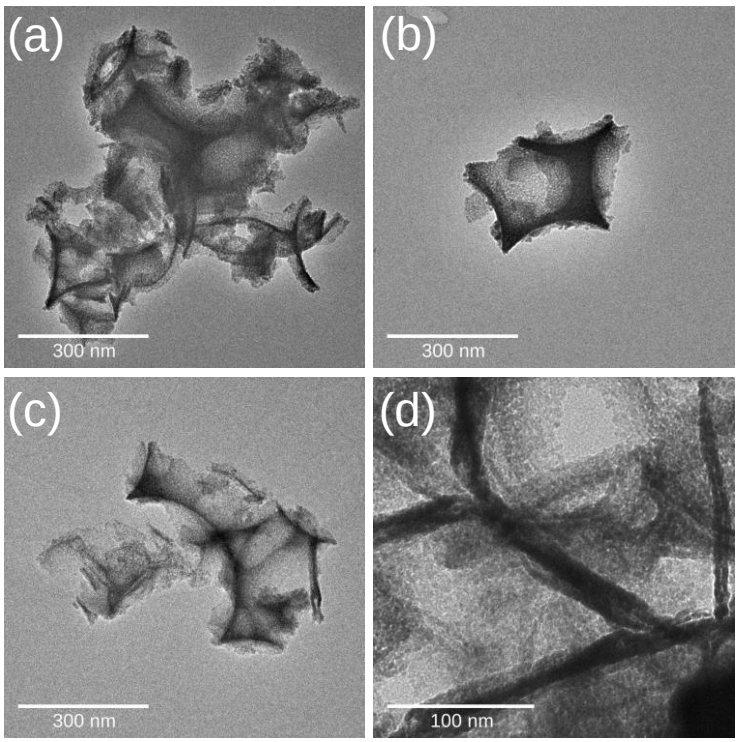


Figure S6.2: Additional TEM images of the SnO_2 shown in the main text. (a)-(c) Various IO fragments at 300 nm resolution. (d) Magnification of thin pore wall at 100 nm resolution.

Figure S6.3 demonstrates the continued stability of SnO_2 IO Li-ion half-cell presented in Figure 6.5 of the main text. Specific capacity and Coulombic efficiency are shown as a function of cycle number for 101-250 cycles. Discharge and charge capacities at 100 cycles are 112 mAh g^{-1} and 111 mAh g^{-1}, respectively. Minimal capacity fluctuations occur, and the retained discharge and charge capacities are both 94 mAh g^{-1} at 250 cycles. Coulombic efficiency remains between 96-100 % throughout.

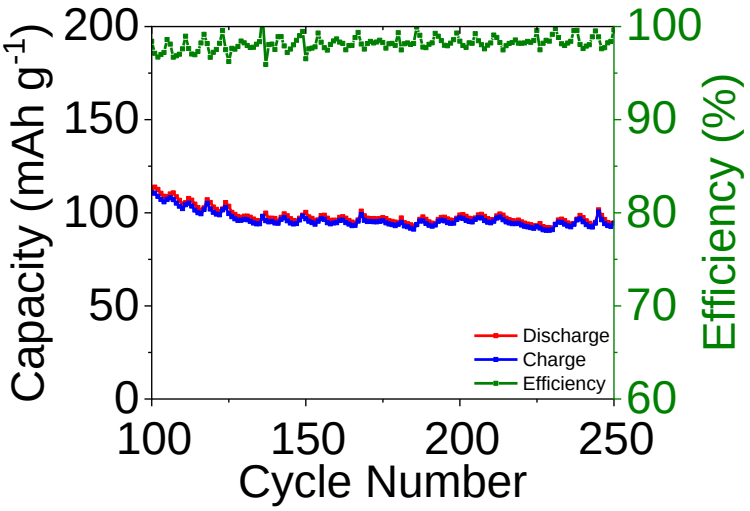


Figure S6.3: Specific capacity of and Coulombic efficiency as a function of cycle number for the same SnO_2 IO Li-ion half-cell from the main text.

Table S6.1 provides a comparison of the obtained capacities for a range of SnO_2-based electrodes for Na-ion batteries. For each literature example, rate testing was performed in a similar manner to that presented in this work. Each material was cycled at progressively higher rates before being cycled once again at the lower rate. The SnO_2 IOs investigated in this work achieve competitive capacities for both the pure SnO_2 nanostructures and carbonaceous nanocomposites referenced in the table.

Figure S6.4 shows additional CV testing at a range of scan rates from 0.05 mV s^{-1} to 5 mV s^{-1}. The equivalent experiment demonstrated in Figure 8 of the main text was obtained after CV was performed vs Li/Li^+ and Na/Na^+ for 5 cycles at 0.01 mV s^{-1}. Here, the first CV scan corresponds to the first application of a voltage to the system. As a result, there is no opportunity for the system to stabilise before results were obtained.

SnO_2 Structure/ Composite	Voltage Window (V)	Current Densities (mA g^{-1})	Cycle Number	Retained Capacity (mAh g^{-1})	Ref.
IO	0.01-3	50/150 /300/450/50	100	298	This work
Nanoparticles	0.01-2.5	20/40/60/80/ 160/320/640/20	45	91	(111)
Microfibers	0.01-2.5	20/40/60/80/ 160/320/640/20	45	44	(111)
Hollow microspheres	0.05-2	20/50/ 100/200/20	25	355	(30)
Porous nanotubes	0.01-3	50/100/200/ 400/800/50	30	256	(107)
Porous nanofibers	0.01-3	50/100/200/ 400/800/50	30	338	(107)
MWCNT/ SnO_2/C	0.01-3	50/150/300/ 500/1000/50	80	337	(46)
SnO_2/ graphene	0.01-3	50/100/200/ 1000/100/50	60	215	(37)
RGO/SnO_2 nanotubes	0.01-3	50/100/200/ 400/100/50	100	231	(42)
SnO_2/ glucose/ graphene	0.01-3	100/200/ 500/1000/2000	30	226	(126)

Table S6.1. Comparison of capacities obtained for various SnO_2 nanostructures employed as Na-ion battery electrodes from the literature.

Like Figure 6.8 of the main text, the peak separations for both systems increase as a function of scan rate, while the separation increases at a far greater rate for the Na-ion case. At the lowest scan rate of 0.05 mV s^{-1}, peak separation is minimal. The separation is greater by a factor of 4 at a scan rate of 0.1 mV s^{-1}, and a large peak separation is maintained for all subsequent scan rates, stabilising at 1 mV s^{-1}.

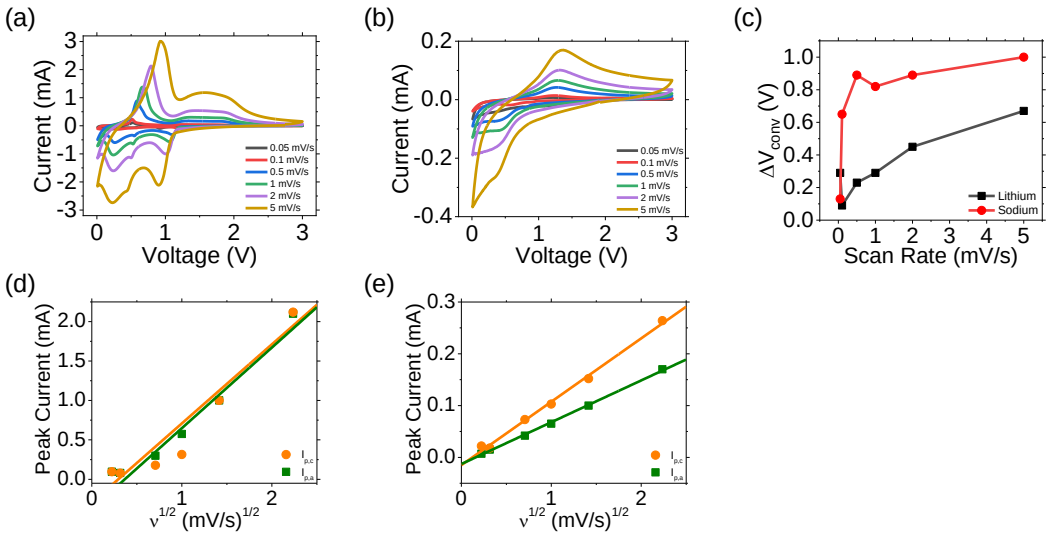


Figure S6.4. CV scan rate testing without prior fixed rate CV scans, which was performed for the results shown in the main text. Cyclic voltammetry for a range of scan rates from 0.05 mVs^{-1} to 5 mVs^{-1} for a SnO_2 IO (a) vs Li/Li^+ and (b) vs Na/Na^+. (c) Potential separation between oxidation and reduction peaks as a function of scan rate for the Li-ion and Na-ion systems. (d) Peak current response as a function of the square root of scan rate for the anodic oxidation ($I_{p,a}$) and cathodic reduction ($I_{p,c}$) reactions in the (d) Li-ion system and (e) Na-ion system.

The analysis of peak current as a function of $v^{1/2}$ to examine the diffusive contribution to the conversion process follows a similar trend to that of the main text. For the Li-ion system, applied linear fits are poor, indicating that the conversion process is not diffusion driven, particularly at lower scan rates. For the Na-ion system, the applied linear fits show excellent agreement for both processes once again. The rate of change of the cathodic reduction peak current is greater than the anodic oxidation process which reiterates the findings of the main text, that the irreversibility of the oxidation process for the Na-ion system increases with cycling, particularly at higher scan rates.

6.6. References

1. B. E. Murdock, K. E. Toghill and N. Tapia-Ruiz, *Advanced Energy Materials*, **11**, 2102028 (2021).
2. C. M. Costa, J. C. Barbosa, R. Gonçalves, H. Castro, F. J. D. Campo and S. Lanceros-Méndez, *Energy Storage Materials*, **37**, 433 (2021).
3. O. Egbue and S. Long, *Engineering Management Journal*, **24**, 52 (2012).
4. D. McNulty, V. Landgraf and S. Trabesinger, *Journal of Materials Chemistry A*, **8**, 26085 (2020).
5. H. Zhang, L. K. Ono, G. Tong, Y. Liu and Y. Qi, *Nature Communications*, **12**, 4738 (2021).
6. E. Sánchez-Díez, E. Ventosa, M. Guarnieri, A. Trovò, C. Flox, R. Marcilla, F. Soavi, P. Mazur, E. Aranzabe and R. Ferret, *Journal of Power Sources*, **481**, 228804 (2021).
7. F. Pan and Q. Wang, *Molecules*, **20**, 20499 (2015).
8. R. Rajagopalan, Y. Tang, X. Ji, C. Jia and H. Wang, *Advanced Functional Materials*, **30**, 1909486 (2020).
9. Y. Wang, P. Niu, J. Li, S. Wang and L. Li, *Energy Storage Materials*, **34**, 436 (2021).
10. G. A. Elia, K. V. Kravchyk, M. V. Kovalenko, J. Chacón, A. Holland and R. G. A. Wills, *Journal of Power Sources*, **481**, 228870 (2021).
11. H. Moriwake, A. Kuwabara, C. A. J. Fisher and Y. Ikuhara, *RSC Advances*, **7**, 36550 (2017).
12. O. Lenchuk, P. Adelhelm and D. Mollenhauer, *Physical Chemistry Chemical Physics*, **21**, 19378 (2019).
13. Z. Wang, S. M. Selbach and T. Grande, *RSC Advances*, **4**, 4069 (2014).
14. D. P. DiVincenzo and E. J. Mele, *Physical Review B*, **32**, 2538 (1985).
15. R. Malini, U. Uma, T. Sheela, M. Ganesan and N. G. Renganathan, *Ionics*, **15**, 301 (2009).
16. C. Zheng, D. Ji, Q. Yao, Z. Bai, Y. Zhu, C. Nie, D. Liu, N. Wang, J. Yang and S. Dou, *Angewandte Chemie International Edition*, **62**, e202214258 (2023).
17. V. Etacheri, R. Marom, R. Elazari, G. Salitra and D. Aurbach, *Energy & Environmental Science*, **4**, 3243 (2011).
18. Y. Yuan, K. Amine, J. Lu and R. Shahbazian-Yassar, *Nature Communications*, **8**, 15806 (2017).
19. F. Klein, B. Jache, A. Bhide and P. Adelhelm, *Physical Chemistry Chemical Physics*, **15**, 15876 (2013).
20. J. Zhang, J. Gai, K. Song and W. Chen, *Cell Reports Physical Science*, **3**, 100868 (2022).
21. B. K. Sovacool, S. H. Ali, M. Bazilian, B. Radley, B. Nemery, J. Okatz and D. Mulvaney, *Science*, **367**, 30 (2020).
22. P. Engels, F. Cerdas, T. Dettmer, C. Frey, J. Hentschel, C. Herrmann, T. Mirfabrikikar and M. Schueler, *Journal of Cleaner Production*, **336**, 130474 (2022).
23. S. W. Gao, X. Z. Gong, Y. Liu and Q. Q. Zhang, *Materials Science Forum*, **913**, 985 (2018).

24. K. Zhao, L. Zhang, R. Xia, Y. Dong, W. Xu, C. Niu, L. He, M. Yan, L. Qu and L. Mai, *Small*, **12**, 588 (2016).
25. S. M. Hwang, Y.-G. Lim, J.-G. Kim, Y.-U. Heo, J. H. Lim, Y. Yamauchi, M.-S. Park, Y.-J. Kim, S. X. Dou and J. H. Kim, *Nano Energy*, **10**, 53 (2014).
26. C. Guan, X. Wang, Q. Zhang, Z. Fan, H. Zhang and H. J. Fan, *Nano Letters*, **14**, 4852 (2014).
27. S. Yang, W. Yue, J. Zhu, Y. Ren and X. Yang, *Advanced Functional Materials*, **23**, 3570 (2013).
28. Q. Zhao, L. Ma, Q. Zhang, C. Wang and X. Xu, *Journal of Nanomaterials*, **2015**, 850147 (2015).
29. X. Ao, J. Jiang, Y. Ruan, Z. Li, Y. Zhang, J. Sun and C. Wang, *Journal of Power Sources*, **359**, 340 (2017).
30. H. He, M. Xu, J. Yang, B. He and J. Xie, *Micro & Nano Letters*, **12**, 777 (2017).
31. N. Wu, W. Du, X. Gao, L. Zhao, G. Liu, X. Liu, H. Wu and Y.-B. He, *Nanoscale*, **10**, 11460 (2018).
32. B. Huang, X. Li, Y. Pei, S. Li, X. Cao, R. C. Massé and G. Cao, *Small*, **12**, 1945 (2016).
33. Y. J. Hong, M. Y. Son and Y. C. Kang, *Advanced Materials*, **25**, 2279 (2013).
34. X. Jia, H. Li, B. Huang, J. Yang and Y. Li, *Advanced Powder Technology*, **34**, 104056 (2023).
35. B. Li, Y. Song, Y. Wang, Z. He and W. Gao, *Materials & Design*, **219**, 110745 (2022).
36. L. Gao, G. Wu, J. Ma, T. Jiang, B. Chang, Y. Huang and S. Han, *ACS Applied Materials & Interfaces*, **12**, 12982 (2020).
37. H. Lai, B. Feng, Y. Jiang, N. Shi, C. Liang, S. Chang, S. Guo, B. Cui and H. Cao, *Materials Letters*, **166**, 292 (2016).
38. Z. Lu, Z. Kong, L. Jing, T. Wang, X. Liu, A. Fu, P. Guo, Y.-G. Guo and H. Li, *Energy & Fuels*, **34**, 13126 (2020).
39. W. Jiang, X. Zhao, Z. Ma, J. Lin and C. Lu, *J Nanosci Nanotechnol*, **16**, 4136 (2016).
40. N. Kamboj, B. Debnath, S. Bhardwaj, T. Paul, N. Kumar, S. Ogale, K. Roy and R. S. Dey, *ACS Nano*, **16**, 15358 (2022).
41. M. Premasudha, B. S. Reddy, N. S. Reddy, J.-H. Ahn, H.-J. Ahn and K.-K. Cho, *Chemical Physics Letters*, **805**, 139970 (2022).
42. M. Yang, X. Li, B. Yan, L. Fan, Z. Yu and D. Li, *Journal of Alloys and Compounds*, **710**, 323 (2017).
43. G. Q. Diao, H. Li, I. Ivanenko, T. Dontsova, I. Astrelin, F. Y. Xie and X. Z. Guo, *IOP Conference Series: Materials Science and Engineering*, **474**, 012022 (2019).
44. X. Liu, M. Wu, M. Li, X. Pan, J. Chen and X. Bao, *Journal of Materials Chemistry A*, **1**, 9527 (2013).
45. M. Wang, Z. Tao, X. He, B. Zhu, X. Zhang, T. Liao, H. Tang, Z. Wei and W. Tang, *Journal of Physics and Chemistry of Solids*, **165**, 110693 (2022).
46. Y. Wang, D. Su, C. Wang and G. Wang, *Electrochemistry Communications*, **29**, 8 (2013).
47. A. Grant, A. Lonergan and C. O'Dwyer, *Optical Materials*, **142**, 114053 (2023).

48. E. Armstrong, M. Osiak, H. Geaney, C. Glynn and C. O'Dwyer, *CrystEngComm*, **16**, 10804 (2014).
49. M. Osiak, E. Armstrong and C. O'Dwyer, *ECS Transactions*, **53**, 85 (2013).
50. D. McNulty, A. Lonergan, S. O'Hanlon and C. O'Dwyer, *Solid State Ionics*, **314**, 195 (2018).
51. A. Lonergan and C. O'Dwyer, *Advanced Materials Technologies*, **8**, 2201410 (2023).
52. X. Zhu, W. Ren, C. Cheng and Y. Yang, *ChemistrySelect*, **2**, 3223 (2017).
53. D. McNulty, H. Geaney, D. Buckley and C. O'Dwyer, *Nano Energy*, **43**, 11 (2018).
54. H. Li, Z. Tang, Y. Liu, J. Robichaud, J. Liang, W. Jiang and Y. Djaoued, *Materials*, **15**, 2904 (2022).
55. E. Armstrong, D. McNulty, H. Geaney and C. O'Dwyer, *ACS Applied Materials & Interfaces*, **7**, 27006 (2015).
56. A. Lonergan, B. Murphy and C. O'Dwyer, *ECS Journal of Solid State Science and Technology*, **10**, 085001 (2021).
57. C. O'Dwyer, *Advanced Materials*, **28**, 5681 (2016).
58. A. Lonergan, C. Hu and C. O'Dwyer, *Physical Review Materials*, **4**, 065201 (2020).
59. G. Collins, E. Armstrong, D. McNulty, S. O'Hanlon, H. Geaney and C. O'Dwyer, *Science and Technology of Advanced Materials*, **17**, 563 (2016).
60. M. Osiak, H. Geaney, E. Armstrong and C. O'Dwyer, *Journal of Materials Chemistry A*, **2**, 9433 (2014).
61. K. R. Phillips, T. Shirman, E. Shirman, A. V. Shneidman, T. M. Kay and J. Aizenberg, *Advanced Materials*, **30**, 1706329 (2018).
62. J. E. S. v. d. Hoeven, A. V. Shneidman, N. J. Nicolas and J. Aizenberg, *Accounts of Chemical Research*, **55**, 1809 (2022).
63. B. Hatton, L. Mishchenko, S. Davis, K. H. Sandhage and J. Aizenberg, *Proc Natl Acad Sci U S A*, **107**, 10354 (2010).
64. J. H. Han, A. V. Shneidman, D. Y. Kim, N. J. Nicolas, J. E. S. van der Hoeven, M. Aizenberg and J. Aizenberg, *Angewandte Chemie International Edition*, **61**, e202111048 (2022).
65. H.-R. Yao, Y.-X. Yin and Y.-G. Guo, *Chinese Physics B*, **25**, 018203 (2016).
66. E. Armstrong and C. O'Dwyer, *Journal of Materials Chemistry C*, **3**, 6109 (2015).
67. M. A. Alothman, R. Kurtulus, I. O. Olarinoye, T. Kavas, C. Mutuwong and M. S. Al-Buriahi, *Optik*, **248**, 168047 (2021).
68. G. I. N. Waterhouse, J. B. Metson, H. Idriss and D. Sun-Waterhouse, *Chemistry of Materials*, **20**, 1183 (2008).
69. Y. Dong, F. Ai, D. Sun-Waterhouse, K.-i. Murai, T. Moriga and G. I. N. Waterhouse, *Chemistry of Materials* (2023).
70. A. Lonergan, D. McNulty and C. O'Dwyer, *Journal of Applied Physics*, **124**, 095106 (2018).
71. K. Wongsaprom, R.-a. Bornphotsawatkun and E. Swatsitang, *Applied Physics A*, **114** (2014).

72. A. Baniasad and M. Ghorbani, *International Journal of Biological Macromolecules*, **86**, 901 (2016).
73. F. A. Akgul, C. Gumus, A. O. Er, A. H. Farha, G. Akgul, Y. Ufuktepe and Z. Liu, *Journal of Alloys and Compounds*, **579**, 50 (2013).
74. Y. Liang and B. Fang, *Materials Research Bulletin*, **48**, 4118 (2013).
75. D. Liu, J. Pan, J. Tang, W. Liu, S. Bai and R. Luo, *Journal of Physics and Chemistry of Solids*, **124**, 36 (2019).
76. A. Leonardy, W.-Z. Hung, D.-S. Tsai, C.-C. Chou and Y.-S. Huang, *Crystal Growth & Design*, **9**, 3958 (2009).
77. G. Zhang, N. Liu, Z. Ren and B. Yang, *Journal of Nanomaterials*, **2011** (2011).
78. X. Wang, X. Wang, Q. Di, H. Zhao, B. Liang and J. Yang, *Materials (Basel)*, **10** (2017).
79. O. Lupan, L. Chow, G. Chai, H. Heinrich, S. Park and A. Schulte, *Journal of Crystal Growth*, **311**, 152 (2008).
80. M. A. Gondal, Q. A. Drmosh and T. A. Saleh, *Applied Surface Science*, **256**, 7067 (2010).
81. M. Parthibavarman, B. Renganathan and D. Sastikumar, *Current Applied Physics*, **13**, 1537 (2013).
82. H. A. Gatea, *Journal of Physics: Conference Series*, **1829**, 012030 (2021).
83. S. Zhao, C. D. Sewell, R. Liu, S. Jia, Z. Wang, Y. He, K. Yuan, H. Jin, S. Wang, X. Liu and Z. Lin, *Advanced Energy Materials*, **10**, 1902657 (2020).
84. G. Liang, X. Sun, J. Lai, C. Wei, Y. Huang, H. Hu, J. Zou and Y. Xu, *Journal of Electronic Materials*, **48**, 3324 (2019).
85. J. A. Weeks, H.-H. Sun, H. S. Srinivasan, J. N. Burrow, J. V. Guerrera, M. L. Meyerson, A. Dolocan, A. Heller and C. B. Mullins, *ACS Applied Energy Materials*, **2**, 7244 (2019).
86. X. Wang, T. Zheng, Y.-J. Cheng, S. Yin, Y. Xia, Q. Ji, Z. Xu, S. Liang, L. Ma, X. Zuo, J.-Q. Meng, J. Zhu and P. Müller-Buschbaum, *Nano Select*, **2**, 642 (2021).
87. R. Li, G. Zhang, Y. Wang, Z. Lin, C. He, Y. Li, X. Ren, P. Zhang and H. Mi, *Nano Energy*, **90**, 106591 (2021).
88. D. Spada, S. Davino, A. Girella, C. Milanese and M. Bini, *Journal of Solid State Electrochemistry*, **25**, 1401 (2021).
89. D. Dixon, M. Ávila, H. Ehrenberg and A. Bhaskar, *ACS Omega*, **4**, 9731 (2019).
90. K. Kisu, M. Iijima, E. Iwama, M. Saito, Y. Orikasa, W. Naoi and K. Naoi, *Journal of Materials Chemistry A*, **2**, 13058 (2014).
91. I. T. Kim, S.-O. Kim and A. Manthiram, *Journal of Power Sources*, **269**, 848 (2014).
92. F. Li, Q. Liu, J. Hu, J. Yang and J. Ma, *Journal of Physics D: Applied Physics*, **53**, 353001 (2020).
93. J. Wang, C. Eng, Y.-c. K. Chen-Wiegart and J. Wang, *Nature Communications*, **6**, 7496 (2015).
94. M. Dirican, Y. Lu, Y. Ge, O. Yildiz and X. Zhang, *ACS Applied Materials & Interfaces*, **7**, 18387 (2015).
95. D. Ma, Y. Li, H. Mi, S. Luo, P. Zhang, Z. Lin and J. Li, *Angewandte Chemie*, **130** (2018).

96. M. Gu, A. Kushima, Y. Shao, J.-G. Zhang, J. Liu, N. D. Browning, J. Li and C. Wang, *Nano Letters*, **13**, 5203 (2013).
97. X. Zhao, Z. Zhang, F. Yang, Y. Fu, Y. Lai and J. Li, *RSC Advances*, **5**, 31465 (2015).
98. C. Liu, Z. G. Neale and G. Cao, *Materials Today*, **19**, 109 (2016).
99. X.-Y. Xue, B. He, S. Yuan, L.-L. Xing, Z.-H. Chen and C.-h. Ma, *Nanotechnology*, **22**, 395702 (2011).
100. R. Hu, Y. Ouyang, T. Liang, H. Wang, J. Liu, J. Chen, C. Yang, L. Yang and M. Zhu, *Advanced Materials*, **29**, 1605006 (2017).
101. A. Sivashanmugam, T. P. Kumar, N. G. Renganathan, S. Gopukumar, M. Wohlfahrt-Mehrens and J. Garche, *Journal of Power Sources*, **144**, 197 (2005).
102. J. Liang, L. Zhang, D. XiLi and J. Kang, *Electrochimica Acta*, **341**, 136030 (2020).
103. L. Li, X. Yin, S. Liu, Y. Wang, L. Chen and T. Wang, *Electrochemistry Communications*, **12**, 1383 (2010).
104. D. McNulty, H. Geaney, Q. Ramasse and C. O'Dwyer, *Advanced Functional Materials*, **30** (2020).
105. S.-z. Yang, Y.-f. Huang, X.-c. Han and G.-h. Han, *Transactions of Nonferrous Metals Society of China*, **31**, 2062 (2021).
106. L. Yin, S. Chai, J. Huang, X. Kong and L. Pan, *Electrochimica Acta*, **238**, 168 (2017).
107. E. C. Duran and H. Kizil, *ECS Transactions*, **77**, 353 (2017).
108. A. Wang, S. Kadam, H. Li, S. Shi and Y. Qi, *npj Computational Materials*, **4**, 15 (2018).
109. H. Adenusi, G. A. Chass, S. Passerini, K. V. Tian and G. Chen, *Advanced Energy Materials*, **13**, 2203307 (2023).
110. X. Lu, F. Luo, Q. Xiong, H. Chi, H. Qin, Z. Ji, L. Tong and H. Pan, *Materials Research Bulletin*, **99**, 45 (2018).
111. Y. Lu, M. Yanilmaz, C. Chen, M. Dirican, Y. Ge, J. Zhu and X. Zhang, *ChemElectroChem*, **2**, 1947 (2015).
112. X. Zhao, M. Luo, W. Zhao, R. Xu, Y. Liu and H. Shen, *ACS Applied Materials & Interfaces*, **10**, 38006 (2018).
113. X. Li, X. Sun, Z. Gao, X. Hu, J. Guo, S. Cai, R. Guo, H. Ji, C. Zheng and W. Hu, *Applied Surface Science*, **433**, 713 (2018).
114. B. Dursun, E. Topac, R. Alibeyli, A. Ata, O. Ozturk and R. Demir-Cakan, *Journal of Alloys and Compounds*, **728**, 1305 (2017).
115. T. Kim, W. Choi, H.-C. Shin, J. Choi, J. M. Kim, M.-S. Park and W.-S. Yoon, *Journal of Electrochemical Science and Technology*, **11**, 14 (2020).
116. Y. Gogotsi and R. M. Penner, *ACS Nano*, **12**, 2081 (2018).
117. J. Maier, *Journal of Power Sources*, **174**, 569 (2007).
118. A. P. V S, R. Shende, M. S. Garapati, R. Dharavath, S. Biswas, S. Loganathan, T. Balasubramanian, K. Rambabu, M. Kamaraj and R. Sundara, *ACS Omega*, **3**, 9945 (2018).
119. J. Ding, Z. Li, H. Wang, K. Cui, A. Kohandehghan, X. Tan, D. Karpuzov and D. Mitlin, *Journal of Materials Chemistry A*, **3**, 7100 (2015).
120. Y. Wang, N. Jiang, D. Pan, H. Jiang, Y. Hu and C. Li, *Chemical Engineering Journal*, **437**, 135422 (2022).

121. M. Hu, Y. Jiang, W. Sun, H. Wang, C. Jin and M. Yan, *ACS Applied Materials & Interfaces*, **6**, 19449 (2014).
122. S. Fang, D. Bresser and S. Passerini, *Advanced Energy Materials*, **10**, 1902485 (2019).
123. J. Górka, L. Baggetto, J. K. Keum, S. M. Mahurin, R. T. Mayes, S. Dai and G. M. Veith, *Journal of Power Sources*, **284**, 1 (2015).
124. J. Yan, W. Shen, L. Wang, Y. Zhuang and S. Guo, *The Journal of Physical Chemistry C*, **126**, 14813 (2022).
125. Y. Chen, Y. Sun, M. Geng, W. Shao, Y. Chen, X. Liu and M. Ou, *Materials Letters*, **304**, 130704 (2021).
126. S. Wei, S. Chu, Q. Lu, W. Zhou, R. Cai and Z. Shao, *ChemistrySelect*, **3**, 4015 (2018).

Chapter 7

Operando Raman Spectroscopy of Metal Oxide Electrodes in Li-ion and Na-ion Battery Systems

Abstract

Identification and mitigation of battery degradation mechanisms are essential to the advancement and adoption of renewable energy technologies, given that efficient storage is required. Understanding the electrode/electrolyte interface is a direct route to improvement, given that this is where diffusion and charge transfer occurs, supplying energy to the system. Commercial battery materials are typically nano dimensional, requiring analytical tools with nano- to atomic-scale resolution. Raman spectroscopy can be used to probe crystallographic changes by tracking the vibrational oscillations of the molecular bonds in these materials. Traditionally, Raman spectroscopy has provided information on battery electrode charges before and after electrochemical cycling, or at various states of charge. Often, these changes are rapid and may disappear upon cell disassembly, prompting an operando approach where spectroscopy is performed in real-time, during electrochemical cycling. However, operando spectroscopy requires novel cell designs, given that cell components can prevent adequate access to the electrode/electrolyte interface. Here, operando Raman spectroscopy is performed for two TiO_2 anode structures and a commercial NMC cathode, using three different electrode stack configurations in a Li-ion battery. Laser-induced fluorescence in the Li-ion battery electrolyte and Raman modes of the sapphire are used as a proxy for measurements. These issues prompt a Na-ion battery using a different electrolyte, for which detailed Raman information is obtained for TiO_2 anode material.

7.1. Introduction

Operando spectroscopies have become a valuable addition to the arsenal of analytical tools used to understand the electrode/electrolyte interface which governs long-term battery performance in real-time.(1) Variations span the electromagnetic spectrum, taking advantage of low-energy acoustic and NMR probes to high-energy X-ray and electron-based spectroscopies. These methods can be applied to a range of battery chemistries beyond Li-ion, including Na-ion,(2-5) Li-S,(6-8) Li(Na)-O_2,(9, 10) and redox flow batteries (RFBs).(11-14) Optical spectroscopies provide access to the surface characteristics of battery materials at the nanoscale using probes in the ultraviolet (UV) to infrared (IR) region of the spectrum which are typically non-destructive, under the correct conditions. These probes, used in operando mode, include fiber optic sensors,(15-19) Fiber Bragg gratings,(20-22) optical microscopy,(23, 24) UV-visible spectroscopy,(25) FTIR spectroscopy,(26-31) and Raman spectroscopy.(32-35)

Operando Raman spectroscopy has been used recently for battery electrode materials and electrolytes to determine material composition with high spatial and temporal resolution. The primary goal is often to identify and monitor the evolution of Raman bands sourced from the anode, cathode, and electrolyte. Many informative reports have elucidated information on intricate processes such as SEI formation,(36-38) lithiation (sodiation) homogeneity,(39-42) charge transfer kinetics,(43-47) and mass transport.(48, 49) The motivation for the operando approach is that many of the electrochemical processes during battery cycling occur over nanosecond to

subnanosecond time domains, while many of the phases which occur as a result can be metastable or short-lived.(50) This includes the induced dipole moments which occur in molecules that are Raman active, caused by a net change in polarizability that leads to the vibrational modes observed in Raman spectra.

While operando Raman spectroscopy is more spatially and temporally powerful than its conventional counterpart, successful performance of the technique requires the consideration of a host of additional factors. For conventional Raman experiments, the laser parameters and electrode preparation are the most important aspects of the setup. For operando Raman measurements, the correct spectroelectrochemical cell design is of paramount importance, with several key considerations. [1] Optical window: The correct optical window material should be chosen such that it is transparent to the incident laser λ. Sapphire is used in this work given its transparency in the region of the 532 nm laser used for experiments. [2] Working distance: The distance between the light source and sample surface should be minimised to maximise the SNR. Shorter working distances increase the solid angle of scattered light detection and reduce the amount of electrolyte-filled space between the electrode and the optical window.(51) [3] Electrode thickness: Electrodes with a thickness of less than a few micrometres are optimal for most conventional Raman microscopes. The specific penetration depth of the Raman laser depends on the laser wavelength and the absorption coefficient of the target specimen.(52, 53) However, small electrodes can cause handling difficulties and increase the risk of misalignment. Very low currents must be

used for such electrodes which can exceed the sensitivity limits of standard galvanostats. [4] Electrolyte choice: Organic carbonate based electrolytes are the commercial standard for Li-ion batteries and are used for the Li-ion batteries examined in this work. However, $LiPF_6$ salt is prone to form fluorescent species,(54, 55) resulting in baselines that mask Raman peaks.(56, 57) Alternative electrolytes can be implemented with more success, as shown here. [5] Electrode pressure: Sufficient mechanical compression of the electrode stack is required to ensure appropriate electrical contact between cell components. Suboptimal contact can lead to unreliable underlying cell electrochemistry.(58) A spring and a hard window can ensure adequate pressure. [6] Cell components reactivity: All cell components must be chemically and electrochemically stable. In operando cell designs, certain plastics should be avoided, such as Teflon due to its decomposition when attacked by Li ions.(59)

The Raman activity of three electrode materials due to electrochemical cycling is investigated in this work: rutile TiO_2 IO, anatase TiO_2 slurry, and a commercial NMC slurry. The results obtained from operando Raman spectroscopy measurements of all three materials in a Li-ion system are explored, using three different electrode stack configurations. Operando measurements for the anatase TiO_2 slurry in a Na-ion system are also included. The two TiO_2 polymorphs, rutile and anatase, belong to the tetragonal crystal system. Rutile belongs to the space group D_{4h}^{14} and has two TiO_2 units per unit cell. There are 15 optical modes, the normal vibrations of which belong to the following irreducible representation: $A_{1g} + A_{2g} + A_{2u} + B_{1g}$

+ B_{2g} + $2B_{1u}$ + E_g + $3E_u$. Four modes are Raman active, represented by the symmetries B_{1g}, E_g, A_{1g} and B_{2g}. Anatase belongs to the space group D_{4h}^{19} and has 15 optical modes represented as: A_{1g} + A_{2u} + $2B_{1g}$ + B_{2u} + $3E_g$ + $2E_u$. Six modes are Raman active with symmetries A_{1g}, $2B_{1g}$, and $3E_g$.

The contributions of molecular bonds to the intensity of Raman modes vary depending on the crystal planes present. The E_g, A_{1g}, and B_{1g} Raman modes correspond to the symmetric stretching vibration, anti-symmetric bending vibration, and symmetric bending vibration of O-Ti-O, respectively. The crystallinity of the TiO_2 polymorph determines the intensity of these Raman bands. Since crystalline TiO_2 typically includes a furnace treatment step, pressure and temperature can be used to alter the crystallinity.

Electrochemical cycling of TiO_2 in a Li-ion battery proceeds as an intercalation mechanism, governed by the equation:(60, 61)

$$\mathbf{Li^+ + TiO_2 + xe^- \leftrightarrow Li_xTiO_2\ (0 \leq x \leq 1)} \quad (7.1)$$

The simplified sum, without mass balance, of the sodiation mechanism of anatase TiO_2 upon electrochemical cycling based on previous reports proceeds as

$$\mathbf{Na^+ + TiO_2 + xe^- \leftrightarrow Na_xTiO_2\ (0 \leq x \leq 1)} \quad (7.2)$$

for the first cycle. For subsequent cycles, the simplified sum is:(62)

$$Na_xTiO_2 \leftrightarrow TiO_2 + Na_xTiO_2 + Na \quad (7.3)$$

For both Li-ion and Na-ion batteries, the intercalation of the active ions with TiO_2 decreases its crystallinity.(63) Consequently, the associated Raman

modes are attenuated as TiO_2 becomes more amorphous while Na ions intercalate the TiO_2 structure to form amorphous Na titanate.

Li Nickel Manganese Cobalt Oxide (NMC) is one of the commercial standard cathode materials employed in Li-ion batteries. The layered metal oxide is formed by partially replacing Co in $LiCoO_2$ by Ni and Mn to improve electrochemical performance. The composition of Ni, Mn and Co are tuned to achieve optimal capacity, rate performance, stability, and lifetime, with a final composition according to $LiNi_xMn_yCo_zO_2$.(64) The most common form is NMC111 ($Li_{1/3}Mn_{1/3}Co_{1/3}O_2$), while Ni-rich forms such as NMC811, NMC622 and NMC532 have become more popular due to the high specific capacity provided. NMC622 is investigated here.(65)

Identification of the optical modes for NMC materials is more complex, given that NMC exists as a mixture of multiple metal oxide phases with several crystal lattice families present. NMC can be visualised as a solid solution of $LiNiO_2$, $LiMnO_2$, and $LiCoO_2$.(66) Layered $LiCoO_2$, $LiNiO_2$, $LiCoO_2$, and $LiCo_{1-x}Ni_xO_2$ all crystallise in the $R\bar{3}m$ space group with hexagonal symmetry. The only two corresponding Raman modes are A_{1g} and E_g, which correspond to the out-of-plane M-O stretch and in plane O-M-O bend, respectively (M = Ni, Co, Mn).(67-69) Due to a Jahn-Teller distortion, layered $LiMnO_2$ has lower symmetry and crystallises in the monoclinic *C2/m* space group, for which three Raman modes are detected that tend to be much weaker than the hexagonal modes. Typically, Raman spectra for NMC are dominated by the A_{1g} and E_g modes. Several additional peaks have been detected, but literature reports are often contradictory.(70) Many of the reports have deconvoluted the two

primary peaks to a total of six peaks assigned to the three metals present.(71, 72) Here, the two characteristic A_{1g} and E_g modes are observed in ex-situ spectra but cannot be identified during operando Raman for the Li-ion system due to the fluorescence mask caused by the fluorescent electrolyte species. However, some additional peaks do appear during cycling at specific voltages, along with dramatic evolution of the overall spectral intensity.

The irreducible representation for the optical modes of sapphire is: $2A_{1g} + 2A_{1u} + 3A_{2g} + 2A_{2u} + 5E_g + 4E_u$.(73) Seven modes are Raman active, represented by the symmetries $2A_{1g}$ and $5E_g$. Sapphire was used in this work as the optical window material. While the focus of Raman measurements is the electrode material, three strong Raman modes of sapphire remain present in all observed Raman spectra. Sapphire takes no part in any of the electrochemical or morphological changes of the target specimen. The modes are therefore used as a proxy to track the underlying spectral evolution which is observed for all three materials examined in a Li-ion system where the modes of electrode and electrolyte are masked by the fluorescence of the electrolyte species. The observed spectral changes, with strong correlation between materials from an electrochemical standpoint, indicate that the underlying changes to the system result in one of two (or both) of the following: (1) changes to the fluorescence of the material during cycling. (2) The reflectance of the light transmitted through sapphire changes because of the underlying electrochemical changes to the target materials.

Herein, we first used operando spectroscopy under continuous laser emission to probe the (de)lithiation behaviour of three electrode materials

using three different electrode stack configurations with the Raman modes of sapphire as proxy, given that the Raman modes of both electrode and electrolyte are masked by laser-induced fluorescence caused by the $LiPF_6$ salt and its interaction with both the carbonate solvents and the electrode. Next, we show that operando Raman spectroscopy performed on a Na-ion battery with $NaClO_4$ salt in PC electrolyte causes less fluorescence and initially Raman modes can be easily detected. However, prolonged laser emission causes a fluorescence buildup which masks the initially observed signal. We show that for spectra that are acquired after laser emission only over short periods prevents the fluorescence mask and the characteristic Raman modes of both electrode and electrolyte are revealed.

7.2. Materials and Methods

7.2.1. Electrodes

(1) TiO_2 IO anodes: Steel substrates (diameter 10 mm, thickness 0.2 mm) were cleaned by successive sonication in acetone (reagent grade 99.5%; Sigma Aldrich), isopropyl alcohol (reagent grade 99.5%; Sigma Aldrich) and deionised water each for 5 mins and dried in inert atmosphere at room temperature followed by UV-ozone treatment for 20 mins. Colloidal solutions of PS spheres in 2.5 % (w/v) aqueous suspension with nominal diameter 510 nm were purchased from Polysciences Inc. The sphere suspension possessed a net negative charge from functionalisation using a sulfate ester during synthesis. Opal templates were formed by evaporation-induced self-assembly (EISA). The substrates were taped to the inside of glass vials with

diameter 20 mm using Kapton tape at the back of the substrate leaving the entire 10 mm diameter surface exposed. The opal templates were infiltrated with a metal alkoxide precursor prepared as $TiCl_4$.2THF mixed with IPA to a 0.1 M concentration. The precursor was added dropwise using a 1 mL syringe for a total of 2-3 drops after which a typical sol-gel process occurred. The infiltrated templates left to dry at 70 °C in a Binder convection oven for 20 mins and then calcinated at 450 °C in air for 1 h which burned the opal template and formed the TiO_2 IO. Mass loadings were 0.1-0.2 mg.

(2) CUSTOMCELLS Commercial NMC cathodes: NMC-622 disks on Al foil, 18 mm diameter as received. Disks were punched to 10 mm and used as is for battery assembly. Mass loadings were 67.5 mg.

(3) TiO_2 slurry coated on Cu mesh: A traditional slurry coating procedure was followed. The TiO_2 active material, conductive carbon (Super-P) and Na carboxymethyl cellulose (CMC) binder were mixed in the mass ratio of 8:1:1. First, the CMC binder was dissolved into deionised water by stirring for 4-8 hours at room temperature. Second, the TiO_2 active material and Super-P were ground in an agate mortar for 20-30 minutes before adding to the mixture. The slurries mixture was coated on Cu mesh (a diameter of 6 mm) after stirring overnight for 12 hours. The obtained electrodes were first dried in a vacuum oven at 80 °C for 12 h before assembling the battery cell. Mass loadings were 0.2-0.3 mg.

(4) TiO_2 slurry coated on separator: The same slurry mixtures described above were coated directly onto a Whatman GF/A separator (10 mm diameter, 260

μm thickness) and dried in a vacuum oven at 80 °C for 12 h before assembling the battery cell. Mass loadings were 0.2-0.3 mg.

7.2.2. Electrolytes

The electrolyte used for all Li-ion cells was 1 M Li hexafluorophosphate ($LiPF_6$) in a 1:1 mixture (v/v) of ethylene carbonate (EC) and dimethyl carbonate (DMC). The electrolyte used for the Na-ion cells was 1 M Na perchlorate ($NaClO_4$) in propylene carbonate (PC).

7.2.3. Operando Cell Assembly

The spectroelectrochemical cell used for operando Raman spectroscopy measurements was the EL-Cell Pat-Cell-Opto-10, shown in Figure 1 (a). Light penetration was permitted by a sapphire optical window (22 mm diameter, 0.3 mm thickness). Three electrode stack configurations were used. For all experiments, the following elements of the setup remained constant:

A half-cell configuration was used, with a single electrode operating as both counter and reference. Following placement of the upper electrode, a contact ring was placed around the electrode stack which created a connection between the counter electrode and electrode contact pins, and a holed stainless steel current collector (4 mm hole) placed on top of the ring such that contact ring, working electrode and current collector were in contact. After cell assembly the cells were stored at room temperature at OCV for 8-12 h to maximise soakage of the separators and electrodes with electrolyte prior to cycling. Each individual electrode stack configuration was constructed as

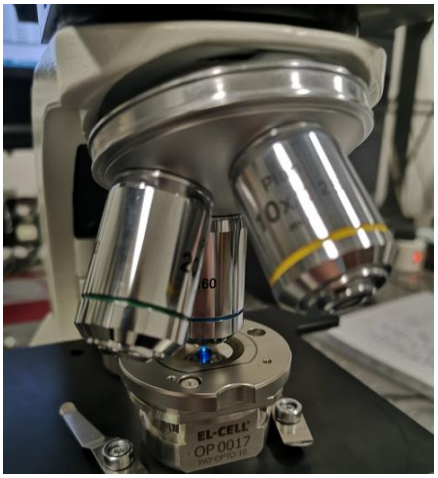
follows listed in order of the stacking direction beginning from the lower electrode to the upper electrode:

(1) ‘Ring system’ electrode stack, shown in Figure 1 (c). This consisted of, from bottom to top, the working electrode (10 mm diameter) of NMC on Al foil substrate or TiO_2 IO on a stainless steel substrate, Whatman GF/A separator (10 mm diameter with a 3 mm diameter hole punched in the center, 260 µm thickness), 10-20 µL electrolyte, a Li metal counter electrode (8 mm diameter with 4 mm diameter hole punched in the center).

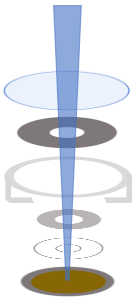
(2) Mesh electrode stack, shown in Figure 1 (b): This consisted of, from bottom to top, a Li metal counter electrode (8 mm diameter), Whatman GF/A separator (10 mm diameter, 260 µm thickness), 20-30 µL electrolyte prepared as 1 M $LiPF_6$ in a 1:1 mixture of EC: DMC, and TiO_2 slurry on Cu mesh as the working electrode (6 mm diameter).

(3) Coated separator electrode stack, shown in Figure 1 (c): This consisted of, from bottom to top, Li/Na metal counter electrode (8 mm diameter), Whatman GF/A separator (10 mm diameter), a second Whatman GF/A separator (10 mm diameter) coated with the TiO_2 slurry working electrode material, 10-15 µL electrolyte.

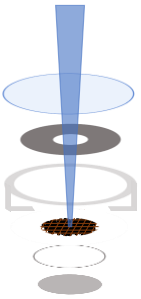
(a)



(b)



(c)



(d)

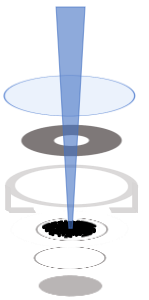


Figure 7.1: (a) Photograph of assembled EL-Cell-Opto-10 under Raman microscope. (b) Schematic of 'ring system' electrode stack. (c) Schematic of mesh electrode stack. (d) Schematic of coated separator electrode stack.

7.2.4. Electrochemical Characterisation

All electrochemical measurements were performed using a multichannel BioLogic VSP Potentiostat/Galvanostat and the Pat-Cell-Opto-10 in half-cell configuration. Cyclic voltammetry (CV) was performed at scan rates of 0.05 mV s^{-1} to 0.1 mV s^{-1} in a potential window of 1-3 V for both the TiO_2 IO electrode and TiO_2 slurry electrode and a potential window of 2.8- 4.3 V for the NMC electrode. Galvanostatic cycling was performed at specific currents from 10 mA g^{-1} to 25 mA g^{-1}. Chronoamperometry was performed for the NMC cathode between CV sweeps at fixed potentials of 3.6 V and 3.8 V.

7.2.5. Operando Raman Spectroscopy

All Raman spectroscopy experiments were carried out using a Renishaw InVia Raman Spectrometer with a 30 mW Ar^+ laser at 532 nm excitation with a laser power in the 20-30 mW range for direct electrode measurements and 50-60 mW for measurements obtained from the spectroelectrochemical cell to combat any attenuation of the beam by cell components. The beam was focused using a 40x objective lens and collected using a RenCam CCD camera.

Continuous laser emission experiments: The laser was switched on and beam emission occurred continuously. Spectral acquisition was programmed to commence at specific intervals throughout the electrochemical sequences under examination. Spectra were acquired with an integration time of 1 s averaged over 10 scans. For TiO_2 IO and NMC cathode experiments, spectra were saved every 5 mins. For the TiO_2 slurry, spectra were saved every 20 mins.

Non-continuous laser emission experiments: At specific intervals throughout the electrochemical sequence under examination, the laser was switched on, beam emission occurred for 1 minute to allow the system to stabilise, and a single spectrum was acquired with an integration time of 1 s averaged over 10 scans. After each acquisition, the laser was switched off immediately.

7.3. Results and Discussion:

Operando spectroscopy of Li-ion batteries using Sapphire Window as Proxy

7.3.1. IO TiO_2 anode – 'Ring system' Electrode Stack

Figure 7.2 (a) shows the Raman spectrum for a bare TiO_2 IO (blue) and for a TiO_2 IO in a Li-ion half-cell at OCV (red). The bare electrode demonstrates the characteristic rutile E_{1g} and A_{1g} modes at 440 cm^{-1} and 610 cm^{-1}, respectively. For the Li-ion half-cell, three peaks appear at 422 cm^{-1}, 582 cm^{-1}, and 757 cm^{-1} which correspond to the A_{1g}, E_g (1), and E_g (2) Raman modes of sapphire. The primary Raman mode of the $LiPF_6$ salt used in the electrolyte also appears in the literature at ~757 cm^{-1} associated with the A_{1g} mode of the PF_6^- anion, its overlap with the highest frequency sapphire mode may contribute to the intensity of the peak.(57)

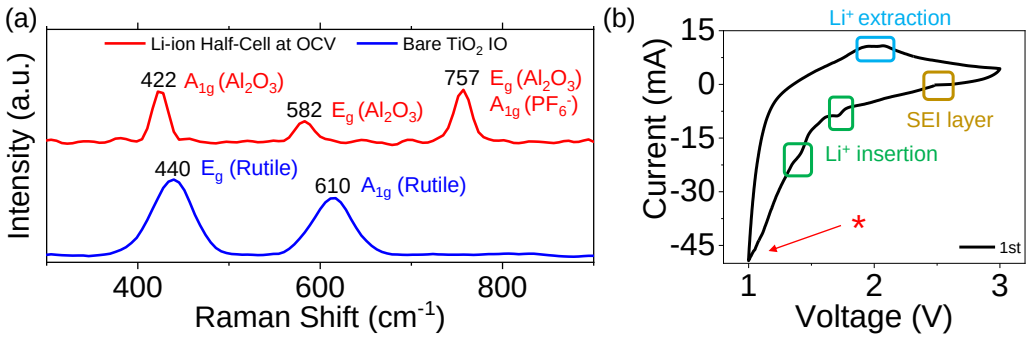


Figure 7.2: (a) Raman spectrum of bare TiO_2 IO (blue) and Raman spectrum with beam focused on TiO_2 IO as a component of assembled Li-ion half-cell at open circuit voltage (OCV) (red). (b) Cyclic voltammogram corresponding to the Li-ion half-cell with TiO_2 IO working electrode.

Figure 7.2 (b) shows the first CV curve obtained for the Li-ion half-cell. In the cathodic scan, minor peaks occur at 1.71 V and 1.4 V where Li^+ insertion occurs. There is also a minor current response at 2.47 V, indicative of SEI formation. In the anodic scan, another minor current response occurs at 2 V

where Li^+ extraction occurs. The relatively small current responses indicate that the insertion and removal processes are incomplete. The potentials at which each of these four current responses occur are in good agreement with previously reported values for a rutile TiO_2 IO cycled in a standard electrochemical cell.(74) A large, sharp peak occurs at 1 V, uncharacteristic of the electrochemical behaviour of TiO_2. While low voltage peaks have been observed for nanoparticulate TiO_2 in Li-ion batteries previously, the sharpness of the current response here indicates that there may be an underlying electrical contact issue.

The 'ring system' electrode stack configuration used here changes the nature of the delivery of current density between counter and working electrodes which undoubtedly effect the electrochemical response of the system. This sharp, low voltage peak may be due to a suboptimal electrode stack configuration. Nevertheless, current response begins at 1.45 V and reaches a maximum at 1 V. The operando Raman measurements during this portion of the CV scan demonstrate interesting changes.

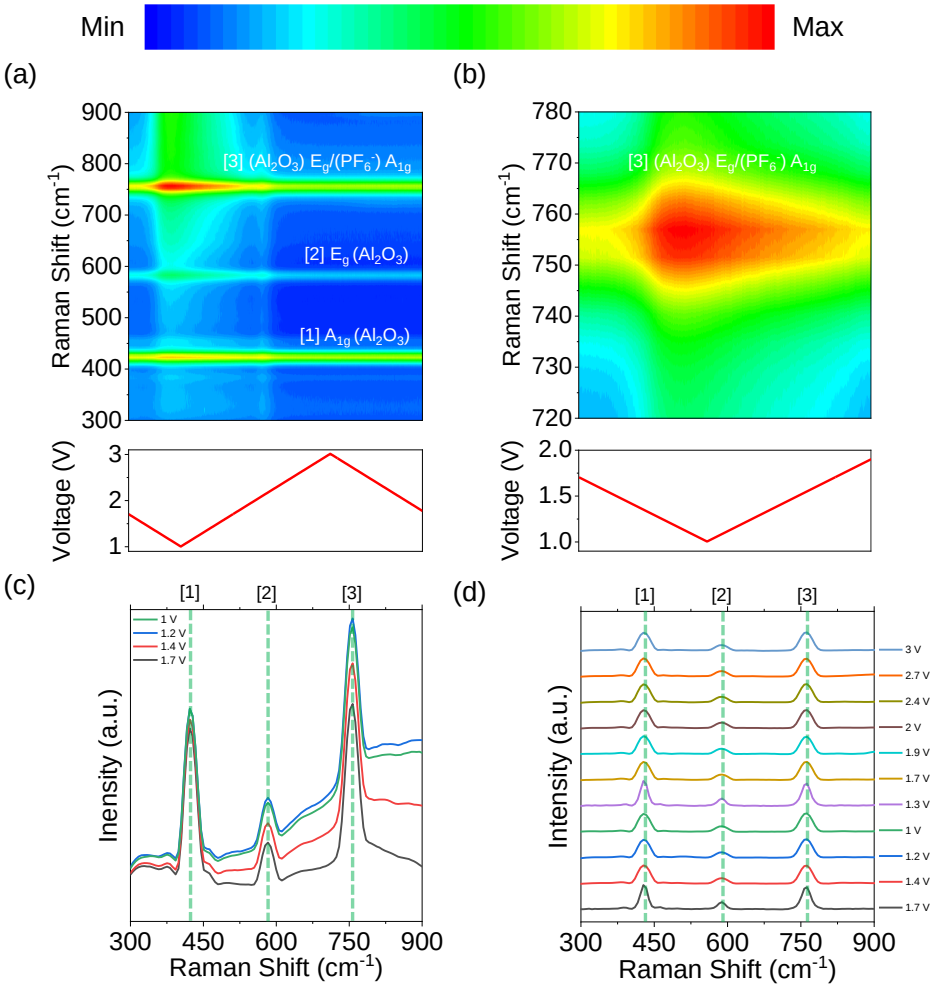


Figure 7.3: Operando Raman spectroscopy of TiO_2 IO in Li-ion half-cell during galvanostatic cycling over 2 cycles at a laser specific power of 20 mW. The 'Ring system' electrode stack configuration described in section 7.2.3 was employed. (a) Raman colormap during the first CV scan over the inspected range of 300-900 cm^{-1} where Raman active modes for rutile TiO_2 and $LiPF_6$ occur and associated voltage profile below. (b) Reduced spectral region from the same Raman colormap highlighting the evolution of the peak associated with the E_g (2) mode of sapphire over the bottom of the cathodic scan. Note 1: x axes for both the colormap and voltage profile correspond to time, for which electrochemical and spectral acquisition are synchronised. Note 2: Background subtraction was not performed. (c) Raw Raman spectra at selected voltages during the bottom of the first cathodic scan. (d) Stacked Raman spectra for selected voltages throughout the first CV scan where background subtraction was performed. Green dashed lines in (c) and (d) mark the three sapphire Raman modes.

Figure 7.3 shows results obtained from operando Raman spectroscopy during the CV scan presented in Figure 7.2 (b). In Figure 7.3 (a), the colormap

shows the evolution of the Raman spectra throughout the CV scan with the associated voltage profile below. The three peaks associated with the sapphire Raman modes are present throughout the scan, labelled as [1], [2], and [3]. In the first portion of the profile there is a cathodic scan from OCV at 1.7 V to 1 V, followed by an anodic scan from 1 V to 3 V. Figure 7.3 (b) shows a reduced spectral region of the colormap from Figure 7.3 (a) corresponding to band [3] and the associated reduced voltage profile below from the beginning of the cathodic scan at 1.7 V to 1.9 V during the anodic scan, where the most notable change to the Raman spectra occurs. While a slight increase in band [1] is also observed in this potential range, band [3] evolves the most. A significant increase in both intensity and bandwidth occurs, where the bandwidth reaches a maximum just prior to the bottom of the cathodic scan. Given that the strongest Raman mode of the $LiPF_6$ electrolyte salt occurs at the same frequency as band [3], it is likely that this maximum increase is a consequence of the overlap between these two bands, with the fluorescent PF_6^- species migrating outward from the electrode towards the incident laser beam as Li^+ is inserted into the electrode during the cathodic scan.

Figure 7.3 (c) shows raw Raman spectra prior to background subtraction from select voltages near the bottom of the cathodic scan where the changes to spectral intensity are clearest. Figure 7.3 (d) shows Raman spectra at select voltages throughout the CV scan after background subtraction. Little observable change occurs for the range of scans. In each case, only the three sapphire Raman modes are observed. Despite the increase in Raman intensity, particularly for band [3] shown in the colormaps,

the relative intensities of the peaks show negligible change for all voltages. The most interesting aspect of the results is the voltages at which the increases in spectral intensity occur during the CV scan. In the following sections, a common theme emerges in relation to this.

7.3.2. NMC cathode – 'Ring system' Electrode Stack

Given the spectral changes observed just before Li insertion for the TiO_2 IO prompted further investigations of the underlying causes. Additionally, question marks remained over the 'ring system' electrode stack configuration due to the weak electrochemical response during the previously shown CV scan. Both observations prompted a change in electrode material. A commercial NMC-622 cathode was chosen, with a different active potential window of 2.8 V – 4.3 V. Operando Raman measurements were performed to evaluate the electrochemical stability of the 'ring system' electrode stack and determine whether changes to the spectral intensity occurred at equivalent potentials, i.e., in the vicinity of the potentials where Li insertion and removal occur.

The CV curves for the first and second scan of the NMC cathode are shown in Figure 7.4 (a), while the first and second galvanostatic charge-discharge curves are shown in Figure 7.4 (b). Addressing the stability of the 'ring system' electrode stack, both the CV curves and charge-discharge curves exhibit the characteristic electrochemical behaviour of NMC cathode material in a Li-ion battery. Operando Raman spectroscopy was performed during both tests. The associated voltage profile for the second CV scan is shown in Figure 7.5 (a), while stacked Raman spectra at select voltages during the scan are

shown in Figure 7.5 (b). Once again, the three Raman modes of sapphire remain with a fixed frequency and intensity at all voltages. However, unlike the TiO_2 IO case, some additional modes appear.

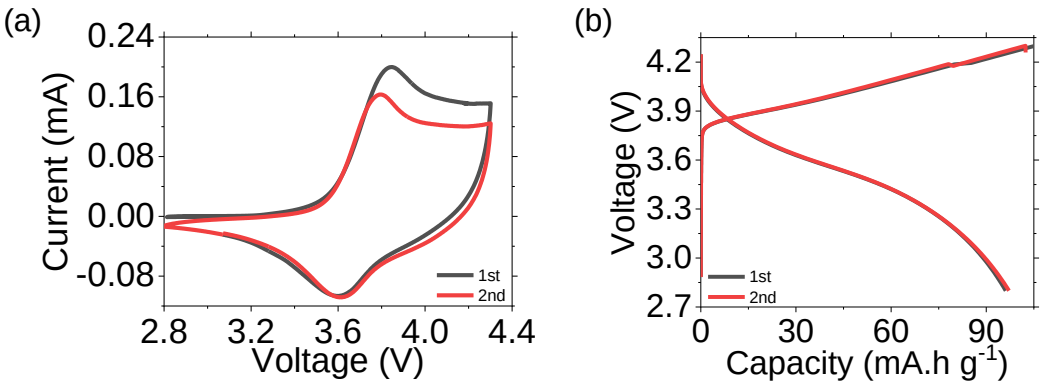


Figure 7.4: (a) CV curves obtained at a scan rate of 0.05 mV s^{-1} and (b) galvanostatic cycling curves obtained at a specific current of 25 mA g^{-1} for the commercial NMC-622 electrode using the 'ring system' electrode stack configuration during which operando Raman measurements were obtained.

Starting from the low frequency side, the first additional Raman mode of note appears at 525 cm^{-1}. The peak begins to appear during the first anodic portion of the scan at 3.7 V and becomes fully formed at 4 V. The peak then disappears at the top of the anodic scan, 4.3 V. The peak then reappears at 3.7 V during the cathodic portion of the scan, and is strongly attenuated at 3.4 V. Given the convoluted nature of the NMC modes, related to M-O symmetrical stretching (A_{1g}) and and O-M-O bending (E_g), clear interpretation of the peaks here is not straightforward. Nevertheless, the peak at 525 cm^{-1} appears close to the two modes related to $LiCoO_2$. Namely, the A_{1g} mode related to Co-O stretching, reported previously for NMC at 530 cm^{-1} and the E_g mode related to O-Co-O bending at 515 cm^{-1}.(70, 75-78) In the same report, the evolution of these Raman modes during Li extraction (charge) were observed with both modes attenuated, and the E_g mode undergoing an anti-Stokes shift.

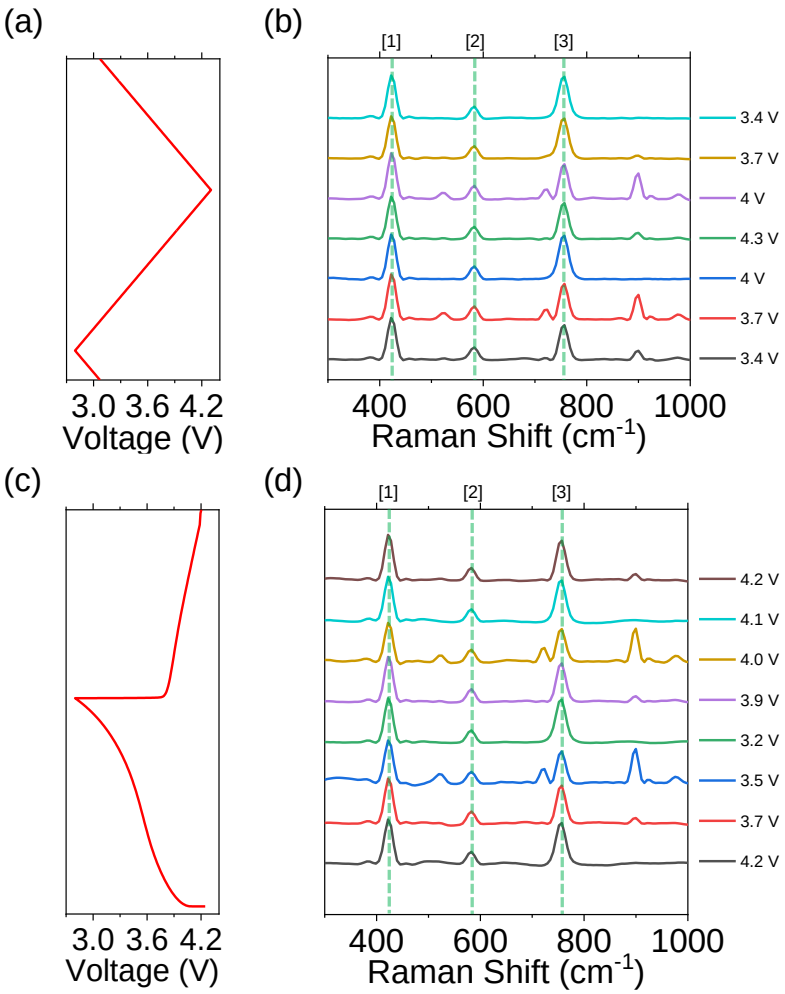


Figure 7.5: Operando Raman spectroscopy measurements of NMC-622 electrode in 'ring system' electrode stack configuration. (a) Voltage profile of a single CV scan in a potential window of 2.8 V to 4.3 V. (b) Stacked Raman spectra acquired at selected voltages during the CV scan for the 450-1050 cm^{-1} spectral region. (c) Voltage profile of a single galvanostatic cycle performed at 25 mA g^{-1} in the same potential window. (d) Stacked Raman spectra acquired at selected voltages during the cycle for the 300-1000 cm^{-1} spectral region. The green dashed lines in (b) and (d) mark the sapphire Raman modes. Laser specific power was 20 mW for all measurements.

The second notable peak occurs at 721 cm^{-1}, near the peak associated with the E_g mode of sapphire and is in good agreement with reported values for the ring-bending (C=O bending) mode of EC, the electrolyte solvent, upon coordination to the Li^+ cation.(79-82) The peak begins to appear at 3.7 V

during the first anodic portion of the scan and follows the same trend as the first additional peak.

The last strong peak occurs at 900 cm^{-1} and evolves similarly to the previous two at the same potentials to reach the largest relative peak intensity besides the ever present sapphire modes. The peak is associated again with EC, arising from interaction between the ring-breathing vibration mode to bound and free Li^+ cations.(81, 83-85) The appearance of these two peaks near the point of Li extraction occurs due to the removal of the Li^+ cations from the NMC electrode resulting in a greater concentration of free Li^+ cations interacting with the organic solvent. Three additional, much weaker peaks occur in close proximity to the highest frequency strong peak at 900 cm^{-1}. One occurs on the red side of it at 865 cm^{-1}, and only appears at 4.3 V, 3.7 V, and 3.4 V. The two weaker peaks on the blue side of it occur at 924 cm^{-1} and 977 cm^{-1} for potentials of 4 V and 3.7 V, and weaker again at 3.4 V. Again, the peaks appear and evolve at the same potentials as the three larger peaks. All can be related to the coordination of the non-aqueous solvents to Li^+ cations, at the points at which Li^+ extraction occurs.

The voltage profile for the second galvanostatic cycle is shown in Figure 7.5 (c) and the stacked Raman spectra at select voltages during the cycle are shown in Figure 7.5 (d). The same peaks appear at the same frequencies and similar voltages. Again, the peaks are most well defined just prior to Li^+ insertion and Li^+ extraction.

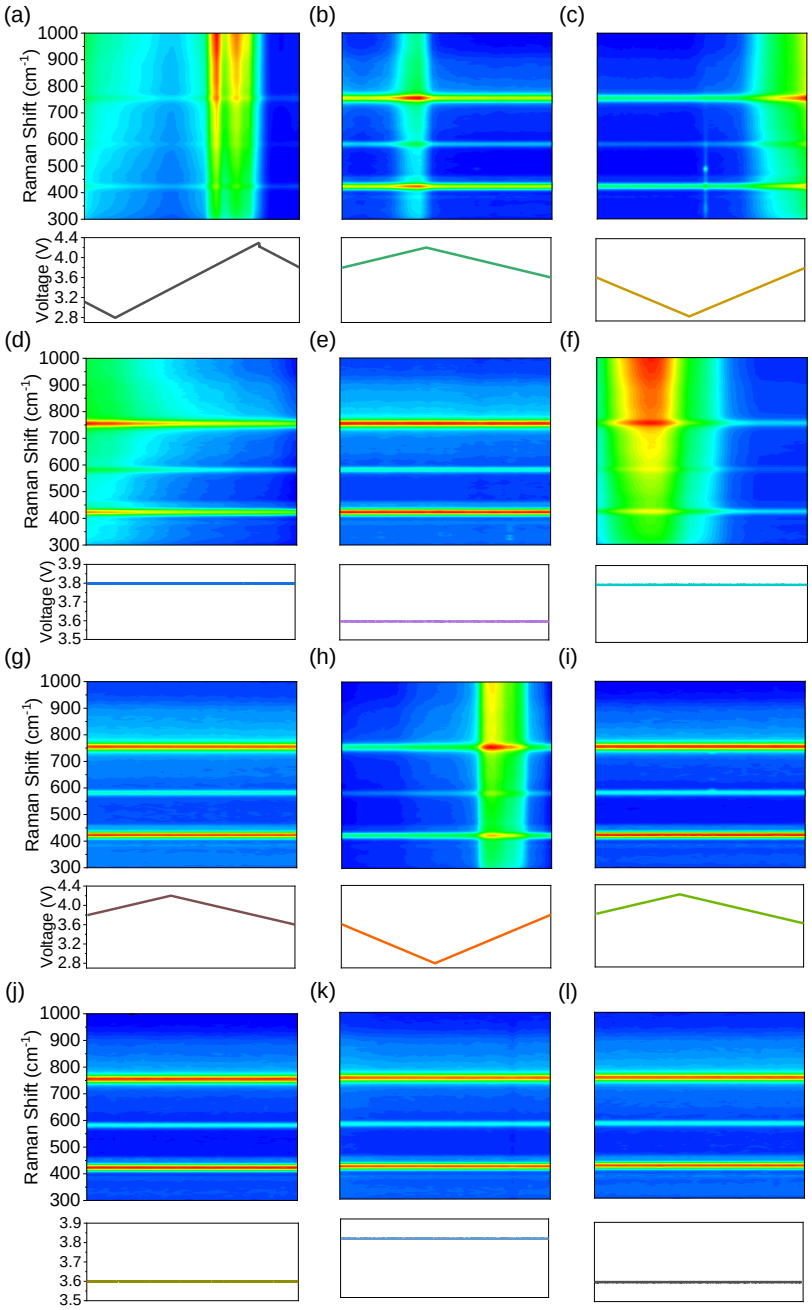


Figure 7.6: Operando Raman spectroscopy from chronoamperometric cycling of commercial NMC cathode in Li-ion half-cell at a specific power of 20 mW. For each stage, colormaps are presented with the associated time-voltage profiles below. For the colormaps, the x and y axes represent time versus Raman shift, while the colour represents Raman intensity. Spectra were acquired every 5 mins. Chronoamperometry was performed over six stages, each consisting of a potential sweep step shown in (a)-(f), followed by a fixed potential step (g)-(l). Note 1: Background subtraction has not been performed. Note 2: A colour scale is applied to the colormaps from each individual stage of the chronoamperometric experiment based on the maximum and minimum intensities during that stage to enhance visualisation of detected changes.

The purpose of the chronoamperometric test was to provoke a phase change in the electrode material. While the evolution of the electrolyte, observed in changes to the intensity of the band associated with the PF_6^- anion is evident, changes to the electrode prove more difficult to elucidate. Li^+ insertion and removal in NMC occurs at 3.6 V and 3.8 V, respectively. The chronoamperometry tests hold the potential where these processes occur.

Figure 7.6 shows each stage of the chronoamperometry test. For each stage, the colour scale is adjusted based on the minimum and maximum intensities observed to maximise visibility of any spectral changes which occur. The colormap for the full experiment is shown in Figure S7.2, along with the associated voltage profile. The experiment consisted of twelve steps, which started as a voltage sweep to the Li^+ extraction voltage of 3.8 V, the voltage was then held constant, followed by a decreasing voltage sweep to the Li^+ insertion voltage of 3.6 V and the voltage was held constant again here. These steps were then repeated so that Raman spectra were obtained during two positive and negative voltage sweeps, two constant voltage steps at the point of Li^+ extraction, and two constant voltage steps at the point of Li^+ insertion. Figure 7 (a)-(c) show the first three voltage sweep steps, while Figure 7.6 (d)-(f) show the constant current stages which follow each step. Figure 7.6 (g)-(i) show the next three voltage scans, with the constant voltage steps that follow each one in Figure 7.6 (j)-(l).

The colormaps support the findings based on the TiO_2 IO and from the stacked NMC spectra. The stacked NMC spectra show the appearance of Raman modes just prior to Li^+ insertion and extraction indicating the interaction

between the electrolyte and the free Li^+. The colormaps from the TiO_2 IO show a massive increase in the spectral intensity at voltages just prior to Li^+ insertion. Here, while the objective was to provoke spectral changes during the constant voltage step, there is a dramatic change in the spectral intensity at voltages just prior to Li^+ intercalation. These changes are most evident in Figure 7.6 (a), (c), (d), (f), and (h).

7.3.3. TiO_2 Slurry – Mesh Electrode Stack

The electrode stack configuration was changed to prevent any misalignment or contact issues. The mesh electrode stack provides direct access of the laser beam to the electrode material. For the 'ring system' electrode stack, the laser beam must be transmitted through the electrolyte filled space between working and counter electrode and reflected through the same space before reaching the detector. For the mesh electrode stack, the beam interacts with the active working electrode material immediately after transmission through the sapphire window. Therefore, only the attenuation of the window material affects the spectrum. An anatase TiO_2 slurry was used as working electrode. The ex-situ Raman spectrum of the electrode slurry is shown in Figure S7.1 (b). Notably, the relative intensities of the Raman modes of the anatase TiO_2 slurry are greatly enhanced compared to those observed for the TiO_2 IO and NMC electrodes.

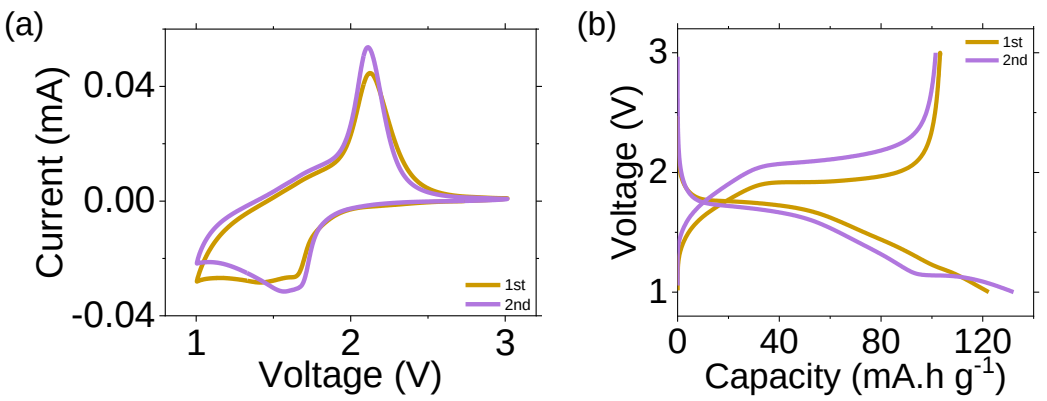


Figure 7.7: (a) CV curves obtained at a scan rate of 0.05 mV s^{-1} and (b) galvanostatic cycling curves obtained at a specific current of 10 mA g^{-1} for the TiO_2 slurry electrode using the 'ring system' electrode stack configuration from which operando Raman measurements were obtained.

Figure 7.7 (a) shows the curves from the first and second CV scans performed for the TiO_2 slurry coated on Cu mesh in a Li-ion half-cell. Figure 7.7 (b) shows the first and second charge-discharge curves from galvanostatic cycling of the half-cell at 25 mA g^{-1}. Characteristic TiO_2 intercalation behaviour is observed in both cases. Both sets of results indicate more electrochemically stable, and more efficient Li intercalation here compared to the TiO_2 IO examined using the 'ring system' electrode stack.

Operando Raman spectroscopy was performed during the two galvanostatic cycles from Figure 7.7 (b). In Figure 7.8 (a), a colormap of the operando Raman spectra acquired over the two cycles is shown with the synchronised voltage profile below. The three sapphire modes are indicated as modes [1], [2], and [3] once again. Similar behaviour as the other two systems occurs. Spectral intensity is significantly increased during the stages where the voltages plateaus occur. They are maximum just prior to the point of Li^+ insertion and extraction. Once again, the intensity is most pronounced

for sapphire mode [3], which overlaps with the peak associated with the PF_6^- Raman mode.

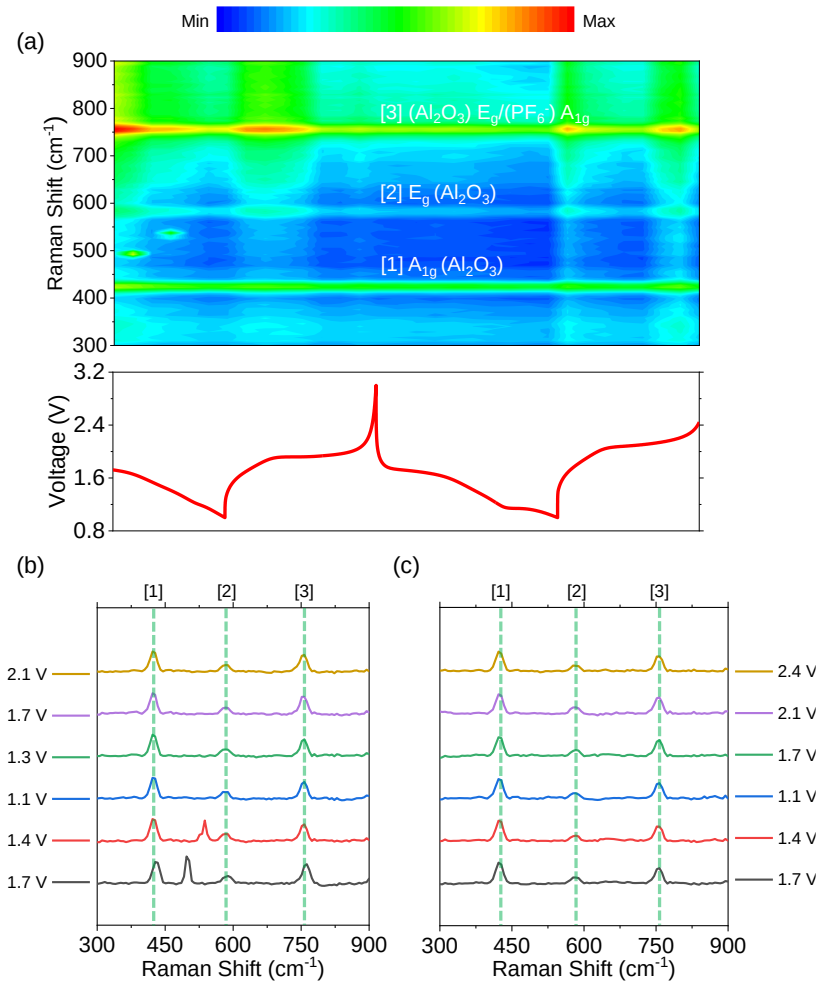


Figure 7.8: Operando Raman spectroscopy of TiO_2 slurry during galvanostatic cycling at 25 mA g^{-1} over 2 cycles with spectra acquired every 20 mins at a laser specific power of 20 mW. (a) Raman colormap in the range of 300-900 cm^{-1} where Raman active modes for TiO_2 and $LiPF_6$ occur over two galvanostatic cycles with the associated voltage profiles below. The green dashed lines in (b) and (c) mark the three sapphire Raman modes.

Figure 7.8 (b) and (c) show stacked operando Raman spectra acquired at select voltages during the first and second galvanostatic cycle, respectively. Like the results shown previously for the TiO_2 IO, there is little observable change seen in the spectra and both the Raman shift and relative intensities

of the three sapphire peaks remain relatively unchanged. However, at 1.4 V and 1.7 V during the first cycle, two clear peaks emerge at 537 cm^{-1} and 498 cm^{-1}, respectively. The origin of these peaks is yet unidentified. The two peaks do not reappear in the second cycle, indicating that both additional peaks may be due to metastable SEI species which form during the first cycle.

The signal that masked the Raman activity of the three electrode types in Li-ion batteries thus far was caused by laser-induced fluorescence of the Li-ion electrolyte species. The effects of the sapphire window and the pressure induced by the sealed cell are shown in Figure S7.3. While these two factors cause some attenuation of the Raman modes, they are still clearly identifiable. A spectrum of the anatase TiO_2 slurry soaked in electrolyte post-assembly is also shown. Here, the anatase peaks remain present, along with peaks associated with decomposed electrolyte species. Clearly, the fluorescence build-up is caused by the active electrolyte and its interaction with the electrode. These findings prompted the change of electrolyte. The next section details operando Raman spectroscopy investigations with a different electrolyte, while also changing to a Na-ion cell chemistry.

7.4. Operando Raman Spectroscopy of TiO_2 Anode in Na-ion Battery – Coated Separator Electrode Stack

In Figure 7.9, the progression of operando Raman spectroscopy investigations performed for the Na-ion half-cell are detailed. Figure 7.9 (a) shows a comparison of the pristine TiO_2 slurry electrode directly and under the sapphire window compared to the assembled Na-ion half-cell at a range of laser specific

powers. The contrast compared to the Li-ion system is immediately evident in the spectra for the Na-ion half-cell. While for the Li-ion system, only the sapphire modes were observed with the rest of the expected modes masked, here the Raman modes of anatase TiO_2 (blue dashed lines) and for the electrolyte species (red dashed lines) can be identified. The range of laser powers are shown such that the spectrum of the assembled cell can first be compared directly at the same power to the ex-situ spectra, and second to show the selection of the specific power used for operando measurements based on the best observable SNR, which was 20 mW. Four characteristic Raman modes of anatase appear in the raw ex-situ Raman spectrum in Figure 7.9 (a). Figure S7.1 (b) shows the ex-situ Raman spectrum of the anatase slurry after background subtraction. The modes appear at 155 cm^{-1}, 399 cm^{-1}, 519 cm^{-1} and 641 cm^{-1} with E_g, B_{1g}, A_{1g} and E_g symmetries, respectively.

Figure 7.9 (b) shows the operando Raman spectrum of the half-cell after one cycle. Here, the laser had been switched off and restarted. Additional modes can be observed, indicated by the gold dashed lines. A strongly polarised mode appears at 284 cm^{-1} which is in good agreement with reported values for vibrations of the O-Ti-O group in Na titanate, along with a much weaker mode at 330 cm^{-1} which is also related to O-Ti-O bond vibrations in the same.(86-89) Another low intensity peak appears at 714 cm^{-1} which is attributed to the skeletal bending mode of the five-membered ring in the PC electrolyte solvent.(90, 91)

Figure 7.9 (c) is included to demonstrate the buildup of fluorescence for measurements taken in continuous laser emission mode. Initially, the modes

which appeared in Figure 7.9 (b) can be identified, but after a period the fluorescence causes a dramatic increase in spectral intensity by multiples, masking all relevant signals. The early spectra for which the modes can still be identified are highlighted and shown more clearly in Figure 7.9 (d).

Due to the fluorescence buildup, the approach to spectral acquisition was changed. Rather than continuous laser emission running simultaneously to electrochemical cycling, the latter was commenced with the laser switched off. For each operando Raman spectrum that was acquired, the laser was switched on for 1 minute, spectrum acquired, and laser switched off again. Figure 7.9 (e) shows the raw operando Raman spectra acquired using this approach at select voltages during discharge of the Na-ion half-cell from 3 V to 0.6 V. While the degree of fluorescence varies, the expected signals can be distinguished in all cases. Figure 7.9 (f) shows stacked Raman spectra corresponding to the same data with background subtraction performed. The first spectrum is acquired at the beginning of discharge at 2.9 V. The spectra are then stacked from bottom to top in order of decreasing voltages. The low current density of 10 mA g^{-1} was applied to capture any short-lived or metastable phases. There is a large difference in voltage from the first to second spectrum due to a rapid discharge in this voltage range where there is a lack of electrochemical activity, evident upon examination of Figure S7.4 (c). The voltage plateau begins at ~ 2.1 V and becomes pronounced at ~1.2 V. As a result, the remaining seven spectra are acquired at voltage increments of 0.1-0.2 V along the slow discharge region between 1.5-0.6 V. The same colour scheme of dashed lines is used to distinguish the various Raman modes as in

Figure 7.9 (a) and (b) and are aligned with the vertices of the identified peaks in the first acquired spectrum at 2.9 V. Any variations in Raman activity can be evaluated relative to this first spectrum. A total of twelve Raman modes are identified, four of which were only captured by operando measurements.

There is a clear attenuation of the three sapphire Raman modes, from the first spectrum acquired at 2.9 V to the second spectrum at 1.5 V. Given that sapphire acts as window material, any electrochemical changes have no effect on its Raman activity. However, as shown by the results presented in this study based on three electrode types in Li-ion batteries, the underlying electrochemical activity of the system has a clear effect on the optical reflectance of sapphire. It has previously been shown that the optical reflectance of sapphire is highly sensitive to surface quality, and this optical reflectance has a substantial effect on the optical vibrational modes.(92-95) The electrochemical cycling of Li-ion and Na-ion batteries has been shown to significantly affect observed optical reflectance, due to the evolution of electrode and electrolyte species.(96-100) It comes as no surprise here that the discharge of the Na-ion battery into this anatase electrode causes an attenuation of the sapphire Raman modes. After this second spectrum, the intensities of the modes remain relatively constant.

Of the remaining 9 modes, the most notable changes occur to the peak associated with Na titanate at 284 cm^{-1}, and the two highest frequency anatase peaks. The peaks associated with Na titanate are present from the beginning of the discharge because the electrode had already undergone galvanostatic cycling. There is a clear evolution of the peak at 284 cm^{-1} during discharge,

which appears first as a sharp, high intensity peak at 2.9 V, then grows broader at 1.5 V, before appearing to extend to a broad, doublet peak at 1.4 V that remains until 1 V, which then shrinks to form a sharper, lower intensity peak at 0.8 V. The increased bandwidth may be due to an increase in the concentration of amorphous Na titanate, and the doublet appearance indicated the presence of an additional Raman mode given that many of the vibrational modes of Na titanate appear in this region.(89, 101)

As described by equation 7.2, the sodiation mechanism of anatase TiO_2 involves the insertion of Na into the TiO_2 lattice, which distorts the lattice and partially reduces TiO_2 to form metallic titanium, Na oxide and amorphous Na titanate. While the complete sodiation of TiO_2 would result in the complete disappearance of the four anatase Raman modes (blue dashes), the sodiation reaction typically remains incomplete which can be partially attributed to the much slower rate of ion diffusion that is characteristic of amorphous materials.(102) Instead, the bands are attenuated as a decrease in peak intensity and a simultaneous increase in bandwidth. Attenuation is most evident for the two highest frequency peaks at 519 cm^{-1} and 641 cm^{-1}.

Of the additional modes captured in operando (gold dashed lines), the same three identified in Figure 7.9 (b) remain, along with an additional mode revealed upon background subtraction which occurs at 204 cm^{-1}, which based on several literature reports is also associated with Na-Ti-O vibrational modes.(86, 103)

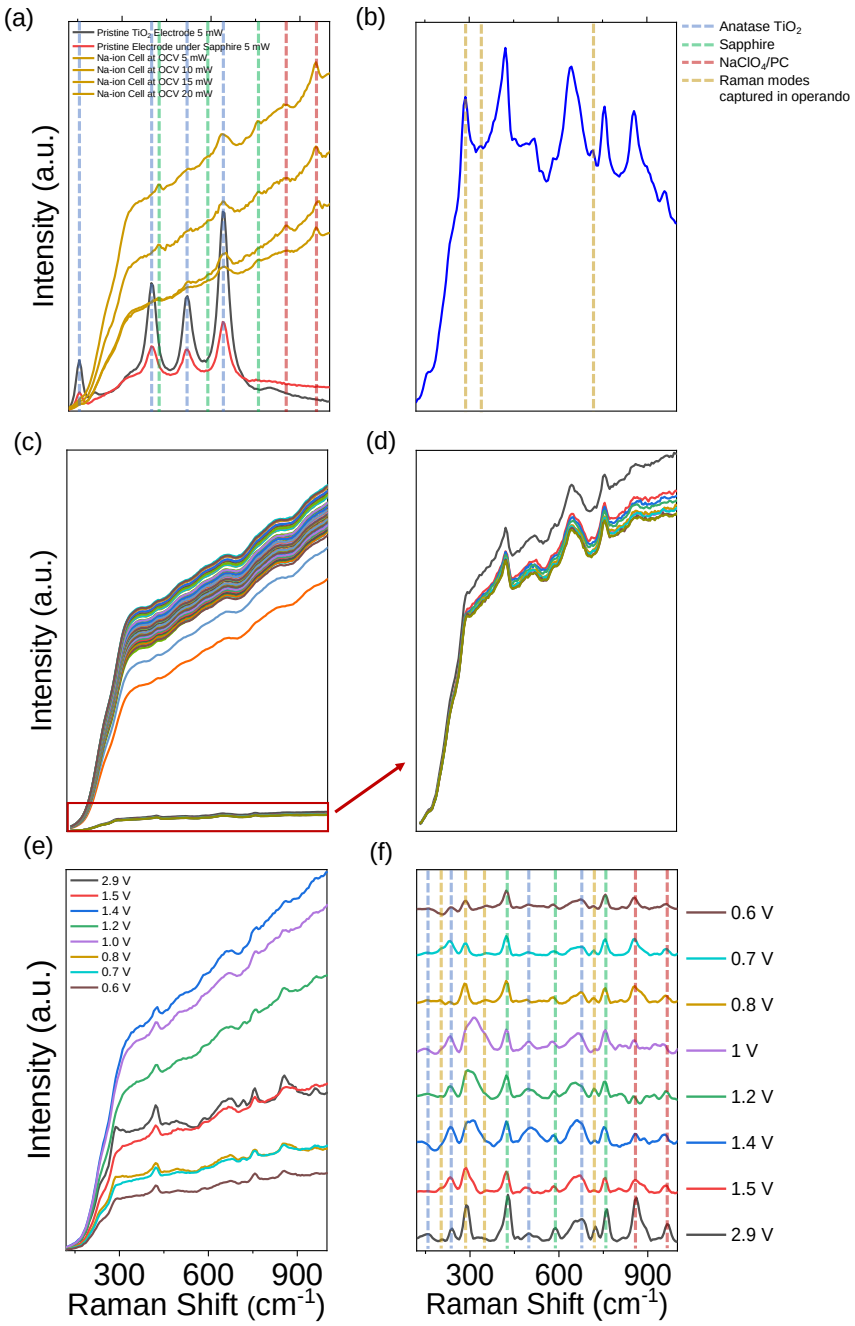


Figure 7.9. (a) Raw Raman spectra of the TiO_2 slurry electrode demonstrating the changes caused by the sapphire window and the cell components compared to the pristine electrode. Characteristic Raman modes are highlighted by dashed lines. (b) Raw Raman spectrum obtained from Na-ion half-cell during discharge, upon instantaneous laser emission with the appearance of new Raman modes highlighted by dashed lines, the colour scheme for the dashed lines throughout this figure is provided by the legend in the upper right hand corner. (c) Raw operando Raman spectra collected during electrochemical discharge with continuous laser emission, demonstrating the formation of the fluorescence mask which hides previously observed Raman modes. The red rectangle highlights spectra for which Raman modes could be distinguished prior to the formation of the mask.

Figure 7.9. (continued) (d) Expansion of the region highlighted by the red rectangle in (c) showing clearly defined Raman modes. (e) Raw operando Raman spectra acquired at a range of voltages during electrochemical discharge where laser emission occurred for 1 minute prior to each measurement. (f) Stacked Raman spectra after background subtraction during discharge generated from the spectra in (e) with the dashed lines used to identify each Raman mode. All operando Raman spectra in (b)-(f) were acquired during galvanostatic discharge from 3-0.5 V at a specific current of 10 mA g^{-1}.

7.5. Conclusions

For all three electrodes, the fluorescence mask produced by the interaction between the laser beam and the fluorescent species that form due to the interaction between the electrode materials and the Li-ion electrolyte prevented monitoring of the active Raman modes of the anode material directly. Nevertheless, for all three electrodes, upon focusing the laser beam onto the electrode surface, the active Raman modes of sapphire (Al_2O_3) were detected. Operando Raman spectra collected here during continuous laser emission show distinct changes in the intensity of the Raman spectra. While the Raman modes of the anode material are obscured, in each case, a dramatic evolution of the spectra occurs at points just before and after Li^+ insertion and removal. While the active electrochemical windows of TiO_2 differ (1-3 V for TiO_2 and 2.7-4.4 V for NMC vs Li/Li^+), similar changes occurred at equivalent voltages with respect to the intercalation voltages with respect to Li. Using the Raman active modes of sapphire as a proxy, the changes to reflectivity and intensity of those modes are shown to coincide with changes occurring in the anode/electrolyte underneath. Furthermore, new Raman modes appear at select voltages during cycling related mainly to interactions between free Li^+ and the electrolyte solvents.

Upon changing from a Li-ion system to a Na-ion system with a less fluorescent electrolyte, the fluorescence mask issue is shown to be mitigated initially. However, the data shows that as spectra were collected under continuous laser emission, the fluorescence mask reemerged. To combat this, operando Raman measurements were obtained using a non-continuous laser emission method. Rather than acquiring a spectrum at fixed time intervals under constant laser emission, for each spectrum in this case, the laser was switched on for 1 minute, spectrum acquired, and the laser switched off. The change in approach reduced the fluorescence buildup, and the characteristic Raman modes were detected. Prior to electrochemical cycling, the characteristic Raman modes of anatase, $NaClO_4$, PC, and sapphire were detected. During electrochemical discharge, the same modes were detected, along with the appearance of new Raman modes, which were discussed in detail, including evidence of the phase change from anatase TiO_2 to amorphous Na titanate.

7.6. Appendix: Supplementary Material

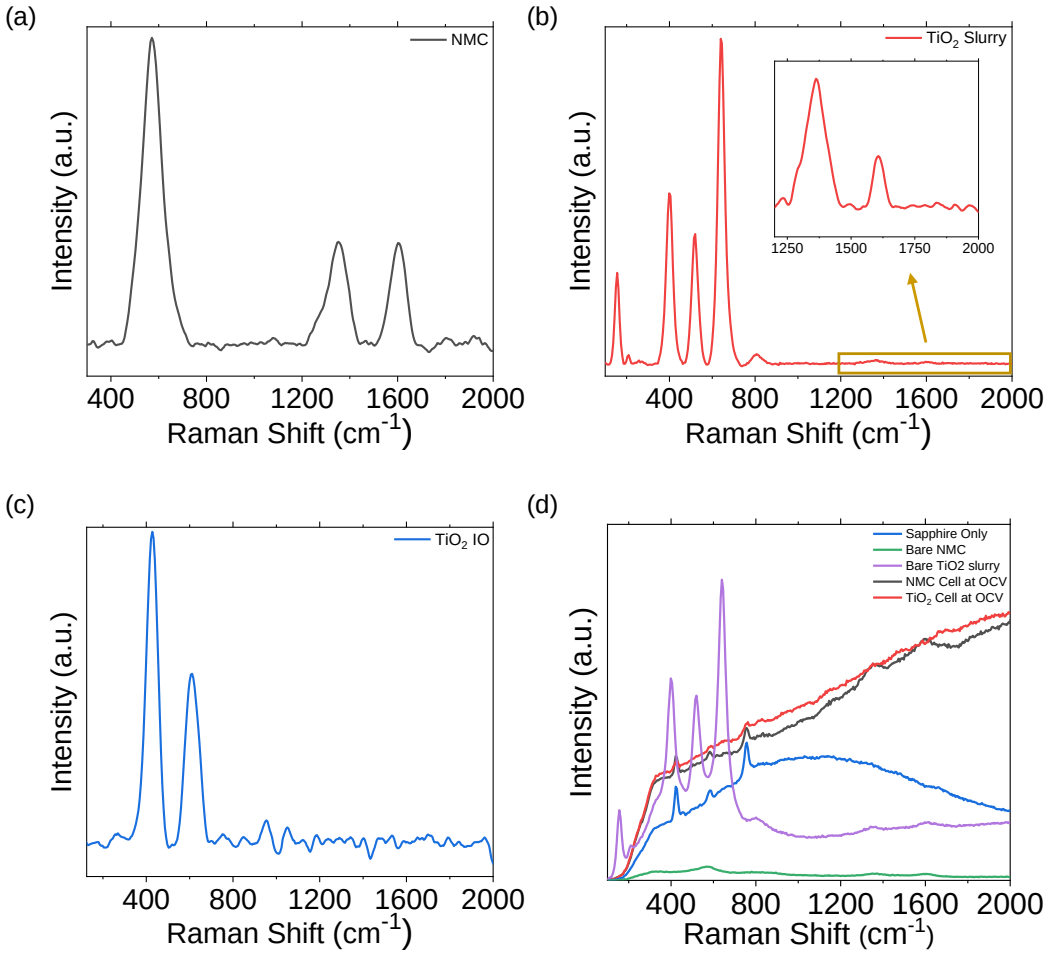


Figure S7.1. Ex-situ Raman spectra after background subtraction for (a) commercial NMC electrode at a laser specific power of 20 mW, (b) TiO_2 slurry (inset highlights region where carbon peaks occur) with at 2 mW, and (c) TiO_2 IO at 20 mW. (d) Raw Raman spectra comparing two of the bare electrodes, sapphire window, and the same electrodes as components of Li-ion half-cells to highlight the appearance of the fluorescence mask.

Figure S7.1 (a)-(c) shows the ex-situ Raman spectra for the three materials investigated using Raman spectroscopy. The spectra region from 125-1000 cm^{-1} is of most importance for the analysis in the main text, given this is the region where the Raman modes for all the electrode and electrolyte species occur. However, the higher frequency region of 1000-2000 cm^{-1} is included here as the carbon modes appear here. For carbonaceous species, a D band

appears characteristic of disordered carbon, present in (a) and (b) here at approx. 1400 cm^{-1} and 1600 cm^{-1}. The presence of the peaks is due to the carbonaceous conductive additives and binders used for the formation of the commercial NMC slurry (a) and the TiO_2 slurry (b). For IOs, one of their defining characteristics is that they are conductive additive and binder-free. Consequently, no carbon modes are present in Figure S1 (c). In Figure S7.1 (a), one broad dominant peak occurs with a vertex at 571 cm^{-1}, which is a good match for the characteristic Eg (Mn) mode. The bandwidth of the peak is large, extending from 443-744 cm^{-1}, the range within which all 6 commonly identified modes of NMC occur.

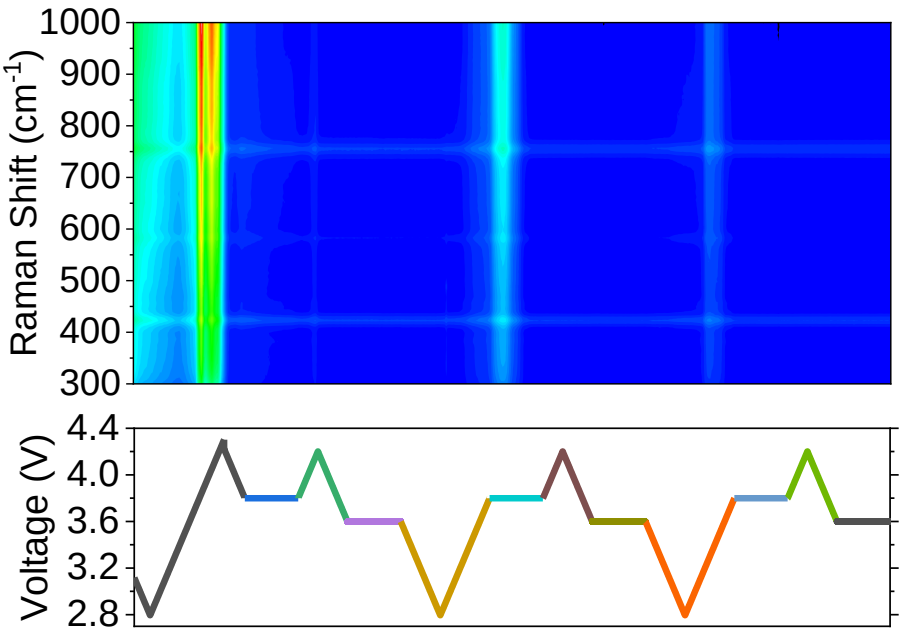


Figure S7.2. Full operando Raman spectroscopy colormap from chronoamperometric cycling of commercial NMC cathode in Li-ion half-cell from which the stages in Figure 7.6 of the main text were extracted. Synchronised voltage profile below.

The chronoamperometry test of the NMC cathode presented in figure 7.6 of the main text show the Raman colormaps for each stage of the test. Each colormap was constructed based on the maximum and minimum spectral intensities for the individual stages. Figure S7.2 shows the colormap which was generated initially generated on the maximum and minimum spectral intensities over the entire experiment. The difficulty in distinguishing any changes to the individual Raman modes and between stages is clear here compared to the more informative version shown in the main text. The voltage-time profile below shows the procession of the test with a linear sweep step followed by a constant current step repeated.

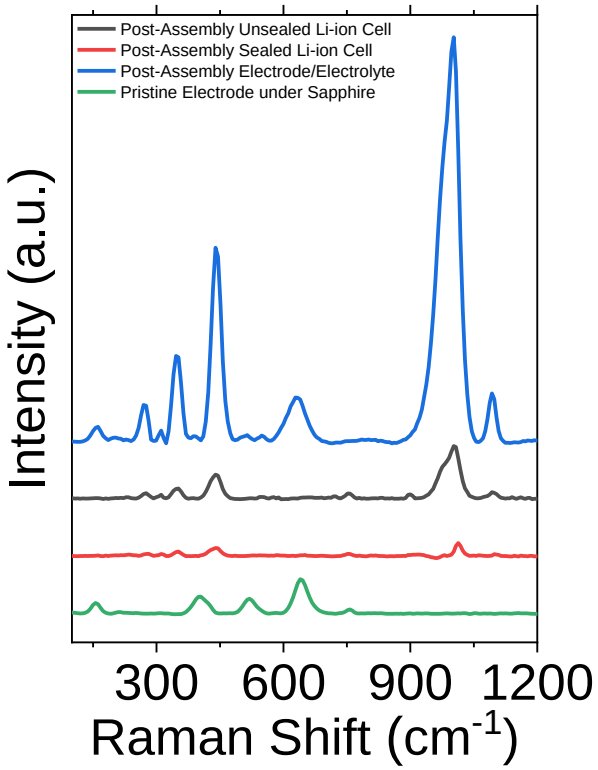


Figure S7.3. Ex-situ Raman spectra acquired from anatase TiO_2 slurry to show the effects of cell components and sealing on Raman signals: Pristine electrode under sapphire window (green), electrode post-assembly in sealed cell (red), electrode in unsealed cell post-assembly (grey), bare electrode with decomposed electrolyte species post-assembly.

Throughout the investigations into the three electrode types in Li-ion batteries in the main text, laser-induced fluorescence caused mainly by interaction with the $LiPF_6^-$/EC/DMC electrolyte acts as a mask to identification and interpretation of active Raman modes. Figure S7.3 shows the effects of pressure, the optical window, and decomposed electrolyte species on the anatase TiO_2 slurry.

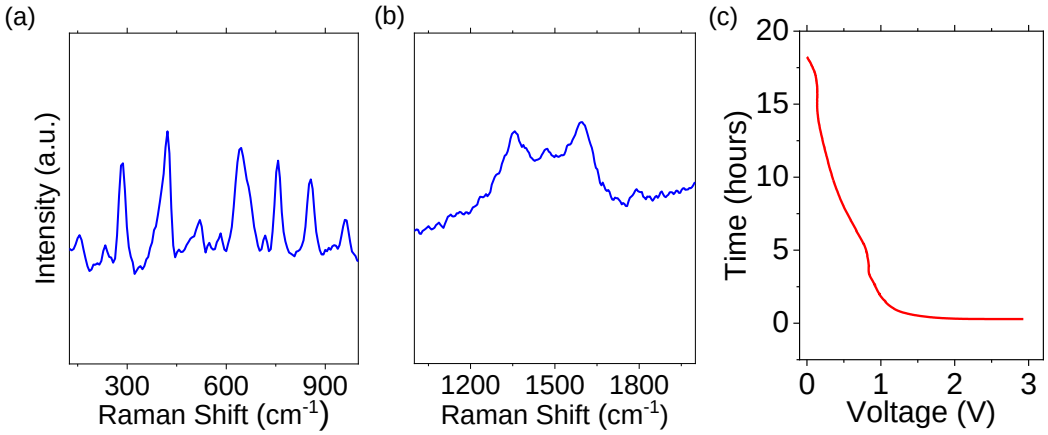


Figure S7.4. Raman spectrum of TiO_2 slurry electrode in Na-ion half-cell during discharge upon first appearance of Na titanate Raman modes obtained using a laser specific power of 20 mW. Lower frequency region of the same spectrum where carbon D and G bands appear along with a lower intensity band corresponding to methylene. (c) Voltage-time profile for the galvanostatic discharge of the Na-ion half-cell at 10 mA g^{-1} from which all spectra in Figure 7.9 of the main text were acquired.

The sapphire window is transparent to the 532 nm Raman laser and despite a thickness of only 0.2 mm, does slightly attenuate the Raman signal compared to the bare electrode. Sealing the cell applies pressure to the electrode material, which can also attenuate the signal. The decomposed electrolyte species also cause signal attenuation where present, as the Raman laser must penetrate through this layer to reach the electrode material. The decomposed electrolyte salt and solvent peaks are clearly observed.

However, on assembly of the Li-ion cell, the fluorescence signal masks identification of these peaks.

Figure S7.4 (a) shows an operando Raman spectrum for the TiO_2 slurry anode in Na-ion half-cell where the Na titanate peaks were first identified. Figure S7.4 (b) shows the presence of the carbon D and G bands in the higher frequency region along with an additional Raman mode between the two, associate with a methylene vibration, with methylene present in PC, the Na-ion electrolyte solvent. In Figure S7.4 (c), the voltage-time profile corresponding to the operando spectra of the Na-ion half-cell tests is shown. The cell was discharged from 3-0.5 V. The discharge from 3-2 V proceeds in less than ~20 minutes, comparably rapid to the remainder of the discharge which proceeds from 2-0.1 V in 18 hours. The contrast in discharge rate is due to the lack of electrochemical activity from 3-2 V. The reactions which govern the sodiation of TiO_2 occur below this range, causing a significant voltage plateau.

7.7. References

1. *Nature Communications*, **13**, 4723 (2022).
2. J. R. Rodriguez, S. B. Aguirre and V. G. Pol, *Electrochimica Acta*, **319**, 791 (2019).
3. D. Dixon, M. Ávila, H. Ehrenberg and A. Bhaskar, *ACS Omega*, **4**, 9731 (2019).
4. J. R. Rodriguez, S. B. Aguirre and V. G. Pol, *Journal of Power Sources*, **437**, 226851 (2019).
5. J. M. Bray, C. L. Doswell, G. E. Pavlovskaya, L. Chen, B. Kishore, H. Au, H. Alptekin, E. Kendrick, M.-M. Titirici, T. Meersmann and M. M. Britton, *Nature Communications*, **11**, 2083 (2020).
6. J.-H. Tian, T. Jiang, M. Wang, Z. Hu, X. Zhu, L. Zhang, T. Qian and C. Yan, *Small Methods*, **4**, 1900467 (2020).
7. J. Tan, D. Liu, X. Xu and L. Mai, *Nanoscale*, **9**, 19001 (2017).
8. E. C. Miller, R. M. Kasse, K. N. Heath, B. R. Perdue and M. F. Toney, *Journal of The Electrochemical Society*, **165**, A6043 (2018).
9. T. C. M. Nepel, C. G. Anchieta, L. F. Cremasco, B. P. Sousa, A. N. Miranda, L. C. C. B. Oliveira, B. A. B. Francisco, J. P. d. O. Júlio, F. C. B. Maia, R. O. Freitas, C. B. Rodella, R. M. Filho and G. Doubek, *Advanced Energy Materials*, **11**, 2101884 (2021).
10. Z. Khan, M. Vagin and X. Crispin, *Advanced Science*, **7**, 1902866 (2020).
11. P. Loktionov, R. Pichugov, D. Konev, M. Petrov, A. Pustovalova and A. Antipov, *Journal of Electroanalytical Chemistry*, **925**, 116912 (2022).
12. C. Jia, Q. Liu, C.-J. Sun, F. Yang, Y. Ren, S. M. Heald, Y. Liu, Z.-F. Li, W. Lu and J. Xie, *ACS Applied Materials & Interfaces*, **6**, 17920 (2014).
13. B. Wu, R. L. E. G. Aspers, A. P. M. Kentgens and E. W. Zhao, *Journal of Magnetic Resonance*, **351**, 107448 (2023).
14. S. V. Modak, W. Shen, S. Singh, D. Herrera, F. Oudeif, B. R. Goldsmith, X. Huan and D. G. Kwabi, *Nature Communications*, **14**, 3602 (2023).
15. C. Gervillié-Mouravieff, C. Boussard-Plédel, J. Huang, C. Leau, L. A. Blanquer, M. B. Yahia, M. L. Doublet, S. T. Boles, X. H. Zhang, J. L. Adam and J. M. Tarascon, *Nature Energy*, **7**, 1157 (2022).
16. R. Wang, H. Zhang, Q. Liu, F. Liu, X. Han, X. Liu, K. Li, G. Xiao, J. Albert, X. Lu and T. Guo, *Nature Communications*, **13**, 547 (2022).
17. E. Miele, W. M. Dose, I. Manyakin, M. H. Frosz, Z. Ruff, M. F. L. De Volder, C. P. Grey, J. J. Baumberg and T. G. Euser, *Nature Communications*, **13**, 1651 (2022).
18. A. Ghannoum, R. C. Norris, K. Iyer, L. Zdravkova, A. Yu and P. Nieva, *ACS Appl Mater Interfaces*, **8**, 18763 (2016).
19. J. Huang, L. Albero Blanquer, J. Bonefacino, E. R. Logan, D. Alves Dalla Corte, C. Delacourt, B. M. Gallant, S. T. Boles, J. R. Dahn, H.-Y. Tam and J.-M. Tarascon, *Nature Energy*, **5**, 674 (2020).
20. K. S. C. Kuang, R. Kenny, M. P. Whelan, W. J. Cantwell and P. R. Chalker, *Composites Science and Technology*, **61**, 1379 (2001).
21. J. A. Guemes and J. M. Menéndez, *Composites Science and Technology*, **62**, 959 (2002).

22. C.-J. Bae, A. Manandhar, P. Kiesel and A. Raghavan, *Energy Technology*, **4**, 851 (2016).
23. R. Pandya, L. Valzania, F. Dorchies, F. Xia, J. Mc Hugh, A. Mathieson, H. J. Tan, T. G. Parton, L. Godeffroy, K. Mazloomian, T. S. Miller, F. Kanoufi, M. De Volder, J.-M. Tarascon, S. Gigan, H. B. de Aguiar and A. Grimaud, *Nature Nanotechnology*, **18**, 1185 (2023).
24. X. Lu, M. Lagnoni, A. Bertei, S. Das, R. E. Owen, Q. Li, K. O'Regan, A. Wade, D. P. Finegan, E. Kendrick, M. Z. Bazant, D. J. L. Brett and P. R. Shearing, *Nature Communications*, **14**, 5127 (2023).
25. K.-H. Shin, C.-S. Jin, J.-Y. So, S.-K. Park, D.-H. Kim and S.-H. Yeon, *Journal of Energy Storage*, **27**, 101066 (2020).
26. A. Vizintin, J. Bitenc, A. Kopač Lautar, K. Pirnat, J. Grdadolnik, J. Stare, A. Randon-Vitanova and R. Dominko, *Nature Communications*, **9**, 661 (2018).
27. M. Matsui, S. Deguchi, H. Kuwata and N. Imanishi, *Electrochemistry*, **83**, 874 (2015).
28. N. Saqib, C. M. Ganim, A. E. Shelton and J. M. Porter, *Journal of The Electrochemical Society*, **165**, A4051 (2018).
29. A. Rafie, R. Pereira, A. A. Shamsabadi and V. Kalra, *The Journal of Physical Chemistry C*, **126**, 12327 (2022).
30. J. Bitenc, A. Vizintin, J. Grdadolnik and R. Dominko, *Energy Storage Materials*, **21**, 347 (2019).
31. N. Saqib, G. M. Ohlhausen and J. M. Porter, *Journal of Power Sources*, **364**, 266 (2017).
32. J. Fawdon, J. Ihli, F. L. Mantia and M. Pasta, *Nature Communications*, **12**, 4053 (2021).
33. W. Zhu, D. Liu, A. Paolella, C. Gagnon, V. Gariépy, A. Vijh and K. Zaghib, *Frontiers in Energy Research*, **6** (2018).
34. R. Zhang, Y. Wu, Z. Chen, Y. Wang, J. Zhu and X. Zhuang, *Journal of Materials Chemistry A*, **11**, 19195 (2023).
35. X.-q. Cheng, H.-j. Li, Z.-x. Zhao, Y.-z. Wang and X.-m. Wang, *New Carbon Materials*, **36**, 93 (2021).
36. A. Gajan, C. Lecourt, B. E. Torres Bautista, L. Fillaud, J. Demeaux and I. T. Lucas, *ACS Energy Letters*, **6**, 1757 (2021).
37. N. Mozhzhukhina, E. Flores, R. Lundström, V. Nyström, P. G. Kitz, K. Edström and E. J. Berg, *The Journal of Physical Chemistry Letters*, **11**, 4119 (2020).
38. D. Chen, M. A. Mahmoud, J.-H. Wang, G. H. Waller, B. Zhao, C. Qu, M. A. El-Sayed and M. Liu, *Nano Letters*, **19**, 2037 (2019).
39. T. E. Rosser, E. J. F. Dickinson, R. Raccichini, K. Hunter, A. D. Searle, C. M. Kavanagh, P. J. Curran, G. Hinds, J. Park and A. J. Wain, *Journal of The Electrochemical Society*, **168**, 070541 (2021).
40. E. Flores, N. Vonrüti, P. Novák, U. Aschauer and E. J. Berg, *Chemistry of Materials*, **30**, 4694 (2018).
41. A. Krause, O. Tkacheva, A. Omar, U. Langklotz, L. Giebeler, S. Dörfler, F. Fauth, T. Mikolajick and W. M. Weber, *Journal of The Electrochemical Society*, **166**, A5378 (2019).
42. Y. Zhang, J. Li, L. Ma, H. Li, X. Xu, X. Liu, T. Lu and L. Pan, *Chemical Engineering Journal*, **427**, 130936 (2022).
43. M. Radtke and C. Hess, *Molecules*, **26** (2021).

44. J.-Y. Shih, G.-Y. Lin, Y.-J. J. Li, T.-F. Hung, R. Jose, C. Karuppiah and C.-C. Yang, *Electrochimica Acta*, **419**, 140356 (2022).
45. D. Chen, D. Ding, X. Li, G. H. Waller, X. Xiong, M. A. El-Sayed and M. Liu, *Chemistry of Materials*, **27**, 6608 (2015).
46. D. M. Josepetti, B. P. Sousa, S. A. J. Rodrigues, R. G. Freitas and G. Doubek, *Journal of Energy Chemistry* (2023).
47. K. Li, D. Lin, H. Huang, D. Liu, B. Li, S.-Q. Shi, F. Kang, T.-Y. Zhang and L. Zhou, *Nano Energy*, **75**, 104977 (2020).
48. R. N. Samajdar, S. Marchesini, S. A. Brown, S. D. Robertson, K. R. Paton, A. J. Pollard and A. J. Wain, *ACS Energy Letters*, **8**, 1864 (2023).
49. C. Huang, Z. Feng, F. Pei, A. Fu, B. Qu, X. Chen, X. Fang, H. Kang and J. Cui, *ACS Applied Materials & Interfaces*, **12**, 35532 (2020).
50. A. Grant and C. O'Dwyer, *Applied Physics Reviews*, **10** (2023).
51. E. Flores, P. Novák and E. J. Berg, *Frontiers in Energy Research*, **6** (2018).
52. Y. Matsuda, N. Kuwata, T. Okawa, A. K. Dorai, O. Kamishima and J. Kawamura, *Solid State Ionics*, **335**, 7 (2019).
53. F. Adar, *Spectroscopy -Springfield then Eugene then Duluth-*, **25**, 16 (2010).
54. L. Cabo-Fernandez, A. Neale, F. Braga, I. Sazanovich, R. Kostecki and L. Hardwick, *Physical Chemistry Chemical Physics*, **21** (2019).
55. G. Bouteau, A. N. Van-Nhien, M. Sliwa, N. Sergent, J.-C. Lepretre, G. Gachot, I. Sagaidak and F. Sauvage, *Scientific Reports*, **9**, 135 (2019).
56. M. Evertz, C. Lürenbaum, B. Vortmann, M. Winter and S. Nowak, *Spectrochimica Acta Part B: Atomic Spectroscopy*, **112**, 34 (2015).
57. Y. Yu, P. Karayaylali, Y. Katayama, L. Giordano, M. Gauthier, F. Maglia, R. Jung, I. Lund and Y. Shao-Horn, *The Journal of Physical Chemistry C*, **122**, 27368 (2018).
58. A. J. Louli, L. D. Ellis and J. R. Dahn, *Joule* (2019).
59. W. Liu, X. Huang, L. Guobao, Z. Wang, H. Huang, L. Zhonghua, R. Xue and L. Chen, *Journal of Power Sources*, **68**, 344 (1997).
60. S. Paul, M. A. Rahman, S. B. Sharif, J.-H. Kim, S.-E.-T. Siddiqui and M. A. M. Hossain, *Nanomaterials*, **12**, 2034 (2022).
61. S. Moitzheim, S. De Gendt and P. M. Vereecken, *Journal of The Electrochemical Society*, **166**, A1 (2019).
62. M. Fehse, A. Henry, A. Zitolo, B. Boury, N. Louvain and L. Stievano, *Applied Sciences*, **10**, 5547 (2020).
63. K. Li, J. Zhang, D. Lin, D.-W. Wang, B. Li, W. Lv, S. Sun, Y.-B. He, F. Kang, Q.-H. Yang, L. Zhou and T.-Y. Zhang, *Nature Communications*, **10**, 725 (2019).
64. H. Sun and K. Zhao, *The Journal of Physical Chemistry C*, **121**, 6002 (2017).
65. X. L. Wang, K. An, L. Cai, Z. Feng, S. E. Nagler, C. Daniel, K. J. Rhodes, A. D. Stoica, H. D. Skorpenske, C. Liang, W. Zhang, J. Kim, Y. Qi and S. J. Harris, *Sci Rep*, **2**, 747 (2012).
66. R. Ruther, A. Callender, H. Zhou, S. Martha and J. Nanda, *Journal of The Electrochemical Society*, **162**, A98 (2015).
67. L. El-Farh, M. Massot, M. Lemal, C. Julien, S. Chitra, P. Kalyani, T. Mohan and R. Gangadharan, *Journal of Electroceramics*, **3**, 425 (1999).

68. M. Inaba, Y. Iriyama, Z. Ogumi, Y. Todzuka and A. Tasaka, *Journal of Raman Spectroscopy*, **28**, 613 (1997).
69. C. M. Julien, *Materials Science and Engineering: R: Reports*, **40**, 47 (2003).
70. S. Marchesini, B. P. Reed, H. Jones, L. Matjacic, T. E. Rosser, Y. Zhou, B. Brennan, M. Tiddia, R. Jervis, M. J. Loveridge, R. Raccichini, J. Park, A. J. Wain, G. Hinds, I. S. Gilmore, A. G. Shard and A. J. Pollard, *ACS Applied Materials & Interfaces*, **14**, 52779 (2022).
71. S.-J. Cho, C.-C. Chung, S. Podowitz-Thomas and J. L. Jones, *Materials Chemistry and Physics*, **228**, 32 (2019).
72. X. Zhang, A. Mauger, Q. Lu, H. Groult, L. Perrigaud, F. Gendron and C. M. Julien, *Electrochimica Acta*, **55**, 6440 (2010).
73. G. H. Watson, Jr., W. B. Daniels and C. S. Wang, *Journal of Applied Physics*, **52**, 956 (1981).
74. D. McNulty, E. Carroll and C. O'Dwyer, *Advanced Energy Materials*, **7**, 1602291 (2017).
75. C. Fan, X. Wang, X. Wu, Y. Chen, Z. Wang, M. Li, D. Sun, Y. Tang and G. Fu, *Advanced Energy Materials*, **13**, 2203244 (2023).
76. H. B. Li, M. H. Yu, X. H. Lu, P. Liu, Y. Liang, J. Xiao, Y. X. Tong and G. W. Yang, *ACS Applied Materials & Interfaces*, **6**, 745 (2014).
77. J. Yang, H. Liu, W. N. Martens and R. L. Frost, *The Journal of Physical Chemistry C*, **114**, 111 (2010).
78. S. R. Shieh and T. S. Duffy, *Physical Review B*, **66**, 134301 (2002).
79. J. L. Allen, O. Borodin, D. M. Seo and W. A. Henderson, *Journal of Power Sources*, **267**, 821 (2014).
80. S.-A. Hyodo and K. Okabayashi, *Electrochimica Acta*, **34**, 1551 (1989).
81. S. Maeda, Y. Kameda, Y. Amo, T. Usuki, K. Ikeda, T. Otomo, M. Yanagisawa, S. Seki, N. Arai, H. Watanabe and Y. Umebayashi, *The Journal of Physical Chemistry B*, **121**, 10979 (2017).
82. E. Cazzanelli, F. Croce, G. B. Appetecchi, F. Benevelli and P. Mustarelli, *Journal of Chemical Physics*, **107**, 5740 (1997).
83. M. Morita, Y. Asai, N. Yoshimoto and M. Ishikawa, *Journal of the Chemical Society - Faraday Transactions*, **94**, 3451 (1998).
84. B. Fortunato, P. Mirone and G. Fini, *Spectrochimica Acta Part A: Molecular Spectroscopy*, **27**, 1917 (1971).
85. J. R. Durig, G. L. Coulter and D. W. Wertz, *Journal of Molecular Spectroscopy*, **27**, 285 (1968).
86. G. Abed, A. Al-sammarraie and B. Al-Abdaly, (2017).
87. J. N. Díaz de León, J. R. Rodríguez, J. Rojas, Y. Esqueda-Barrón, L. Cardenas, C. Ramesh Kumar, G. Alonso-Nuñez and S. Fuentes-Moyado, *Frontiers in Chemistry*, **7** (2019).
88. J. Liu, M. N. Banis, B. Xiao, Q. Sun, A. Lushington, R. Li, J. Guo, T.-K. Sham and X. Sun, *Journal of Materials Chemistry A*, **3**, 24281 (2015).
89. S. Chaar, J. Silva, F. Nobre, J. Passos, L. Aguilera, J. Silva, R. Silva, F. Guerrero, F. Pontes and Y. Leyet, *Materials Research*, **24** (2021).
90. G. J. Janz, J. Ambrose, J. W. Coutts and J. R. Downey, *Spectrochimica Acta Part A: Molecular Spectroscopy*, **35**, 175 (1979).
91. S. Xiao, J. Kolb, M. Malik, X. Lu, M. Laroussi, R. Joshi, E. Schamiloglu and K. Schoenbach, *Plasma Science, IEEE Transactions on*, **34**, 1653 (2006).

92. P. J. Zanzucchi, M. T. Duffy and R. C. Alig, *Journal of The Electrochemical Society*, **125**, 299 (1978).
93. Y. Wang, S. Liu, G. Peng, S. Zhou and J. Xu, *Journal of Crystal Growth*, **274**, 241 (2005).
94. W. Jia and W. M. Yen, *Journal of Raman Spectroscopy*, **20**, 785 (1989).
95. P. J. Zanzucchi and M. T. Duffy, *Appl. Opt.*, **17**, 3477 (1978).
96. J. Hedman, D. Nilebo, E. Larsson Langhammer and F. Björefors, *ChemSusChem*, **13**, 5731 (2020).
97. R. Pandya, A. Mathieson, B. D. Boruah, H. B. de Aguiar and M. de Volder, *Nano Letters*, **23**, 7288 (2023).
98. Y. Zhang, Y. Li, Z. Guo, J. Li, X. Ge, Q. Sun, Z. Yan, Z. Li and Y. Huang, *eScience*, 100174 (2023).
99. J. Hedman, R. Mogensen, R. Younesi and F. Björefors, *ACS Applied Energy Materials*, **5**, 6219 (2022).
100. B. Chen, H. Zhang, J. Xuan, G. J. Offer and H. Wang, *Advanced Materials Technologies*, **5**, 2000555 (2020).
101. R. A. Zárate, S. Fuentes, J. P. Wiff, V. M. Fuenzalida and A. L. Cabrera, *Journal of Physics and Chemistry of Solids*, **68**, 628 (2007).
102. I. Zeydabadi-Nejad, N. Zolfaghari, M. Mousavi Mashhadi, M. Baghani and M. Baniassadi, *Sustainable Energy Technologies and Assessments*, **47**, 101438 (2021).
103. M. Giarola, A. Sanson, F. Monti, G. Mariotto, M. Bettinelli, A. Speghini and G. Salviulo, *Physical Review B*, **81**, 174305 (2010).

Chapter 8

Conclusions and Future Perspectives

8.1. Thesis Conclusions

Rapid advancement and incorporation of rechargeable battery technology for the storage of renewable energy using sustainable materials is a key access route towards mitigating the rapidly increasing carbon footprint associated with climate change. Success in this regard will be based upon sufficiently developed analytical tools used to identify, with specificity, suboptimal features of current technologies and troubleshoot their root causes, along with building accurate models to predict the performance of new technologies. These requirements prompt the cooperation between the environmental science, materials science, computer science, photonics, electrochemistry, and of course, battery communities. Such cooperation between communities provides a view of the energy problem through a variable lens that can build an arsenal of complementary battery performance diagnostics. Macroporous metal oxide battery electrodes provide a host of properties beneficial to energy storage and supply including high surface area to volume ratio for high gravimetric energy density and tolerance for the inevitable structural deformation which deteriorates operation. Furthermore, these exciting materials provide opportunities for the incorporation of operando probes which can be used to monitor battery performance in real time. This PhD capitalised on the synergy between optical, structural, and electrochemical characteristics of PhC electrode materials that can be used to implement operando battery performance diagnostics in real-time.

The literature review in **Chapter 2** provided a comprehensive overview of operando spectroscopic methods applied to battery electrode materials.

State-of-the-art spectroscopic tools using incident energy spanning the electromagnetic spectrum were included. The review was written from the point of view of the battery chemist interested in applying these techniques to their system. For each technique, the underlying concepts inherent to understanding its application were summarised. Exemplary case studies were referenced to showcase some of the key insights gleaned from their application to a range of battery technologies, typically addressing recurring issues specific to each system. Examples included the polysulfide “shuttle” effect in Li-S batteries, volume expansion in conversion/alloy electrode materials, and dendrite formation in Li metal batteries. Perhaps the most useful aspect of the review were the detailed requirements provided in optimising the methodology for successful analysis, where the key was shown typically to lie in the appropriate operando cell design. For each group of techniques, cell design, benefits, limitations, and resolution were summarised. The review stands as a manual which can act both as a starting point for early-stage researchers eager to delve into operando measurements for the first time, and the experienced researcher seeking to optimise current methodologies.

Chapter 3 described the sample preparation, experimental methodologies and characterisation methods used throughout the thesis. For any parties interested in replicating these experiments, careful attention to the details provided therein will allow replication of results. The provided details regarding characterisation methods simplify interpretation of the associated results presented in each chapter. These details are particularly useful for less intuitive analyses which are used to describe key outcomes of each study,

such as the three-dimensional angle-resolved transmission spectra in Chapters 4-5, the differential capacity colormaps in Chapter 6, and the operando Raman spectroscopy colormaps in Chapter 7.

Chapter 4 evaluated the criteria required for the simultaneous control of both thickness and order for opal PhCs grown using a particular adaptation of the long established evaporation-induced self-assembly (EISA) method of colloidal crystal growth under the conditions of large sphere solution surface area and low evaporation temperature compared to typical literature reports. The effects of order and thickness on the associated optical fingerprints were determined using angle-resolved transmission spectra. The relationship between volume fraction and crystal thickness were established using five sphere solution volume fractions at three evaporation temperatures. For highly ordered opals, light propagation within their structures can be described using the Bragg-Snell model. The conditions under which the model breaks down were identified as the three lowest volume fractions at the lowest evaporation rate where evaporation is too slow and available spheres are too few to facilitate the consistent growth of close-packed sphere arrays such that FCC symmetry could be maintained. The investigation revealed the extent to which the PBG (PBG) and other spectral features can be employed to assess the degree of (dis)order and crystal thickness in opal growth.

Chapter 5 demonstrated further observations based on opal growth by EISA. Opals under all investigated conditions exhibited a thickness gradient along which stacking order decreased. A reduction in the reflectivity along the gradient was observed. The results revealed a clear asymmetry in the spectral

response of the opal, observed as an increase in transmission intensity in the spectral window of the PBG along the thickness gradient. This chapter underscored the care needed in assessing the overall transmission response for opals that that may be used for applications where order and periodicity are crucial, such as macroporous battery electrodes.

Chapter 6 presented a comparative investigation into the performance of macroporous IO (IO) SnO_2 electrodes in Li-ion and Na-ion batteries. The work in this chapter was motivated by the abundance, low-cost, and sustainability of Na as charge carrier and SnO_2 as anode material. The central issue addressed in this chapter was the large volume expansion which arises in SnO_2 electrodes during cycling that accompanies the high energy density that the system offers.

Galvanostatic cycling demonstrated that the capacity retention of the Na-ion system was remarkably higher than the Li-ion system. Cyclic voltammetry analysis at a range of scan rates indicated that the irreversibility of the oxidation reaction from metallic Sn to SnO_2, while sacrificing the capacity delivered by the reaction, reduced the extent of volume expansion which stabilised the system. Rate capability testing demonstrated rate performance commensurate with a range of SnO_2-based nanostructures from the literature, including excellent capacity recovery after high-rate cycling due to the characteristics of the IO structure. The macroporosity of the IO can acts as a buffer for volume expansion and the thin IO pore walls reduce ion diffusion distances, where ion diffusion is the rate limiting step in the transportation mechanism of ions in both Li-ion and Na-ion batteries. Differential capacity

analysis performed on the data extracted from these rate tests supported the earlier CV analysis, indicating that the irreversibility of the conversion reaction from metallic Sn to SnO_2 during cycling was maintained here, and contributed to the competitive rate performance of the system.

In **Chapter 7**, a method was devised to show how battery materials and electrolytes behave in real-time using operando Raman scattering spectroscopy. The key development was several iterations of material and battery cell assembly that can allow the reactive chemistry of organic electrolytes and group 1 metals to operate perfectly outside the Argon glovebox environment in a hermetically sealed cell with a sapphire glass window. This allowed the electrolyte to be examined during charging and discharging, probing not only the PhC battery materials, but also thin film commercial NMC formulations used in current Li-ion cells, as well as material in Na-ion systems, for the first time. Furthermore, a method was developed to examine the battery behaviour by monitoring the changes of optical density near the interface with the sapphire window, so that the changes to intensity of the sapphire Raman modes acted as a proxy for evolving processes in the battery, all examined as a function of voltage and state of charge of the cell.

In summary, the PhD thesis summarised here showcased how the structure of battery electrode materials can be directed towards excellence using non-destructive optical spectroscopy. These macroporous electrodes demonstrated excellent capacity retention and rate performance using abundant and environmentally friendly materials. With both structural reproduction and electrochemical performance established, the design and

implementation of the first PhC lab-based tool for real-time battery diagnostics was demonstrated in a body of work that progressed from fundamental optics and electrochemistry to the design of a high-level operando methodology.

8.2. Future Perspectives

The importance of batteries in today's world is undoubted. From a research perspective, and in our lab too, searching for new classes of sustainable materials and electrode technology development is a main goal. This is becoming ever more important as Na-ion technology begins to ramp up internationally to deal with sustainability issues around Li supply and its recyclability. What many groups are starting to realise, in parallel with computational predictions of materials and behaviour, is that real-time operando methods are going to become very important for assessing material chemistry and electrochemistry for many technologies, including batteries. Basically, we want to be able to monitor the state of health of batteries continuously during operation to minimise their degradation – but also to predict better materials.

Initiatives are currently in place at an international level to radically transform the discovery and development of ultra-high-performance, safe, sustainable, and affordable batteries for use in everyday applications, from portable electronics to grid-level energy storage. At the forefront of these initiatives is Battery 2030+, a long-term roadmap for forward looking European battery research, involving a collective effort across the continent. Nanostructure design, new sustainable battery materials, and methods that quickly and accurately uncover what happens inside the cell in real time are

the cutting edge of these initiatives. Developing such a system can crosscut into many arenas. We have a new method here that has a lot of future potential. The technique developed here, involving proving out modifications to create bespoke cells and successful examination of materials and electrolytes in several types of batteries in real-time can be used push the frontiers of increasingly complex modern energy storage technology. This technique is a synergistic approach combining principles from physics, materials chemistry, electrochemistry, and spectroscopy which demonstrates how communication between these communities may act as a stepping stone to a green energy future and a valuable aid to current global initiatives.